Institut für Theoretische Physik
FAKULTÄT MATHEMATIK UND NATURWISSENSCHAFTEN
TECHNISCHE UNIVERSITÄT DRESDEN

Genetic Oscillations and Vertebrate Embryonic Development

DISSERTATION
zur Erlangung des akademischen Grades
Doctor rerum naturalium
(Dr. rer. nat.)

vorgelegt von
DAVID JOSEF JÖRG
geboren am 7. September 1983
in Weinheim

MAX-PLANCK-INSTITUT
FÜR PHYSIK KOMPLEXER SYSTEME

DRESDEN, 2014

Eingereicht am
03.07.2014

Verteidigt am
17.12.2014

Erster Gutachter
PROF. DR. FRANK JÜLICHER
Zweiter Gutachter
PROF. DR. STEPHAN GRILL

Abstract

Recurrent processes are a general feature of living systems, from the cell cycle to circadian day-night rhythms to hibernation and flowering cycles. During development and life, numerous recurrent processes are controlled by genetic oscillators, a specific class of genetic regulatory networks that generates oscillations in the level of gene products. A vital mechanism controlled by genetic oscillators is the rhythmic and sequential segmentation of the elongating body axis of vertebrate embryos. During this process, a large collection of coupled genetic oscillators gives rise to spatio-temporal wave patterns of oscillating gene expression at tissue level, forming a dynamic prepattern for the precursors of the vertebrae. While such systems of genetic oscillators have been studied extensively over the past years, many fundamental questions about their collective behavior remain unanswered. In this thesis, we study the behavior and the properties of genetic oscillators from the single oscillator scale to the complex pattern forming system involved in vertebrate segmentation.

Genetic oscillators are subject to fluctuations because of the stochastic nature of gene expression. To study the effects of noisy biochemical coupling on genetic oscillators, we propose a theory in which both the internal dynamics of the oscillators as well as the coupling process are inherently stochastic. We find that stochastic coupling of oscillators profoundly affects their precision and synchronization properties, key features for their viability as biological pacemakers. Moreover, stochasticity introduces phenomena not known from deterministic systems, such as stochastic switching between different modes of synchrony.

During vertebrate segmentation, genetic oscillators play a key role in establishing a segmental prepattern on tissue scale. We study the spatio-temporal patterns of oscillating gene expression using a continuum theory of coupled phase oscillators. We investigate the effects of different biologically relevant factors such as delayed coupling due to complex signaling processes, local tissue growth, and tissue shortening on pattern formation and segmentation. We find that the decreasing tissue length induces a Doppler effect that contributes to the rate of segment formation in a hitherto unanticipated way. Comparison of our theoretical findings with experimental data reveals the occurrence of such a Doppler effect *in vivo*. To this end, we develop quantification methods for the spatio-temporal patterns of gene expression in developing zebrafish embryos.

On a cellular level, tissues have a discrete structure. To study the interplay of cellular processes like cell division and random cell movement with pattern formation, we go beyond the coarse-grained continuum theories and develop a three-dimensional cell-based model of vertebrate segmentation, in which the dynamics of the segmenting tissue emerges from the collective behavior of individual cells. We show that this model is able to describe tissue formation and segmentation in a self-organized way. It provides the first step of theoretically describing pattern formation and tissue dynamics during vertebrate segmentation in a unified framework involving a three-dimensional tissue with cells as distinct mechanical entities.

Finally, we study the synchronization dynamics of generic oscillator systems whose coupling is subject to phase shifts and time delays. Such phase shifts and time delays are induced by complex signaling processes as found, e.g., between genetic oscillators. We show how phase shifts and coupling delays can alter the synchronization dynamics while leaving the collective frequency of the synchronized oscillators invariant. We find that in globally coupled systems, fastest synchronization occurs for non-vanishing coupling delays while in spatially extended systems, fastest synchronization can occur on length scales larger than the coupling range, giving rise to novel synchronization scenarios. Beyond their potential relevance for biological systems, these results have implications for general oscillator systems, e.g., in physics and engineering.

In summary, we use discrete and continuous theories of genetic oscillators to study their dynamic behavior, comparing our theoretical results to experimental data where available. We cover a wide range of different topics, contributing to the general understanding of genetic oscillators and synchronization and revealing a hitherto unknown mechanism regulating the timing of embryonic pattern formation.

Zusammenfassung

Wiederkehrende Prozesse sind ein allgemeines Merkmal lebender Systeme, vom Zellzyklus über zirkadiane Tag-Nacht-Rhythmen bis hin zu Winterschlaf- und Blütezyklen. Während der Entwicklung und des Lebensverlaufs lebender Systeme werden eine Vielzahl solcher wiederkehrender Prozesse von genetischen Oszillatoren gesteuert, einer spezifischen Klasse von genetisch regulativen Netzwerken, die Oszillationen in der Konzentration von Genprodukten erzeugen. Ein lebenswichtiger Mechanismus, der von genetischen Oszillatoren gesteuert wird, ist die rhythmische und sequenzielle Segmentierung der Körperachse in Wirbeltierembryonen. Während dieses Vorgangs erzeugt ein großer Verbund gekoppelter genetischer Oszillatoren raumzeitliche Wellenmuster auf Gewebeebene, die ein vorgängiges dynamisches Muster für die Wirbelvorläufer bilden. Obwohl solche Systeme genetischer Oszillatoren in der Vergangenheit umfangreich studiert wurden, bleiben viele grundsätzliche Fragen über ihr kollektives Verhalten offen. In dieser Dissertation studieren wir das Verhalten und die Eigenschaften genetischer Oszillatoren vom einzelnen Oszillator bis hin zum komplexen Musterbildungssystem, das an der Wirbeltiersegmentierung beteiligt ist.

Genetische Oszillatoren sind Fluktuationen ausgesetzt, bedingt durch die stochastische Natur der Genexpression. Um die Effekte biochemischer Kopplung auf genetische Oszillatoren zu studieren, entwickeln wir eine Theorie, in welcher sowohl die interne Dynamik der Oszillatoren als auch der Kopplungsprozess als inhärent stochastisch beschrieben werden. Es wird gezeigt, dass stochastische Kopplung der Oszillatoren sowohl ihre Präzision als auch ihre Synchronisationseigenschaften tiefgreifend beeinflussen kann, beides Schlüsselmerkmale für ihre Viabilität als biologische Zeitgeber. Weiterhin führt die Stochastizität zu Phänomenen, die von deterministischen Systemen nicht bekannt sind, wie dem stochastischen Wechsel zwischen verschiedenen Modi der Synchronisation.

Während der Wirbeltiersegmentierung spielen genetische Oszillatoren eine Schlüsselrolle bei der Erzeugung eines vorgängigen Segmentmusters auf Gewebeebene. Wir studieren die raumzeitlichen Muster oszillierender Genexpression anhand einer Kontinuumstheorie gekoppelter Phasenoszillatoren. Wir untersuchen den Einfluss verschiedener biologisch relevanter Faktoren, wie verzögerter Kopplung aufgrund komplexer Signalprozesse, lokalem Gewebewachstum und Gewebeverkürzung auf Musterbildung und Segmentbildung. Es wird gezeigt, dass die Gewebeverkürzung einen Dopplereffekt verursacht, der zur Geschwindigkeit der Segmentbildung auf eine bisher unvorhergesehene Weise beiträgt. Wir vergleichen unsere theoretischen Ergebnisse mit experimentellen Daten und stellen das Auftreten eines solchen Dopplereffekts *in vivo* fest. Zu diesem Zweck entwickeln wir Quantifikationsmethoden für die raumzeitlichen Genexpressionsmuster in sich entwickelnden Zebrafisch-Embryonen.

Auf zellulärer Ebene haben Gewebe eine diskrete Struktur. Um die Wechselwirkung zwischen zellulären Prozessen wie Zellteilung und zufälliger Zellbewegung mit der Musterbildung zu studieren, gehen wir über Kontinuumstheorien hinaus und entwickeln ein dreidimensionales zellbasiertes Modell der Wirbeltiersegmentierung, in welchem die Dynamik des segmentierenden Gewebes durch das kollektive Verhalten einzelner Zellen entsteht. Wir zeigen, dass dieses Modell in der Lage ist, in einer selbstorganisierten Weise Gewebebildung und Segmentierung zu beschreiben. Dieses Modell bildet eine Ausgangsbasis, um Musterbildung und Gewebedynamik während der Segmentierung in einem einheitlichen Framework zu beschreiben, das ein dreidimensionales Gewebe mit Zellen als eigenständigen mechanischen Einheiten umfasst.

Schließlich studieren wir das Synchronisationsverhalten von generischen Oszillatorsystemen, deren Kopplung Phasenverschiebungen und Zeitverzögerungen unterliegt. Solche Phasenverschiebungen und Zeitverzögerungen werden von komplexen Signalprozessen verursacht, wie sie bspw. zwischen genetischen Oszillatoren stattfinden. Es wird gezeigt, wie solche Verzögerungen und Phasenverschiebungen die Synchronisationsdynamik verändern können, während sie die kollektive Frequenz der synchronisierten Oszillatoren invariant lassen. Weiterhin zeigen wir, dass global gekoppelte Systeme bei nicht-verschwindenden Kopplungsverzögerungen am schnellsten synchronisieren. In räumlich ausgedehnten Systemen kann die schnellste Synchronisation auf Längenskalen stattfinden, die größer sind als die Kopplungsreichweite, was zu neuartigen Synchronisationsszenarien führt. Über ihre potenzielle Relevanz für biologische Systeme hinaus haben diese Ergebnisse Bedeutung für allgemeine Oszillatorsysteme in Physik und Technik.

Zusammengefasst benutzen wir diskrete und kontinuierliche Theorien genetischer Oszillatoren zum Studium ihres dynamischen Verhaltens und vergleichen unsere theoretischen Ergebnisse mit experimentellen Daten sofern verfügbar. Wir behandeln dabei ein breites Spektrum an Themen und tragen zum allgemeinen Verständnis von genetischen Oszillatoren und Synchronisationsprozessen bei, wobei wir einen bisher unbekannten Mechanismus aufdecken, der den zeitlichen Ablauf embryonischer Musterbildung reguliert.

Acknowledgement

I would like to thank Prof. Frank Jülicher for the opportunity to work with him and to profit from his advice, support, encouragement, and criticism over the last years. Furthermore, I am indebted to Luis G. Morelli and Saúl Ares, two great scientists from whom I learned most of what I know about the theory of genetic oscillations and vertebrate segmentation. I thank Lucas Wetzel and Pablo Sartori Velasco for a fantastic time at and around MPI–PKS, scientifically and non-scientifically. Furthermore, I thank current and former members of the Biological Physics Division at MPI–PKS for providing a great working atmosphere and inspiring discussions, in particular (in alphabetical order) Silvanus Alt, Johannes Baumgart, Anna Erzberger, Benjamin Friedrich, Adrian Jacobo, Gary Klindt, Samuel Krüger, Matthias Merkel, Amitabha Nandi, Jochen Schneider, André Scholich, Koichiro Uriu, Steffen Werner, and David Zwicker.

The collaborative work with experimental scientists added a dimension to my work that I don't want to miss anymore. The reason for this is Prof. Andrew C. Oates and his lab members. In particular, I want to thank Daniele Soroldoni, Alexis B. Webb, and Ravi A. Desai, with whom I had the pleasure to collaborate, as well as (in alphabetical order) Christina Eugster, Rachna Narayanan, Annelie Oswald, Sandra Richter, Laurel Rohde, and Guillaume Valentin. Many results presented in this thesis arose out of this collaboration. I also want to thank Ayelen Coccoz, Shruti M. Desai, and Claire Poulet for their hospitality during various research stays. Many thanks to Prof. Stephan Grill for accepting to review this thesis.

My deepest gratitude goes to my family, my parents Christa and Benno Jörg for their constant and warm support, as well as Johannes Jörg, Marianne Sturm, Theo Metzler, and Brigitte Ochlich. I thank Julia Kynast for her great support, her infectious joie de vivre, and for enduring my moods during the last years. *In loving memory of Wolfgang Sturm.*

Contents

1 INTRODUCTION 1

1.1 Recurrence and Periodicity in Biology 1
- *1.1.1 Biological clocks* 1
- *1.1.2 Genetic oscillators* 2
- *1.1.3 Periodicity in development: vertebrate segmentation* 3
- *1.1.4 Functional relevance of temporal regularity* 4

1.2 Vertebrate Segmentation 5
- *1.2.1 The clock-and-wavefront model* 5
- *1.2.2 Wave patterns of oscillating genes* 6
- *1.2.3 Mechanisms of pattern formation* 6
- *1.2.4 Pattern coherence in a noisy environment* 7
- *1.2.5 Current view and open questions* 8
- *1.2.6 Zebrafish as a model organism* 9

1.3 Contents of this Thesis 10

2 MARKOV CHAIN MODELS OF COUPLED GENETIC OSCILLATORS 13

2.1 Markov Chain Models of Oscillators and Coupling 13
- *2.1.1 Markov chain model of an autonomous oscillator* 13
- *2.1.2 Markov chain model of coupled oscillators* 15
- *2.1.3 Quality factor as a measure for precision* 16
- *2.1.4 Cross correlation as a measure for synchrony* 18
- *2.1.5 Mutual information* 19
- *2.1.6 Product turnover* 19

2.2 Analysis of the Autonomous Oscillator 20
- *2.2.1 Time evolution of expectation values* 20
- *2.2.2 Deterministic limit* 21
- *2.2.3 Amplitude estimates* 21
- *2.2.4 Frequency and decorrelation rate estimates* 25

2.3 Precision and Synchronization of Coupled Oscillators 28
- *2.3.1 Complex signaling introduces coupling delays* 28
- *2.3.2 Enhancement of precision by coupling* 29
- *2.3.3 Is increased quality due to higher product turnover?* 31
- *2.3.4 Synchronization through coupling* 32
- *2.3.5 Stochastic switching between in-phase and anti-phase synchrony* 33
- *2.3.6 The collective frequency depends on coupling properties* 34
- *2.3.7 Nature of the coupling mechanism* 36

2.4 Phase Oscillator Approximation 38
- *2.4.1 Phase description of coupled oscillators* 38

2.4.2 Coupling with distributed delays 38
2.4.3 Synchronized states 39
2.4.4 Stability of the synchronized states 40
2.4.5 Comparison with the Markov chain model 43

2.5 Summary 46

3 CONTINUUM THEORY OF PATTERN FORMATION WITH OSCILLATORS 51

3.1 Pattern Formation with Oscillators 51
3.1.1 Coupled oscillators in a moving medium 51
3.1.2 Formation of kinematic wave patterns 53
3.1.3 Segment formation 54
3.1.4 Steady state 55

3.2 Oscillators with Delayed Coupling 57
3.2.1 Dynamic equation 57
3.2.2 Steady state 58
3.2.3 Effects of coupling delays on pattern formation 58
3.2.4 When do coupling delays have to be considered? 58

3.3 Coupled Oscillators in a Growing Medium 59
3.3.1 Dynamic equation 59
3.3.2 Steady state 61
3.3.3 Effects of local growth on pattern formation 61

3.4 Coupled Oscillators in a Medium of Changing Length 61
3.4.1 Dynamic equation 61
3.4.2 Decreasing tissue length induces a Doppler effect 62

3.5 Coupled Oscillators Interacting with Morphogens 66
3.5.1 Dynamic equations 66
3.5.2 Steady states of morphogen gradients 68
3.5.3 Self-organized segmentation 68

3.6 Summary 70

4 QUANTITATIVE BIOLOGY OF VERTEBRATE SEGMENTATION 77

4.1 Tissue Shortening and Tissue Deformation 77
4.1.1 Analysis of brightfield time-lapse movies 77
4.1.2 Time evolution of the presomitic mesoderm length 77
4.1.3 Velocity profile in the segmented region 78

4.2 Wave Patterns of Gene Expression 81
4.2.1 Imaging gene expression at tissue level 82
4.2.2 Using a wavelet transform to generate phase maps 82
4.2.3 Average phase map 84

4.3 Comparison of Theoretical and Experimental Results 86
4.3.1 Morphological segmentation 86
4.3.2 Kinematic wave patterns 87

4.4 A Doppler Effect in Embryonic Pattern Formation 88
4.4.1 A Doppler effect and a dynamic wavelength effect occur in vivo 88
4.4.2 The anterior frequency coincides with the rate of segmentation 90

4.5 Summary 91

5 CELL-BASED MODEL OF SELF-ORGANIZED SEGMENTATION 93

5.1 Cell-based Model with Dissipative Particle Dynamics 93
5.1.1 State space 94
5.1.2 Equations of motion 95
5.1.3 Interparticle forces 95
5.1.4 Boundary forces 97
5.1.5 Cell division 98
5.1.6 Morphogen dynamics 98
5.1.7 Phase dynamics 99
5.1.8 Cell differentiation 99

5.2 Self-organized Segmentation 100
5.2.1 Tissue formation and extension 100
5.2.2 Formation of a morphogen gradient and the presomitic mesoderm 101
5.2.3 Formation of kinematic waves 101
5.2.4 Segment formation 102

5.3 Summary 103

6 REGULATION OF SYNCHRONIZATION BY PHASE SHIFTS AND COUPLING DELAYS 109

6.1 Coupled Oscillators with Delays and Phase Shifts 109
6.1.1 Synchronization dynamics depends on coupling properties 109
6.1.2 Complex signaling induces coupling delays and phase shifts 109
6.1.3 Phase oscillator description 110
6.1.4 Equivalence of delays and phase shifts in the synchronized state 111

6.2 Motivating Examples 112
6.2.1 Synchronization of a globally coupled system 112
6.2.2 Synchronization of a nearest-neighbor coupled system 112

6.3 General Analysis of Synchronization Rates 113
6.3.1 Linear stability analysis 113
6.3.2 Characteristic equation 114
6.3.3 Synchronization rates of long-wavelength modes 115
6.3.4 Synchronization rates of short-wavelength modes 116
6.3.5 Symmetry of short and long wavelengths for large delays 117

6.4 Globally Coupled and Spatially Extended Systems 117
6.4.1 Fastest synchronization for non-zero delays 118
6.4.2 Fastest synchronization for intermediate wavelengths 118

6.5 Summary 120

7 SUMMARY AND OUTLOOK 123

A ANALYTICAL TREATMENT OF THE MARKOV CHAIN MODELS 129

A.1 Time Evolution of Expectation Values 129

A.2 Closed Governing Equations for Expectation Values 131
A.2.1 *Closed integro-differential equation for* $\langle x_n \rangle$ 131
A.2.2 *Closed integro-differential equation for* Γ 132
A.3 Characteristic Equation for the Autocorrelation 132
A.3.1 *Characterisic equation* 132
A.3.2 *Closed frequency estimate* 133
A.3.3 *Approximation of* η 134

B PHASE OSCILLATORS WITH DISTRIBUTED DELAYS 137
B.1 Phase Dynamics with Distributed Delays 137
B.2 Analytical Results for Synchronized States 138
B.2.1 *Collective frequency* 138
B.2.2 *Characteristic equation* 139

C SPATIAL CONTINUUM LIMITS OF COUPLED PHASE OSCILLATORS 141
C.1 Continuum Limit of Coupled Oscillators 141
C.1.1 *Derivation of the continuum limit* 141
C.1.2 *Phase dynamics in a comoving frame* 142
C.2 Continuum Limit of Delay-Coupled Oscillators 142
C.2.1 *Derivation of the continuum limit* 142
C.2.2 *Phase dynamics in a comoving frame* 144
C.3 Steady State Solution 144
C.3.1 *Phase profile* 144

D ANALYTICAL APPROXIMATION OF DOPPLER EFFECT AND DYNAMIC WAVELENGTH EFFECT 145

E STEADY STATES OF MORPHOGEN GRADIENTS 149
E.1 Approximation of the Steady State of Q 149
E.2 Approximation of the Steady State of R 153

F EXPERIMENTAL PHASE MAPS OF KINEMATIC WAVE PATTERNS 155
F.1 Generating Phase Maps using a Wavelet Transform 155
F.2 Construction of the Average Phase Map 157

G DECOUPLING PERTURBATION MODES BY FOURIER TRANSFORMATION 161

H NUMERICAL SIMULATIONS AND DATA PROCESSING 163

List of Figures 166

References 167

“*Erfahrung ist die Ursache.*
Die Welt ist die Folge.”

“Experience is the cause.
The world is the consequence.”

—Heinz von Foerster

Chapter 1
Introduction

> "While we can conceive of a sum [or aggregate] as being composed gradually, a system as a total of parts with its [multiplicative] interrelations has to be conceived of as being composed instantly." [157]
> —Ludwig von Bertalanffy

In this chapter, we introduce the concept of a biological clock and one of its most prominent representatives, the genetic oscillator. We discuss the importance of periodic processes for living systems and give a brief introduction to vertebrate segmentation, a vital developmental process controlled by genetic oscillators. Finally, we give an overview over the contents of this thesis.

1.1 Recurrence and Periodicity in Biology

The Latin word *tempus* refers to both *time* and the anatomical *temple*. Reportedly, this coincidence dates back to the Hippocratic physicians who used to feel the pulse at the temporal artery [27]. In fact, the heartbeat is a prototypical example for the vital dependence of living systems on periodic processes that develop and sustain life.

1.1.1—
Biological clocks

Biological clocks are subsystems of living organisms that are able to exhibit recurrent activity through their internal dynamics. The name 'clock' suggests that the activity of these systems is not only recurrent but also periodic, that is, activity does not only repeat but does so in regular time intervals. In higher organisms, a variety of different biological clocks control the temporal progress of vital metabolic and developmental processes [36, 158]. A prominent example for a biological clock is the circadian clock in mammals [35, 53], operating in the hypothalamus, more specifically in the neuron clusters called suprachiasmatic nuclei. In this system, a self-regulatory biochemical mechanism leads to oscillations in the cellular concentration of specific proteins with a period of about 24 hours (hence the name *circa:dian*). The circadian clock is thus able to anticipate the day-night cycle. It accordingly adjusts the metabolism, resulting in an increased efficiency of resource usage by preparing the organism for either activity or recovery, depending on the daytime [153]. This adaptation mechanism constitutes a selective advantage; different types of circadian clocks have evolved also in non-mammalian species [53]. The experience of a jet lag after a transcontinental flight can be related to a phase lag of the circadian clock with respect to the local day-night cycle [153], impairing or even reverting its favorable effect on the metabolism. The jet lag is remedied as the circadian rhythm is resynchronized to the local day-night cycle. This mostly happens through entrainment

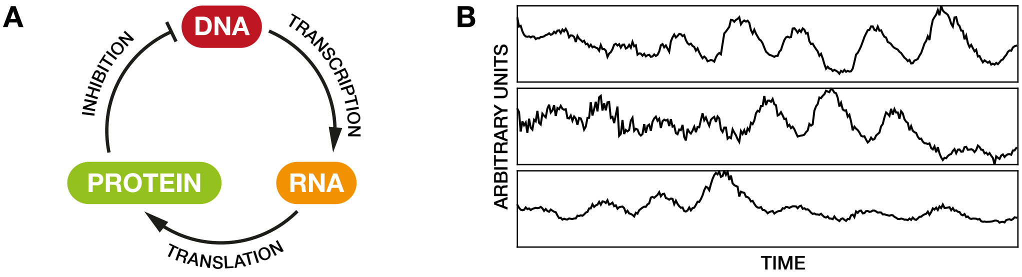

Figure 1.1 **A.** Simplified schematic depiction of a genetic oscillator. **B.** Experimental time series of genetic oscillations in single cells dissociated from the presomitic mesoderm of zebrafish embryos [154]. The amplitude is related to the concentration level of a specific protein. [Data courtesy of Alexis B. Webb.]

by external cues, so-called *zeitgebers*, such as the natural light cycles. The latter are sensed through the eyes from which the suprachiasmatic nucleus receives direct innervation. In the absence of external cues, the circadian clock runs freely with remarkable precision, i.e., temporal regularity, for weeks or even years [53]. While the circadian clock is probably the best-known example for a biological clock, there are numerous other biological clocks fulfilling vital functions in governing the temporal progress of recurrent processes in living systems.

1.1.2— Genetic oscillators

Which molecular mechanisms lead to periodic activity within cells? A typical such mechanism is autoinhibitory gene expression [50, 81, 94]. The core mechanism is summarized in Fig. 1.1A: a specific protein is produced by the transcription of DNA into mRNA and the subsequent translation of mRNA. The protein, in turn, inhibits the transcription of its own gene. Both protein and mRNA are degraded. Since the different stages of gene expression introduce a time delay between transcription and inhibition, this mechanism effectively forms a delayed negative-feedback loop that can give rise to oscillations in the mRNA and protein concentrations (Fig. 1.1B). On a molecular level, the regulatory DNA, which is required to direct the enzyme RNA polymerase to initiate transcription, is bound and blocked by the protein. Whenever the protein level is high, this blockade shuts down production. As the remaining proteins decay, the regulatory DNA is freed, production becomes possible again and the process starts over. The finite time required by transcription and translation processes causes a recurrent overshoot of the concentration levels and thus ensures that no steady-state protein level is reached, in which production would exactly balance decay without oscillations [100]. Systems invoking this mechanism are called *genetic oscillators* and the genes whose protein level exhibits oscillations are often referred to as *cyclic genes* [110]. Genetic oscillators have been extensively studied in the past, both experimentally [29, 31, 39, 47, 79, 83, 90, 97, 131, 162] and theoretically [43, 94, 127, 151, 164]. Multi-cellular systems that comprise populations of genetic oscillators are, e.g., the circadian clock mentioned in Sec. 1.1.1 and the so-called ‘segmentation clock’, a developmental mechanism that we encounter in the next section.

Compared to man-made reference clocks, genetic oscillators often show limited precision, that is, they exhibit considerable period fluctuations over time (see, e.g., Fig. 1.1B) [79]. These fluctuations are caused by physiological processes interfering with gene expression, often referred to as ‘noise in gene expression’ [69, 113, 115, 145].

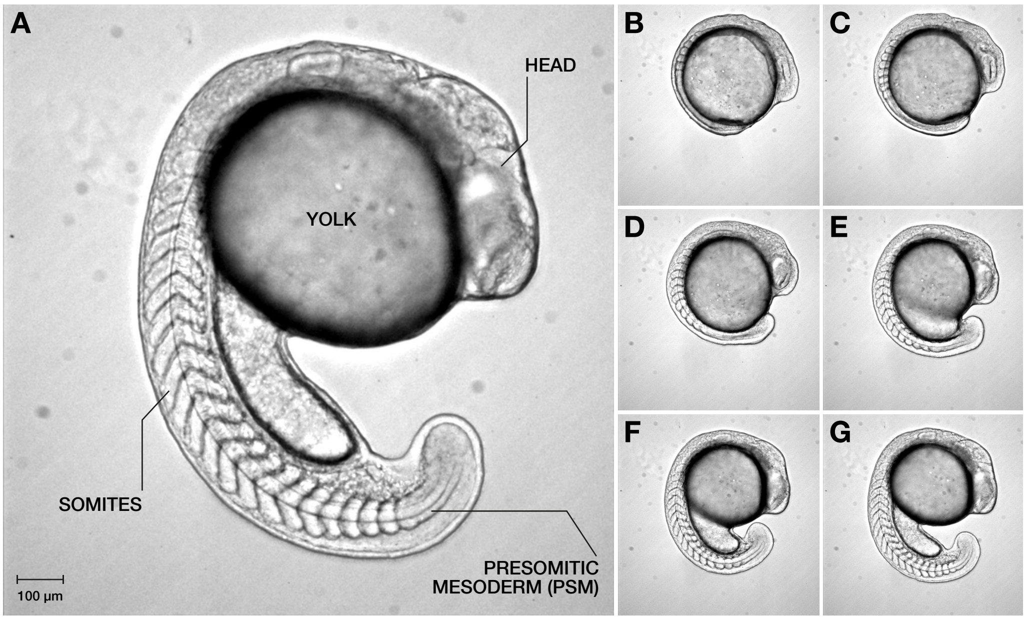

Figure 1.2 Segmentation of the embryonic body axis in zebrafish (*Danio rerio*). Brightfield microscopy images show the embryo in a lateral view. **A.** Snapshot of the embryo at the 21 somite stage. **B–G.** Snapshots at different stages of segmentation: 5 somites (B), 8 somites (C), 11 somites (D), 14 somites (E), 17 somites (F), and 20 somites (G). [Images courtesy of Daniele Soroldoni. Labelling by the author.]

Period fluctuations can limit an oscillator's viability as a clock, that is, its ability to stay correlated with periodic changes of its surroundings. In this context, the question arises which properties of genetic oscillators determine their precision and which strategies biological systems can develop to improve their precision [32, 93, 109]. As such oscillators typically appear in large assemblies, the role of biochemical oscillator coupling for precision and synchronization of these oscillators is of particular interest.

1.1.3— Periodicity in development: vertebrate segmentation

A periodic process that is vital for the development of vertebrate embryos is the segmentation of the elongating body axis, termed *somitogenesis* (Fig. 1.2). During this stage of development, the precursors of the vertebrae, called *somites*, form rhythmically and sequentially from a previously unsegmented progenitor tissue, the *presomitic mesoderm* (PSM) [102]. From a dorsal view, the presomitic mesoderm is a U-shaped tissue that embraces the notochord (Fig. 1.3), the main embryonic skeletal element of lower vertebrates [52]. The somites are cell clusters of mesoderm surrounded by a confining epithelial cell layer. They form in pairs with the notochord in the center by segregating from the presomitic mesoderm at its anterior end.

Somite formation proceeds sequentially from head to tail in regular time intervals, which, depending on the vertebrate species, can range from 25 minutes in zebrafish to about five hours in humans [118]. While frogs develop about ten vertebrae, the number of vertebrae can exceed three hundred in snakes [51]. The regularity of the time intervals between the formation of successive segments has provoked the assumption of a biological clock [24], termed *segmentation clock*, which operates in the presomitic mesoderm and controls the temporal succession of events leading to the formation of new segments. In a simplified picture, one cycle of this segmentation clock coincides with the formation of one new segment [67]. Indeed, experimental

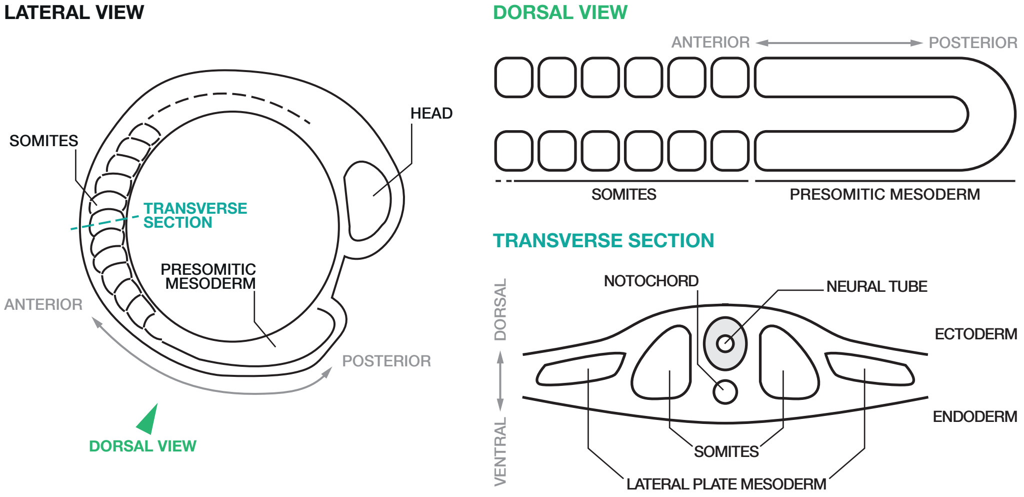

Figure 1.3 Schematic depictions of the zebrafish presomitic mesoderm and formed somites in lateral, dorsal, and transversal view. Transverse section scheme adapted from Ref. [118].

evidence for oscillating gene expression in the presomitic mesoderm has been found in various vertebrate species, such as zebrafish [55, 58, 101], mouse [19, 88], chick [68, 103], snake [51], and frog [82]. These findings provide hints that the core mechanism of vertebrate segmentation by means of genetic oscillations is conserved among vertebrate species, including humans, with differences on the genetic level [111]. Moreover, recent findings of oscillatory gene expression during the segmentation of arthropods [123] and root primordia in plants [95] indicate that oscillation-based segmentation mechanisms may not be restricted to the realm of vertebrates [116].

Failure of segmentation due to, e.g., mutations of oscillating genes and/or their controlled inhibition in experiments can cause morphological defects that range from a mild distortion of segment boundaries to severe axial deformations [65, 102, 117, 126, 150]. In humans, failure of proper segmentation due to mutations and external factors such as hypoxia during development have been related to the occurrence of congenital scoliosis [12, 111, 136]. An overview over the details of the segmentation mechanism will be given in Sec. 1.2.

1.1.4— Functional relevance of temporal regularity

Biological clocks introduce temporal regularity to the processes that they control. The functional relevance of this temporal regularity, however, depends on the specific biological process at hand. For the circadian clock introduced in Sec. 1.1.1, temporal regularity is crucial. Only if the clock stays correlated with the environmental day-night changes through its internal dynamics, it can adjust the metabolism in a way that is favorable for the organism. This is another way of saying that the clock has to repeat its cycle in regular time intervals with only a limited degree of fluctuation. Furthermore, the length of these intervals has to be specifically about 24 hours to meet the functional requirements of the clock. Other examples for clocks, for which temporal regularity and the specific clock period are functionally relevant are the *circannual clocks* with a period of about a year, which, e.g., control the active and hibernating physiological states of certain hibernating mammals [105].

In the case of vertebrate segmentation, introduced in the previous section, the functional role of temporal regularity is less obvious. Rather than temporal regularity of the process, the appropriate morphological properties of its products, the formed

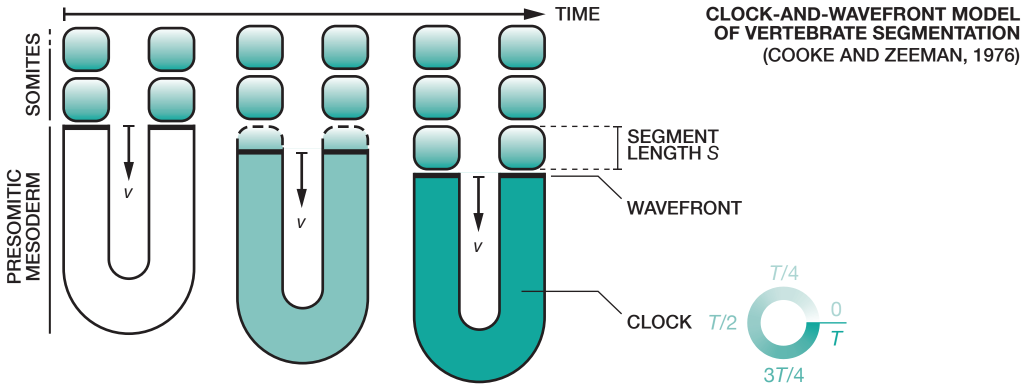

Figure 1.4 Clock-and-wavefront model of vertebrate segmentation [24]: A biological clock, located in the presomitic mesoderm, controls the timing of segment formation. A cycle of the clock with period T coincides with the formation of one segment. Assuming a moving wavefront with speed v that converts the state of the clock into morphological segments, the size of the formed segments is given by $S = vT$, Eq. (1.1).

segments, are crucial for the viability of the organism [102]. In fact, experiments have shown that the period of segment formation is strongly temperature-dependent, while the size of the formed segments is preserved under temperature variations [128]. This implies that the functional role of temporal regularity in segmentation is different from its role in, e.g., the circadian clock. In vertebrate segmentation, as we will see in the next section, the 'clock' mechanism is in fact part of a much more complex pattern forming system.

1.2 Vertebrate Segmentation

1.2.1—
The clock-and-wavefront model

In 1976, Jonathan Cooke and Erik Christopher Zeeman suggested an explanatory principle for vertebrate segmentation that has become a paradigm in the field. The so-called *clock-and-wavefront model* [24] invokes a multi-cellular clock of yet unspecified nature that operates in the presomitic mesoderm and generates coherent oscillations on tissue scale. At the anterior end of the presomitic mesoderm, a wavefront travelling in posterior direction freezes the local phase (the instantaneous state in the oscillation cycle). Hence, this mechanism leads to a spatially periodic pattern being a record of the clock dynamics at the wavefront (Fig. 1.4) [102]. Subsequently, this spatial pattern is read out by a biochemical process that triggers a cell fate decision based on the frozen spatial pattern and thus leads to the spatially periodic formation of epithelial segment boundaries. The spatial prepattern can thus be understood as a layout for the formation of a new segment. The length S of a newly formed segment is accordingly determined by the period T of the clock and the speed v with which the wavefront sweeps over the oscillating tissue, through the simple relation

$$S = vT \, , \tag{1.1}$$

see Fig. 1.4. Hence, a fast clock (small period) results in small segments, while a slow clock (large period) results in large segments. Likewise, a slow wavefront results in smaller segments, while a fast wavefront results in larger segments.

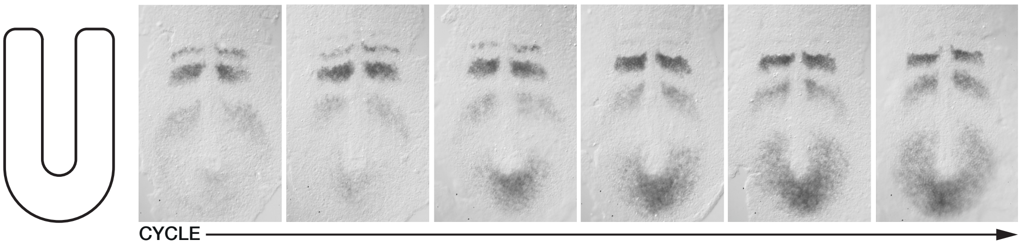

Figure 1.5 In-situ hybridization of zebrafish embryos shows *deltaC* mRNA expression patterns in the presomitic mesoderm during different stages of segmentation. [Images courtesy of Andrew C. Oates.]

1.2.2— Wave patterns of oscillating genes

It was not until 1997 that first experimental hints of a molecular clock controlling vertebrate segmentation were discovered, by Palmeirim *et al.* [103]. In chick embryos, the gene *c-hairy1* was identified, strongly expressed in the presomitic mesoderm. In-situ hybridizations, in which this gene was stained in a fixed embryo, revealed not only signatures of cyclic gene expression but of complex dynamic patterns of striped high expression regions in the presomitic mesoderm. (Fig. 1.5 displays analogous patterns of *deltaC* mRNA in the presomitic mesoderm of zebrafish.) This was in contrast to the simple picture, in which the presomitic mesoderm as a whole oscillates in unison. Rather, these findings indicated that at each point in time, different parts of the presomitic mesoderm are at different stages of the oscillation cycle.

With the advent of transgenic live reporter lines in the late 2000s, these studies were complemented by real-time imaging of oscillatory gene expression [10, 78, 88, 133, 134]. In contrast to in-situ hybridization techniques, these transgenic lines do not require the embryo to be fixed at a certain stage of development and thus enable real-time imaging of gene expression products *in vivo*. In these reporter lines, oscillating genes assumed to be functional for segmentation are tagged with a fluorescent protein that emits light of a specific wavelength upon exposure to laser light. These lines thus enable to distinguish tissue regions with high and low expression of cyclic genes by their fluorescence intensity level. Using transgenic mouse and zebrafish reporter lines, wave-like patterns of gene expression sweeping through the presomitic mesoderm from posterior to anterior could be observed [10, 78, 133]. Masamizu *et al.* [88] found first experimental hints that single cells dissociated from the presomitic mesoderm of mouse are able to exhibit autonomous genetic oscillations. This provided another piece of evidence that the wave patterns observed in the presomitic mesoderm are a manifestation of the coordinated oscillatory behavior of single cells exhibiting a phase profile on tissue scale. The propagation of these wave patterns is not due to material transport, except for the constant flow of cells away from the posterior tip, which, however, is much slower than the wave propagation [65]. The biochemical and mechanical mechanisms that convert the prepattern generated by genetic oscillations into morphological segments is not well understood and subject to ongoing research [28].

1.2.3— Mechanisms of pattern formation

The observed wave patterns of oscillating genes in the presomitic mesoderm are a manifestation of the fact that at a specific point in time, different parts of the presomitic mesoderm are at different phases in the oscillation cycle. This discovery necessitated a revision of a simple clock-and-wavefront picture, in which the tissue as a whole oscillates in unison. A prominent mechanism that gives rise to such wave patterns is a frequency profile across the tissue, that is, a gradual decay of the frequency of cell-autonomous oscillators from posterior to anterior (Fig. 1.7) [5, 23, 64, 49, 51, 93]. Due to this gradual frequency mismatch, a profile of phase differences evolves across the tissue and manifests itself as traveling wave patterns in anterior direction. (We will recapitulate and illustrate the basic principles of pattern formation in the presence of a frequency profile in Chapter 3.) For wave patterns that emerge from such a mechanism, the term *kinematic waves* has been coined [102]. This terminology emphasizes that no information is propagated through the tissue as the motion of waves arises from the simultaneously concerted behavior of all constituents. In this respect, the motion of kinematic waves is comparable to the apparent motion of a cursor on a computer screen, which is due to the coordinated flashing of pixels [102]. This is in contrast to *dynamic waves* such as sound waves or electromagnetic waves, which are local perturbations of a medium that propagate due to local interactions and are capable of transmitting information.

On a biological level, it has been hypothesized that a frequency profile is due to a decay of oscillation frequency with physiological age of a cell as it traverses the presomitic mesoderm [64, 70], or due to the effect of morphogen gradients, which provide positional information in the tissue [49, 51]. Morphogens are signaling molecules that play a crucial role in patterning tissues by regulating transcriptional responses and cell-fate decisions [119]. In fact, a variety of morphogens such as Wnt, FGF (fibroblast growth factor), and Retinoic Acid have been identified in the presomitic mesoderm of many vertebrates [8, 9, 34]. During segmentation of the body axis, Wnt and FGF levels are highest in the posterior of the presomitic mesoderm and decay towards the anterior, whereas Retinoic Acid forms an opposing gradient with highest levels in the somites and decaying levels in posterior direction (see also Fig. 3.10A) [8, 102]. Besides their proposed role in establishing a frequency gradient, these morphogen gradients have also been suggested to control the ability of cells to oscillate and to undergo differentiation [8]. Moreover, it has been shown in zebrafish that perturbation of the Wnt gradient changes the rate of length decrease of the presomitic mesoderm during segmentation as well as the size of formed segments [11].

Alternative approaches have described the waves of gene expression in the presomitic mesoderm as dynamic waves due to a specific type of intercellular coupling [96]. Such a mechanism would imply the propagation of information through the tissue. Another completely different road is taken by approaches describing segmentation as a result of Turing patterning, that is, reaction and diffusion of different biochemical species giving rise to spatially periodic patterns [37, 80].

1.2.4— Pattern coherence in a noisy environment

The observation of wave patterns of high spatial and temporal coherence implies that cellular oscillations in the presomitic mesoderm are locally synchronous on spatial scales comparable to the wavelength, which itself typically extends over multiple cell diameters. The ability of cells to achieve this high degree of local synchrony has been attributed to biochemical signaling between cells that couples their oscillatory dynamics. In 2000, Jiang *et al.* [65] found that in-situ hybridizations of zebrafish mutants lacking a functional *Notch* signaling pathway did not exhibit coherent stripe patterns of gene expression. Rather, they observed ‘salt-and-pepper patterns’ of strongly varying gene expression levels in neighboring regions, indicating that the cell-autonomous oscillators were lacking local synchrony [81].

Later experiments, in which the Notch signaling pathway in developing embryos was temporarily inhibited during segmentation, confirmed this ‘desynchronization hypothesis’: In Ref. [117], Riedel-Kruse *et al.* showed that inhibition of Notch sig-

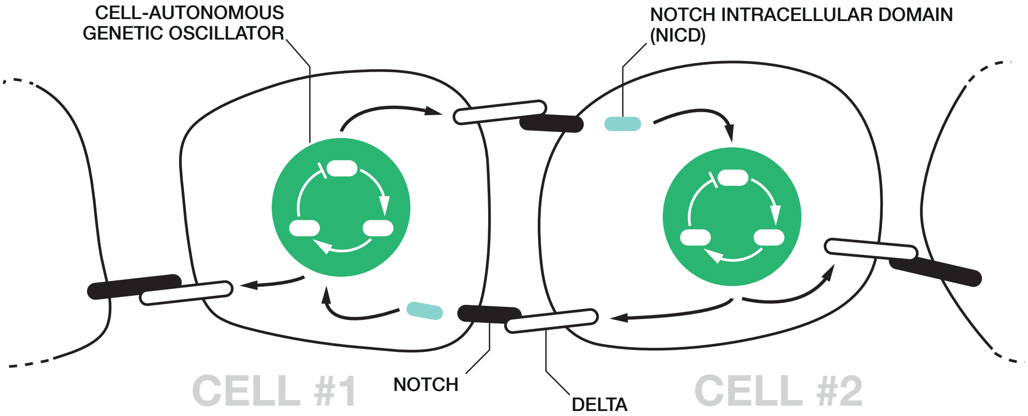
CELL-AUTONOMOUS GENETIC OSCILLATOR
NOTCH INTRACELLULAR DOMAIN (NICD)
CELL #1
NOTCH
DELTA
CELL #2

Figure 1.6 Schematic depiction of the Delta–Notch signal transduction pathway. (See Sec. 1.2.4 for details.) Figure adapted from Ref. [102].

naling at the beginning of segmentation leads to a loss of coherent stripe patterns, accompanied by segmentation defects. Coherent patterns and proper segmentation could be rescued at later stages of somitogenesis by washing out the inhibiting molecules, thereby reactivating Notch signaling. Recent experiments involving live reporter lines and imaging of the presomitic mesoderm with single-cell resolution indicate that the cellular oscillations of wildtype embryos are locally in-phase, while those of mutants with non-functional Notch signaling are desynchronized [31].

Hence, Notch signaling is thought to play a major role in coupling the dynamics of adjacent cellular oscillators [60, 102, 135, 160]. Fig. 1.6 shows a schematic depiction of the Delta–Notch signal transduction pathway. The functional proteins of an intracellular genetic oscillator (green) regulate the transcription of the *Delta* ligand (white). The functional Delta proteins, in turn, bind to the *Notch* receptor (black) of an adjacent cell in contact [62]. Upon binding, the intracellular domain of Notch (cyan) is released and regulates expression of the cyclic genes in the receiving cell. Thus, this signaling pathway couples the dynamics of the cellular oscillators of cells in contact. Mathematical models of this coupling mechanism support the role of the Delta–Notch signaling pathway in synchronizing the oscillations of cells in contact [81]. Beyond its role in locally synchronizing genetic oscillations, intercellular coupling has been suggested to regulate the rate of segment formation by introducing a considerable delay in cell-cell communication that is able to alter the collective frequency of coupled oscillators [56].

1.2.5— Current view and open questions

In this thesis, we adopt the hypothesis that the wave patterns in the presomitic mesoderm are kinematic waves that emerge from a frequency profile on tissue level, as outlined in the previous section. In Ref. [102], Oates *et al.* have built a unifying framework that summarizes the basic ingredients of any theory invoking such a mechanism of pattern formation with oscillators. Fig. 1.7 schematically depicts the three tiers of the framework: on the bottom tier, cell-autonomous oscillators provide the basic oscillating elements needed for the formation of kinematic waves. On the middle tier, adjacent cells couple through biochemical signaling and thereby tend to locally synchronize. This local synchronization is considered as being key to establish coherent patterns of gene expression in a noisy environment (Sec. 1.2.4). On the upper tier, a tissue-level frequency gradient causes time-dependent phase differences

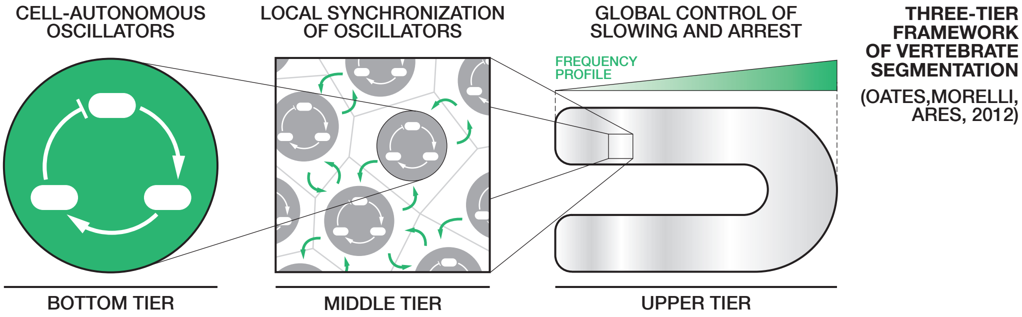
CELL-AUTONOMOUS OSCILLATORS
LOCAL SYNCHRONIZATION OF OSCILLATORS
GLOBAL CONTROL OF SLOWING AND ARREST
FREQUENCY PROFILE
THREE-TIER FRAMEWORK OF VERTEBRATE SEGMENTATION
(OATES,MORELLI, ARES, 2012)
BOTTOM TIER
MIDDLE TIER
UPPER TIER

Figure 1.7. Three-tier framework of vertebrate segmentation. Figure adapted from Ref. [102].

between different regions in the tissue and is thus responsible for the emergence of kinematic waves on tissue level (Sec. 1.2.3). This framework is independent of the specific molecular implementation of its constituent mechanisms, which might vary across different vertebrate species or might be unknown.

While this framework describes the basic mechanism of pattern formation, it does not address its interplay with the dynamics of the underlying tissue. Cells in the posterior part of the presomitic mesoderm, the tailbud, are subject to random movement and dynamic rearrangement [76, 86]. Moreover, it is known from time-lapse microscopy imaging that the length of the presomitic mesoderm substantially decreases during the segmentation process (see, e.g., Fig. 1.2). While it has been shown that random cell movement in the tailbud can promote synchronization of oscillators [146, 147, 148, 149], it is still not understood whether and how tissue dynamics affect the kinematic wave patterns and the rate of morphological segment formation. So far, this aspect of segmentation has rarely been addressed in the literature. Many coarse-grained theories of the segmentation clock consider the system to operate at a steady state, in which the presomitic mesoderm stays at a constant length throughout segmentation [5, 24, 49, 93, 96]. Only few theories explicitly account for the length decrease of the presomitic mesoderm during segmentation [23], but they have not addressed its impact on pattern formation.

1.2.6— Zebrafish as a model organism

As outlined in Sec. 1.1.3, vertebrate segmentation has been studied in different animals such as chick, frog, mouse, snake, and zebrafish. In this thesis, we support our theoretical work on vertebrate segmentation with experimental data from zebrafish embryos gained by our experimental collaborators. Zebrafish (Fig. 1.8) is a popular model organism for several reasons. The embryos are transparent and are therefore particularly suitable for imaging morphogenesis during development. Moreover, in zebrafish, several genes have been identified to be part of the oscillatory genetic network involved in the segmentation of the body axis [102]. The number of these cyclic genes has been reported to be lower in zebrafish than in other vertebrate model organisms such as mouse and chick [75], which suggests that the corresponding oscillatory genetic network might be simpler to study. Advances in the generation of transgenic reporter lines for various vertebrates have made it possible to image the expression of these cyclic genes *in vivo* and *in vitro*, at tissue level and single cell level, and in real-time [31, 133, 134]. Our experimental collaborators have recently developed transgenic zebrafish reporter lines for these genes that allow the visualization of cyclic gene expression on tissue and single-cell level [133].

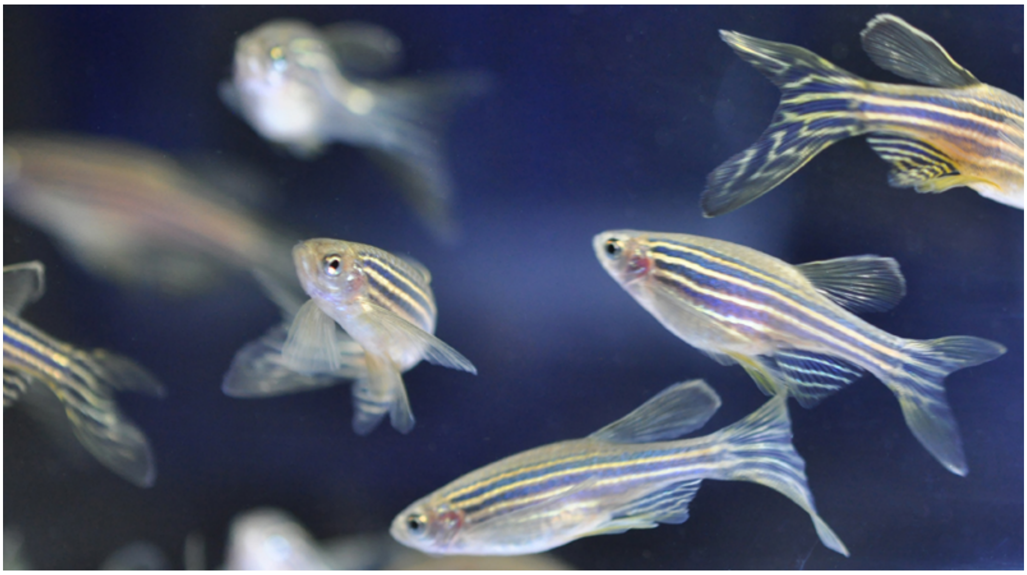

Figure 1.8. Adult zebrafish (*Danio rerio*). [Image courtesy of Christopher Dooley.]

1.3 Contents of this Thesis

In this thesis, we study theoretical models of genetic oscillator systems from the single oscillator scale to the complex pattern forming system operating during vertebrate segmentation. Moreover, we quantify experimental data obtained by our collaborators to compare them with theoretical predictions.

In Chapter 2, we present generic Markov chain models of coupled genetic oscillators, in which both the intracellular oscillator and the intercellular coupling between oscillators are inherently stochastic. We study how properties of the coupling process affect the precision and synchronization of oscillators (see also Sec. 1.1.2) and investigate the effects of stochasticity on the collective dynamics of the oscillators. Furthermore, we present a phase oscillator approximation of the coupled system and compare it with our stochastic model.

In Chapter 3, we introduce a continuum theory of coupled phase oscillators to study the interplay of tissue dynamics, oscillator coupling, and pattern formation during vertebrate segmentation (see also Sec. 1.2.5). We first introduce the basic mechanism of pattern formation with oscillators in the presence of a frequency gradient using the theory in its simplest form. We then sequentially extend the theory by biologically relevant factors such as coupling delays due to complex signaling between cells, local growth of the tissue, and decreasing tissue length. We study the effects of these factors on the formation of kinematic wave patterns in the presomitic mesoderm and on the timing of morphological segment formation. Moreover, we present a hypothetic mechanism based on interacting morphogens and oscillators that describes self-organized segmentation and dynamically accounts for the length decrease of the tissue and the termination of the segmentation process after a finite number of segments.

In Chapter 4, we introduce and apply quantification methods for experimental data on vertebrate segmentation. We obtain dynamical properties of the unsegmented tissue such as velocity fields and length changes, which we use to parametrize our theory. Moreover, we develop and apply a technique to quantify the spatio-temporal patterns of kinematic waves in the presomitic mesoderm and compare these experimental results with the theoretical predictions obtained from our theory in Chapter 3.

In Chapter 5, we devise a three-dimensional cell-based model that combines tissue mechanics, morphogen dynamics, and oscillator dynamics. We show that this model is able to describe the self-organized segmentation of a dynamically growing tissue and relate it to the coarse-grained continuum theory introduced in Chapter 3. We propose this model as a starting point to study the interplay of tissue mechanics, morphogen dynamics, and oscillator dynamics during vertebrate segmentation in a unified framework.

Motivated by the biological oscillator systems studied in the chapters before, we turn to generic systems of coupled oscillators in Chapter 6 and study their synchronization dynamics in the presence of coupling delays and phase shifts. While coupling delays and phase shifts play an equivalent role for the dynamic frequency of the synchronized oscillators, we show that they play a crucially different role for the dynamics of transients to the synchronized state. We demonstrate how this behavior results in novel synchronization scenarios.

We conclude with Chapter 7, where we discuss the achievements made in this thesis and give suggestions for future work.

Chapter 2

Markov Chain Models of Coupled Genetic Oscillators

In this chapter, we introduce Markov chain models of genetic oscillators in which both the autonomous oscillators and the coupling between oscillators are intrinsically stochastic. We first investigate the features of an autonomous oscillator and provide effective amplitude and frequency estimates. We then study the effects of oscillator coupling on precision, synchronization, and collective frequency—key properties for the biological function of oscillator assemblies. Finally, we devise a phase oscillator approximation that is able to capture the key features of stochastically coupled oscillators with coupling delays.

2.1 Markov Chain Models of Oscillators and Coupling

We introduce stochastic Markov chain models of autonomous and coupled genetic oscillators, in which the expression of cyclic genes and signaling genes is represented by a stochastic multi-step process, an approach pioneered by Morelli and Jülicher [94]. This multi-step process provides an effective description of the different stages of gene expression and trafficking. Instead of explicitly describing the individual biomolecular processes such as transcription, splicing, translation, binding, and intracellular transport [2], we here focus on a generic description with identical intermediate steps. The statistical distribution of molecule numbers generated by such a multi-step process with identical steps serves as an approximation of the corresponding distribution in noisy biochemical systems with different steps.

2.1.1—Markov chain model of an autonomous oscillator

Before turning to a system of two coupled genetic oscillators, we introduce a Markov chain model of a single autonomous oscillator as first presented in Ref. [94]. In this description, genetic oscillations are obtained through autoinhibition with delays [81]: a finite time after the initiation of gene expression, a functional protein inhibits the transcription of its own gene (Sec. 1.1.2). The interaction scheme of the model is depicted in Fig. 2.1A. An oscillator consists of $n+1$ steps, enumerated by $i = 0, \ldots, n$, representing the different stages of gene expression. At each point in time, the state of a step i is given by its molecule occupation number x_i. Consequently, the state of the system is characterized by the state vector $\mathbf{x} = (x_0, \ldots, x_n)$. The occupation number x_n of the last step represents the amount of functional products (circle in Fig. 2.1A). Production of molecules takes place at the initial step $i = 0$ with a probabilistic rate that is a monotonically decreasing function of the amount x_n of functional products, thereby leading to autoinhibition. Molecules jump from step i to $i+1$ with a transition rate λ and decay at the final step $i = n$ with rate κ. Since

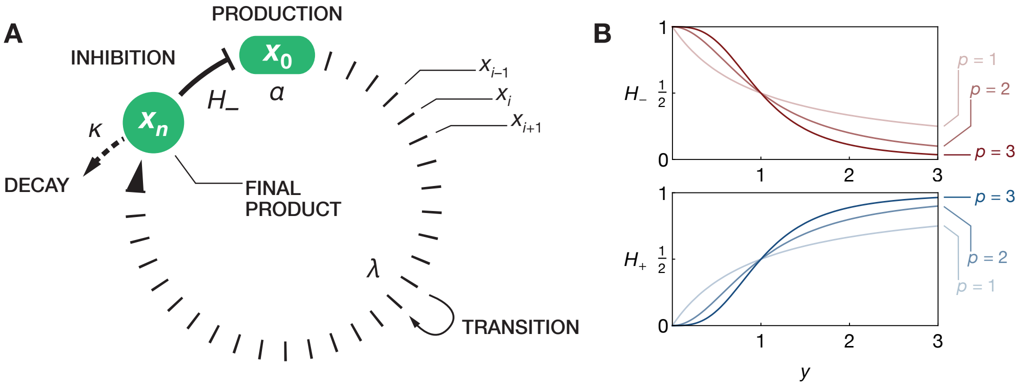

Figure 2.1 **A.** Schematic depiction of the Markov chain model of a genetic negative-feedback oscillator. Figure adapted from Ref. [94]. **B.** Hill functions H_- (red) and H_+ (blue), Eq. (2.4), as a function of y for different values of the Hill exponent p. The dashed gray lines mark the point $y = 1$, where the functions H_+ and H_- take half of their supremum.

molecules have to traverse this multi-step process before becoming a functional product, autoinhibition is delayed (Fig. 2.1A). The resulting feedback delay is essential to obtain oscillations (Sec. 2.2).

We describe the stochastic dynamics of this model by a master equation [44]. The probability density $P(\mathbf{x}, t)$ is defined by the property that $P(\mathbf{x}, t)\,\mathrm{d}t$ is the probability to find the system in the state $\mathbf{x}$ in the time interval $[t, t+\mathrm{d}t]$, where $\mathbf{x} = (x_0, \dots, x_n)$ is the state vector of all occupation numbers. The master equation describes the time evolution of P. For our model, it is given by

$$\frac{\partial}{\partial t} P(\mathbf{x}, t) = \Lambda P(\mathbf{x}, t) \ , \tag{2.1}$$

where Λ is an operator describing the stochastic dynamics of the oscillator,

$$\begin{aligned} \Lambda = \lambda \sum_{i=0}^{n-1} ((x_i + 1)\mathbb{E}_i^+ \mathbb{E}_{i+1}^- - x_i) + \kappa((x_n + 1)\mathbb{E}_n^+ - x_n) \\ + \alpha H_-(x_n/q)(\mathbb{E}_0^- - 1) \ . \end{aligned} \tag{2.2}$$

Here, $\mathbb{E}_i^\pm$ are creation (+) and annihilation (−) operators that increase or decrease the respective product level x_i by one,

$$\mathbb{E}_i^\pm P(x_0, \dots, x_n, t) = P(x_0, \dots, x_i \pm 1, \dots, x_n, t) \ . \tag{2.3}$$

Repression of gene expression is described by a function of the Hill type [100],

$$H_\pm(y) = \frac{1}{1 + y^{\mp p}} \ , \tag{2.4}$$

where p is the Hill exponent, which determines the shape of $H_\pm$ (Fig. 2.1B). For any value of p, the functions $H_\pm$ take values between 0 and 1 for positive y, with H_+ being monotonically increasing and H_- being monotonically decreasing in y. Both functions take the value 1/2 at $y = 1$. The factor $H_-(x_n/q)$ in the production term in Eq. (2.2) thus describes the inhibition of production by the final product x_n. Here we have simplified the model presented in Ref. [94] by omitting an amplification step

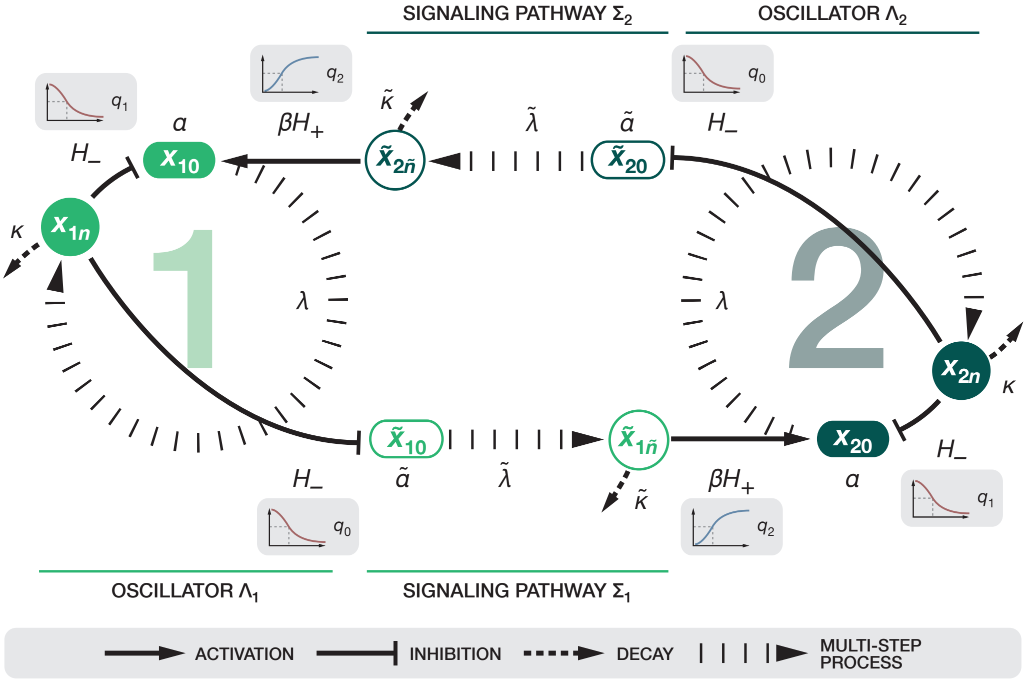
SIGNALING PATHWAY Σ_2
OSCILLATOR Λ_2
q_1
q_2
q_0
$\tilde{\kappa}$
$\tilde{\lambda}$
$\tilde{a}$
H_-
α
βH_+
x_{10}
$\tilde{x}_{2\tilde{n}}$
$\tilde{x}_{20}$
κ
x_{1n}
1
λ
λ
2
x_{2n}
κ
$\tilde{x}_{10}$
$\tilde{x}_{1\tilde{n}}$
x_{20}
H_-
H_-
$\tilde{a}$
$\tilde{\lambda}$
βH_+
α
$\tilde{\kappa}$
q_0
q_2
q_1
OSCILLATOR Λ_1
SIGNALING PATHWAY Σ_1
ACTIVATION
INHIBITION
DECAY
MULTI-STEP PROCESS

Figure 2.2 Schematic depiction of the Markov chain model of two coupled genetic negative-feedback oscillators, Eqs. (2.5–2.7). Shaded insets show sketches of the Hill functions $H_\pm$ that describe activation (blue) and inhibition (red) and indicate the threshold level (see also Fig. 2.1B).

that accounts for translational bursting. Alternative approaches to describe genetic negative-feedback oscillators with feedback delays have included non-Markovian approaches with explicit feedback delays [21, 22, 89]. We here focus on a Markovian approach with many intermediate steps instead of explicit time delays. Instead of only describing a single discrete delay, this allows for a distribution of feedback delay times, which is expected to arise in noisy biochemical systems [87].

To obtain numerical results for this model, we use a stochastic simulation algorithm to compute exact realizations of trajectories (see Appendix H for details). Fig. 2.3A shows examples for time series of the final product level x_n for different values of the production rate α.

2.1.2— Markov chain model of coupled oscillators

We use the model for an autonomous oscillator presented in the previous section to build a novel model of coupled genetic oscillators, in which also the coupling process is inherently stochastic. Coupling between genetic oscillators is achieved through a mechanism inspired by the Delta–Notch signal transduction pathway (Sec. 1.2.4): signaling molecules are produced in the sending oscillator and initiate a cascade of events that eventually leads to the activation of the cyclic gene in the receiving oscillator. This cascade of events is represented by a multi-step process with identical steps, similar to the multi-step process of the oscillator. The production of signaling molecules is regulated by the cyclic protein of the sending oscillator, so that the amount of exchanged signaling molecules carries information about its oscillatory state. Hence, this mechanism couples the oscillatory dynamics of both oscillators. Since signaling molecules have to traverse a multi-step process, oscillator coupling is delayed. Due to the stochastic nature of the signaling process, the model introduced here does not only describe fluctuations in molecule numbers but also effectively accounts for fluctuations of the coupling delay.

The interaction scheme of the model is depicted in Fig. 2.2. We invoke two identical instances $\mu = 1$ and $\mu = 2$ of the autonomous oscillator presented in the previous section. The number of molecules at step $i = 0, \dots, n$ of oscillator μ is denoted by $x_{\mu i}$. The oscillators are equipped with identical signaling pathways, which couple their dynamics. Analogous to the multi-step process for an autonomous oscillator, a signaling pathway consists of $\tilde{n} + 1$ steps and its state is characterized by the number of molecules that occupy each step $i = 0, \dots, \tilde{n}$, denoted by $\tilde{x}_{\mu i}$. Production of molecules takes place at the initial step $i = 0$ with a probabilistic rate that is a monotonically decreasing function of the current amount $x_{\mu n}$ of functional products of the sending oscillator μ. Molecules jump from step i to $i + 1$ with a transition rate $\tilde{\lambda}$ and decay at the final step $i = \tilde{n}$ with rate $\tilde{\kappa}$. Molecules at the final step $i = \tilde{n}$ enhance the production of cyclic molecules at the initial step $i = 0$ of the receiving oscillator. The state of the coupled system is characterized by the state vector $\mathbf{x} = (x_{10}, \dots, x_{1n}, x_{20}, \dots, x_{2n}, \tilde{x}_{10}, \dots, \tilde{x}_{1\tilde{n}}, \tilde{x}_{20}, \dots, \tilde{x}_{2\tilde{n}})$. The master equation for the coupled model is given by

$$\frac{\partial}{\partial t} P(\mathbf{x}, t) = \sum_{\mu=1,2} (\Lambda_\mu + \Sigma_\mu) P(\mathbf{x}, t) \ , \tag{2.5}$$

where Λ_μ describes the stochastic dynamics of the oscillator μ with $\mu = 1, 2$ and Σ_μ the stochastic dynamics of the outgoing signaling pathway of oscillator μ, see Fig. 2.2. The operators Λ_μ and Σ_μ are given by

$$\begin{aligned}\Lambda_\mu = \lambda \sum_{i=0}^{n-1} ((x_{\mu i} + 1) \mathbb{E}^+_{\mu i} \mathbb{E}^-_{\mu, i+1} - x_{\mu i}) + \kappa((x_{\mu n} + 1)\mathbb{E}^+_{\mu n} - x_{\mu n}) \\ + H_-(x_{\mu n}/q_1)[\alpha + \beta H_+(\tilde{x}_{\bar{\mu}\tilde{n}}/q_2)](\mathbb{E}^-_{\mu 0} - 1) \ ,\end{aligned} \tag{2.6}$$

$$\begin{aligned}\Sigma_\mu = \tilde{\lambda} \sum_{x=0}^{\tilde{n}-1} ((\tilde{x}_{\mu i} + 1) \tilde{\mathbb{E}}^+_{\mu i} \tilde{\mathbb{E}}^-_{\mu, i+1} - \tilde{x}_{\mu i}) + \tilde{\kappa}((\tilde{x}_{\mu \tilde{n}} + 1)\tilde{\mathbb{E}}^+_{\mu \tilde{n}} - \tilde{x}_{\mu \tilde{n}}) \\ + \tilde{\alpha} H_-(x_{\mu n}/q_0)(\tilde{\mathbb{E}}^-_{\mu 0} - 1) \ ,\end{aligned} \tag{2.7}$$

where the index $\bar{\mu}$ refers to the respective other oscillator, $\bar{\mu} = 2\delta_{\mu,1} + 1\delta_{\mu,2}$, and $\mathbb{E}^\pm_{\mu i}$ and $\tilde{\mathbb{E}}^\pm_{\mu i}$ are creation and annihilation operators that increase or decrease the respective product levels $x_{\mu i}$ or $\tilde{x}_{\mu i}$ by one, in analogy to Eq. (2.3). The factors $H_-(x_{\mu n}/q_1)$ and $H_-(x_{\mu n}/q_0)$ in the production terms in Eqs. (2.6) and (2.7) describe the inhibition of production by the final product $x_{\mu n}$ of the oscillator, while $H_+(\tilde{x}_{\bar{\mu}\tilde{n}}/q_2)$ describes activation of production by the final product $\tilde{x}_{\bar{\mu}\tilde{n}}$ of the signaling pathway.

As for the single oscillator model introduced in the previous section, we obtain numerical results for this model by numerically computing exact realizations of trajectories (see Appendix H for details). Fig. 2.3C shows examples for time series of the final product levels x_{1n} and x_{2n}. In the following sections, we introduce the key observables that describe the precision and synchronization properties of the oscillators. We will obtain analytical and numerical results for these observables in Secs. 2.2 and 2.3.

2.1.3— Quality factor as a measure for precision

The precision of an oscillator is defined by the number of oscillations over which period fluctuations are small compared to a reference clock with high precision. Hence, it provides a measure how well an oscillator can serve as a clock. To assess the precision of noisy genetic oscillators in the present setting, we define the temporal

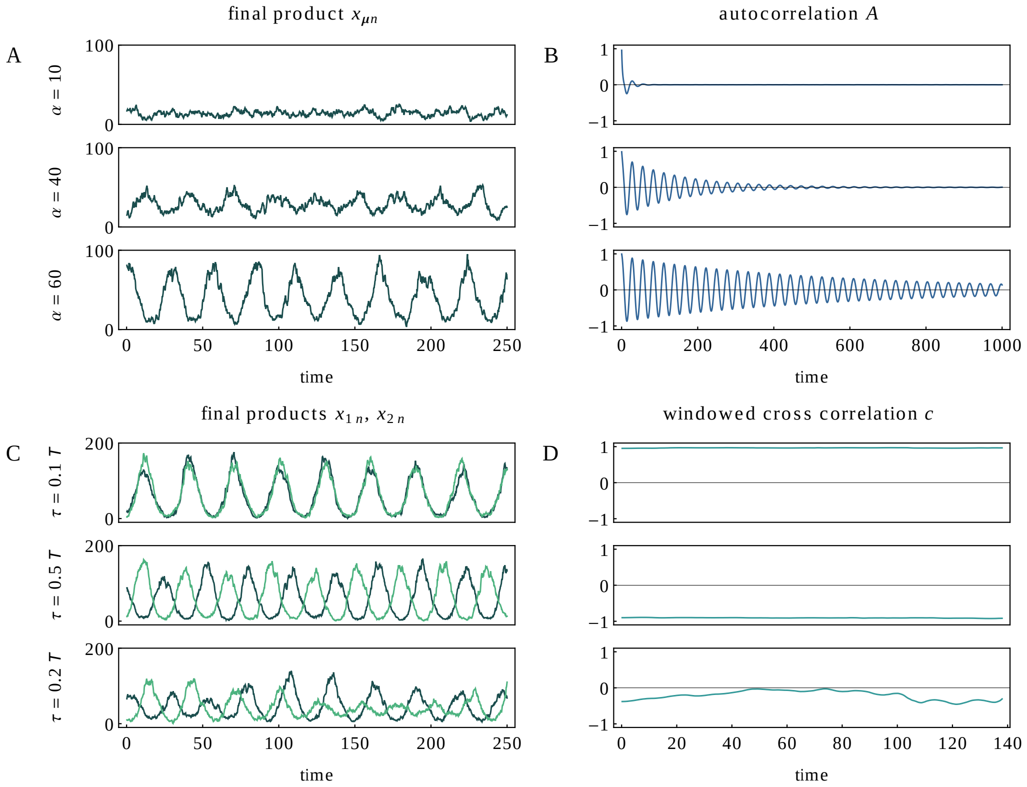

Figure 2.3 Sample trajectories of exact realizations. **A.** The final product x_n as a function of time for an uncoupled oscillator with different production rates α. **B.** Autocorrelation $A(t)$, Eq. (2.9), for the respective time series in panel A. **C.** Final products x_{1n} and x_{2n} of two coupled oscillators for different signaling delays $\tau = \tilde{n}/\tilde{\lambda}$ with constant $\tilde{n}$ and varying $\tilde{\lambda}$ (see Sec. 2.3.1 for details). Time delays are given in multiples of the oscillation period $T = 2\pi/\omega$. **D.** Windowed cross correlation c, Eq. (2.18), for the respective time series in panel C. All other parameters given in Table 2.1.

correlation function $\Gamma_{\mu\nu}$ between the final products $x_{\mu n}$ and $x_{\nu n}$ of the oscillators μ and ν,

$$\Gamma_{\mu\nu}(t) = \langle x_{\mu n}(t' + t) x_{\nu n}(t') \rangle - \langle x_{\mu n} \rangle \langle x_{\nu n} \rangle \ . \tag{2.8}$$

The averages are taken over t'. To determine the precision of an oscillator, we compute the normalized temporal autocorrelation function of a single oscillator and then average over multiple realizations of the stochastic system, denoted by $\langle \cdot \rangle_{\mathrm{R}}$,

$$A(t) = \left\langle \frac{\Gamma_{\mu\mu}(t)}{\Gamma_{\mu\mu}(0)} \right\rangle_{\mathrm{R}} \ . \tag{2.9}$$

The autocorrelation typically has a functional form of the type

$$A(t) \propto \mathrm{e}^{-kt} \cos \omega t \ , \tag{2.10}$$

see Fig. 2.3B for examples. Here, ω is the frequency of oscillations and k is the decorrelation rate. We use the function (2.10) to fit the numerically obtained autocorrelation $A(t)$, Eq. (2.9), using k and ω as fit parameters. The quality factor Q is defined as the dimensionless ratio of the correlation time k^{-1} and the period $2\pi\omega^{-1}$ of oscillations [94, 106],

$$Q = \frac{k^{-1}}{2\pi\omega^{-1}} \ . \tag{2.11}$$

The quality factor corresponds to the number of cycles over which period fluctuations are small and thus serves as a measure for oscillator precision.

2.1.4— Cross correlation as a measure for synchrony

The synchrony of two oscillators refers to the degree of correlation of their dynamics. We here assess the synchrony of the two coupled genetic oscillators by computing the normalized instantaneous cross correlation of their final products and taking the average over realizations,

$$C = \left\langle \frac{\Gamma_{12}(0)}{\sqrt{\Gamma_{11}(0)\Gamma_{22}(0)}} \right\rangle_{\mathrm{R}} \ . \tag{2.12}$$

Here, $\Gamma_{\mu\nu}$ is the correlation function (2.8). The cross correlation C takes values between -1 and 1, where 1 indicates perfect correlation, 0 no correlation and -1 perfect anti-correlation. If the time series from which C is computed exhibit persistent oscillations, $C \sim 1$ corresponds to in-phase synchrony and $C \sim -1$ corresponds to anti-phase synchrony, see Fig. 2.3C,D for examples.

We also assess the synchrony of the oscillators and the signaling pathways as their correlations contain information about the nature of the coupling mechanism. Each oscillator has an outgoing pathway whose production rate at the initial step is inhibited by the final step of the oscillator, and an incoming pathway whose final step activates production at the initial step of the oscillator (Fig. 2.2). Analogously to C, Eq. (2.12), we define the cross correlation C_{out} of the final products of an oscillator and the outgoing pathway and the cross correlation C_{in} of the final products of an oscillator and the incoming pathway. To this end, we introduce the correlation functions

$$\tilde{\Gamma}_{\mu\nu}(t) = \langle \tilde{x}_{\mu\tilde{n}}(t'+t)\tilde{x}_{\nu\tilde{n}}(t')\rangle - \langle \tilde{x}_{\mu\tilde{n}}\rangle\langle \tilde{x}_{\nu\tilde{n}}\rangle \tag{2.13}$$

and

$$\Delta_{\mu\nu}(t) = \langle x_{\mu n}(t'+t)\tilde{x}_{\nu\tilde{n}}(t')\rangle - \langle x_{\mu n}\rangle\langle \tilde{x}_{\nu\tilde{n}}\rangle \tag{2.14}$$

and define the cross correlations C_{out} and C_{in} as

$$C_{\mathrm{out}} = \left\langle \frac{\Delta_{\mu\mu}(0)}{\sqrt{\Gamma_{\mu\mu}(0)\tilde{\Gamma}_{\mu\mu}(0)}} \right\rangle_{\mathrm{R}} \ , \tag{2.15}$$

$$C_{\mathrm{in}} = \left\langle \frac{\Delta_{\mu\bar{\mu}}(0)}{\sqrt{\Gamma_{\mu\mu}(0)\tilde{\Gamma}_{\bar{\mu}\bar{\mu}}(0)}} \right\rangle_{\mathrm{R}} \ , \tag{2.16}$$

where the index $\bar{\mu}$ refers to the respective other oscillator, $\bar{\mu} = 2\delta_{\mu,1} + 1\delta_{\mu,2}$.

Since we will also encounter cases in which the same oscillatory time series entails both regions of in-phase and anti-phase correlations that average out in the global cross correlation Eq. (2.12), we also introduce a time-dependent windowed cross correlation. In contrast to the above quantities, we define this correlation measure on a single trajectory of the model. The windowed cross correlation is given by

$$c_{\mu\nu}(t) = \langle\!\langle x_{\mu n}x_{\nu n}\rangle\!\rangle_t - \langle\!\langle x_{\mu n}\rangle\!\rangle_t\langle\!\langle x_{\nu n}\rangle\!\rangle_t \ , \tag{2.17}$$

where $\langle\!\langle f \rangle\!\rangle_t = w^{-1} \int_{-w/2}^{w/2} f(t+t')\,\mathrm{d}t'$ and w is the time window over which the cross correlation is taken. The normalized windowed cross correlation between the two oscillators is obtained as

$$c(t) = \frac{c_{12}(t)}{\sqrt{c_{11}(t)c_{22}(t)}} \ . \tag{2.18}$$

Fig. 2.3D shows the windowed cross correlation of the corresponding example trajectories in Fig. 2.3C.

2.1.5—Mutual information

Mutual information is a concept from information theory, which has recently been used to analyze information flow and information capacity of genetic regulatory networks [140, 141, 142]. As a supplementary measure that also takes into account higher order correlations, we define the mutual information of the time series of the oscillators' final products. This measure indicates how well the state of oscillator 1 can be inferred from knowing the state of oscillator 2 and vice versa. Let $p_\mu(x)$ be the probability that the final product $x_{\mu n}$ of oscillator μ has occupation number x and let $p_{12}(x,x')$ be the joint probability that the final products x_{1n} and x_{2n} of oscillators 1 and 2 have occupation numbers x and x', respectively. The mutual information I of the oscillators is defined as the Kullback–Leibler divergence D_{KL} of the product $p_1(x)p_2(x')$ of the marginal distributions $p_\mu(x)$ and the joint probability distribution $p_{12}(x,x')$ [26],

$$I = D_{\mathrm{KL}}(p_{12} \| p_1 p_2) = \sum_{x,x'} p_{12}(x,x') \log_2 \left(\frac{p_{12}(x,x')}{p_1(x)p_2(x')} \right) \ . \tag{2.19}$$

With base 2 in the logarithm, it has units of bits. The mutual information has the property of being zero if and only if $p_{12}(x,x') = p_1(x)p_2(x')$ and thus takes into account all correlations between random variables. This is in contrast to the cross correlation, Eq. (2.12), which only measures linear correlations between variables [26]. We compute the probabilities p_1, p_2, and p_{12} as relative frequencies of occupation numbers in realizations of trajectories.

2.1.6—Product turnover

Gene expression consumes energy [2, 130, 152]. Assuming that an average energetic cost can be assigned to each produced functional molecule, the average number of produced and decaying molecules per unit time can be related to the energetic cost of sustaining oscillations of a certain quality. To assess how the precision of an oscillator is affected by this turnover of gene expression products, we compute the product turnover as the average number K of molecules that decays during an oscillation period[1].

---

[1] Formally, K can be expressed as

$$K = T \cdot \left\langle \lim_{k\to\infty} \frac{1}{t_k} \sum_{i=1}^{k-1} \delta_{x_{\mu n}(t_{i+1}) - x_{\mu n}(t_i), -1} \right\rangle_{\mathrm{R}} \ , \tag{2.20}$$

where $T = 2\pi/\omega$ is the period of the oscillator and ω is computed as described in Sec. 2.1.3. Furthermore, $\{t_i\}$ is a time discretization of an exact realization of the model (Sec. 2.1.1). The sum inside the angular brackets counts the number of times that a molecule decays at the final step $x_{\mu n}$. The quantity in angular brackets is thus the mean decay rate of the final product. Since the system is symmetric in both oscillators and signaling pathways, K does not depend on μ.

2.2 Analysis of the Autonomous Oscillator

In this section, we review and extend results for the uncoupled autonomous oscillator introduced in Sec. 2.1.1. We show how an effective description of an uncoupled oscillator in terms of a single delay differential equation arises in the deterministic limit of this model. This deterministic limit reveals that the full model of such a single oscillator is a stochastic generalization of previously studied deterministic models of negative-feedback oscillators. Moreover, we provide new results on amplitude and frequency estimates for an autonomous oscillator.

2.2.1— Time evolution of expectation values

We first derive the time evolution of the expectation values $\langle x_i \rangle$ of molecule numbers. This will allow us to characterize the distribution of feedback delays and to systematically obtain a deterministic limit of the system. An autonomous oscillator is described by Eqs. (2.1) and (2.2). The exact time evolution of the expectation values $\langle x_i \rangle = \sum_{\mathbf{x}} x_i P(\mathbf{x}, t)$ can be derived from the master equation (2.1), see Appendix A. This yields

$$\frac{\mathrm{d}}{\mathrm{d}t}\langle x_0 \rangle = \alpha \langle h(x_n) \rangle - \lambda \langle x_0 \rangle \ , \tag{2.21}$$

$$\frac{\mathrm{d}}{\mathrm{d}t}\langle x_i \rangle = \lambda \langle x_{i-1} \rangle - \lambda \langle x_i \rangle \ , \qquad 1 \leq i \leq n-1 \tag{2.22}$$

$$\frac{\mathrm{d}}{\mathrm{d}t}\langle x_n \rangle = \lambda \langle x_{n-1} \rangle - \kappa \langle x_n \rangle \ , \tag{2.23}$$

where h is given by

$$h(x) = H_-(x/q) = \frac{1}{1 + (x/q)^p} \ , \tag{2.24}$$

with H_- defined in Eq. (2.4). The cyclic hierarchy of differential equations (2.21–2.23) can be closed to obtain an integro-differential equation for the expectation value $\langle x_n \rangle$ of the final product. This equation has been presented in Ref. [94] and we provide its derivation in Appendix A for self-containedness. The result is

$$\frac{\mathrm{d}}{\mathrm{d}t}\langle x_n(t) \rangle \simeq -\kappa \langle x_n(t) \rangle + \alpha \int_0^t G_{\lambda,n}(t-t') \, \langle h(x_n(t')) \rangle \, \mathrm{d}t' \ , \tag{2.25}$$

where

$$G_{\lambda,n}(t) = \frac{\lambda^n}{(n-1)!} t^{n-1} \mathrm{e}^{-\lambda t} \tag{2.26}$$

is the Gamma distribution for the case of integer n. It characterizes the arrival times of molecules that traverse the multi-step process of the oscillator. The mean $u = \int_0^\infty t \, G_{\lambda,n}(t) \, \mathrm{d}t$ and variance $v^2 = \int_0^\infty t^2 \, G_{\lambda,n}(t) \, \mathrm{d}t - u^2$, which correspond to the mean arrival time and its variance, are given by

$$u = n/\lambda \ , \tag{2.27}$$

$$v^2 = n/\lambda^2 \ . \tag{2.28}$$

Henceforth, we call u the mean feedback delay to distinguish it from the mean signaling delay, which will be considered when addressing the system of two coupled oscillators.

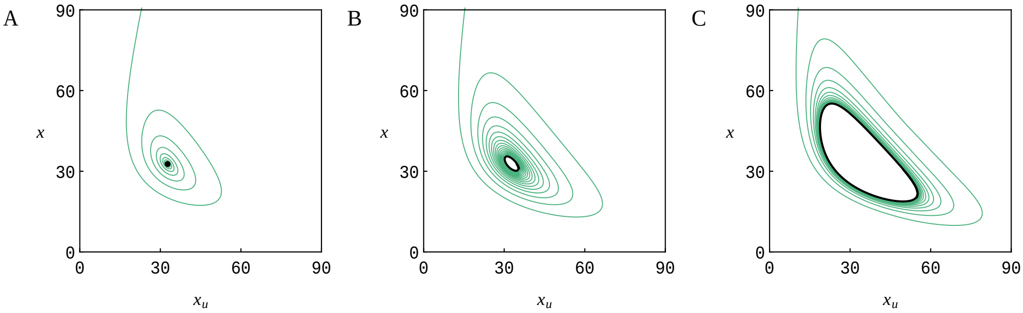

Figure 2.4 Numerical solutions to the deterministic limit Eq. (2.29) for $u = 3$ (A), $u = 4$ (B), and $u = 5$ (C). The instantaneous product level x is displayed versus the delayed product level x_u. For small u, the trajectory spirals into an attracting fixed point (black dot in panel A). For sufficiently large u, the system exhibits a limit cycle (black contours in panels B, C) corresponding to sustained oscillations. Other parameters are $\alpha = 60$, $\kappa = 0.5$, $q = 20$, and $p = 2$.

2.2.2— Deterministic limit

From Eq. (2.25), a deterministic limit can be obtained in two steps. First, we consider a mean-field approximation through the replacement $\langle h(x_n)\rangle \to h(\langle x_n\rangle)$. This yields a closed integro-differential equation for $\langle x_n\rangle$. Second, we take the limit in which the variance v^2 of arrival times vanishes at constant mean feedback delay u. This amounts to taking the limit $n \to \infty$ with $\lambda = n/u$. In this limit, the Gamma distribution converges to a Dirac δ-distribution, $G_{\lambda,n}(t) \to \delta(t-u)$. From Eq. (2.25), we thus obtain

$$\frac{\mathrm{d}x}{\mathrm{d}t} = \alpha h(x_u) - \kappa x \,, \tag{2.29}$$

where $x(t) = \langle x_n(t)\rangle$ and $x_u(t) = x(t-u)$. Systems of the type (2.29), known as Mackey–Glass systems [50, 85], have been extensively studied as models for negative-feedback oscillators [81, 91, 92, 100, 127]. Hence, the Markov chain model for an autonomous oscillator can be considered as a generalization of a Mackey–Glass system to include stochastic feedback delays. Fig. 2.4 displays numerical solutions to Eq. (2.29), where the instantaneous variable x is displayed versus the delayed variable x_u. For small feedback delays u, the trajectory spirals into a fixed point (Fig. 2.4A), whereas for sufficiently large u, the system exhibits a limit cycle (Fig. 2.4B,C), corresponding to sustained oscillations [155]. The shape of these limit cycles indicates that the delayed variable x_u is anti-correlated with the instantaneous variable x (large values of x_u for small values of x and vice versa), a behavior that we will discuss again when addressing the synchrony relations in the coupled system (Sec. 2.3.7).

2.2.3— Amplitude estimates

The deterministic limit Eq. (2.29) can be used to build a simple heuristic argument that provides analytical estimates of the amplitude of oscillations and the mean product level. We will demonstrate that even for the stochastic Markov chain model, these estimates yield effective bounds for the amplitude of noisy oscillations in specific parameter regions. First, we seek two values x^+ and x^- that satisfy

$$\alpha h(x^\pm) = \kappa x^\mp \,, \tag{2.30}$$

where all quantities are defined as in Eq. (2.29). Eq. (2.30) states that h alternates between x^+ and x^- up to the prefactor κ/α. We will show later in this section

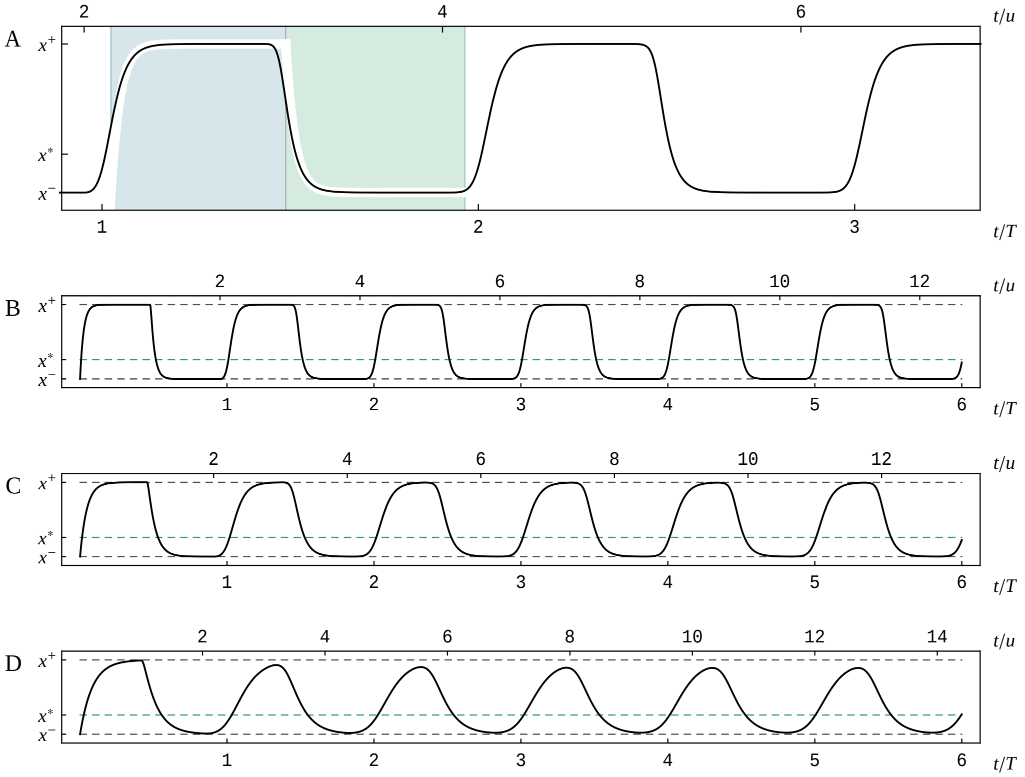

Figure 2.5 **A.** Numerical solution of the deterministic limit Eq. (2.29) for $u = 20\kappa^{-1}$ (solid black). The thick white curves show solutions to the approximations Eqs. (2.31) (blue shaded time interval) and Eqs. (2.34) (green shaded time interval) in the respective time intervals. **B.** Numerical solutions of the deterministic limit Eq. (2.29) (solid black) for $u = 20\kappa^{-1}$ (A), $u = 10\kappa^{-1}$ (B), and $u = 5\kappa^{-1}$ (C). The dashed lines indicate the amplitude estimates x^+, x^-, and x^*, Eqs. (2.36) and (2.37). T is the period of oscillations. Other parameters are $\alpha = 60$, $\kappa = 0.5$, $q = 20$, and $p = 2$.

that such values exist for typical choices of h and compute them explicitly. We now consider Eq. (2.29) for the final product x. Since Eq. (2.29) is a delay equation, it is not sufficient to specify an initial condition at a singular point. Rather, an initial history of the length of the delay u has to be provided [17]. We here consider the initial history $x|_{-u<t<0} = x^-$ and solve Eq. (2.29) for successive time intervals of length u. For the interval $0 < t < u$, we obtain

$$\begin{aligned} \left.\frac{\mathrm{d}x}{\mathrm{d}t}\right|_{0<t<u} &= \alpha h(x^-) - \kappa x \\ &= \kappa(x^+ - x) \end{aligned} \tag{2.31}$$

using Eq. (2.30). The solution reads

$$x\big|_{0<t<u} = x^+ - (x^+ - x^-)\mathrm{e}^{-\kappa t} \ . \tag{2.32}$$

Therefore, x exponentially converges towards x^+. In the limit $u \gg \kappa^{-1}$, the term proportional to $\mathrm{e}^{-\kappa t}$ decays fast compared to u and we can assume

$$x\big|_{\kappa^{-1}<t<u} \simeq x^+ \ . \tag{2.33}$$

Accordingly, we obtain in the next time interval

$$\begin{aligned}\left.\frac{\mathrm{d}x}{\mathrm{d}t}\right|_{u+\kappa^{-1}<t<2u} &\simeq \alpha h(x^{+}) - \kappa x \\ &= \kappa(x^{-} - x)\end{aligned} \tag{2.34}$$

and thus, x converges to x^{-} within the time scale κ^{-1} so that we can assume $x|_{u+2\kappa^{-1}<t<2u} \simeq x^{-}$. Hence, the system has returned to its initial value and the process starts over. This behavior is illustrated in Fig. 2.5A, where a numerical solution of the deterministic limit Eq. (2.29) is compared with solutions of Eqs. (2.31) and (2.34) for the appropriate time windows. We find that for feedback delays much larger than the decay time, $u \gg \kappa^{-1}$, the values x^{+} and x^{-} (which we explicitly compute below) are indeed identical to the maximum and minimum amplitude of the oscillations (Fig. 2.5B,C). For feedback delays of the same order as the decay time, $u \sim \kappa^{-1}$, the values x^{+} and x^{-} provide upper and lower bounds for the amplitude (Fig. 2.5D). Intuitively, if the transient time between plateau values is of the same order as the feedback delay, the system cannot reach the plateau values sufficiently fast and the above argument breaks down.

These considerations motivate the computation of the values x^{+} and x^{-} as amplitude estimates: Eq. (2.30) implies that these values satisfy $\mathcal{L}(x^{\pm}) = x^{\pm}$, where $\mathcal{L}$ is the iterated function

$$\mathcal{L}(x) = \alpha\kappa^{-1} h(\alpha\kappa^{-1} h(x)) \ . \tag{2.35}$$

The values x^{+} and x^{-} can thus be found by determining the fixed points of $\mathcal{L}$. As an example, we explicitly compute these values for h being a Hill function, Eq. (2.24), with Hill exponent $p = 2$. The function $\mathcal{L}$ then has five fixed points, of which two are generically complex and can therefore be ruled out as amplitude estimates. The remaining three fixed points x^{-}, x^{+}, and x^{*} can be real depending on the parameters, and are given by

$$x^{\pm} = \left(g_0 \pm \sqrt{g_0^2 - 1}\right) q \ , \tag{2.36}$$

$$x^{*} = \left(g_1 - \frac{1}{3g_1}\right) q \ , \tag{2.37}$$

where g_0 and g_1 are the dimensionless quantities

$$g_0 = \frac{\alpha}{2\kappa q} \ , \tag{2.38}$$

$$g_1 = \left(g_0 + \sqrt{g_0^2 + \frac{1}{27}}\right)^{1/3} \ . \tag{2.39}$$

It is straightforward to show that the fixed points x^{+} and x^{-} satisfy Eq. (2.30). For $g_0 > 1$, the fixed points x^{-} and x^{+} are real and are therefore candidates for amplitude estimates. The third fixed point x^{*} satisfies $\alpha h(x^{*}) = \kappa x^{*}$ and is therefore also a fixed point of the non-iterated function $\alpha\kappa^{-1}h$. It corresponds to the steady state solution of Eq. (2.29), which is unstable if the system exhibits a limit cycle. We will show below that the fixed point x^{*} provides an effective estimate for the mean product level even in the presence of oscillations.

While the preceding argument relies on an approximation of the deterministic case and its effectivity has to be demonstrated by comparison with numerical solutions, similar fixed point methods have been used to determine the existence of

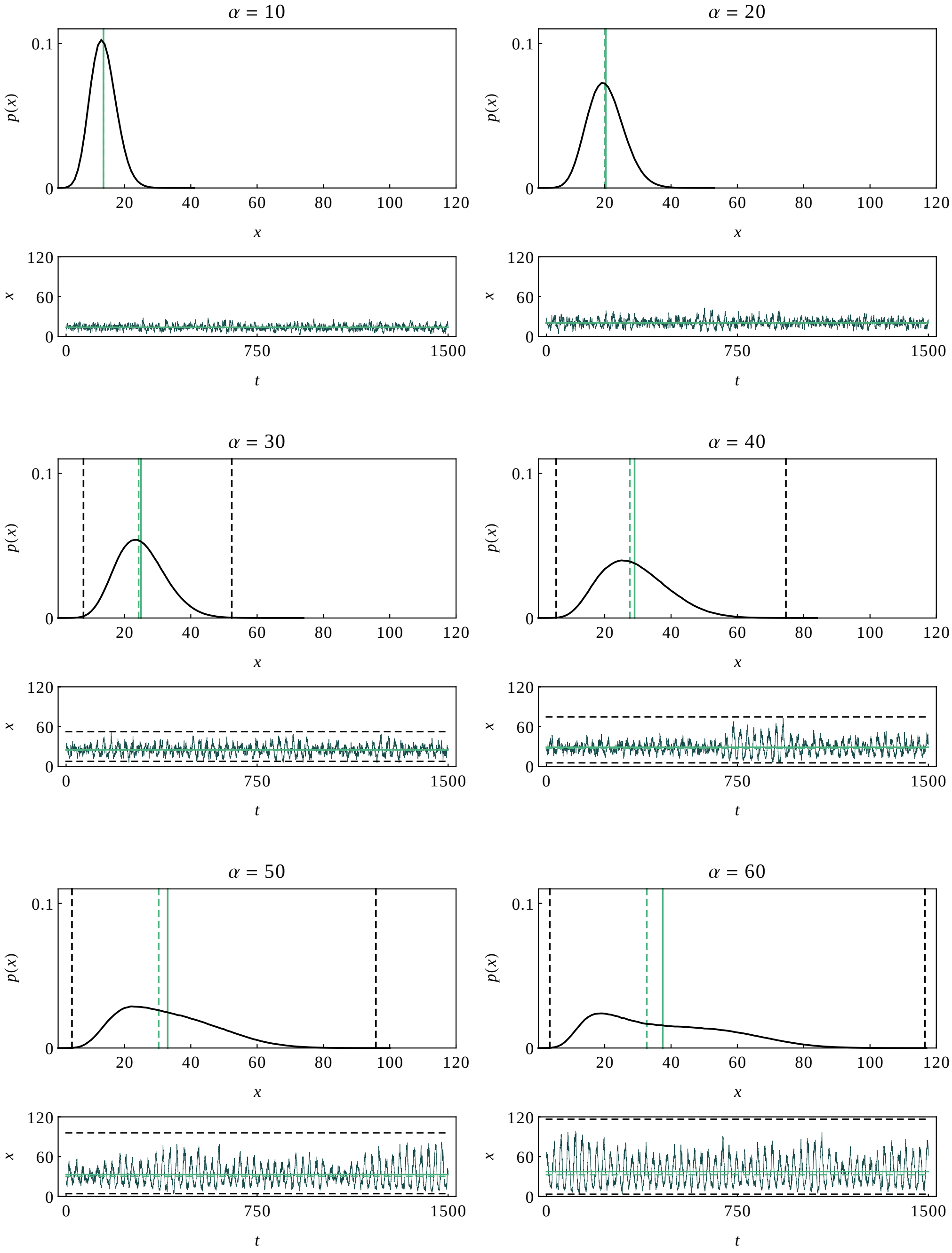

Figure 2.6 Relative frequencies $p(x)$ of occupation numbers of the final product $x = x_n$ (black solid), obtained from numerical simulations of the Markov chain model of an uncoupled oscillator, Eqs. (2.1) and (2.2), for different α. The vertical lines indicate the estimates for maximum and minimum amplitude x^+ and x^- (dashed black), Eq. (2.36), and the mean product level x^* (dashed green), Eq. (2.37), as well as the actual mean product level $\bar{x} = \int_0^\infty x\, p(x)\, \mathrm{d}x$ (solid green). For $\alpha = 10$ and $\alpha = 20$, the corresponding values of x^+ and x^- are complex and hence are not displayed. The plot below each histogram shows an excerpt of a corresponding trajectory. The dashed lines in these plots indicate the same quantities as above. Parameters are $n = 18$, $\lambda = 1.5$, $\kappa = 0.5$, and $q_1 = 20$.

oscillatory solutions in cyclic delay systems in a mathematically rigorous way [40]. Fig. 2.5 demonstrates the effectivity of this method to analytically estimate the amplitude for the deterministic limit Eq. (2.29). In Fig. 2.6, we compare the estimates Eqs. (2.36) and (2.37) with relative frequencies of molecule numbers of the final product x_n obtained from numerical simulations of the Markov chain model. We find that the estimates x^+ and x^- effectively provide conservative bounds for the maximum and minimum amplitudes, respectively.

2.2.4—Frequency and decorrelation rate estimates

A simple estimate for the frequency of an uncoupled oscillator can be found on purely heuristic grounds [81]. Consider a system starting out with zero molecules, $x_i = 0$ for all i. Hence, production at the initial step $i = 0$ proceeds without inhibition. On average, it takes a time $u = n/\lambda$, where u is the mean feedback delay, Eq. (2.27), before the bulk of the produced molecules reaches the final step $i = n$ of the oscillator. When the product level x_n at the final step $i = n$ increases, production at the initial step $i = 0$ decreases due to auto-inhibition. Consequently, the number of molecules traversing the multi-step process starts to decrease. Again, on average, it takes a time u before the decreased molecule levels reach the final step $i = n$ of the multi-step process. Upon this decrease of x_n, inhibition of production at the initial step $i = 0$ becomes weaker, which leads to stronger production and the process starts over. One of these cycles thus consumes a time $T \simeq 2u$ and a simple frequency estimate $\omega = 2\pi/T$ is therefore given by

$$\omega \simeq \frac{\pi}{u} \ . \tag{2.40}$$

Going beyond such heuristic reasoning, we now show how to systematically obtain estimates for the frequency and decorrelation rate of an uncoupled oscillator based on the stochastic dynamics of the system. In Sec. 2.1.3, we have demonstrated that these quantities are encoded in the temporal behavior of the autocorrelation function of the final product, Eq. (2.9). The autocorrelation of final products of an uncoupled oscillator is given by

$$\Gamma(t) = \langle x_n(t'+t)x_n(t')\rangle - \langle x_n\rangle^2 \ , \tag{2.41}$$

in analogy to Eq. (2.8). The master equation (2.5) can be used to derive an approximate integro-differential equation for Γ by neglecting higher order correlations. This equation has been presented in Ref. [94]; we provide its derivation in Appendix A for self-containedness. The result is given by

$$\frac{\mathrm{d}\Gamma}{\mathrm{d}t} \simeq -\kappa\Gamma(t) + \eta \int_0^t G_{\lambda,n}(t-t')\,\Gamma(t')\,\mathrm{d}t' \ , \tag{2.42}$$

where $G_{\lambda,n}$ is the Gamma distribution Eq. (2.26), and

$$\eta = \alpha h'(\bar{x}) + \alpha h'''(\bar{x})\frac{\Gamma(0)}{2} \ . \tag{2.43}$$

Here, $\bar{x}$ and $\Gamma(0)$ are the mean and the variance of the final product level x_n,

$$\bar{x} = \langle x_n\rangle \ , \tag{2.44}$$

$$\Gamma(0) = \langle x_n^2\rangle - \bar{x}^2 \ . \tag{2.45}$$

To obtain an estimate for the frequency ω and the decorrelation rate k of oscillations, we assume that the autocorrelation function has the typical time dependence (2.10).

For convenience, instead of the real ansatz (2.10), we use the complex ansatz $\Gamma(t) = \Gamma_0 \mathrm{e}^{-zt}$ with $z = k + \mathrm{i}\omega$ in Eq. (2.42). If the time scales ω^{-1} and k^{-1} characterizing the oscillations are separated such that $k < \omega \ll \lambda$, an algebraic equation for z can be approximated. In the presence of oscillations, this separation of time scales is expected: the correlation time k^{-1} typically extends over multiple oscillations with period $2\pi\omega^{-1}$ (examples shown in Fig. 2.3B) and the period itself is typically much larger than the average jump time λ^{-1} between two steps of the multi-step process. The derivation of the characteristic equation for the complex exponent z is provided in Appendix A. The result is given by

$$z \simeq \kappa - \eta \left(\frac{\lambda}{\lambda - z} \right)^n . \tag{2.46}$$

This equation can be numerically solved to obtain the frequency $\omega = \operatorname{Im} z$ and the decorrelation rate $k = \operatorname{Re} z$. Moreover, using the separation of time scales introduced above, a closed approximate equation for the frequency $\omega = \operatorname{Im} z$ can be derived from Eq. (2.46). This approximation is independent of $k = \operatorname{Re} z$ and holds in the limit of large step numbers n (Appendix A). The result is given by

$$\omega \simeq \frac{\pi}{u} \left(1 + \frac{1}{\eta u} \right) , \tag{2.47}$$

where $u = n/\lambda$ is the mean feedback delay, Eq. (2.27). The term in brackets yields a correction factor to the simple estimate (2.40), which we had obtained on purely heuristic grounds. Note that the constant η, defined in Eq. (2.43), depends on the mean $\bar{x}$ and the variance $\Gamma(0)$ of the final product level, which itself depend on all model parameters. In Appendix A, we show how to use the amplitude estimates introduced in Sec. 2.2.3 to obtain a closed estimate for η, considering h to be a Hill function, Eq. (2.24), with Hill exponent $p = 2$. The result is given by

$$\eta \simeq -2\kappa \left(1 - \frac{1}{2/3 + (\alpha/\kappa q)^{2/3}} \right) . \tag{2.48}$$

Eq. (2.47) thus provides an analytical estimate for the frequency ω that explicitly depends on the model parameters and can thus be solved independently of numerical simulations.

Fig. 2.7 shows comparisons of frequencies and decorrelation rates obtained from numerical simulations of the full Markov chain model (dots), from numerical solutions of the approximate characteristic equation[2] (2.46) (solid lines) and the closed estimate (2.47) (dashed lines), where for the latter two, the estimate (2.48) for η has been used. The estimate for the frequency ω obtained from Eq. (2.46) is mostly in very good agreement with results from simulations, while the approximation Eq. (2.47) provides a very good approximation for large n, but fails to describe the frequency for small n. This is expected as Eq. (2.47) has been derived for large n. The behavior of the decorrelation rate k is captured well for small step numbers n. For larger n, however, the relative error of k becomes large and Eq. (2.46) yields small negative values for k (not discernible in Fig. 2.7). Since $k < 0$ would correspond to an exponentially growing autocorrelation, the estimates for k are not sensible for large n.

---

[2] In general, the polynomial equation (2.46) has many solutions. Fig. 2.7 displays the numerical solution with the smallest decorrelation rate $k = \operatorname{Re} z$, which governs the long-time behavior of the autocorrelation.

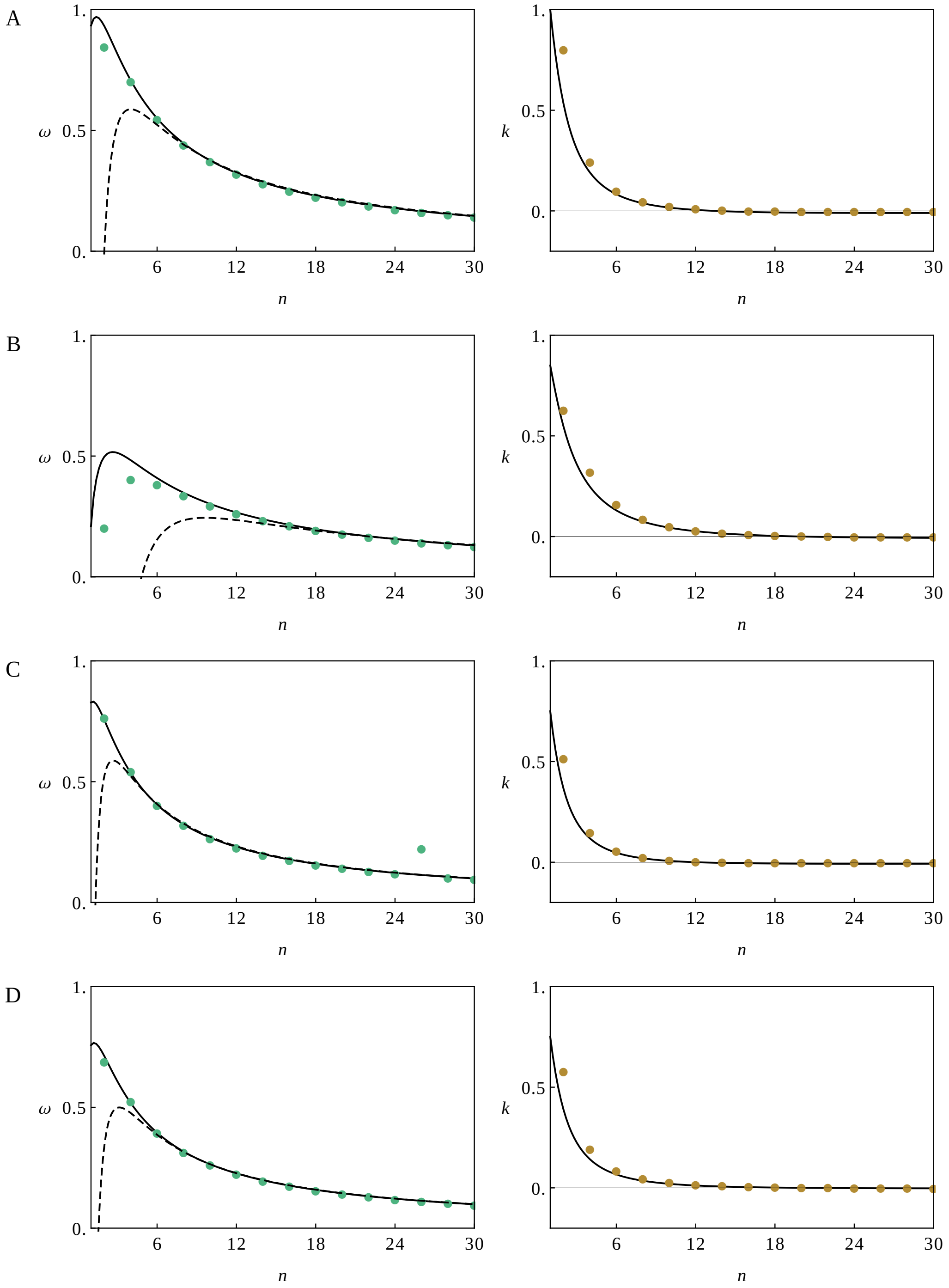

Figure 2.7 Frequencies ω (green) and decorrelation rates k (orange) as a function of the step number n obtained from simulations of the full Markov chain model (dots), from numerical solutions of the approximate characteristic equation (2.46) (solid lines) and the approximation (2.47) (dashed lines). Parameters are
A. $\alpha = 60$, $\lambda = 1.5$, $\kappa = 0.5$, $q = 20$,
B. $\alpha = 30$, $\lambda = 1.5$, $\kappa = 0.2$, $q = 20$,
C. $\alpha = 60$, $\lambda = 1.0$, $\kappa = 0.5$, $q = 20$,
D. $\alpha = 60$, $\lambda = 1.0$, $\kappa = 0.5$, $q = 40$.

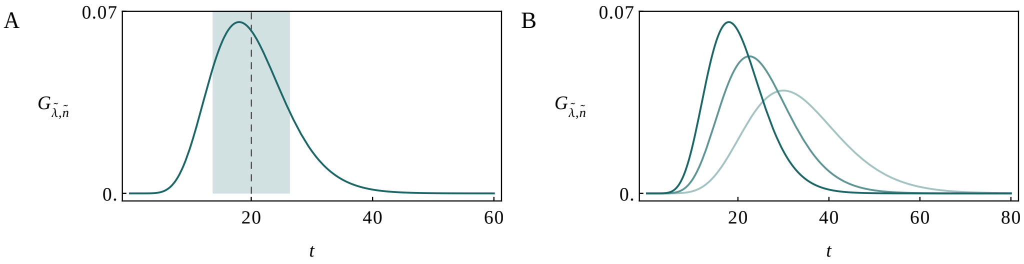

Figure 2.8 A. Gamma distribution $G_{\tilde{\lambda},\tilde{n}}$, Eq. (2.49), for $\tilde{\lambda} = 0.5$ and $\tilde{n} = 10$ (Table 2.1). The dashed line shows the mean τ, Eq. (2.50); the shaded region indicates the standard deviation $\pm\sigma$ from the mean, given by Eq. (2.51). **B.** Gamma distribution $G_{\tilde{\lambda},\tilde{n}}$, Eq. (2.49), for $\tilde{n} = 10$ and $\tilde{\lambda} = 0.5$ (dark), $\tilde{\lambda} = 0.4$ (lighter), and $\tilde{\lambda} = 0.3$ (light).

2.3 Precision and Synchronization of Coupled Oscillators

We now turn to the Markov chain model of two coupled genetic oscillators, described by Eqs. (2.5–2.7). We study how coupling between oscillators leads to synchronization and affects their precision and frequency.

2.3.1—Complex signaling introduces coupling delays

An important property of the signaling pathway is the effective delay that it introduces to the coupling between the oscillators. In contrast to models with explicit coupling delays [21, 89], in our model these coupling delays arise effectively through the finite time required for production, transition, and decay of signaling molecules. In analogy to the multi-step process within each oscillator (see Sec. 2.2.1), molecules traversing the multi-step process of the signaling pathway are subject to a distribution of arrival times, given by

$$G_{\tilde{\lambda},\tilde{n}}(t) = \frac{\tilde{\lambda}^{\tilde{n}}}{(\tilde{n}-1)!} t^{\tilde{n}-1} \mathrm{e}^{-\tilde{\lambda} t} \; . \tag{2.49}$$

This is the Gamma distribution introduced in Eq. (2.26) but with the jump rate $\tilde{\lambda}$ and step number $\tilde{n}$ of the signaling pathways instead of the oscillators. The mean signaling delay τ and the corresponding variance σ^2 are given by

$$\tau = \tilde{n}/\tilde{\lambda} \; , \tag{2.50}$$

$$\sigma^2 = \tilde{n}/\tilde{\lambda}^2 \; , \tag{2.51}$$

in the same way as the mean feedback delay u of an oscillator and the variance v^2 of feedback delay times, Eqs. (2.27) and (2.28). Fig. 2.8A shows a Gamma distribution $G_{\tilde{\lambda},\tilde{n}}$ together with the mean τ and the standard deviation σ. Note that the distribution Eq. (2.49) only describes the delays caused by the signaling molecules traversing $\tilde{n}$ steps with transition rate $\tilde{\lambda}$. It does not include the possibly delaying effects of production and decay of the signaling molecules. Indeed, we will find below that the total coupling delay between the oscillators is mainly determined by the signaling delay τ but also receives a contribution from the decay time of the signaling molecules.

In the following, we study the system's properties as a function of the mean signaling delay τ. According to Eq. (2.50), τ can be varied by varying either $\tilde{n}$, $\tilde{\lambda}$, or both of them simultaneously. We here keep the number of steps $\tilde{n}$ fixed while

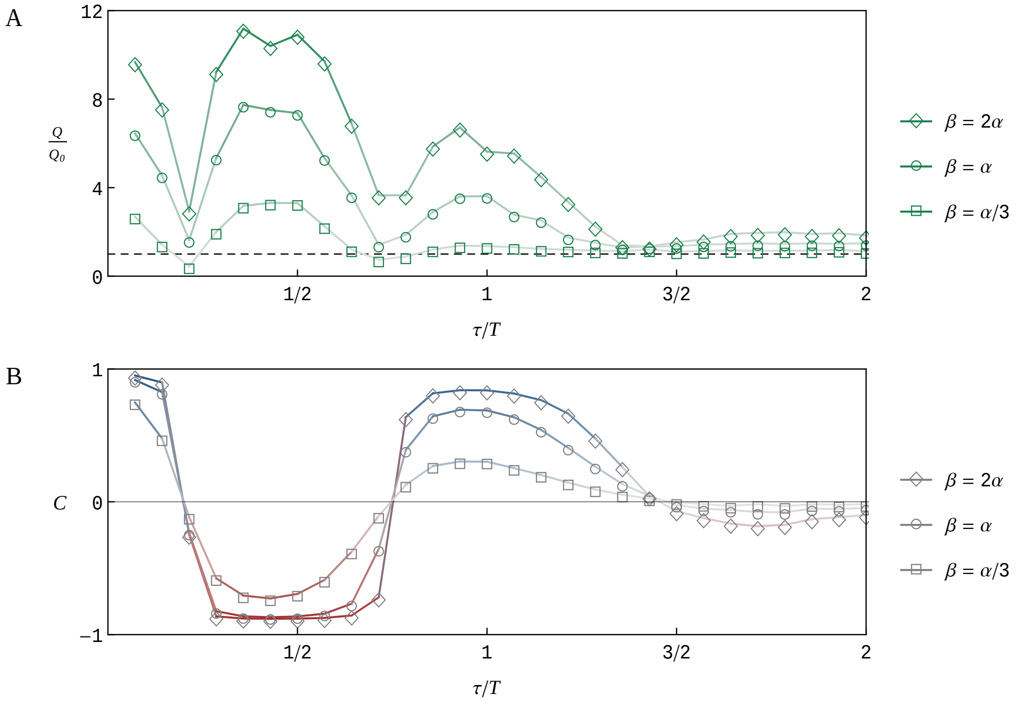

Figure 2.9 **A.** Quality factor Q, Eq. (2.11), and **B.** cross correlation C, Eq. (2.12). Both quantities are shown as a function of the signaling delay τ, parametrized by Eq. (2.52). Q_0 denotes the quality of an uncoupled oscillator (dashed line in panel A) and T its period (Table 2.1). Different symbols indicate different values of the activation strength β (see legend). Parameters are given in Table 2.1. The color code for the lines is the same as for the density plots in Fig. 2.10.

varying τ through the jump rate $\tilde{\lambda}$,

$$\tilde{\lambda}(\tau) = \tilde{n}/\tau \ . \tag{2.52}$$

With this parametrization of the signaling delay, the standard deviation σ of arrival times, determined by Eq. (2.51), is a constant multiple of the signaling delay, $\sigma = \tau/\sqrt{\tilde{n}}$. Hence, this parametrization enables to study the effects of different dispersions of delay times as τ is varied (see Fig. 2.8B for examples).

2.3.2— Enhancement of precision by coupling

From studies of an uncoupled genetic oscillator, it is known that the number of molecules in the system and the number n of steps of its multi-step process are the major factors that determine its precision [94]. We now address the question of how precision is affected by coupling. We assess the precision of the oscillators through the quality factor Q (Sec. 2.1.3). Fig. 2.9A shows typical examples for the dependence of the quality factor Q on the signaling delay τ. Different curves correspond to different values of the activation strength β. Intuitively, the magnitude of β regulates the coupling strength of the oscillators, with $\beta = 0$ corresponding to complete decoupling (see Fig. 2.2). For small delays, the quality factor is increased compared to an uncoupled oscillator, whose quality is indicated by the dashed line in Fig. 2.9A. The difference between the quality of coupled and uncoupled oscillators depends on the activation rate β. This finding indicates that stochastic coupling with short signaling delays can considerably increase the precision of the oscillators. For

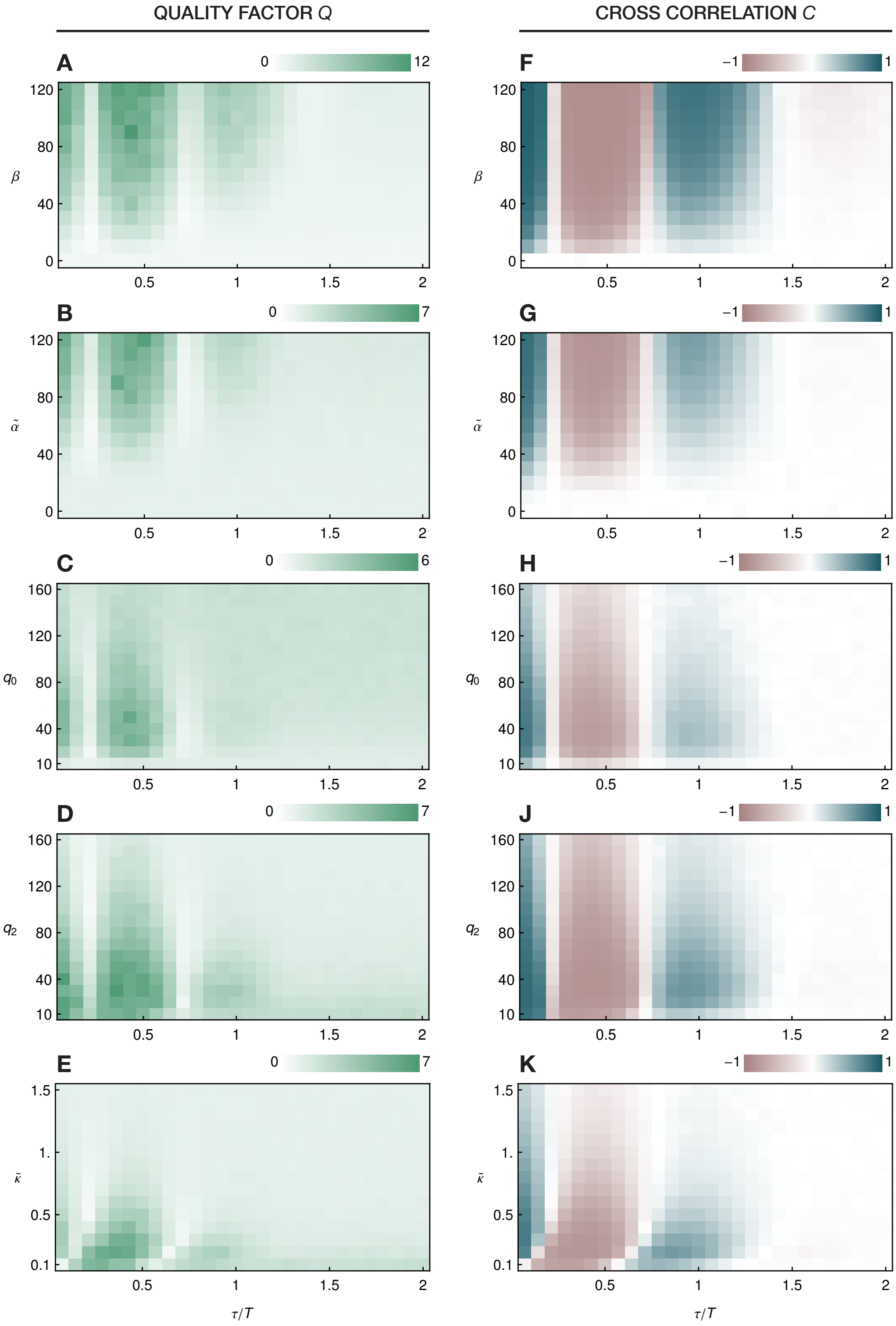

Figure 2.10 **A–E.** Quality factor Q/Q_0, Eq. (2.11), in multiples of the quality Q_0 of an uncoupled oscillator. **F–K.** Cross correlation C of the final products of both oscillators, Eq. (2.12). Both quantities are displayed as a function of the signaling delay τ/T, where T is the period of an uncoupled oscillator, and the other parameters of the signaling pathway. Parameters that are not varied are given in Table 2.1.

higher delays, the quality factor displays local maxima for delays which are integer multiples of $T/2$ and local minima for delays which are odd multiples of $T/4$, where T is the period of an uncoupled oscillator. The height of these maxima decreases with increasing delays. For large delays, the quality remains slightly above the value Q_0 of an uncoupled oscillator. We will return to the phenomenon of alternating regions of high and low quality and the decay of the quality for large delays when we analyze the synchronization properties of the system.

To browse the parameter space systematically and see whether this behavior also appears in different parameter regions, we vary other parameters of the signaling pathway simultaneously with the signaling delay. Figs. 2.10A–E display the results as density plots. The amount by which the quality is enhanced increases with increasing activation rate β (Fig. 2.10A), as already indicated in Fig. 2.9A. A similar behavior of the quality factor is found if the production rate $\tilde{\alpha}$ of signaling molecules is varied (Fig. 2.10B).

When varying the thresholds q_0 and q_2 for activation and repression, the picture changes qualitatively (Fig. 2.10C,D). As a function of the threshold level q_0 that regulates the inhibition of signaling molecules by the final product $x_{\mu n}$ of the sending oscillator, we find isolated 'islands' of high quality in parameter space (Fig. 2.10C). These islands appear where q_0 is of the same order as the mean product level $\langle x_{\mu n} \rangle \simeq 40$ and have a simple explanation: for $\langle x_{\mu n} \rangle \ll q_0$, inhibition effectively never sets in as the threshold level q_0 is never reached, while for $\langle x_{\mu n} \rangle \gg q_0$, the production of signaling molecules is always inhibited. Hence, in these parameter regions, the signaling pathways do not reflect the oscillatory behavior of the sending oscillator. Analogously, similar 'islands' of high quality appear for the activation threshold q_2 being of the same order as the mean product level of the signaling molecule $\langle \tilde{x}_{\mu \tilde{n}} \rangle$ (Fig. 2.10D).

A third type of behavior of the quality factor is found when the decay rate $\tilde{\kappa}$ of the signaling molecule is varied simultaneously with the signaling delay (Fig. 2.10E). For small values of $\tilde{\kappa}$, the high quality regions are tilted towards smaller signaling delays. This indicates that the total coupling delay is not only determined by the signaling delay τ but also by the decay time $\tilde{\kappa}^{-1}$.

2.3.3— Is increased quality due to higher product turnover?

The preceding results show that coupling can increase the precision of genetic oscillators by more than an order of magnitude. From previous studies of uncoupled noisy oscillators, it is known that an increased production rate of cyclic molecules tends to increase the precision as the effects of stochasticity are suppressed by high molecule numbers [94]. This opens the possibility that the increased precision observed in the presence of coupling is solely due to the higher number of cyclic molecules caused by the additional activation through the signaling pathway. To assess whether this is the case, we compare the precision of uncoupled and coupled oscillators with the same product turnover K, Eq. (2.20), that is, with the same number K of decaying cyclic molecules per period of oscillation.

To obtain a specific value K of the turnover for an uncoupled oscillator, we adjust its basal production rate correspondingly, $\alpha = \alpha(K)$, while keeping all other parameters fixed to reference values (Table 2.1). In the coupled system, the same value K can be achieved by adjusting the activation rate, $\beta = \beta(K)$, while keeping all other parameters (including the basal production rate α) fixed to reference values. We then compare the precision of coupled and uncoupled oscillators with the same turnover K. Fig. 2.11 shows the results for the quality factor Q of coupled and uncoupled oscillators for different values of the mean signaling delay τ. Each bubble

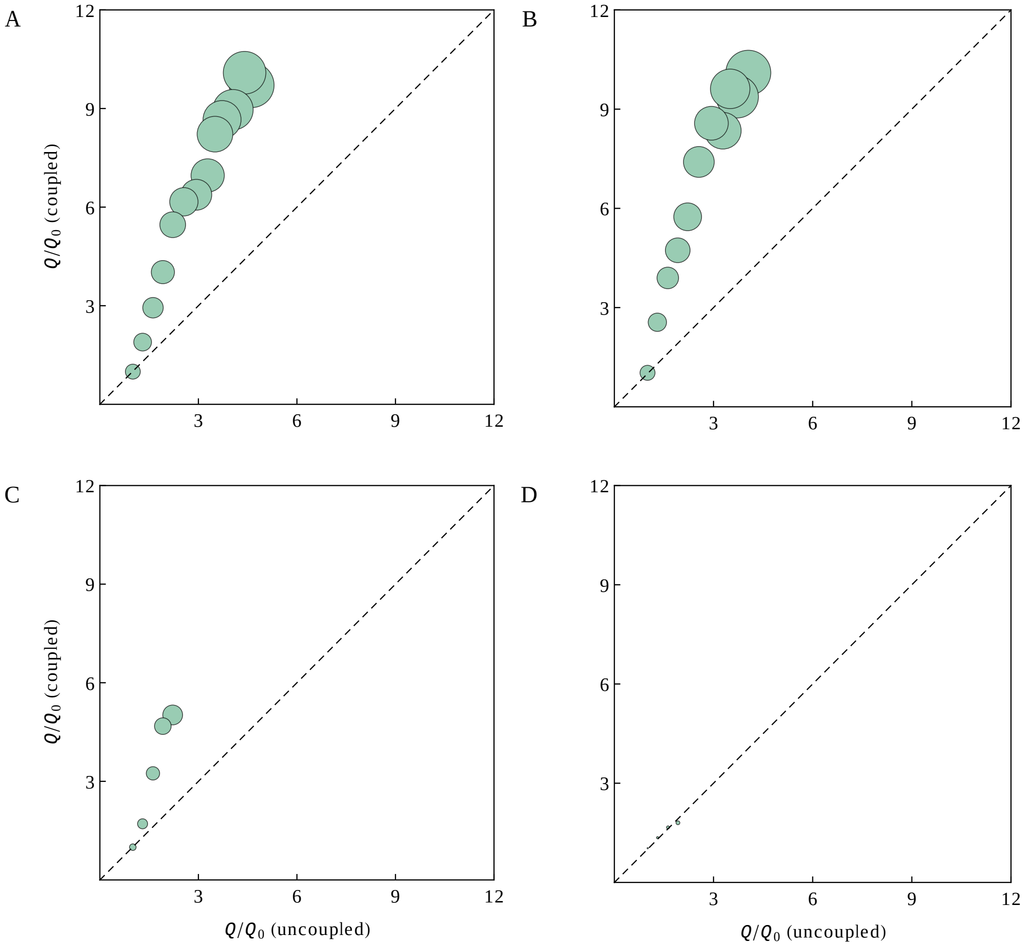

Figure 2.11 Quality of coupled and uncoupled oscillators with the same product turnover K, Eq. (2.20), for $\tau/T = 1/10$ (A), $\tau/T = 1/2$ (B), $\tau/T = 1$ (C), and $\tau/T = 2$ (D), where T is the period of an uncoupled oscillator. The size of the bubble indicates the relative magnitude of different values of K (see Sec. 2.3.2 for details). The dashed line marks the diagonal. The other parameters are provided in Table 2.1.

corresponds to a specific value K of product turnover, where the size of the bubble indicates the relative value of K. The x-position of each bubble is the quality of an uncoupled oscillator with basal production rate $\alpha = \alpha(K)$. The y-position of each bubble is the quality of a coupled oscillator with basal production rate $\alpha = \alpha_0$ and activation rate $\beta = \beta(K)$. Since all bubbles are located distinctly above the diagonal, the precision of coupled oscillators is significantly higher as compared to uncoupled oscillators with the same product turnover. This demonstrates that the increase in precision is not solely due to an increased number of cyclic molecules.

2.3.4— Synchronization through coupling

It has been known for a long time that in the presence of coupling, oscillators tend to synchronize, even if coupling is weak [138]. We now investigate how the properties of stochastic coupling between oscillators affect their tendency to synchronize their oscillations. We assess the degree of synchrony of two oscillators through the cross correlation C (Sec. 2.1.4). Fig. 2.9B shows typical examples for the dependence of the cross correlation C on the signaling delay τ. The different curves correspond to different values of the activation strength β. For small delays, the system attains a state of high positive correlation, $C \simeq 1$, indicating in-phase synchronized oscillations. As for the quality factor Q, the magnitude of the cross correlation C depends on the activation strength β, with increased correlation observed for higher values of β. As the signaling delay approaches $T/2$, the cross correlation changes its sign and decreases to values close to $C \simeq -1$, indicating anti-phase synchronized oscillations. For delays close to a full period T, positive correlations are recovered again but of decreased magnitude compared to the initial maximum for small delays. For large delays, the cross correlation gradually decays to zero. These findings indicate that coupling is attractive: in the absence of delays, the system tends to lock to an in-phase synchronized state, while finite delays introduce an effective phase shift between oscillators that can lead to anti-phase synchronization depending on the value of the delay. We will investigate how the specific coupling mechanism considered here leads to such a behavior in Sec. 2.3.7.

As for the quality factor Q, we systematically browse the parameter space and display the results as density plots in Figs. 2.10F–K. Again, we find that the general trend as a function of the signaling delay τ is captured by Fig. 2.9B with the magnitude of C determined by the other parameters of the signaling pathway. Importantly, parameter regions with high quality and a high degree of correlation or anti-correlation coincide (Figs. 2.10A–K). In particular, both the quality and the magnitude of the cross correlation decay for large signaling delays. This is explained as follows: The production rate of signaling molecules oscillates, entrained by the sending oscillator through inhibition. This gives rise to oscillating molecules levels propagating along the signaling pathway. However, with increasing signaling delay, the dispersion of arrival times of the signaling molecules increases (Sec. 2.3.1). When the standard deviation σ of arrival times, given by Eq. (2.51), reaches a significant fraction of the oscillation period, oscillations are gradually lost along the signaling pathway due to noise. Hence, as the delay increases, the last step of the signaling pathway carries less and less information about the oscillatory state of the sending oscillator. For large delays, this leads to an effective decoupling of the oscillators.

As a complementary measure for the degree of correlation of both oscillators, we display the mutual information I of the final products of both oscillators, Eq. (2.19), in Figs. 2.13F–K. Even though the mutual information I takes into account correlations of all orders, we observe that it follows the same trend as the magnitude $|C|$ of the cross correlation C (Figs. 2.10F–K), which only measures linear correlations. We thus conclude that the cross correlation C is sufficient to understand the interdependence of both oscillators. Furthermore, in contrast to I, the sign of C carries information about the type of synchrony attained by the system.

2.3.5—
Stochastic switching between in-phase and anti-phase synchrony

Between the regions of the signaling delay in which a distinct in-phase or anti-phase correlation is observed, the quality Q and the cross correlation C of both oscillators are low (local minima in Fig. 2.9B and bright columns in Figs. 2.10A–K). This indicates that in these regions, the dynamics of both oscillators are poorly correlated on average. However, closer examination of the oscillatory time series reveals that both oscillators are indeed highly correlated if finite time windows are considered: the oscillators stochastically switch between in-phase and anti-phase correlated oscillations[3]. This behavior is illustrated in Fig. 2.12A, showing the trajectories of the final oscillator products x_{1n} and x_{2n} of an exact realization of the system for $\tau \simeq T/4$. The system starts out with a high degree of anti-phase correlation, then

---

[3] Such a phenomenon has recently also been found in models of noisy Hodgkin–Huxley neurons [4].

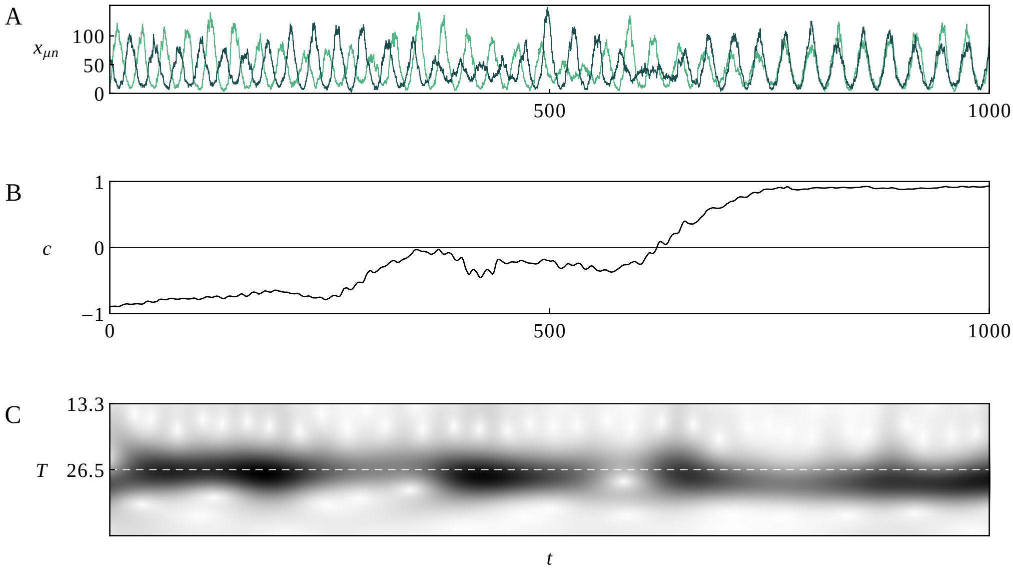

Figure 2.12 Stochastic switching between in-phase and anti-phase correlations. **A.** Trajectories of the final product levels x_{1n} and x_{2n} of an exact realization of the model for $\tau \simeq T/4$ and all other parameters given by Table 2.1. **B.** Time-dependent windowed cross correlation $c(t)$, Eq. (2.18), with $w = 4T$ of the time series shown in panel A. **C.** Wavelet transform of the time series in panel A, where dark regions indicate the strong period components. The white dashed line serves as a visual guide.

undergoes an extended transient region before it attains a highly correlated in-phase state. This behavior is reflected in the corresponding windowed cross correlation c, Eq. (2.18), which goes from values close to -1 to values close to 1 (Fig. 2.12B). This phenomenon of alternating in-phase and anti-phase correlations likely contributes to the low quality observed for corresponding values of the signaling delay as it destroys long-term correlations of the oscillations.

Fig. 2.12C shows a so-called wavelet scalogram of x_{1n}, which is a time-dependent power spectrum[4] [143]. Dark colors correspond to strong period components, bright colors to weak components. In the beginning, the dominant period components are centered around the period indicated by the white dashed line. After transition to the in-phase synchronized state, the period has increased: the dashed line now marks the upper boundary of the dominant period components. This indicates that the collective frequency of the oscillators is related to the type of synchrony (in-phase or anti-phase) that they attain. We will address this phenomenon in the next section.

2.3.6— The collective frequency depends on coupling properties

If the oscillators attain an in-phase or anti-phase synchronized state, this implies that both oscillators evolve with a collective frequency. It is well-known that in the presence of coupling delays, this collective frequency can differ from the frequency of an uncoupled oscillator [129, 163]. To assess whether this is also the case for the model of coupled genetic oscillators presented here, we obtain the collective frequency of the oscillators (Sec. 2.1.3) as a function of the signaling delay and other parameters of the signaling pathway (Figs. 2.13A–E).

As a function of the signaling delay τ, these plots reveal sharp changes of the

---

[4] For details on the wavelet transform, see Chapter 4, Sec. 4.2.2.

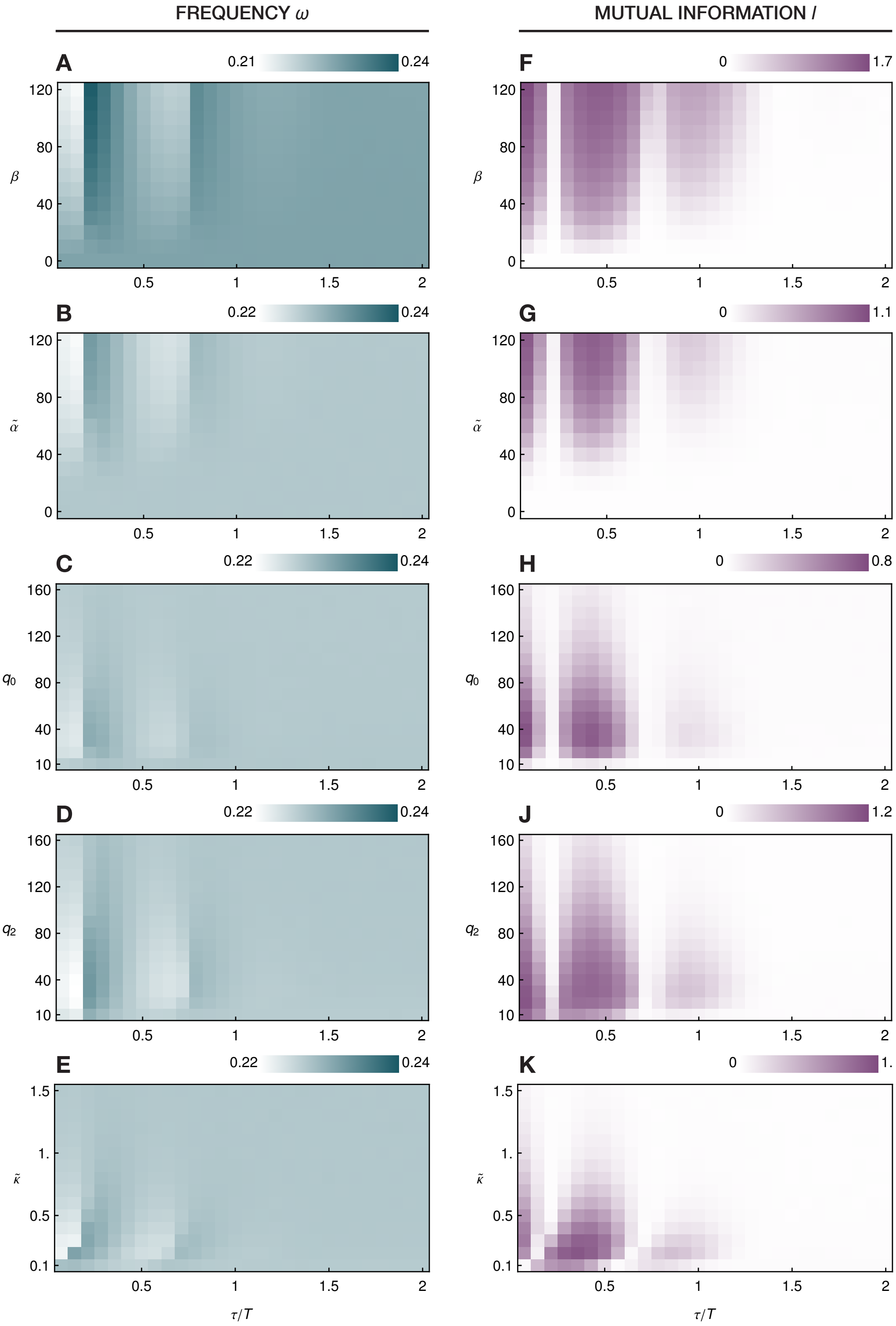

Figure 2.13 **A–E.** Frequency ω from fits of Eq. (2.10) to Eq. (2.9). **F–K.** Mutual information I in bits, Eq. (2.19). Axes scaling and parameters as in Fig. 2.10.

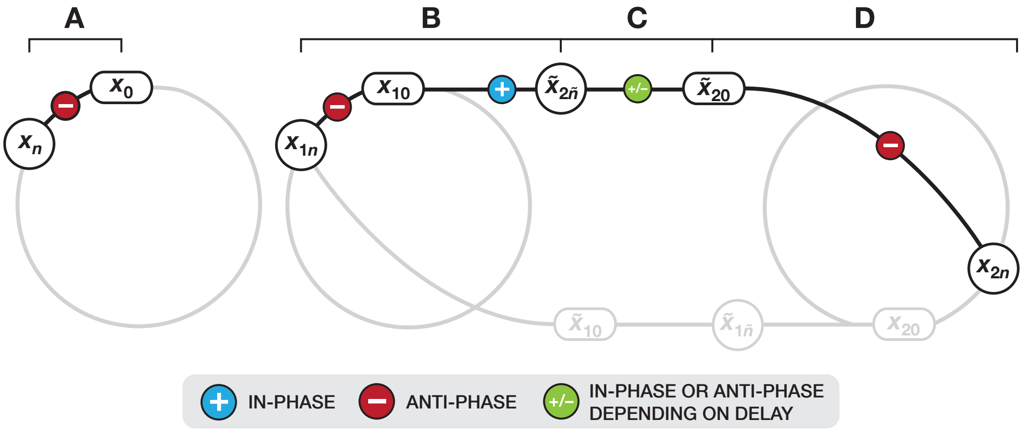

Figure 2.14 Synchrony relations between different molecule numbers in the presence of oscillations for the autonomous oscillator (A) and the coupled system (B–D), see Sec. 2.3.7 for details. Symbols indicate the synchrony relation between oscillations of molecule numbers connected by the corresponding lines (see legend). The synchrony relation between any two molecule numbers can be obtained by multiplying all signs along any connecting path in the diagram.

frequency at odd multiples of $T/4$. This indicates that the collective frequency of in-phase correlated states is different from the collective frequency of anti-phase correlated states, consistent with the observations made in the previous section. For high signaling delays, the effect of coupling on the collective frequency vanishes as the oscillators effectively decouple (Sec. 2.3.4). We will return to this observation and investigate it in more detail when studying the phase oscillator approximation in Sec. 2.4.

2.3.7— Nature of the coupling mechanism

In the previous sections, we found that oscillator coupling leads to in-phase or anti-phase synchronization, depending on the signaling delay. In particular, we found that coupling is attractive (Sec. 2.3.4), that is, coupling promotes in-phase synchrony in the absence of signaling delays. We now investigate how the specific coupling mechanism considered here leads to such an attractive behavior.

To this end, we study the synchrony relations between different molecule levels in the system. In an uncoupled oscillator, since the production rate $\alpha H_-(x_n/q_1)$ of molecules depends on the final product level x_n (Fig. 2.1), oscillations of the final produce level x_n induce oscillations of the production rate. Since H_- acts inhibitory, these oscillations of the production rate are in anti-phase with the product level x_n (Fig. 2.14A). In the presence of coupling, the final product level also regulates the production of signaling molecules. Hence, oscillations of the final product level also induce anti-phase oscillations in the production rate of signaling molecules (Fig. 2.14D). The synchrony between the first and the last step of the signaling pathway is determined by the signaling delay, which introduces an effective phase shift between the first and the last step (Fig. 2.14C). The oscillating signaling molecule levels, in turn, lead to an oscillating activation of production in the receiving oscillator. Intuitively, a robust synchronized state of both oscillators—irrespective whether in-phase or anti-phase synchronized—is only possible if this oscillating activation is in-phase synchronized with the oscillations of the production rate due to autoinhibition (Fig. 2.14B). This intuitive picture implies that the final product of the signaling pathway is always anti-phase correlated with the final product of the re-

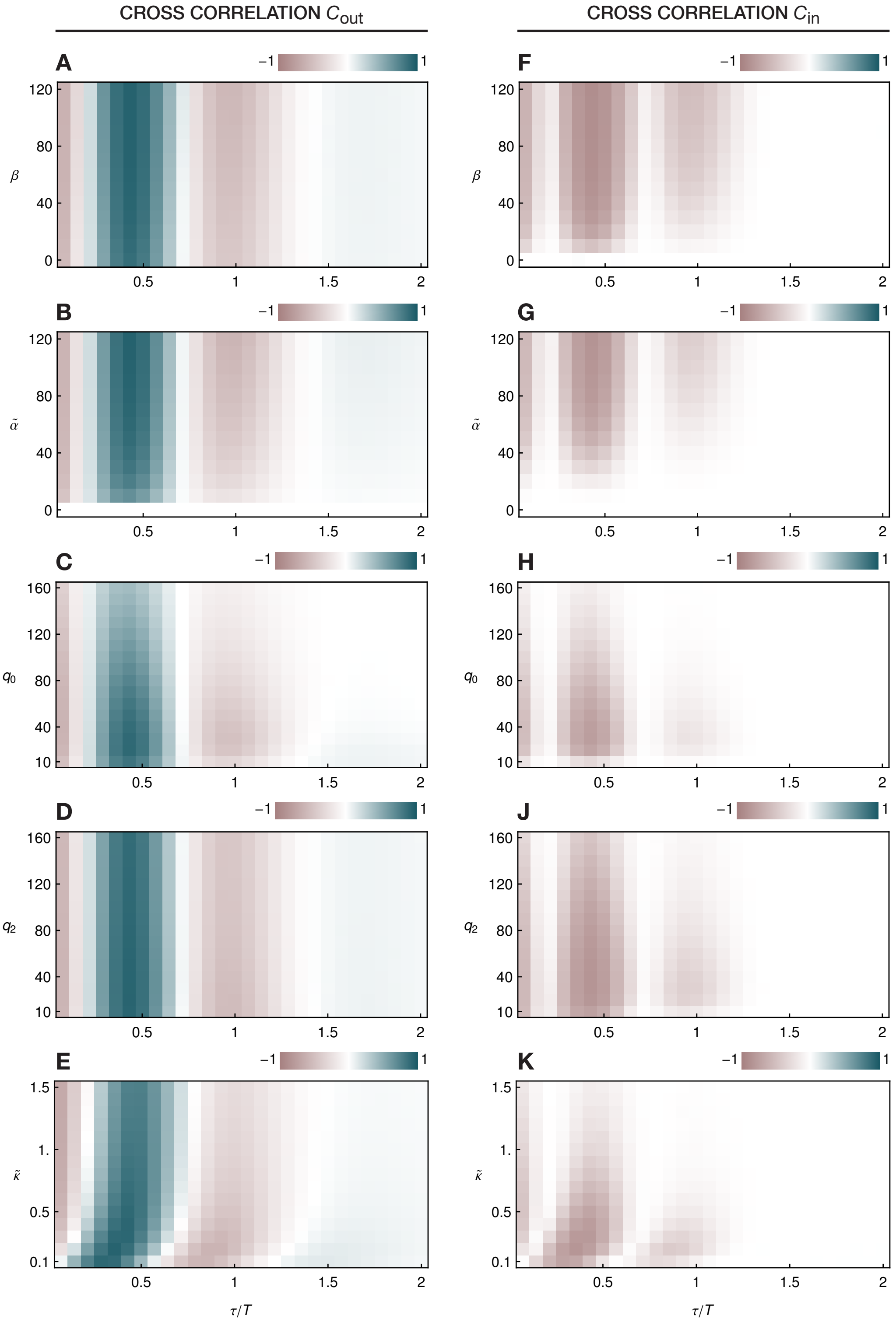

Figure 2.15 **A–E.** Cross correlation C_{out} of the final products of an oscillator and the outgoing signaling pathway, Eq. (2.16). **F–K.** Cross correlation C_{in} of the final products of an oscillator and the incoming signaling pathway, Eq. (2.16). Axes scaling and parameters as in Fig. 2.10.

ceiving oscillator ($\tilde{x}_{2\tilde{n}}$ and x_{1n} in Fig. 2.14B). In fact, this behavior is confirmed by numerical studies of the cross correlation C_{in} of these two molecule levels, Eq. (2.15): Figs. 2.15F–K show that C_{in} is always negative, independent of whether both oscillators are in-phase or anti-phase synchronized (compare with Figs. 2.10F–K). Only the magnitudes of C_{in} and C are correlated.

2.4 Phase Oscillator Approximation

2.4.1— Phase description of coupled oscillators

We complement the analysis of the Markov chain model of coupled genetic oscillators with a comparison with a system of coupled phase oscillators, taking into account distributed coupling delays. Such a phase description reduces the complexity of limit cycle oscillators to the dynamics of a single phase variable representing the state of the oscillator [1, 77, 158]. Hence, it considerably simplifies the theoretical description of a dynamic oscillator system. We first briefly introduce how coupling of oscillators is represented in such a phase oscillator picture. The phase dynamics for an uncoupled deterministic oscillator is given by

$$\frac{\mathrm{d}\phi}{\mathrm{d}t} = \omega \ , \tag{2.53}$$

where ϕ is the phase of the oscillator and ω is its intrinsic frequency. Hence, the phase of the uncoupled oscillator evolves linearly, $\phi(t) = \omega t + \phi_0$. Coupling between two identical oscillators is described by an additional term that evaluates the phase difference between the two oscillators and adjusts their frequencies accordingly,

$$\frac{\mathrm{d}\phi_\mu}{\mathrm{d}t} = \omega + \varepsilon \sin(\phi_{\bar{\mu}} - \phi_\mu) \ . \tag{2.54}$$

Here, ϕ_μ is the phase of oscillator $\mu = 1, 2$, ε is the coupling strength with the dimension of a frequency, and $\bar{\mu} = 2\delta_{\mu,1} + 1\delta_{\mu,2}$ denotes the index of the respective other oscillator. Eq. (2.54) is the simplest example of a so-called Kuramoto model of coupled phase oscillators [77]. According to Eq. (2.54), a phase difference between both oscillators changes their dynamic frequency. Consequently, the oscillators speed up or slow down to even out their phase difference. It is straightforward to show that the oscillators tend to lock to a stable in-phase synchronized state, $\phi_1(t) = \phi_2(t) = \omega t$, in which they both oscillate with their intrinsic frequency ω [129].

2.4.2— Coupling with distributed delays

We now extend the phase model Eq. (2.54) to include the effects of time delays in the coupling. If there is a discrete signaling delay τ between both oscillators, this extension is accomplished by simply retarding the argument of the sending oscillator's phase, that is, replacing $\phi_{\bar{\mu}}(t)$ by $\phi_{\bar{\mu}}(t - \tau)$ in Eq. (2.54) [63, 129, 163]. The effects of such discrete signaling delays on the properties of synchronized states and the synchronization dynamics have been studied extensively [38, 66, 129, 163]. In the Markov chain model described in the previous sections, oscillator coupling was achieved through the stochastic exchange of signaling molecules between the oscillators. The effective signaling delay between the oscillators was determined by the arrival times of the signaling molecules. We found that these arrival times were characterized by a distribution of delay times instead of a single discrete delay (Sec. 2.3.1). We thus expect that a phase model capable of describing the key features of this system must also include a distribution of delay times instead of a single discrete delay. In Appendix B, we show how to extend Eq. (2.54) to take into account the effects of distributed delays. Assuming that the distribution of delay

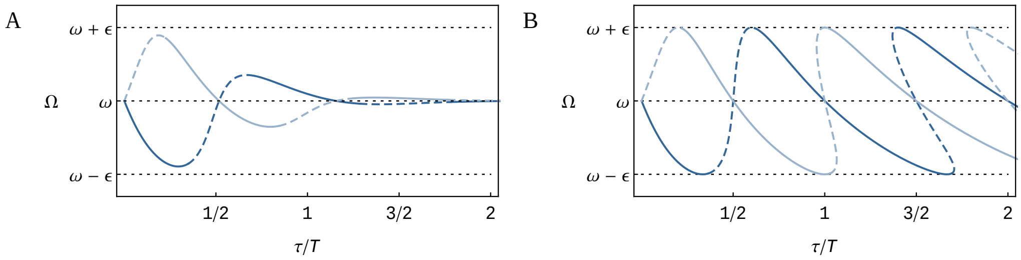

Figure 2.16 The collective frequency Ω for the system with distributed delays (A) and discrete delays (B) and for the in-phase synchronized state (dark blue) and the anti-phase synchronized state (light blue), as a function of the signaling delay τ, parameterized by Eq. (2.52). **A.** Solutions to Eq. (2.58) (dark blue) and Eq. (2.59) (light blue). **B.** Solutions to Eq. (2.60) (dark blue) and Eq. (2.61) (light blue). Solid lines show stable solutions, dashed lines show unstable solutions (see Sec. 2.4.4 for details). Parameters for both plots are $\omega = 2\pi/28$ and $\varepsilon = \omega/4$. The other parameters for plot A are given in Table 2.1.

times in the phase model is identical to the distribution $G_{\tilde{\lambda},\tilde{n}}(t')$ of arrival times of signaling molecules, Eq. (2.49), we obtain

$$\frac{\mathrm{d}\phi_\mu}{\mathrm{d}t} = \omega + \varepsilon \int_0^\infty G_{\tilde{\lambda},\tilde{n}}(t') \sin(\phi_{\bar{\mu}}(t-t') - \phi_\mu(t))\, \mathrm{d}t' \ , \tag{2.55}$$

where $\tilde{\lambda}$ is the jump rate and $\tilde{n}$ the number of steps of the signaling pathways. The corresponding mean signaling delay τ and its variance σ^2 are given by Eqs. (2.50) and (2.51).

2.4.3—Synchronized states

For the Markov chain model, we found that in the presence of coupling, oscillators can exhibit a high degree of positive or negative correlation that we have characterized as in-phase and anti-phase synchrony (Sec. 2.3.4). We compare the properties of these types of synchrony with those of in-phase and anti-phase solutions to the phase model Eq. (2.55). The in-phase synchronized state of the phase model is given by

$$\phi_\mu(t) = \Omega t \tag{2.56}$$

for $\mu = 1, 2$, that is, both oscillators evolve with the same collective frequency Ω and have no phase lag relative to each other. The anti-phase synchronized state is given by

$$\begin{aligned} \phi_1(t) &= \bar{\Omega} t \ , \\ \phi_2(t) &= \bar{\Omega} t + \pi \ , \end{aligned} \tag{2.57}$$

that is, both oscillators propagate with the same frequency $\bar{\Omega}$ but exhibit a phase lag of π. Using the ansatz (2.56) in Eq. (2.55) yields an implicit equation for the collective frequency of the in-phase synchronized state,

$$\Omega = \omega - \varepsilon \left(\frac{1}{1 + \Omega^2/\tilde{\lambda}^2} \right)^{\tilde{n}/2} \sin \left(\tilde{n} \arctan \frac{\Omega}{\tilde{\lambda}} \right) \ . \tag{2.58}$$

Details of the derivation of this equation are provided in Appendix B. It is straightforward to check that the collective frequency $\bar{\Omega}$ of the anti-phase synchronized state (2.57) is obtained by the replacement $\varepsilon \to -\varepsilon$ in Eq. (2.58),

$$\bar{\Omega} = \omega + \varepsilon \left(\frac{1}{1 + \bar{\Omega}^2/\tilde{\lambda}^2} \right)^{\tilde{n}/2} \sin\left(\tilde{n} \arctan \frac{\bar{\Omega}}{\tilde{\lambda}} \right) . \tag{2.59}$$

Eqs. (2.58) and (2.59) are transcendental equations, which cannot be solved for the collective frequency in a closed form. However, we straightforwardly obtain the bounds $|\Omega - \omega| \leq |\varepsilon|$ and $|\bar{\Omega} - \omega| \leq |\varepsilon|$, that is, the collective frequencies Ω and $\bar{\Omega}$ are located in a window of width $2|\varepsilon|$ around the intrinsic frequency ω. Furthermore, we find that $\Omega, \bar{\Omega} \to \omega$ in the limit $\tilde{\lambda} \to 0$, implying that for increasing signaling delays due to an decreased jump rate, the collective frequency becomes independent of coupling. The case of a discrete delay τ can be recovered from Eqs. (2.58) and (2.59) by taking the limit $\tilde{n} \to \infty$ with $\tilde{\lambda} = \tilde{n}/\tau$, which yields

$$\Omega = \omega - \varepsilon \sin(\Omega\tau) \ , \tag{2.60}$$

$$\bar{\Omega} = \omega + \varepsilon \sin(\bar{\Omega}\tau) \ . \tag{2.61}$$

These results for a discrete delay τ are well-known in the literature [5, 38, 71, 98, 129, 163] and show that Eqs. (2.58) and (2.59) yield the correct limiting case.

Fig. 2.16 shows exact solutions[5] to Eqs. (2.58–2.61), in which $\tilde{n}$ is fixed and the mean signaling delay $\tau = \tilde{n}/\tilde{\lambda}$ is varied by varying $\tilde{\lambda}$ according to Eq. (2.52). In contrast to the case of discrete delays, the collective frequency in the case of distributed delays shows a decaying dependence on the mean delay τ for large τ. We will demonstrate that such a behavior also occurs in the Markov chain model after analyzing the stability of these states in the next section.

2.4.4— Stability of the synchronized states

For the Markov chain model, we found that the effective signaling delay determines whether in-phase or anti-phase correlations are observed (Sec. 2.3.4). Since both in-phase and anti-phase synchronized states are solutions to the phase model Eq. (2.55), we have to assess under which circumstances these states are stable or unstable. To this end, we linearize the dynamics around the synchronized state [18, 137]. We first address the stability of the in-phase synchronized state, Eq. (2.56). We use the standard ansatz [137]

$$\phi_\mu(t) = \Omega t + \delta \xi_\mu(t) \tag{2.63}$$

in Eq. (2.55), where δ is an expansion parameter and ξ_μ is a perturbation of order unity. We obtain the time evolution of the perturbation ξ_μ by expanding Eq. (2.55) to first order in δ,

$$\frac{\mathrm{d}\xi_\mu}{\mathrm{d}t} = \varepsilon \int_0^\infty G_{\tilde{\lambda},\tilde{n}}(t') \cos(\Omega t') \left(\xi_{\bar{\mu}}(t - t') - \xi_\mu(t) \right) \mathrm{d}t' + \mathcal{O}(\delta) \ . \tag{2.64}$$

This equation is inconvenient to work with since the dynamics of the oscillator μ depends on the dynamics of the respective other oscillator $\bar{\mu}$. Hence, we decouple the

---

[5] A curve that includes all collective frequency solutions to Eq. (2.58) with fixed $\tilde{n}$ and $\tilde{\lambda} = \tilde{\lambda}(\tau) = \tilde{n}/\tau$ can be parameterized exactly. We introduce a phase variable $\theta = \Omega\tau$ and insert $\Omega = \theta/\tau = \theta\tilde{\lambda}/\tilde{n}$ in Eq. (2.58) to obtain

$$\Omega(\theta) = \omega - \varepsilon \left(\frac{1}{1 + \theta^2/\tilde{n}^2} \right)^{\tilde{n}/2} \sin\left(\tilde{n} \arctan \frac{\theta}{\tilde{n}} \right) . \tag{2.62}$$

The corresponding curve in the (τ, Ω)-plane is given by $\mathcal{L} = \{(\tau(\theta), \Omega(\theta)) \ ; \ \theta \geq 0\}$, where $\tau(\theta) = \theta/\Omega(\theta)$. The solutions to Eq. (2.59) can be obtained analogously.

dynamics by defining the collective modes $\psi_\nu = \xi_1 + \nu\xi_2$ with $\nu = +1, -1$. Inverting this definition yields $\xi_1 = (\psi_+ + \psi_-)/2$ and $\xi_2 = (\psi_+ - \psi_-)/2$, which shows that exciting the collective mode ψ_+ shifts both oscillators by the same amount and thus corresponds to a global phase shift, whereas ψ_- is the phase difference between both oscillators. Dropping terms of order δ, the dynamics of these collective modes are given by

$$\frac{\mathrm{d}\psi_\nu}{\mathrm{d}t} = \varepsilon \int_0^\infty G_{\tilde{\lambda},\tilde{n}}(t') \cos(\Omega t') \left(\nu\psi_\nu(t-t') - \psi_\nu(t)\right) \mathrm{d}t' \ . \tag{2.65}$$

The characteristic equation for these modes is obtained using the exponential ansatz $\psi_\nu(t) = \mathrm{e}^{\gamma_\nu t}$. The sign of $\operatorname{Re}\gamma_\nu$ then determines whether perturbations decay ($\operatorname{Re}\gamma_\nu < 0$) or grow ($\operatorname{Re}\gamma_\nu > 0$) and thus whether the synchronized state is stable or unstable [3]. Using this ansatz in Eq. (2.65), we obtain

$$\gamma_\nu = \varepsilon \int_0^\infty G_{\tilde{\lambda},\tilde{n}}(t) \cos(\Omega t) \left(\nu \mathrm{e}^{-\gamma_\nu t} - 1\right) \mathrm{d}t \ . \tag{2.66}$$

In general, this equation can have many solutions in γ_ν as shown below. The synchronized state is linearly stable if and only if $\operatorname{Re}\gamma_\nu < 0$ holds for all solutions γ_ν to Eq. (2.66) and for both $\nu = +1$ and $\nu = -1$. Since the Gamma distribution $G_{\tilde{\lambda},\tilde{n}}$, given by Eq. (2.26), decays as $\mathrm{e}^{-\tilde{\lambda}t}$, the RHS of Eq. (2.66) only converges if $\operatorname{Re}\gamma_\nu > -\tilde{\lambda}$. This implies that the decay rate $\operatorname{Re}\gamma_\nu$ of small perturbations to the synchronized state cannot be faster than the jump rate $\tilde{\lambda}$. The integral in Eq. (2.66) can be solved analytically for the case that it converges, see Appendix B. The resulting characteristic equation is given by

$$\frac{\gamma_\nu}{\varepsilon} = \nu E(\gamma_\nu) - E_0 \ , \tag{2.67}$$

where

$$E(\gamma) = \frac{\tilde{\lambda}^{\tilde{n}}}{2} \left(\frac{1}{(\tilde{\lambda} + \gamma + \mathrm{i}\Omega)^{\tilde{n}}} + \frac{1}{(\tilde{\lambda} + \gamma - \mathrm{i}\Omega)^{\tilde{n}}} \right) \tag{2.68}$$

and $E_0 = E(0)$. Eq. (2.67) does not possess a closed analytical solution for arbitrary $\tilde{n}$. We thus seek an approximation of solutions to Eq. (2.67) near the stability boundary at $\gamma_\nu = 0$. We expand Eq. (2.67) to first order in γ_ν at $\gamma_\nu = 0$ to obtain a closed self-consistent expression,

$$\gamma_\nu \simeq \frac{(\nu - 1)E_0}{\varepsilon^{-1} - \nu E_1} \ , \tag{2.69}$$

where $E_1 = \mathrm{d}E/\mathrm{d}\gamma|_{\gamma=0}$. For the two modes, we thus obtain approximate solutions in the vicinity of $\gamma_\nu = 0$,

$$\gamma_+ \simeq 0 \ , \tag{2.70}$$

$$\gamma_- \simeq -\frac{2E_0}{\varepsilon^{-1} + E_1} \ . \tag{2.71}$$

In fact, $\gamma_+ = 0$ is a solution to the exact characteristic equation (2.67) and we expect that a global phase shift is neutrally stable, that is, neither grows nor decays. Such a behavior is known from phase models with discrete delays [38]. Eq. (2.71) provides

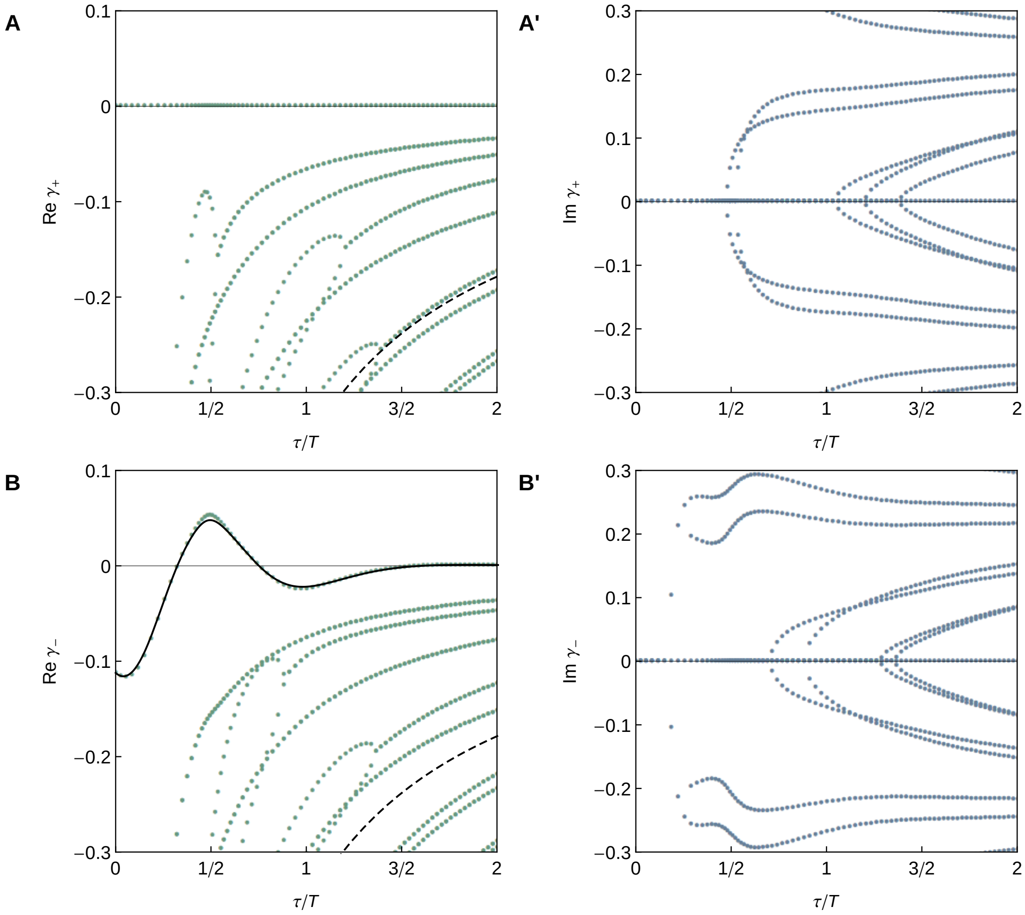

Figure 2.17 Real and imaginary parts of numerical solutions to Eq. (2.67) for the *in-phase* synchronized state (2.56) for γ_+ (A, A') and γ_- (B, B') as a function of the signaling delay τ, parameterized by Eq. (2.52). The solid black line in panel B shows the analytical approximation Eq. (2.69). The dashed black curve in panels A and B shows $\mathrm{Re}\,\gamma = -\tilde{\lambda}(\tau)$; points below this curve are solutions to Eq. (2.67), but not to Eq. (2.66). Other parameters are $\omega = 2\pi/28$ and $\varepsilon = \omega/4$.

a closed approximation for small $|\gamma_-|$ that depends on the coupling strength ε and furthermore on the collective frequency Ω, the jump rate $\tilde{\lambda}$, and the step number $\tilde{n}$ through E_0 and E_1.

It is straightforward to check that the corresponding results for the anti-phase synchronized state, Eq. (2.57), are obtained by replacing $\varepsilon \to -\varepsilon$ in Eqs. (2.67) and (2.69),

$$-\frac{\gamma_\nu}{\varepsilon} = \nu E(\gamma_\nu) - E_0 \ , \tag{2.72}$$

$$\gamma_\nu \simeq \frac{(\nu-1)E_0}{-\varepsilon^{-1} - \nu E_1} \ . \tag{2.73}$$

Numerical solutions to Eqs. (2.67) and (2.69) for the in-phase synchronized state are shown in Fig. 2.17, those to Eqs. (2.72) and (2.73) for the anti-phase synchronized state are shown in Fig. 2.18. For the collective mode $c = +1$, which corresponds to a global phase shift, we numerically find for given parameters that the largest real

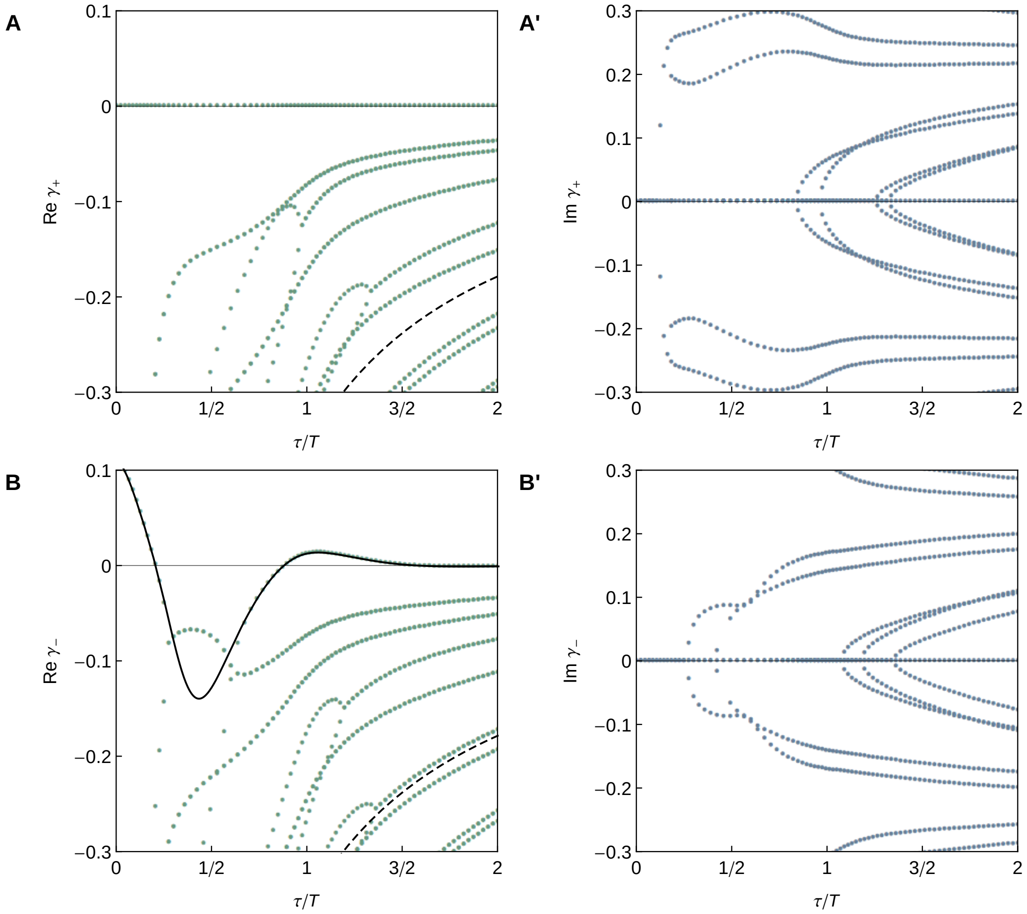

Figure 2.18 Real and imaginary parts of numerical solutions to Eq. (2.72) for the *anti-phase* synchronized state (2.57) for γ_+ (A, A') and γ_- (B, B') as a function of the signaling delay τ, parameterized by Eq. (2.52). Conventions and parameters as in Fig. 2.17.

part of all solutions is indeed $\mathrm{Re}\,\gamma_+ = 0$ for both the in-phase and the anti-phase synchronized state (Figs. 2.17A and 2.18A). The collective mode $c = -1$ exhibits stable regions ($\mathrm{Re}\,\gamma_- < 0$) as well as unstable regions ($\mathrm{Re}\,\gamma_+ > 0$) (Figs. 2.17B and 2.18B). Moreover, the synchronized states approach neutral stability for large delays as the magnitude of $\mathrm{Re}\,\gamma_+$ decays to zero for large τ. We used these results to indicate the stable and unstable solutions in Fig. 2.16. Depending on the chosen parameter set, the regions where in-phase and anti-phase synchronized states are stable can overlap, indicating multistability of both states for certain values of the signaling delay τ (Fig. 2.16A).

2.4.5— Comparison with the Markov chain model

We now assess whether the phase model Eq. (2.55) can capture the features of the Markov chain model described by Eqs. (2.5–2.7). To this end, we compare the collective frequency Ω obtained from the phase model (Sec. 2.4.3) to the frequency spectrum of oscillations from the Markov chain model. As before, we fix the number of steps $\tilde{n}$ of the signaling pathway in the Markov chain model and vary the mean signaling delay τ by changing the jump rate $\tilde{\lambda}$ according to Eq. (2.52). For the distribution $G_{\tilde{\lambda},\tilde{n}}$ of delay times in the phase model, we adopt the parameter values of $\tilde{\lambda}$ and $\tilde{n}$ used in the Markov chain model. For the intrinsic frequency ω in the phase

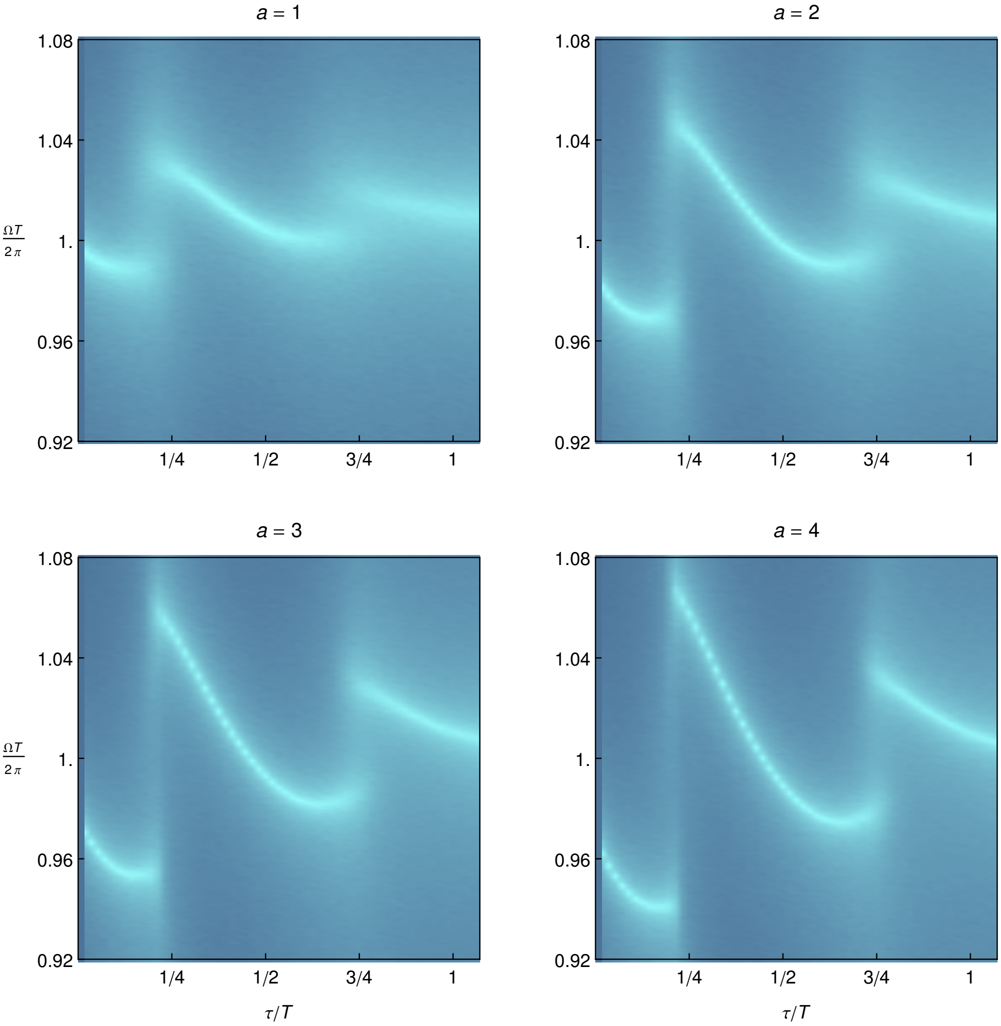

Figure 2.19 Density plots of logarithmic power spectra of oscillations in the Markov chain model. Bright regions correspond to strong frequency components. The collective frequency Ω is given in multiples of the uncoupled frequency $2\pi/T$. The different plots correspond to different activation strengths $\beta = a\beta_0$ with $\beta_0 = 30$ and $a = 1, \ldots, 4$. Other parameters are given in Table 2.1.

model, we use the estimate obtained from the characteristic equation Eq. (2.46). The coupling strength ε is the only parameter in the phase model that has to be determined phenomenologically. We here assume that ε scales linearly with the activation strength β in the Markov chain model, which determines how strong the signaling pathways influence the production rate in the receiving oscillator (Fig. 2.2). Once we fix the ratio $\mathcal{R} = \varepsilon/\beta$ by hand, there are no free parameters left for the phase model and we are able to compare its results to the Markov chain model.

Fig. 2.19 shows the frequency spectrum of the Markov chain system for different values of the activation strength β. The density plots display the logarithmic power spectral density of the oscillations of the final oscillator products[6]. These plots

---

[6] The power spectral density S of a signal $x(t)$ is defined by $S(\omega) = |\hat{x}(\omega)|^2$, where $\hat{x}(t) = \int x(t) \mathrm{e}^{-\mathrm{i}\omega t}\, \mathrm{d}t$ is the Fourier transform of $x(t)$. We obtain S using the Wiener–Khinchin theorem, which states that $S(\omega) = \hat{A}(\omega)$, where $\hat{A}$ is the Fourier transform of the autocorrelation A of the signal x, Eq. (2.9) [72]. The logarithmic power spectral density is given by $\mathcal{S}(\omega) = \log S(\omega)$.

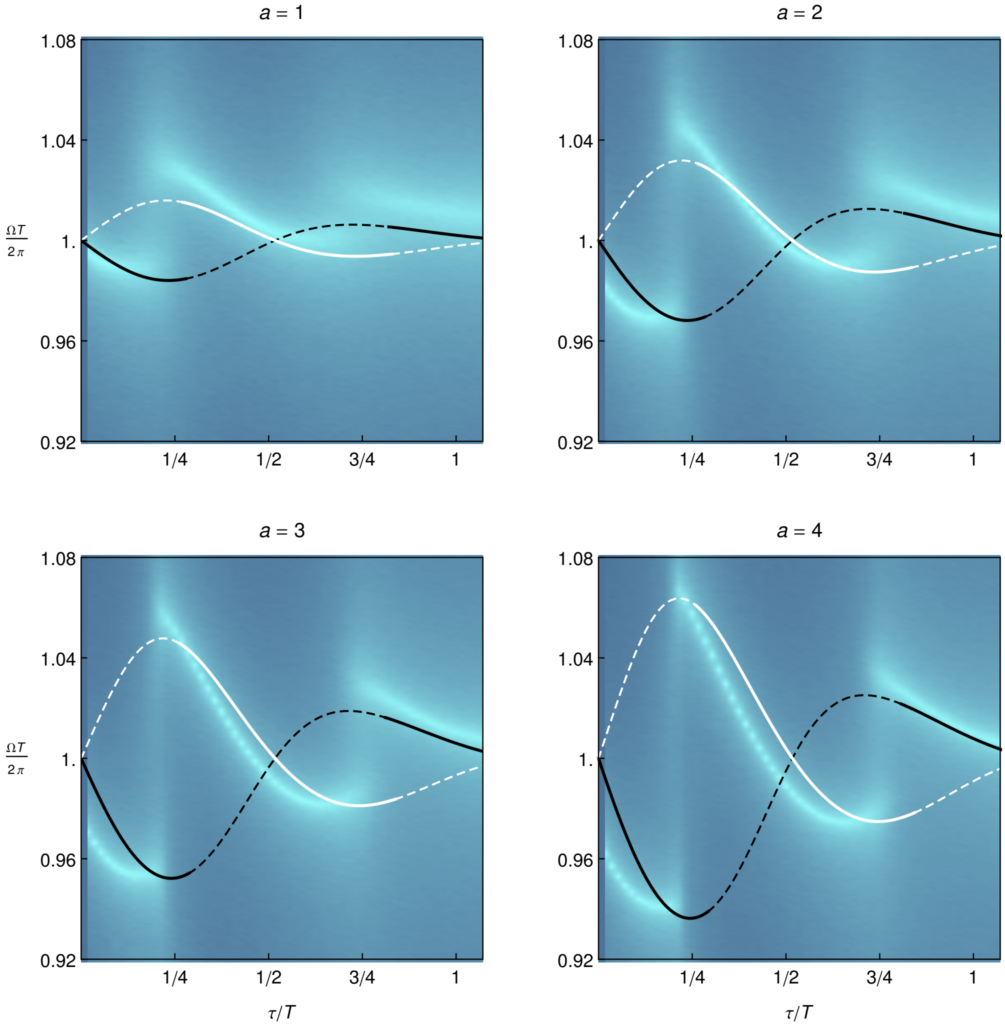

Figure 2.20 The same plots as in Fig. 2.19 with overlayed in-phase (black) and anti-phase (white) collective frequencies of the phase model, Eq. (2.58). Solid lines indicate stable solutions, dashed lines indicate unstable solutions. The parameters for the phase model are adopted from the Markov chain model except for the coupling strength, which is given by $\varepsilon = \mathcal{R}\beta$ with $\mathcal{R} = 1.33 \times 10^{-4}$.

show that the dominant frequency components change at odd multiples of $T/4$ as already observed in Sec. 2.3.6. In these transition regions, the power spectrum is bimodal as two distinct frequency components simultaneously display high spectral power. This is expected because of stochastic switching between in-phase and anti-phase synchrony with different frequencies found earlier (Sec. 2.3.5). Moreover, the dominant frequency components deviate less and less from the uncoupled frequency as the signaling delay τ increases, an observation that we already made in Sec. 2.3.6.

In Fig. 2.20, we display the same density plots as in Fig. 2.19 together with solutions for the collective frequency Ω, Eq. (2.58), obtained from the phase oscillator model. The comparison shows that both the collective frequency as well as the stability regions of in-phase and anti-phase solutions can be captured well by the phase model. In particular, the phase model describes the decaying dependence of the collective frequency on the signaling delay τ for large values of τ. Moreover, the phase model exhibits regions in which the in-phase and anti-phase solution are simultaneously stable. This implies that sufficiently strong fluctuations can drive the system out of one synchronized state into the basin of attraction of the other. This is consistent with the stochastic switching between in-phase and anti-phase synchrony found in the Markov chain model (Sec. 2.3.5), where fluctuations of molecule numbers are an intrinsic property of the system.

The quantitative deviations of the phase model from the Markov chain model can have various reasons. First, we have observed that the decay time of signaling molecules contributes to the total coupling delay in the Markov chain model (Sec. 2.3.4). For simplicity, we have omitted to describe this contribution in the phase model. Since the total coupling delay is one of the major factors determining the properties of the synchronized states, this omission might contribute to the quantitative deviations observed in Fig. 2.20. Second, for our phase model Eq. (2.55) we have chosen the coupling function to be sinusoidal, a generic choice for attractive oscillator coupling [38, 77]. In general, if a phase model is systematically derived from a limit cycle oscillator through a phase reduction, the detailed shape of the coupling function depends on the specific dynamics of the oscillators and may deviate from a sinusoidal behavior [41, 73]. Since both the collective frequency and the stability of synchronized states depend on the coupling function, this deviation might introduce quantitative differences in the phase model and the Markov chain model. Third, in our phase description, the autonomous oscillators are solely described by their intrinsic frequency ω, while the Markov chain model describes their full internal dynamics. This internal dynamics might lead to a more complex response to oscillator coupling than captured by our phase model and hence affect the collective frequency and the stability properties of synchronized states. However, representing the aforementioned features of the Markov chain model in a phase oscillator description leads to substantial complications of the latter, while the simple phase model presented here can already capture the key features to a very good degree.

2.5 Summary

In this chapter, we presented Markov chain models of coupled genetic oscillators, in which both the internal dynamics of the oscillators as well as the coupling processes are inherently stochastic. We have shown that our description of an uncoupled genetic oscillator is a stochastic generalization of established deterministic models of biochemical negative-feedback oscillators. We provided effective analytical estimates for the amplitude and the frequency of an uncoupled oscillator in terms of its biochemical parameters such as molecule production and decay rates and threshold levels. Comparison of these estimates to numerical simulations of our model showed very good agreement.

We then turned to the system of two coupled genetic oscillators and investigated how the properties of stochastic coupling affect their collective dynamics. In particular, coupling can lead to a considerable increase in precision of the oscillators at only slightly increased product turnover within the oscillators. Furthermore, coupling induces synchronization of the oscillators to in-phase or anti-phase correlated states. The effective coupling delay arising from the dynamics of the signaling pathway is a major factor governing precision, synchronization, and collective frequency of the coupled system. For certain values of the couping delay, we found stochastic switching between in-phase and anti-phase synchronized states, an effect induced by stochasticity. Moreover, we showed how the coupling mechanism presented here leads to attractive oscillator coupling, that is, tends to in-phase synchronize the oscillators for vanishing coupling delays.

We complemented our study of coupled genetic oscillators with a phase oscillator approximation with distributed signaling delays, which we compared with the Markov chain model. We found that such a phase model can describe the key features of the Markov chain model, such as the occurrence of in-phase and anti-phase synchronized states, their stability, and the dependence of the collective frequency on the model parameters. Furthermore, the phase model provided an approach to describe the stochastic switching between in-phase and anti-phase synchrony found in the Markov chain model: for specific values of the signaling delay both synchronized states are simultaneously stable, which allows noise-induced switching between both states.

Parameters and Symbols used in Chapter 2

PARAM.	**UNIT**	**VALUE**	
			OSCILLATORS
n	1	18	number of steps
α	NT^{-1}	60	production rate
β	NT^{-1}	20	activation strength due to signaling
λ	T^{-1}	1.5	transition rate between steps
κ	T^{-1}	0.5	decay rate for the final product
q_1	N	20	threshold level for auto-inhibition
q_2	N	100	threshold level for activation by signaling
p	1	2	Hill exponent
			SIGNALING PATHWAYS
$\tilde{n}$	1	10	number of steps
$\tilde{\alpha}$	NT^{-1}	60	production rate
$\tilde{\lambda}$	T^{-1}	0.5	transition rate between steps
$\tilde{\kappa}$	T^{-1}	0.5	decay rate for the final product
q_0	N	20	threshold level for repression
			REFERENCE VALUES (RESULTS)
Q_0	1	20.8	quality of an uncoupled oscillator
T	T	27	period of an uncoupled oscillator

Table 2.1 List of parameters and numerical values used in this chapter. Here, T is the unit of time and N is the unit 'one molecule'.

LIST OF SYMBOLS

P	probability density function
$\mu, \nu, \ldots$	indices of oscillators and signaling pathways
$i, j, \ldots$	indices of oscillator steps and pathway steps
$\mathbb{E}^{\pm}_{\mu i}$	creation ($+$) and annihilation ($-$) operators
Λ_μ	master equation operator for the oscillator μ
Σ_μ	master equation operator for the signaling pathway μ
$x_{\mu i}$	occupation number of step i in the coupled oscillator μ
$\tilde{x}_{\mu i}$	occupation number of step i in signaling pathway μ
x_i	occupation number of step i in the uncoupled oscillator
x	$x = x_n$, final product of an uncoupled oscillator
x_u	$x_u(t) = x(t-u)$, final product with delayed argument
$H_\pm$, h	Hill functions
$\Gamma_{\mu\nu}$	correlation function of oscillator products
$\tilde{\Gamma}_{\mu\nu}$	correlation function of pathway products
$\Delta_{\mu\nu}$	correlation function of oscillator and pathway products
Γ	autocorrelation function of the product of an uncoupled oscillator
A	normalized autocorrelation function of the product of a coupled oscillator
$\bar{x}$	$\bar{x} = \langle x_n \rangle$, expectation value of the final product number
z	complex exponent in the characteristic equation for Γ
ω	oscillation frequency
k	decorrelation rate
Q	quality factor
C	cross correlation of oscillator products
C_{out}	cross correlation of oscillator product and outgoing pathway product
C_{in}	cross correlation of oscillator product and incoming pathway product
$c_{\mu\nu}$	windowed cross correlation
c	normalized windowed cross correlation of oscillator products
I	mutual information
K	product turnover
$G_{\lambda,n}$	Gamma distribution
u	mean feedback delay (mean of $G_{\lambda,n}$)
v^2	variance of feedback delays (variance of $G_{\lambda,n}$)
τ	mean signaling delay (mean of $G_{\tilde{\lambda},\tilde{n}}$)
σ^2	variance of signaling delays (variance of $G_{\tilde{\lambda},\tilde{n}}$)
$\mathcal{L}$	concatenation of Hill functions
g_0, g_1	expressions occurring in solutions in Sec. 2.2.3
η	coefficient resulting from power series expansion of Hill functions
ϕ_μ	phase of oscillator μ
ξ_μ	perturbation of oscillator μ to the synchronized state
ψ_ν	collective mode ν for which the linearized dynamics decouple
γ_ν	exponent describing the relaxation of ψ_ν
ε	coupling strength
Ω	collective frequency
E	function that enters the characteristic equation for γ_ν
$\mathcal{S}$	logarithmic power spectral density
$\mathcal{R}$	ratio of ε and β

Chapter 3

Continuum Theory of Pattern Formation with Oscillators

In this chapter, we develop a continuum theory of coupled phase oscillators that describes the key features of vertebrate segmentation. We first introduce the basic principles of pattern formation with coupled oscillators using simplifying assumptions. We then sequentially extend our theory to take into account coupling delays, local growth, and a time-dependent tissue length and study the effects of these factors on pattern formation. We show that our theory describes a Doppler effect in pattern formation, which will be compared to experimental data in Chapter 4. We complement this study by proposing a model of interacting morphogens that can account for the dynamic decrease in tissue length in a self-organized way.

3.1 Pattern Formation with Oscillators

3.1.1— Coupled oscillators in a moving medium

In this section, we introduce the basic principles of pattern formation with oscillators as observed during vertebrate segmentation. Our theory combines three key ingredients relevant for pattern formation: (i) autonomous oscillators with a frequency profile, (ii) local oscillator coupling, and (iii) advective flow of the medium (see Chapter 1, Secs. 1.2.3–1.2.5). We describe the genetic oscillators in the segmenting tissue, the presomitic mesoderm, as a collection of coupled phase oscillators in a continuous medium. In this description, the state of a genetic oscillator is characterized solely by its phase in the cycle of oscillatory gene expression, disregarding the detailed biochemical mechanism giving rise to oscillations [93]. In Chapter 2, we have shown that such phase models can capture the key features of more detailed models of coupled genetic oscillators while considerably simplifying the theoretical description (Sec. 2.4).

To set up our theory, we define a one-dimensional embryonic coordinate system, in which the spatial coordinate x measures the distance from the posterior tip $x = 0$ along the body axis in a reference frame comoving with the presomitic mesoderm (Fig. 3.1A). The anterior end of the presomitic mesoderm is denoted by $x = a$. A phase field ϕ describes the state of the genetic oscillators in the presomitic mesoderm, that is, $\phi(x, t)$ represents the state of oscillation of a cell or a locally synchronous group of cells at position x and time t. The dynamic equation for the phase field ϕ

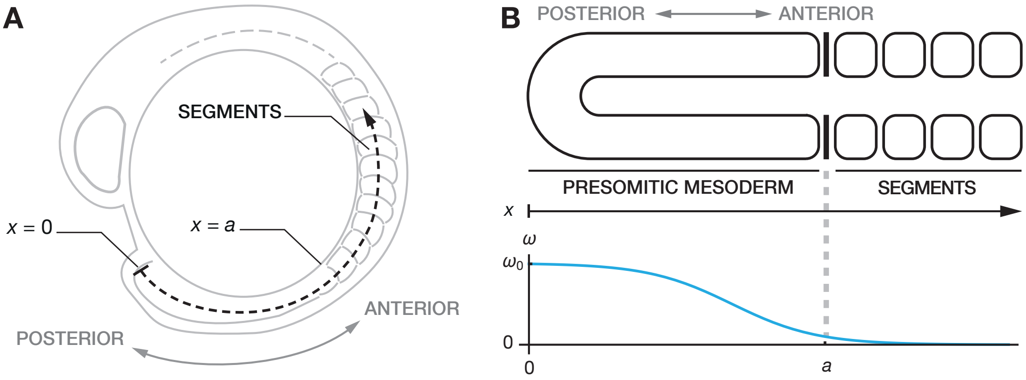

Figure 3.1 **A.** One-dimensional embryonic coordinate system in a reference frame comoving with the posterior tip of the presomitic mesoderm. The origin $x = 0$ is the posterior tip, the x-axis points in anterior direction along the body axis (black dashed line). The position $x = a$ marks the anterior end of the presomitic mesoderm. **B.** Sketch of a typical form of the frequency profile, Eq. (3.2), see also Table 3.1.

is given by

$$\frac{\partial \phi}{\partial t} + v_0 \frac{\partial \phi}{\partial x} = \omega(x) + \frac{\varepsilon(x)}{2} \frac{\partial^2 \phi}{\partial x^2} \ . \tag{3.1}$$

The intrinsic frequency of the oscillators is described by a frequency profile $\omega(x)$ that attains its maximum at the posterior tip and gradually decays towards the anterior (Fig. 3.1B). Motion of the oscillators with the cell flow is described by homogeneous advection with a velocity v_0 in anterior direction. This useful simplification corresponds to the assumption that cells enter the presomitic mesoderm at the posterior tip $x = 0$ with speed v_0. We will replace this assumption by a more physical velocity field in a later section. Local oscillator coupling with strength $\varepsilon(x)$ is described by a term that is formally equivalent to a diffusion term but has a different interpretation: it tends to even out local phase differences and thus describes the system's tendency to locally synchronize. Eq. (3.1) is the spatial continuum limit of a system of nearest-neighbor coupled phase oscillators in a moving medium (see Appendix C for a detailed derivation).

We consider frequency and coupling profiles of the form

$$\omega(x) = \omega_0 \Gamma(x/a) \ , \tag{3.2}$$

$$\varepsilon(x) = \varepsilon_0 \Gamma(x/a) \ , \tag{3.3}$$

where ω_0 is the maximum frequency and ε_0 the maximum coupling strength at the posterior tip $x = 0$, a is the length of the presomitic mesoderm, and $\Gamma(\xi)$ is a spatial profile that satisfies $\Gamma|_{\xi=0} = 1$ and smoothly decays to zero with a characteristic decay length of unity (Table 3.1). We consider a scenario in which oscillators enter the presomitic mesoderm at the posterior tip with speed v_0 and are in synchrony with the oscillators at $x = 0$. We therefore employ open boundary conditions,

$$\left.\frac{\partial \phi}{\partial x}\right|_{x=0} = 0 \ . \tag{3.4}$$

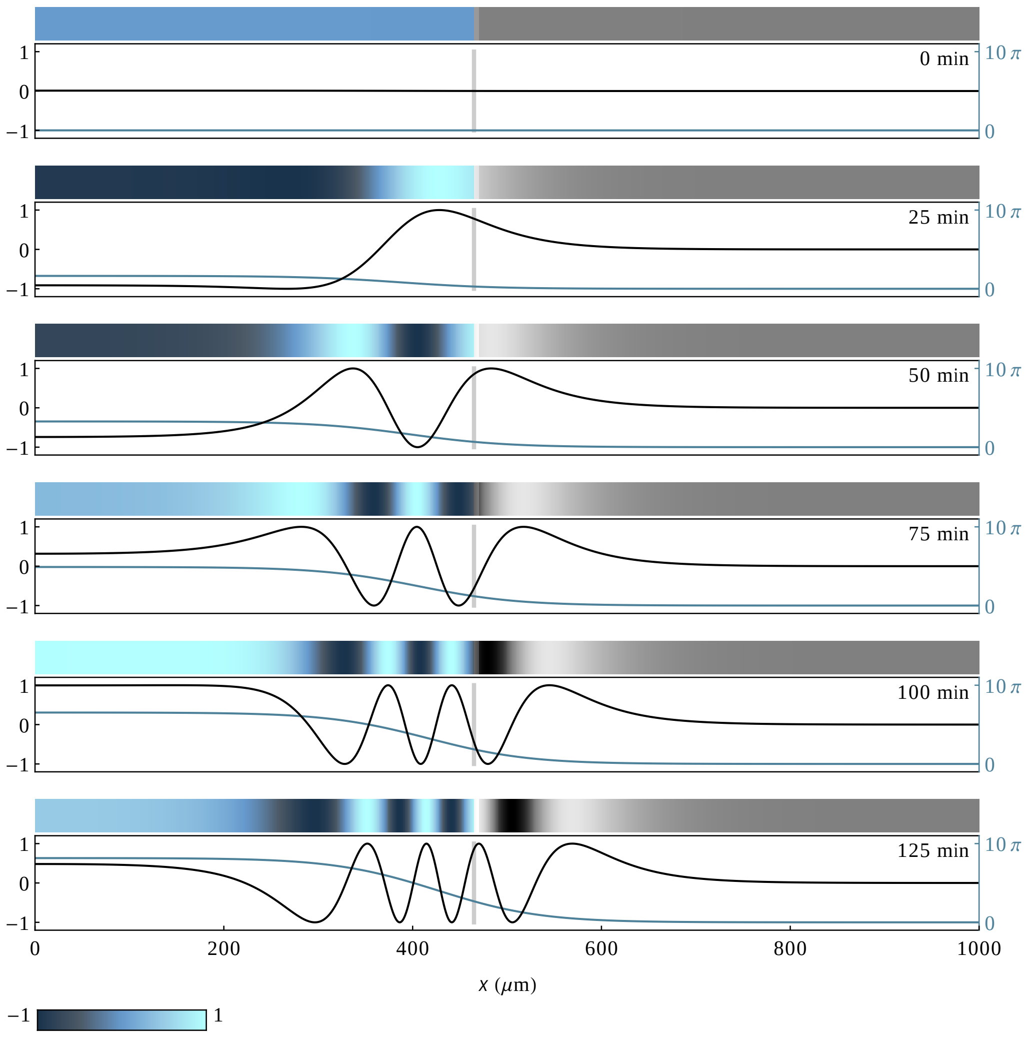

Figure 3.2 Snapshots of numerical solutions to Eq. (3.1) with parameters given in Table 3.2. For each point in time t, the lower plot shows the phase $\phi(x)$ (blue) and the corresponding oscillatory signal $\sin\phi(x)$ (black). The gray vertical line indicates the position of the arrest front, $x = a$. The density plots show the same snapshots in a representation where high values of $\sin\phi$ correspond to bright, low values to dark colors.

3.1.2— Formation of kinematic wave patterns

We now illustrate how the theory Eq. (3.1) describes the formation of kinematic waves that travel through the presomitic mesoderm. Fig. 3.2 shows snapshots of the system's time evolution for the parameters and profile functions specified in Tables 3.1 and 3.2. Fig. 3.3 shows the same system in a kymograph representation, that is, in a space-time density plot displaying the oscillatory signal $\sin\phi(x,t)$, where the abscissa indicates space and the ordinate indicates time.

Starting from zero initial conditions,

$$\phi\big|_{t=t_0} = 0 \ , \tag{3.5}$$

a phase gradient builds up along the presomitic mesoderm due to the frequency profile and advection in anterior direction. This phase gradient corresponds to a pattern of kinematic waves, as can be seen in the density plots of the oscillatory signal $\sin\phi$ in Fig. 3.2. The total number of kinematic waves simultaneously present

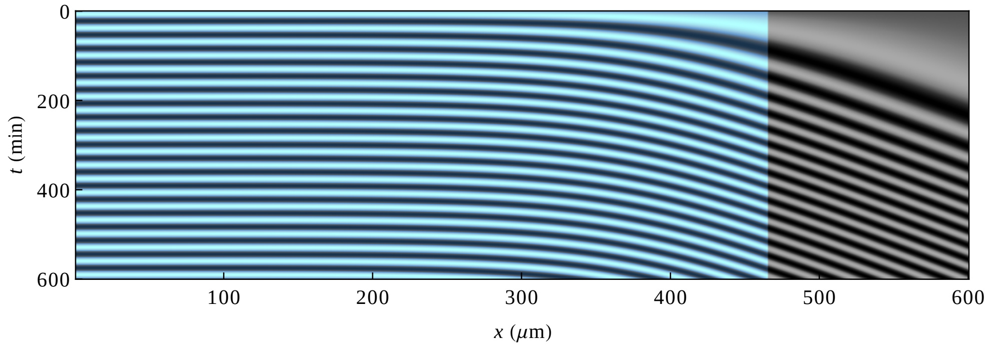

Figure 3.3 Kymograph of the oscillatory signal sin $\phi(x, t)$ for the same system as in Fig. 3.2. The color code is the same as in Fig. 3.2.

at one instant of time is given by the phase difference between posterior tip and anterior end,

$$K(t) = \frac{\phi(0,t) - \phi(a,t)}{2\pi} \ . \tag{3.6}$$

The number of kinematic waves is an important quantity: it relates the phase field ϕ to an observable that can be robustly measured in experiments [102]. Fig. 3.4A shows $K(t)$ for the system shown in Figs. 3.2 and 3.3.

The kinematic waves propagate in anterior direction at a speed much faster than the advective speed v_0. This can be seen by considering the motion of a point with a constant phase ϕ_*. The trajectory $x_*(t)$ of this point satisfies $\phi(x_*(t), t) = \phi_*$. Differentiating this equation with respect to time yields a differential equation for the local velocity of the kinematic waves,

$$\begin{aligned} \frac{\mathrm{d}x_*}{\mathrm{d}t} &= -\frac{(\partial\phi/\partial t)}{(\partial\phi/\partial x)}\bigg|_{x=x_*(t)} \\ &= v_0 + \frac{\omega\lambda}{2\pi} + \frac{\varepsilon}{2\lambda}\frac{\partial\lambda}{\partial x}\bigg|_{x=x_*(t)} \ , \end{aligned} \tag{3.7}$$

where in the second equality, we have used Eq. (3.1) to replace $\partial\phi/\partial t$ and introduced the local wavelength λ of the pattern[1],

$$\lambda(x,t) = -\frac{2\pi}{(\partial\phi/\partial x)} \ . \tag{3.8}$$

According to Eq. (3.7), the local velocity of kinematic waves is thus given by (i) the advection speed v_0, (ii) a contribution depending on the local frequency ω and the local wavelength λ, and (iii) a contribution depending on the local coupling strength ε and λ. Note that the wavelength λ itself depends on all model parameters.

3.1.3— Segment formation

We interpret the anterior end of the presomitic mesoderm, $x = a$, as the arrest front, that is, the point where the phase information is converted into morphological segments. Hence, we stipulate that whenever the anterior phase $\phi(a, t)$ exceeds a

---

[1] Since the phase $\phi(x, t)$ is monotonically decreasing in x due to the frequency gradient (see, e.g., Fig. 3.2), the minus sign in the definition of λ ensures that λ is positive.

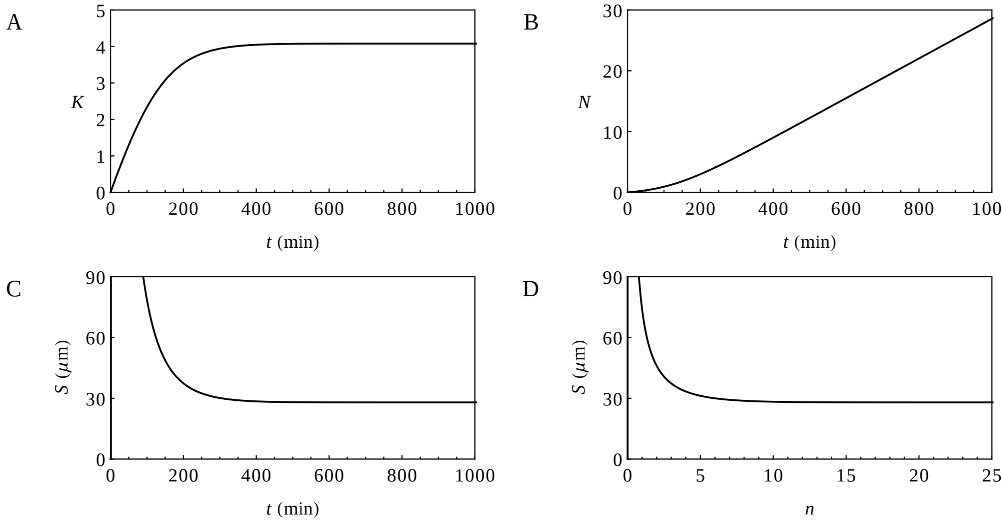

Figure 3.4 **A.** Number of kinematic waves K in the presomitic mesoderm, Eq. (3.6), as a function of time. **B.** Total number of formed segments N, Eq. (3.9), as a function of time. **C, D.** Segment length S at formation as a function of time (C), Eq. (3.10), and as a function of segment number (D), Eq. (3.11). All plots show the same system as in Figs. 3.2 and 3.3.

multiple of 2π, a new segment boundary is drawn at the anterior end $x = a$. Thus, the number of formed segments at time t is given by

$$N(t) = \frac{\phi(a,t) - \phi(a,0)}{2\pi} \ . \tag{3.9}$$

In our theory, the segment length S upon formation is given by the wavelength at the anterior end,

$$S(t) = \lambda(a,t) \ , \tag{3.10}$$

with λ defined in Eq. (3.8). While the formation of a segment takes a finite amount of time, for simplicity we here describe the segment length upon formation by the continuous function $S(t)$, assuming that the wavelength λ does not significantly vary during the formation of one segment. This assumption will be confirmed in numerical solutions for chosen parameters.

The time $t_{\mathrm{F}}(n)$ at which segment n forms is defined by $N(t_{\mathrm{F}}(n)) = n$. The length of formed segments, Eq. (3.10), and the number of kinematic waves in the presomitic mesoderm, Eq. (3.6), can thus be expressed as a function of the segment number[2]. Fig. 3.4B–D shows the time evolution of the number of formed segments N and the segment length S at formation for the same system as in Figs. 3.2 and 3.3.

3.1.4— Steady state

After an initial transient time, the system attains a steady state, in which the kinematic wave pattern repeats with a collective frequency, as shown by Figs. 3.3

---

[2] For the functions that depend on the segment number n, we use the same symbols as for those that depend on time t,

$$S(n) = S|_{t=t_{\mathrm{F}}(n)} \ , \tag{3.11}$$

$$K(n) = K|_{t=t_{\mathrm{F}}(n)} \ . \tag{3.12}$$

It will be clear from the context which one of them is referred to.

and 3.4. This implies that the dynamic frequency is constant along the entire presomitic mesoderm, $\partial\phi/\partial t = \Omega$. This may seem counterintuitive since the presence of a frequency profile implies that oscillations proceed with different frequencies in different parts of the presomitic mesoderm. Indeed, the autonomous frequency ω in the anterior is smaller than in the posterior. However, the dynamic frequency $\partial\phi/\partial t$ at a specific position x also receives contributions from the advection of the wave pattern through this point in space and from coupling. Since at steady state, the wavelength of the pattern is shorter in the anterior, the frequency $v_0/\lambda(x)$ that locally emerges from the advection of a wave pattern with wavelength $\lambda(x)$ at a speed v_0 through a constant point in space is larger in the anterior. We find that at steady state, this contribution to the dynamic frequency exactly balances the mismatch of autonomous frequencies due to the frequency profile. To see this formally, we make the steady state ansatz

$$\phi(x,t) = \Omega t + \psi(x) \ , \tag{3.13}$$

where Ω is the collective frequency, and $\psi(x)$ is a time-independent phase profile along the presomitic mesoderm. This ansatz implies that the oscillatory signal associated to the phase $\phi(x,t)$, e.g., $\sin\phi(x,t)$, is periodic with period $T = 2\pi/\Omega$. Using this ansatz in Eq. (3.1), we find that the collective frequency and the phase profile obey

$$\Omega + v_0 \frac{\mathrm{d}\psi}{\mathrm{d}x} = \omega(x) + \frac{\varepsilon(x)}{2} \frac{\mathrm{d}^2\psi}{\mathrm{d}x^2} \ . \tag{3.14}$$

The boundary condition (3.4) implies a boundary condition for the phase profile,

$$\left.\frac{\mathrm{d}\psi}{\mathrm{d}x}\right|_{x=0} = 0 \ . \tag{3.15}$$

Eq. (3.14) can be solved for arbitrary frequency profiles ω using variation of constants. However, it is more instructive to assume that coupling is weak and that the coupling term only provides a minor correction to the collective frequency and the phase profile. For values of the coupling strength inferred from experimental data [93, 117] (Table 3.2), we find numerically that this assumption is warranted. Evaluating Eq. (3.14) at $x = 0$ with the boundary condition (3.15) for the case $\varepsilon_0 = 0$, we find that the collective frequency is given by

$$\Omega = \omega_0 \ , \tag{3.16}$$

the maximum of the frequency profile at the posterior tip. For the phase profile ψ, we obtain the solution

$$\psi(x) = \int_0^x \frac{\omega(x') - \omega_0}{v_0} \, \mathrm{d}x' \ . \tag{3.17}$$

The local wavelength, Eq. (3.8), is consequently given by

$$\lambda(x) = \frac{2\pi v_0}{\omega_0 - \omega(x)} \ . \tag{3.18}$$

Hence, the wavelength is large in the vicinity of the posterior tip $x = 0$, where $\omega(x) \simeq \omega_0$ and decreases towards the anterior. At the arrest front, where $\omega|_{x=a} \simeq 0$, we obtain $\lambda \simeq 2\pi v_0/\omega_0$. Therefore, the frequency that emerges from transporting the wave pattern through the arrest front with advection speed v_0 coincides with the frequency of oscillations in the posterior, $2\pi v_0/\lambda|_{x=a} \simeq \omega_0$, as outlined in the beginning of this section.

The velocity with which the kinematic waves travel through the tissue can be obtained according to Eq. (3.7). At steady state, we can define a time-independent velocity field $u(x)$ for the speed of kinematic waves by requiring $u(x_*(t)) = \mathrm{d}x_*/\mathrm{d}t$, where $x_*(t)$ is the trajectory of a point with constant phase, see Eq. (3.7). Using Eqs. (3.7) and (3.18), we find

$$u(x) = \frac{v_0}{1 - \omega(x)/\omega_0} \ . \tag{3.19}$$

Since $0 \leq \omega(x) \leq \omega_0$, $u(x)$ is always positive and larger than v_0, indicating that the kinematic waves move in anterior direction and faster than the underlying medium. Kinematic waves are fastest in the vicinity of the posterior tip, where $\omega(x)/\omega_0$ is close to 1 and slow down towards the anterior. This slowdown is indicated by the downward tilt of ridges with constant phase in the kymograph Fig. 3.3.

The length of the segments upon formation is given by Eqs. (3.10) and (3.18), which yield

$$S = v_0 T \ , \tag{3.20}$$

where we have used $\omega|_{x=a} \simeq 0$ and introduced the collective period $T = 2\pi/\Omega = 2\pi/\omega_0$. We thus recover the clock-and-wavefront relation (1.1) between segment length, advection speed and collective period. Therefore, at steady state, the system acts as a clock with a well-defined period T despite the presence of a frequency gradient and the appearance of kinematic wave patterns.

3.2 Oscillators with Delayed Coupling

3.2.1— Dynamic equation

In Chapter 2, we have shown that coupling delays, which arise in complex signaling processes between oscillators, can have profound effects on their precision and synchronization. Moreover, coupling delays affect the timing of segment formation as shown earlier [56, 93]. We now study the effects of coupling delays on the kinematic wave patterns. To this end, we extend the theory from Sec. 3.1 to take into account time delays in the coupling of oscillators. Note that Eq. (3.1) has been derived as the spatial continuum limit of a discrete system of nearest-neighbor coupled oscillators (Sec. 3.1.1 and Appendix C). To systematically obtain the corresponding theory with delayed coupling, we repeat the derivation of such a continuum limit for a discrete oscillator system with coupling delays. We have presented this derivation for a discrete coupling delay τ in Ref. [5]; for self-containedness, we provide the derivation in Appendix C. The resulting continuum theory is given by

$$\begin{aligned} \frac{\partial \phi}{\partial t} + v_0 \frac{\partial \phi}{\partial x} = \omega(x) &+ Z\varepsilon(x)\sin(\bar{\phi}_\tau - \phi) - \frac{\varepsilon(x)}{2}\sin(\bar{\phi}_\tau - \phi)\left(\frac{\partial \bar{\phi}_\tau}{\partial x}\right)^2 \\ &+ \frac{\varepsilon(x)}{2}\cos(\bar{\phi}_\tau - \phi)\frac{\partial^2 \bar{\phi}_\tau}{\partial x^2} \ , \end{aligned} \tag{3.21}$$

where τ is the coupling delay and $\bar{\phi}_\tau(x,t) = \phi(x - v_0\tau, t - \tau)$. Here, Z is a renormalization constant that arises during the derivation of the spatial continuum limit[3].

---

[3] The constant Z stems from the expansion in the lattice spacing of the discrete oscillator system and is given by $Z = 1/s^2$, where s is the lattice spacing (see Appendix C for a details). We here use $s = 10\mu\mathrm{m}$, corresponding to the length scale of a cell.

Note that Eq. (3.21) is non-local in time and space. For the case without delays, $\tau = 0$, in which $\bar{\phi}_\tau - \phi = 0$, Eq. (3.21) reduces to Eq. (3.1).

3.2.2— Steady state

Like the theory without coupling delays, Eq. (3.1), the theory with delays can exhibit a steady state of the type $\phi(x, t) = \Omega t + \psi(x)$, Eq. (3.13), for time-independent parameters. This steady state solution satisfies

$$\begin{aligned}\Omega + v_0 \frac{\mathrm{d}\psi}{\mathrm{d}x} &= \omega(x) + Z\varepsilon(x)\sin(\bar{\psi}_\tau - \psi - \Omega\tau) - \frac{\varepsilon(x)}{2}\sin(\bar{\psi}_\tau - \psi - \Omega\tau)\left(\frac{\mathrm{d}\bar{\psi}_\tau}{\mathrm{d}x}\right)^2 \\ &\quad + \frac{\varepsilon(x)}{2}\cos(\bar{\psi}_\tau - \psi - \Omega\tau)\frac{\mathrm{d}^2\bar{\psi}_\tau}{\mathrm{d}x^2} \ ,\end{aligned} \tag{3.22}$$

where $\bar{\psi}_\tau(x) = \psi(x - v_0\tau)$ (see also Appendix C). Since Eq. (3.22) is non-local in space, it is not sufficient to provide a boundary condition at a singular point. Rather, an initial history for the region $-v_0\tau < x < 0$ has to be specified [17],

$$\psi\big|_{x<0} = 0 \ . \tag{3.23}$$

Evaluating Eq. (3.22) at $x = 0$ using these boundary conditions, we find an implicit equation for the collective frequency,

$$\Omega = \omega_0 - Z\varepsilon_0 \sin(\Omega\tau) \ . \tag{3.24}$$

The collective frequency Ω is thus governed by the posterior frequency ω_0, the coupling strength $Z\varepsilon_0$, and the coupling delay τ. In Chapter 2, we have already encountered the transcendental equation (3.24) and analyzed its properties (Sec. 2.4.3): for a chosen value of τ, Eq. (3.24) can exhibit multiple solutions (Fig. 2.16B). Moreover, Eq. (3.24) is well-known to determine the synchronized state of systems of identical oscillators with delayed coupling [5, 38, 129, 163]. For the case of no delay, $\tau = 0$, we recover Eq. (3.16).

To obtain the length S of segments at formation, Eq. (3.10), we evaluate Eq. (3.22) at $x = a$. Using $\omega|_{x=a} \simeq 0$ and $\varepsilon|_{x=a} \simeq 0$, we find $\mathrm{d}\psi/\mathrm{d}x = -\Omega/v_0 = -2\pi/v_0T$ and thus $S = v_0T$, the clock-and-wavefront relation (1.1) that has already been discovered for the case of no delays, Eq. (3.20). Note that in the case with delays, the collective period T is however determined by Eq. (3.24).

3.2.3— Effects of coupling delays on pattern formation

As can be seen from Eq. (3.22), the steady state phase profile ψ depends on the coupling delay τ both directly and indirectly through its dependence on $\Omega = \Omega(\tau)$. Fig. 3.5 shows examples of steady state phase profiles for different values of the coupling delay τ. Important observables such as the number of kinematic waves and the segment length depend non-monotonically on the coupling delay. Remarkably, systems that exhibit the same collective frequency Ω can exhibit quite different phase profiles (gray and yellow profiles in Fig. 3.5): Eq. (3.24) is invariant under a change of the coupling delay τ by a full collective period, $\tau \to \tau + 2\pi/\Omega$. However, Eq. (3.22) for the spatial phase profile is not invariant under this change as τ also enters in the argument of the delayed phase profile $\bar{\psi}_\tau$.

3.2.4— When do coupling delays have to be considered?

We conclude that together with the frequency profile ω, coupling delays affect pattern formation and the timing of segment formation. Experiments, in which these coupling delays were manipulated in zebrafish wildtype and mutant embryos, indicate that they play a role in regulating the timing of segmentation and the robustness of kinematic wave patterns against noise [56]. Furthermore, it has been shown that

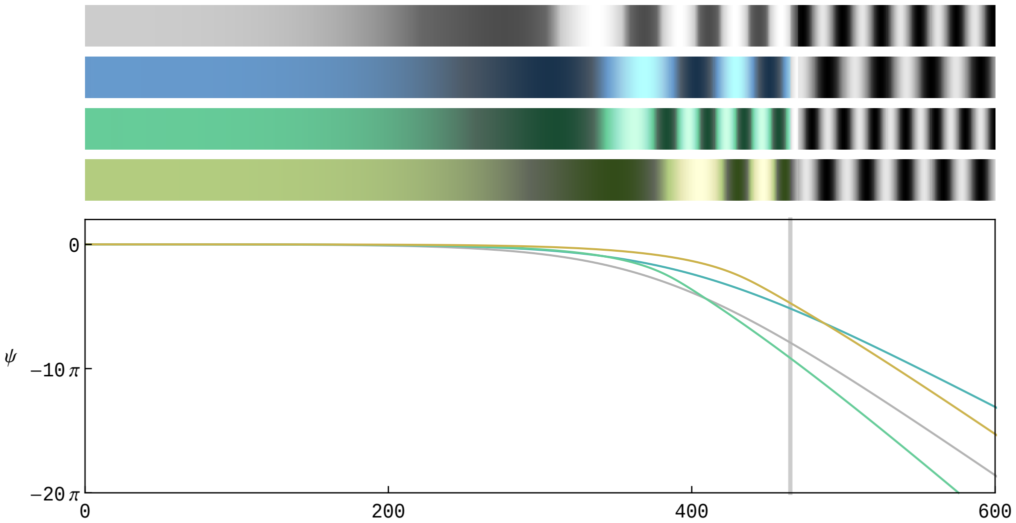

Figure 3.5 Steady state phase profiles ψ in the presence of coupling delays: $\Omega\tau = 0$ (gray), $\Omega\tau = \pi/4$ (blue), $\Omega\tau = 7\pi/4$ (green), and $\Omega\tau = 2\pi$ (yellow). The other parameters are given in Table 3.2. The collective frequencies corresponding to these phase profiles are $\Omega = \omega$ (gray, yellow), $\Omega = \omega + \varepsilon/\sqrt{2}$ (blue), and $\Omega = \omega - \varepsilon/\sqrt{2}$ (green). Color code analogous to Fig. 3.2.

theories similar to Eq. (3.21) can account for experimentally observable changes in timing and noisiness of wave patterns upon alteration of coupling delays [56].

In the remainder of this chapter, we investigate pattern formation and segmentation dynamics in the deforming presomitic mesoderm of wildtype zebrafish. Hence, we do not compare scenarios with different coupling delays. In such a case, a description without coupling delays leads to a considerable simplification. In Ref. [45], Geisler determined the parameter regions of Eq. (3.22) that yield theoretical results compatible with the key features of wildtype zebrafish segmentation. These key observables include the segment length, the period of segment formation and the number of kinematic waves in the presomitic mesoderm. Importantly, it has been shown for large regions in parameter space that a change of the coupling delay can be compensated by an appropriate change of the shape of the frequency profile to obtain the same key observables. For simplicity, we therefore resort to a description without delays in the following.

3.3 Coupled Oscillators in a Growing Medium

3.3.1—Dynamic equation

The theory introduced in Sec. 3.1 describes the extending tissue in a simplified way: cells enter the presomitic mesoderm at the posterior tip with the same speed v_0 with which they leave at the anterior end. To account for tissue growth in a more systematic way, we now introduce a position-dependent velocity profile $v(x)$. The dynamic equation for the phase field ϕ is now given by

$$\frac{\partial \phi}{\partial t} + v(x)\frac{\partial \phi}{\partial x} = \omega(x) + \frac{\varepsilon(x)}{2}\frac{\partial^2 \phi}{\partial x^2} \; . \tag{3.25}$$

The velocity profile v is the integral of a growth profile k,

$$k(x) = \frac{\mathrm{d}v}{\mathrm{d}x} \; . \tag{3.26}$$

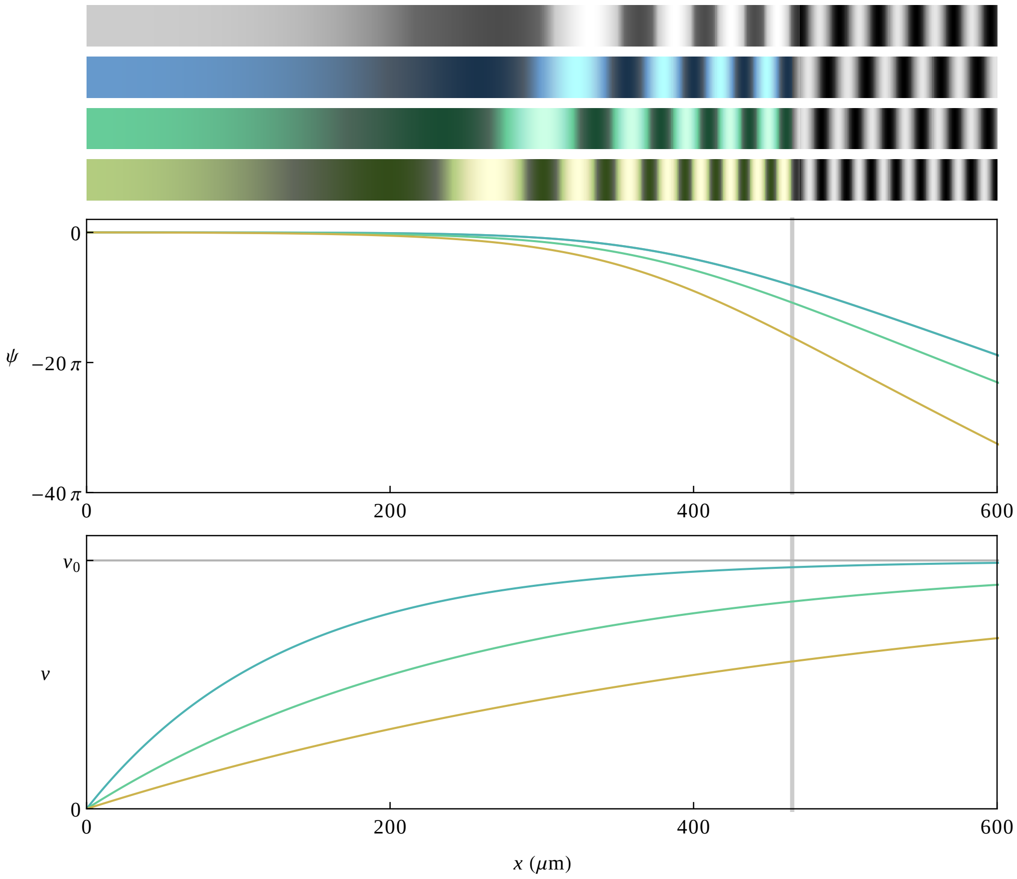

Figure 3.6 Steady state phase profiles ψ and velocity fields v for $\mu = 0.9$ (yellow), $\mu = 1.8$ (green), $\mu = 3.6$ (blue), and $\mu = \infty$ corresponding to no growth (gray). The curves of the blue and gray phase profiles lie on top of each other. The other parameters are given in Table 3.2. Color code analogous to Fig. 3.2.

We here assume that growth is mainly taking place in the posterior region of the presomitic mesoderm and becomes weaker towards the anterior. In Chapter 4, we quantify the velocity field in the segmented region of zebrafish embryos and motivate this assumption (Sec. 4.1.3). We consider a growth field of the form

$$k(x) = k_0 \mathrm{e}^{-\mu x/a} \ , \tag{3.27}$$

where k_0 is the maximum growth rate at $x = 0$, a is the length of the presomitic mesoderm, and μ is a scaling factor that regulates the decay length of the growth field. Assuming that the velocity in the direction of the body axis vanishes at the posterior tip, $v|_{x=0} = 0$, the corresponding velocity profile can be written as

$$v(x) = \int_0^x k(x')\,\mathrm{d}x' = v_0 \Delta(x/a) \ , \tag{3.28}$$

where $v_0 = ak_0/\mu$ and $\Delta(\xi)$ is a spatial profile function specified in Table 3.1. In Chapter 4, we show that a velocity profile of the form Eq. (3.28) is compatible with the experimentally obtained velocity profile in the segmented region (Sec. 4.1.3).

3.3.2— Steady state

Like the theory with a spatially constant velocity in Sec. 3.1, the system with a velocity profile can exhibit a steady state of the type $\phi(x,t) = \Omega t + \psi(x)$, Eq. (3.13), for time-independent parameters. An approximate solution for the case of weak coupling can be obtained analogously to Eqs. (3.16) and (3.17) as

$$\Omega = \omega_0 \ , \tag{3.29}$$

$$\psi(x) = \int_0^x \frac{\omega(x') - \omega_0}{v(x')} \, \mathrm{d}x' \ . \tag{3.30}$$

3.3.3— Effects of local growth on pattern formation

Whether a position-dependent velocity profile of the type Eq. (3.28) substantially affects pattern formation depends both on the shape of the velocity profile v and the shape of the frequency profile ω. If the frequency profile does not significantly deviate from its posterior value ω_0 over the characteristic length over which the velocity profile varies, it suppresses the effects of posterior growth on pattern formation. This behavior is illustrated in Fig. 3.6, where steady state solutions of the phase profile ψ for velocity fields with different μ are compared. For large μ (blue profile), the phase profile only slightly deviates from that with a constant velocity (corresponding to $\mu = \infty$, gray profile) described by Eq. (3.1). For smaller values of μ (green and yellow profiles), that is, for a longer range over which the velocity profile reaches its plateau value v_0, the number of kinematic waves in the presomitic mesoderm increases. Formally, this can be seen by computing the number of kinematic waves K, Eq. (3.6), from the steady state result Eq. (3.30),

$$K = \frac{1}{2\pi} \int_0^a \frac{\omega_0 - \omega(x')}{v(x')} \, \mathrm{d}x' \ . \tag{3.31}$$

Since the velocity field v appears in the denominator of the integrand, smaller velocities tend to increase the number of kinematic waves.

3.4 Coupled Oscillators in a Medium of Changing Length

3.4.1— Dynamic equation

In the previous sections, we have considered the length a of the presomitic mesoderm to be constant during segmentation like many previous theories [5, 49, 93, 96], with notable exceptions [23]. This simplification was useful to demonstrate the basic mechanism of pattern formation and the effects of coupling delays and local growth on pattern formation. However, experimental data show that the length of the presomitic mesoderm substantially decreases during segmentation (see, e.g., Chapter 4, Sec. 4.1.2). If our theory is to describe the dynamics of vertebrate segmentation as observed in experiments, we have to go beyond the steady state scenarios investigated in the previous sections. Hence, we further extend the theory presented in Sec. 3.3 by taking into account the decreasing length of presomitic mesoderm. We will apply the resulting theory specifically to segmentation in developing wildtype zebrafish embryos.

We here consider a scenario in which the frequency, coupling, and velocity profiles scale with the decreasing length of the presomitic mesoderm; this simple prescription regulates the length of the oscillating region in our theory. Hence, we replace the constant length a of the presomitic mesoderm by a time-dependent length $a(t)$ and let the frequency, coupling, and velocity profiles inherit this time dependence through their dependence on the relative position $x/a(t)$, see Eqs. (3.2), (3.3), and

(3.28). The dynamic equation for the phase is thus given by

$$\frac{\partial \phi}{\partial t} + v(x/a(t))\frac{\partial \phi}{\partial x} = \omega(x/a(t)) + \frac{\varepsilon(x/a(t))}{2}\frac{\partial^2 \phi}{\partial x^2} \ , \tag{3.32}$$

where

$$\begin{aligned} \omega(x/a(t)) &= \omega_0 \Gamma(x/a(t)) \ , \\ \varepsilon(x/a(t)) &= \varepsilon_0 \Gamma(x/a(t)) \ , \\ v(x/a(t)) &= v_0 \Delta(x/a(t)) \ , \end{aligned} \tag{3.33}$$

with the profile functions Γ and Δ given in Table 3.1. We quantify the time-dependent length $a(t)$ of the presomitic mesoderm from experimental data on wild-type zebrafish development in Chapter 4. We find that the presomitic mesoderm shortens linearly, but with with two different speeds v_1 and v_2 in two different time intervals, $t < t^*$ and $t > t^*$, where t^* marks the time point of transition. To capture this behavior, we introduce a function that smoothly interpolates between these two shortening speeds (Sec. 4.1.2),

$$a(t) = a_0 + \frac{v_1 + v_2}{2}t - \frac{v_1 - v_2}{2}T^* \log\cosh\frac{t - t^*}{T^*} \ , \tag{3.34}$$

see Eq. (4.2) and Fig. 4.3A. Here, a_0 is a constant length offset and T^* is time interval over which the shortening speed changes from v_1 to v_2.

Fig. 3.7A shows a kymograph of a numerical solution to Eq. (3.32) with parameters given in Table 3.2. The decreasing length of the presomitic mesoderm is apparent as is the change of the phase pattern over time. Hence, unlike the theories considered in the previous sections, the theory Eq. (3.32) does not attain a steady state of the type $\phi(x,t) = \Omega t + \psi(x)$, Eq. (3.13), in which a kinematic wave pattern repeats with a collective frequency Ω. Rather, the kinematic wave pattern continuously changes during the evolution of the system.

This also implies that the system with decreasing tissue length is sensitive to the choice of initial conditions as opposed to a system operating at a steady state. Starting from zero initial conditions at time $t = t_0$, Eq. (3.5), it takes a finite time until a kinematic wave pattern builds up (see also Sec. 3.1.2). So far, experimental data on the wave pattern and the presomitic mesoderm length in this initial transient period are not available and it is outside the scope of the present theory to describe the initiation of pattern formation *in vivo*. Instead, we here stipulate that the time $t = 0$ corresponds to the formation of the 6th segment. To obtain an initial phase pattern at $t = 0$, we use the following procedure: we start the system at time $t_0 < 0$ with zero initial conditions, where the initial time t_0 is a parameter. Furthermore, we introduce a time t_1 with $t_0 < t_1 < 0$ at which the length of the presomitic mesoderm starts to evolve according to Eq. (3.34). For times $t < t_1$, the presomitic mesoderm remains at the constant size $a(t_1)$.

3.4.2— Decreasing tissue length induces a Doppler effect

The absence of a steady state solution implies that the rate of segment formation cannot simply be identified with a collective frequency Ω. Rather, we have to determine the local dynamic frequency Ω_{A} at the moving arrest front, the anterior end of the presomitic mesoderm. In Sec. 3.1.3, we have stipulated that this frequency is identified with the rate of segment formation as the arrest front converts the phase information into segment boundaries. A first hint of how these changed conditions affect the frequency at the arrest front is given by Fig. 3.7. It shows that the arrest front (transition point between blue and gray region) moves towards the posterior

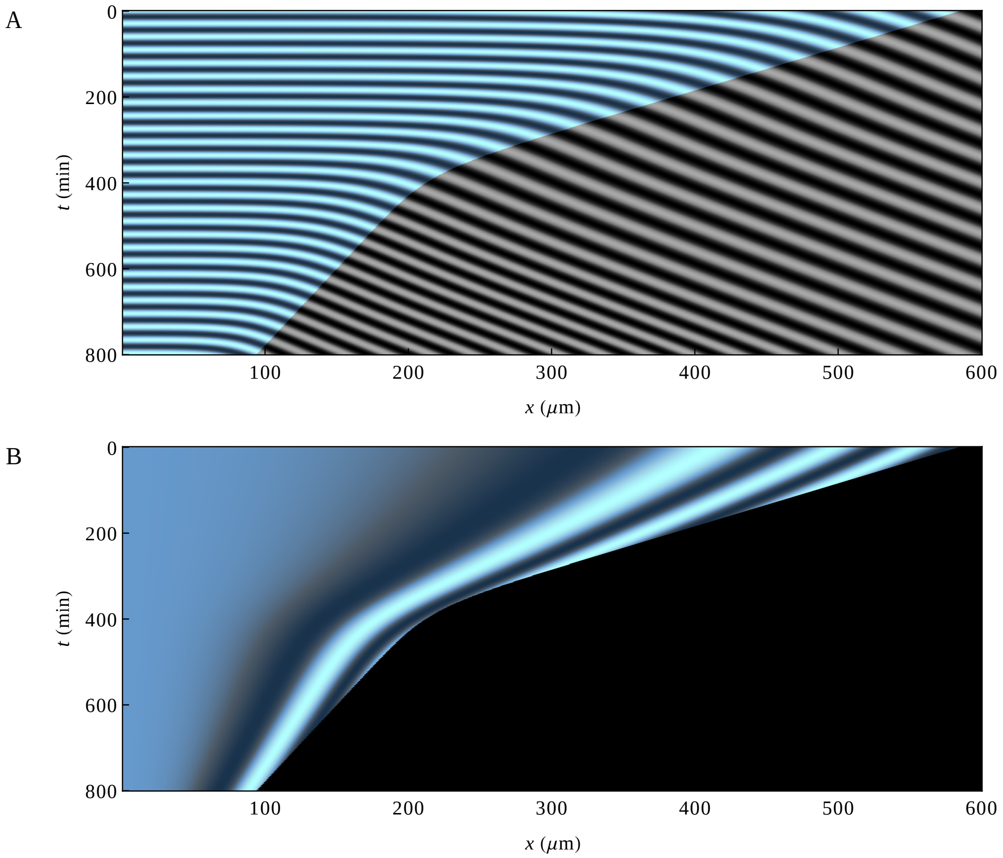

Figure 3.7 A. Kymograph of the oscillatory signal $\sin \phi(x,t)$ for a numerical solution to Eq. (3.32). **B.** Kymograph of the oscillatory signal $\sin \psi(x,t)$ of the phase profile, Eq. (3.38), for the same system as in A. Only the presomitic mesoderm region, $x < a(t)$, is shown. The parameters are provided in Table 3.2. The color code is the same as in Fig. 3.3.

and hence travels into the kinematic waves as the length of the tissue decreases. This behavior is reminiscent of a Doppler effect, in which the arrest front plays the role of a moving observer traveling towards a wave-emitting source (Fig. 3.8). As in a classical Doppler effect, we thus expect that the frequency experienced by the moving arrest front is larger than in the steady state scenarios considered before, where the arrest front was not moving. To investigate whether this is the case, we study the behavior of the phase ϕ_{A} at the arrest front and the phase ϕ_{P} at the posterior tip, given by

$$\phi_{\mathrm{A}}(t) = \phi(a(t),t) \ , \tag{3.35}$$

$$\phi_{\mathrm{P}}(t) = \phi(0,t) \ . \tag{3.36}$$

Fig. 3.9A shows the time evolution of ϕ_{A} and ϕ_{P}. After the initial transient marked by the shaded area, the steeper slope of the anterior phase ϕ_{A} indicates that the frequency experienced by the moving anterior end is indeed faster than the posterior dynamic frequency. This implies that the rate of segment formation, which we assume to be equal to the anterior frequency, does not anymore solely depend on the time scale of genetic oscillations, represented by the frequency profile ω. Rather, it now depends on a second time scale, which is set by both the speed with which the tissue

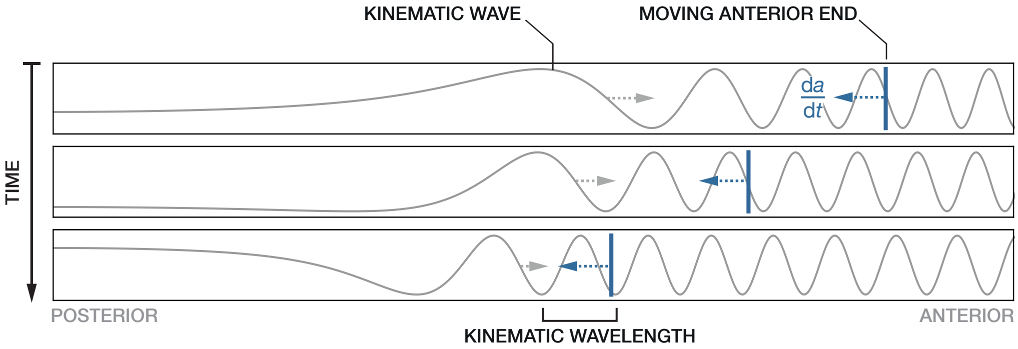

Figure 3.8 Schematic depiction of the Doppler effect induced by the decreasing tissue length. The arrest front at the anterior end of the presomitic mesoderm (blue vertical line) moves into the kinematic waves (gray curves) with speed $\mathrm{d}a/\mathrm{d}t$. In addition, the wavelength of the kinematic waves locally changes over time.

length decreases and the wavelength of the kinematic waves. To illustrate this, we rewrite the anterior phase as

$$\phi_{\mathrm{A}}(t) = \phi_{\mathrm{P}}(t) + \psi(a(t), t) \ , \tag{3.37}$$

where we have defined the time-dependent phase profile[4]

$$\psi(x,t) = \phi(x,t) - \phi_{\mathrm{P}}(t) \ . \tag{3.38}$$

The time evolution of the phase profile corresponding to the phase field ϕ in Fig. 3.7A is shown in Fig. 3.7B. The anterior and posterior dynamic frequencies Ω_{A} and Ω_{P} are given by

$$\Omega_{\mathrm{A}} = \frac{\mathrm{d}\phi_{\mathrm{A}}}{\mathrm{d}t} \ , \tag{3.39}$$

$$\Omega_{\mathrm{P}} = \frac{\mathrm{d}\phi_{\mathrm{P}}}{\mathrm{d}t} \ , \tag{3.40}$$

We obtain a relation between these frequencies by using Eq. (3.37) in Eq. (3.39),

$$\Omega_{\mathrm{A}} = \Omega_{\mathrm{P}} + \Omega_{\mathrm{D}} + \Omega_{\mathrm{W}} \ , \tag{3.41}$$

where

$$\Omega_{\mathrm{D}} = \frac{\mathrm{d}a}{\mathrm{d}t} \frac{\partial \psi}{\partial x}\bigg|_{x=a(t)} \ , \tag{3.42}$$

$$\Omega_{\mathrm{W}} = \frac{\partial \psi}{\partial t}\bigg|_{x=a(t)} \ . \tag{3.43}$$

Eq. (3.41) reveals that the frequency Ω_{A} at the arrest front is given by the posterior frequency Ω_{P} and two contributions that depend on the phase profile ψ. The contribution Ω_{D} is caused by the change of tissue length and accounts for the effects of the arrest front moving towards the kinematic waves. It describes a Doppler effect

---

[4] Under steady state conditions considered in the previous sections, this definition of the phase profile coincides with the one given by Eq. (3.13).

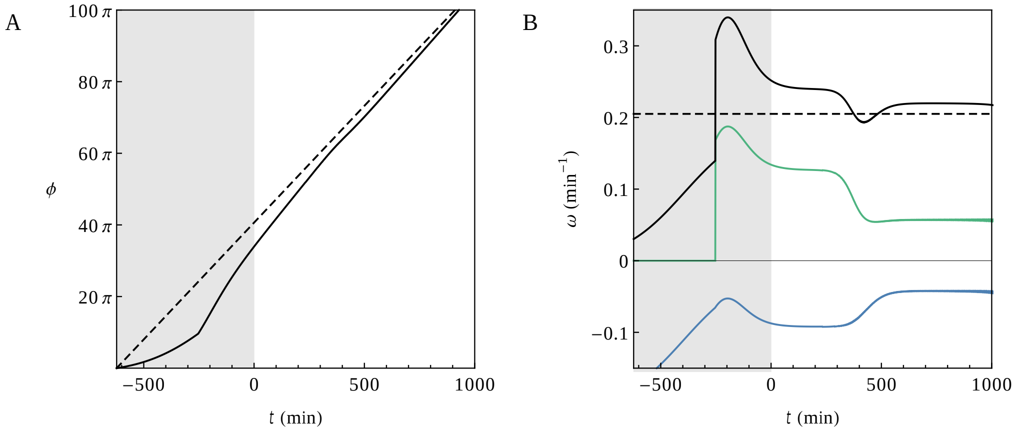

Figure 3.9 **A.** Anterior phase ϕ_{A} (solid), Eq. (3.35) and posterior phase ϕ_{P} (dashed), Eq. (3.36), as a function of time. **B.** The anterior frequency Ω_{A} (solid black), Eq. (3.39), and its three contributions as given by Eq. (3.41): the posterior frequency Ω_{P} (dashed black), Eq. (3.40), the Doppler contribution Ω_{D} (green), Eq. (3.42), and the dynamic wavelength contribution Ω_{W} (blue), Eq. (3.43). The dotted gray lines show the analytical approximation Eq. (3.45) of the anterior frequency Ω_{A} in the respective time ranges. The parameters are provided in Table 3.2. In both plots, the shaded areas mark the initial transient time to build up a kinematic wave pattern (see main text).

in which $\mathrm{d}a/\mathrm{d}t$ is the speed of the moving observer (the arrest front) travelling into a wave with wavelength $2\pi/(\partial\psi/\partial x)$. The contribution Ω_{W} is caused by the change of the phase profile ψ over time, which corresponds to a dynamic change of the kinematic wavelength. We therefore term this phenomenon ‘dynamic wavelength effect’. In contrast to the theories considered before, the rate of segment formation now depends on the spatial features of the kinematic wave pattern. Fig. 3.9B displays these two contributions to the frequency Ω_{A} at the arrest front. In Chapter 4, we will show by comparison to experiments that these effects, a Doppler and a dynamic wavelength effect, indeed occur during the segmentation of zebrafish embryos.

Eq. (3.41) is a kinematic relation that holds independent of any dynamic theory. We now use the dynamic equation (3.32) to derive an explicit relation between anterior and posterior frequency. For this purpose, it is instructive to further exploit the analogy to the Doppler effect. In a classical simple Doppler effect, a source emits dynamic waves with a constant frequency Ω_{source} and wavelength $\lambda = c \cdot \Omega_{\text{source}}$, where c is the speed of wave propagation in the medium. The frequency Ω_{obs} perceived by an observer moving towards the source with constant speed v_{obs} is given by

$$\Omega_{\text{obs}} = (1+\gamma)\Omega_{\text{source}} \ , \tag{3.44}$$

where $\gamma = v_{\text{obs}}/c$. A similar relation between the anterior and posterior frequencies Ω_{A} and Ω_{P} can be derived for a linearly decreasing tissue length, $a(t) = a_0 - v_* t$, where v_* is the speed with which the tissue shortens. The derivation of this relation is provided in Appendix D. The result is given by

$$\Omega_{\mathrm{A}} \simeq (1+\gamma)(1-\eta)\Omega_{\mathrm{P}} \ , \tag{3.45}$$

where

$$\gamma = \frac{v_*}{v_0} \ , \tag{3.46}$$

$$\eta = \int_0^1 \frac{\gamma}{(1+\gamma\xi)^2} \frac{\omega(\xi)}{\omega_0} \, \mathrm{d}\xi \ . \tag{3.47}$$

Eq. (3.45) is independent of time even though $a(t)$ is not and thus neither the frequency, coupling, and velocity profiles. The term $1 + \gamma$ describes a Doppler effect analogous to Eq. (3.44), where v_* corresponds to the speed of the moving observer (the arrest front) and v_0 corresponds to the speed of wave propagation in the medium (the advective speed due to cell flow). The term $1 - \eta$ appears in addition to the Doppler effect and describes the effects caused by the change of the phase profile, which itself depends on the relative shortening rate γ and the frequency profile ω. Since $\eta > 0$, this term presents a contribution that opposes the Doppler effect.

Since Eq. (3.34) for the length $a(t)$ of the presomitic mesoderm describes two temporal regions $t < t^*$ and $t > t^*$, in which $a(t)$ decreases linearly with rates $v_* = v_1$ and $v_* = v_2$, respectively, Eq. (3.45) can be used for each of these regions to approximate the anterior frequency Ω_A. The result is displayed in Fig. 3.9B as dotted gray lines in the respective temporal regions and demonstrates the validity of Eq. (3.45).

3.5 Coupled Oscillators Interacting with Morphogens

The theories introduced in the previous sections account for the decreasing tissue length through the explicit time dependence of the length $a(t)$ of the presomitic mesoderm and the dependence of frequency, coupling, and velocity profiles on $a(t)$. However, how the length of the presomitic mesoderm is controlled in the embryo is not understood. We expect that a combination of biochemical and mechanical mechanisms leads to a self-organized shortening of the tissue during segmentation. To complement this study, we here propose a hypothetic mechanism that is able to dynamically generate this length decrease in a self-organized way. In Chapter 1, we introduced several morphogen gradients, which distribute spatial information throughout the presomitic mesoderm (Sec. 1.2.3): The morphogens Wnt and FGF (fibroblast growth factor) are expressed in the posterior and form a gradient towards the anterior, while RA (Retinoic Acid) forms an opposing gradient with highest levels in the formed segments (Fig. 3.10A). Our theory will thus be based on posteriorly and anteriorly located morphogen gradients that interact with each other and the oscillators to dynamically generate a time-dependent frequency gradient and shortening of the tissue.

3.5.1— Dynamic equations

In our theory, a morphogen Q is produced in an extended domain in the posterior region of the presomitic mesoderm. A morphogen R is produced in the entire segmented region with enhanced production in the formed segments. Both morphogens are subject to advection, diffusion, and decay. Moreover, they degrade each other. The presomitic mesoderm is defined as the region in which the level of Q is above a defined threshold value Q^*, the segmented region is located where Q is below this value. The morphogens interact with the oscillator dynamics through the frequency profile ω and the coupling profile ε, which are directly proportional to the level of Q. Furthermore, the level of Q sets the local growth rate $\partial v/\partial x$ in the system. Hence,

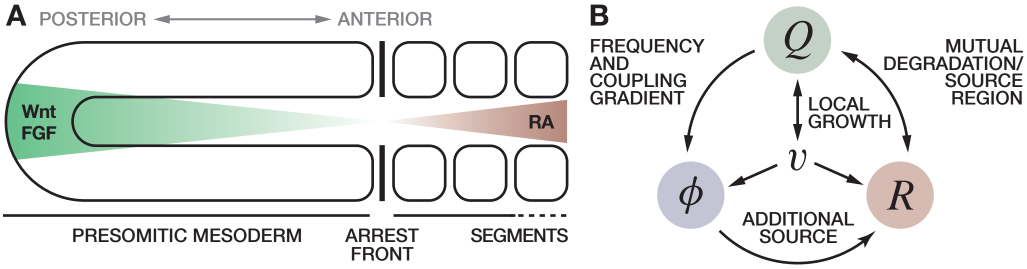

Figure 3.10 **A.** Location of morphogen gradients in the presomitic mesoderm and the formed segments. The morphogens Wnt and FGF (fibroblast growth factor) are expressed in the posterior and form a gradient towards the anterior, while RA (Retinoic Acid) forms an opposing gradient with highest levels in the formed segments. Figure adapted from Ref. [102]. **B.** Interaction scheme of the components of the theory Eqs. (3.48–3.50).

in contrast to the theories considered before, no functional forms for frequency and velocity fields need to be prescribed. The interaction scheme of the theory is summarized in Fig. 3.10B. The dynamic equations for the morphogen levels $Q(x,t)$ and $R(x,t)$ and the phase field $\phi(x,t)$ are given by[5]

$$\frac{\partial Q}{\partial t}+\frac{\partial}{\partial x}(vQ)=\alpha J(x) \qquad\qquad\qquad\qquad + E\frac{\partial^2}{\partial x^2}Q-(h_0+h_1R)Q\;, \tag{3.48}$$

$$\frac{\partial R}{\partial t}+\frac{\partial}{\partial x}(vR)=(\beta_1X(\phi)+\beta_0)\mathbb{1}_{Q<Q^*}+D\frac{\partial^2}{\partial x^2}R-(k_0+k_1Q)R\;, \tag{3.49}$$

$$\frac{\partial \phi}{\partial t}+v\frac{\partial}{\partial x}\phi \quad =\omega \qquad\qquad\qquad\qquad\quad + \varepsilon\frac{\partial^2}{\partial x^2}\phi\;. \tag{3.50}$$

Here, α and β_0 are basal production rates for Q and R, respectively, β_1 is the production rate of R in the formed segments, $J(x)=\mathbb{1}_{0<x<x_0}$ is a source function of Q with x_0 being the spatial extension of the source and $\mathbb{1}$ an indicator function being 1 where the condition in the subscript is fulfilled and 0 elsewhere. Furthermore, D and E are diffusion constants, h_0 and k_0 are decay rates, h_1 and k_1 indicate the degree of mutual degradation of the two morphogens, and

$$X(\phi)=\frac{1+\cos\phi}{2} \tag{3.51}$$

is the oscillatory signal associated to the phase ϕ, which satisfies $0<X(\phi)<1$. The dependence of the production rate of R on $X(\phi)$ in the region where $Q<Q^*$ mimicks production in the center of the formed segments.

At each point in time, the local growth rate is given by

$$\frac{\partial v}{\partial x}=\kappa Q \tag{3.52}$$

with boundary condition $v|_{x=0}=0$, where κ is a proportionality constant. The morphogen Q also controls the frequency gradient ω and the coupling gradient ε according to

$$\omega=\omega_0Q/Q_0\;, \tag{3.53}$$

$$\varepsilon=\varepsilon_0Q/Q_0\;, \tag{3.54}$$

---

[5] Note that, while the phase equation (3.50) is formally similar to the reaction–diffusion equations (3.48) and (3.49), the interpretation of the dynamics in terms of a coarse-grained oscillator system with coupling is crucially different. See Sec. 3.1.1 for details.

where Q_0 is a reference level for Q. For the morphogens, we consider no-flux boundary conditions at the posterior tip $x = 0$,

$$\left.\frac{\partial Q}{\partial x}\right|_{x=0} = \left.\frac{\partial R}{\partial x}\right|_{x=0} = 0 \ , \tag{3.55}$$

and open boundary conditions for the phase field,

$$\left.\frac{\partial \phi}{\partial x}\right|_{x=0} = 0 \ . \tag{3.56}$$

The position $a(t)$ of the anterior end of the presomitic mesoderm is defined as the point where the level of Q reaches the threshold level Q^*,

$$Q(a(t), t) = Q^* \ . \tag{3.57}$$

To simplify the model, we nondimensionalize all quantities such that $\alpha = E = h_0 = 1$[6]. As initial condition, we consider a steady state of both morphogens in the absence of phase dynamics ($\beta_1 = 0$), in which there is a posteriorly located profile of Q that decays in anterior direction and an anteriorly located profile of R that decays in posterior direction (example shown in Fig. 3.11, $t = 0$). We then let the system evolve with the initial condition $\phi|_{t=0} = 0$ for the phase field.

The effects of a single morphogen gradient controlling the frequency and length of the presomitic mesoderm have been studied earlier, however with an explicit time dependence of the morphogen production rate [23], which we avoid here. Reaction-diffusion models of interacting morphogens coupled to a clock with static period have attempted to describe somitogenesis without explicitly accounting for the dynamics of oscillators [14, 15]. Furthermore, reaction-diffusion models similar to Eqs. (3.48) and (3.49) without coupling to an oscillator field have been used to study the interaction of Fgf and Retinoic Acid (RA) gradients [13].

3.5.2— Steady states of morphogen gradients

The full model, Eqs. (3.48–3.54), in which the three components Q, R, and ϕ are coupled, is nonlinear and difficult to treat analytically. The nonlinearities arise from the mutual degradation of the morphogens and the dependence of the velocity field on the level of Q. However, it is possible to decouple the dynamics the morphogens using simplifying assumptions and obtain analytical approximations of their steady state distributions, characterized by $\partial Q/\partial t = 0$ and $\partial R/\partial t = 0$. Even though the full model never exhibits such decoupled steady state distributions, these approximations provide useful insights on how parameters affect the overall shape of the gradients and facilitate the choice of parameters. We present these approximations together with detailed derivations in Appendix E.

3.5.3— Self-organized segmentation

We now illustrate that the system proposed here is capable of describing segmentation and length decrease of the presomitic mesoderm in a self-organized way. To this end, we numerically solve Eqs. (3.48–3.54) with the initial and boundary conditions specified in Sec. 3.5.1 and the parameters specified in Table 3.3. Fig. 3.11 shows snapshots of the system for different time points. Fig. 3.12 shows the system's time evolution in a kymograph representation as used earlier. Since the initial posterior profile of the morphogen Q corresponds to a frequency profile through Eq. (3.53), a kinematic wave pattern builds up (Fig. 3.11, $t = 0.5$) by the basic mechanism described in Sec. 3.1. As soon as these waves leave the presomitic mesoderm, that

---

[6] This is accomplished by rescaling time, space, and morphogen levels according to $t \to t/\bar{T}$, $x \to x/\bar{L}$, $Q \to Q/\bar{C}$, and $R \to R/\bar{C}$ with $\bar{T} = 1/h_0$, $\bar{L} = (E/h_0)^{1/2}$, and $\bar{C} = \alpha/h_0$.

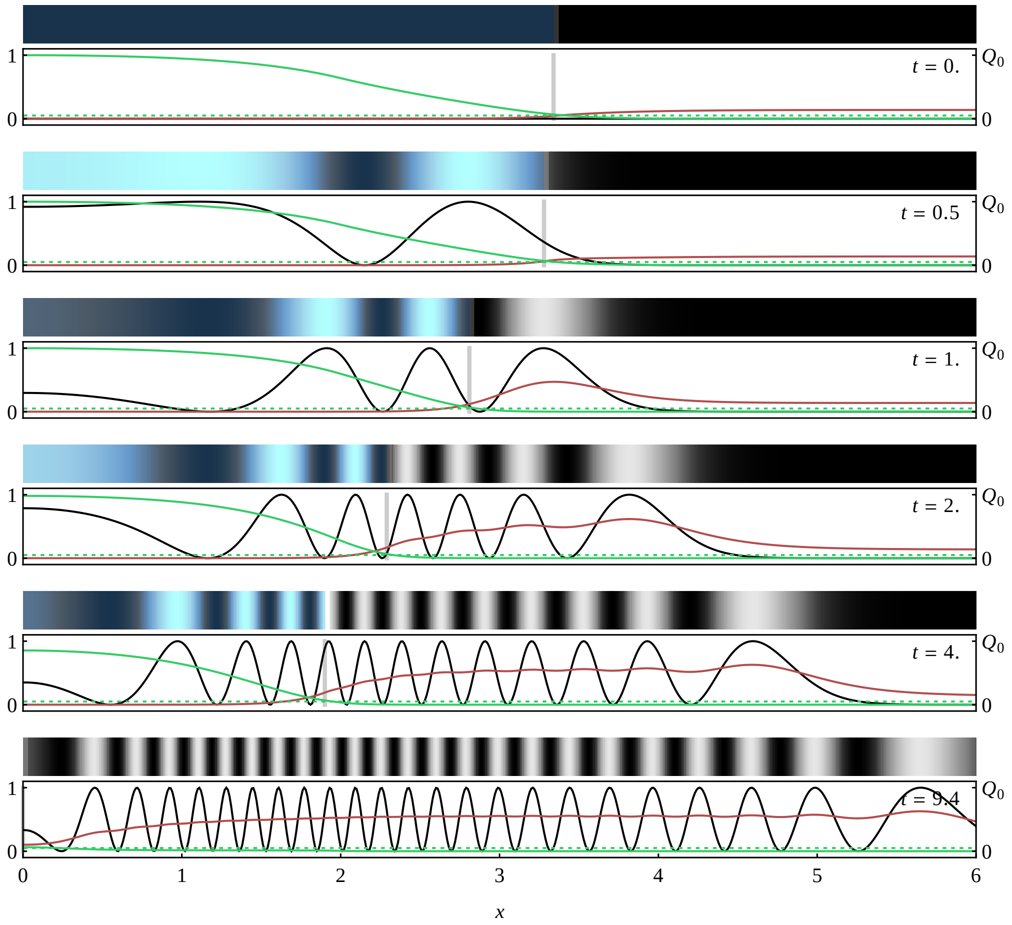

Figure 3.11 Snapshots of numerical solutions to Eqs. (3.48–3.54). For each point in time, the lower panel shows the oscillatory signal $X(\phi)$ (black, values indicated by left axis), and the morphogen levels of Q (green) and R (red) (values indicated by right axis). The vertical gray line marks the anterior end of the presomitic mesoderm, $x = a(t)$, with $a(t)$ determined by Eq. (3.57). The upper panels show density plots of the phase field in the same representation as in Fig. 3.2. Space and time are specified in dimensionless units (see main text).

is, as they enter the region where $Q < Q^*$, they locally enhance the production of the morphogen R according to Eq. (3.49) (Fig. 3.11, $t = 1$). Since R degrades Q, the thus increasing levels of R lead to an enhanced decay of Q in the vicinity of the arrest front (at $Q = Q^*$) and the profile of Q retreats towards the posterior (Fig. 3.11, $t = 2$). Consequently, the presomitic mesoderm shortens as the region where $Q > Q^*$ becomes smaller. Eventually, the region vanishes after the system has produced a finite number of segments (Fig. 3.11, $t = 8$).

Therefore, the theory introduced here can account for the length decrease of the presomitic mesoderm through its internal dynamics. Moreover, it presents a hypothetic mechanism that dynamically terminates the segmentation process after a finite number of segments.

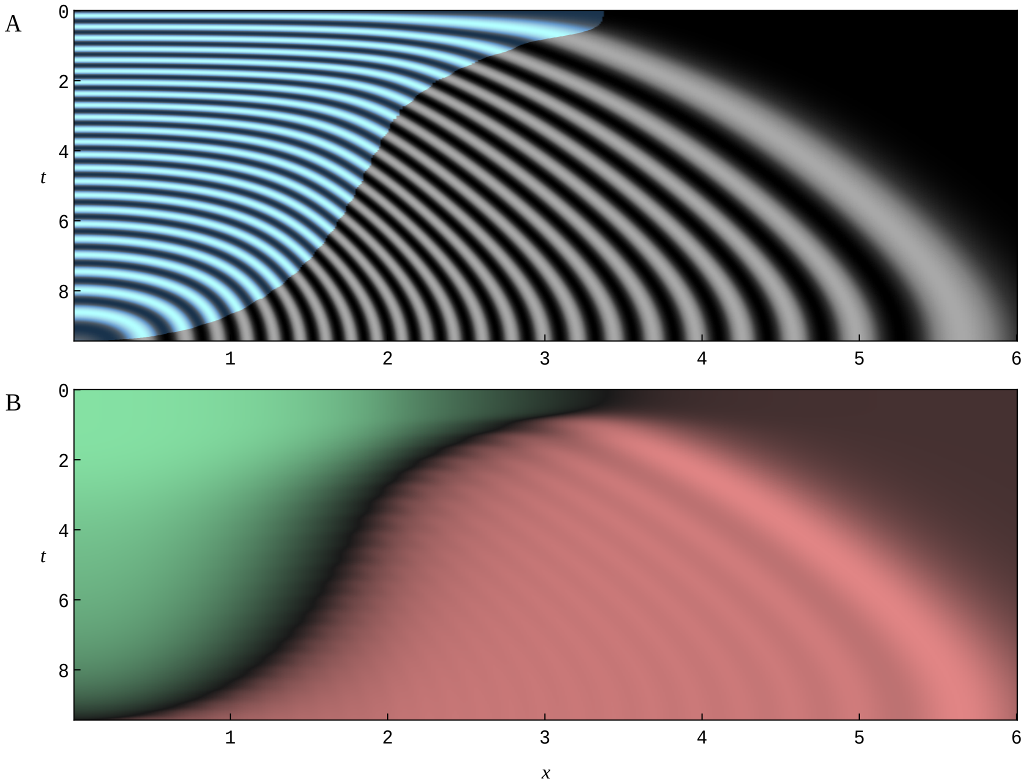

Figure 3.12 **A.** Kymograph of the oscillatory signal $X(\phi)$. The color code is the same as in Fig. 3.11. **B.** Kymograph of the relative morphogen levels Q (green) and R (red) for the same system as in Fig. 3.11. Bright colors correspond to high morphogen levels, dark colors correspond to low morphogen levels. Space and time are specified in dimensionless units (see main text).

3.6 Summary

In this chapter, we have introduced a continuum theory of coupled phase oscillators in a dynamic medium and applied it to describe the dynamics of vertebrate segmentation. We first described the basic mechanism of pattern formation using a simplified steady state description of the presomitic mesoderm. We then successively included the effects of biologically relevant factors such as coupling delays due to complex signaling, local growth, and decreasing tissue length and studied their effects on the spatio-temporal kinematic wave patterns and segment formation. We found that coupling delays can have a profound impact on pattern formation and yield different wave patterns for the same collective frequency. Concerning local growth, we found that it only has a minor impact on pattern formation if growth is restricted to the posterior region, where the frequency profile is almost flat. The most profound effects on pattern formation and the timing of segmentation were found when introducing a decreasing tissue length to our theory. The decreasing tissue length causes a Doppler effect as the anterior end of the tissue moves into the kinematic waves of gene expression. This effect introduces a new time scale, which contributes to the rate of segment formation. The Doppler effect is accompanied by a second effect, the dynamic change of the pattern wavelength, which contributes to the rate of segment formation on equal footing. This prediction will be compared with experiments in Chapter 4.

To complement this study, we proposed a hypothetic mechanism of interacting morphogens and phase oscillators that describes segmentation and the decreasing tissue length in a self-organized way without explicit time dependence of the parameters. We showed that this theory is able to dynamically account for the length decrease of the presomitic mesoderm through the interplay of opposing morphogen gradients and the oscillator dynamics. The proposed mechanism leads to a termination of the segmentation process after a finite number of segments. Moreover, we derived analytical approximations for the steady state distributions of the morphogen gradients in the presence of self-interactions (Appendix E).

Parameters and Symbols used in Chapter 3

PROFILE FUNCTION	SHAPE PARAMETERS	USAGE
$\Gamma(\xi) = \dfrac{1-\tanh(\kappa_1\xi-\kappa_0)}{1+\tanh\kappa_0}$ 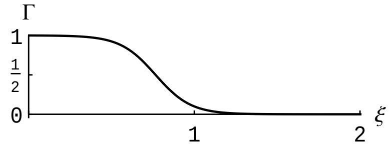 	κ_1, κ_0	frequency and coupling profile, Eqs. (3.2) and (3.3)
$\Delta(\xi) = 1 - \mathrm{e}^{-\mu\xi}$ 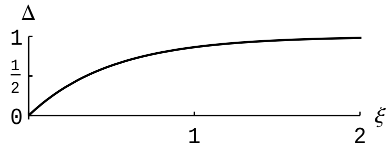 	μ	velocity profile Eq. (3.28)

Table 3.1 Profile functions for the frequency, coupling, and velocity profile. The plots show examples with shape parameters given in Table 3.2.

PARAM.	UNIT	VALUE		SEC.
ω_0	T^{-1}	0.205	maximum frequency	3.1
ε_0	$\mathrm{L}^2\mathrm{T}^{-1}$	7	coupling strength	
v_0	LT^{-1}	0.78	relative velocity in the segmented region	
κ_0	1	3.8	shape parameter of profiles	
κ_1	1	4.7	shape parameter of profiles	
a	L	465	length of the presomitic mesoderm	
t_0	T	0	time to start with zero initial conditions	
μ	1	1.8	shape parameter of the velocity profile	3.3
a_0	L	465	offset length of the presomitic mesoderm	3.4
v_1	LT^{-1}	1.00	speed of tissue shortening for $t < t^*$	
v_2	LT^{-1}	0.28	speed of tissue shortening for $t > t^*$	
t_0	T	-620	time to start with zero initial conditions	
t_1	T	-250	time at which the tissue starts to shorten	
t^*	T	370	time point of transition between shortening rates	
T^*	T	57	size of the transition region	

Table 3.2 List of parameters and numerical values used in this chapter. Using the theory presented in Sec. 3.4, this parameter set describes segmentation in wildtype zebrafish embryos. See Chapter 4 for details on how this parameter set was obtained. The physical units are $\mathrm{T} = 1\,\mathrm{min}$ and $\mathrm{L} = 1\,\mu\mathrm{m}$.

PARAM.	**UNIT**	**VALUE**	
			MORPHOGEN Q
α	NT^{-1}	1	production rate
x_0	L	2	spatial extension of the source
h_0	T^{-1}	1	decay rate
h_1	$\mathrm{N}^{-1}\mathrm{T}^{-1}$	300	degradation rate
E	$\mathrm{L}^2\mathrm{N}^{-1}\mathrm{T}^{-1}$	1	diffusion constant
Q^*	N	0.05	threshold level for arrest front position
Q_0	N	0.7	reference level
			MORPHOGEN R
β_0	NT^{-1}	0.5	basal production rate
β_1	NT^{-1}	3	additional production rate in formed segments
k_0	T^{-1}	5	decay rate
k_1	$\mathrm{N}^{-1}\mathrm{T}^{-1}$	40	relative rate of degradation by Q
D	$\mathrm{L}^2\mathrm{N}^{-1}\mathrm{T}^{-1}$	0.5	diffusion constant
			PHASE FIELD ϕ
ω_0	T^{-1}	20	ratio between frequency and level of Q
ε_0	$\mathrm{L}^2\mathrm{T}^{-1}$	0.06	ratio between coupling strength and level of Q
			VELOCITY FIELD v
κ	$\mathrm{N}^{-1}\mathrm{T}^{-1}$	0.4	ratio between growth rate and level of Q

Table 3.3 List of parameters and numerical values used in Sec. 3.5. Here, T is the unit of time, L is the unit of length, and N is the unit of morphogen concentration. Note that the column 'Unit' indicates the *physical* units of the respective parameter while the column 'Value' indicates its value in the nondimensionalization scheme introduced in Sec. 3.5.1.

LIST OF SYMBOLS

x	position variable, distance from the posterior tip
t	time
ϕ	phase field
ψ	phase profile
a	length of the presomitic mesoderm
ξ	dimensionless position variable
ω	frequency profile
ε	coupling profile
v	velocity profile
k	growth profile
u	velocity field of kinematic waves
Ω	collective frequency
T	collective period
K	number of kinematic waves in the presomitic mesoderm
N	total number of formed segments
S	length of segments upon formation
t_F	time point of segment formation
x_*	position of a point with constant phase ϕ_*
λ	local wavelength of kinematic waves
ϕ_A	phase at the arrest front

ϕ_{P}	phase at the posterior tip
Ω_{A}	frequency at the arrest front
Ω_{P}	frequency at the posterior tip
Ω_{D}	Doppler frequency contribution to Ω_{A}
Ω_{W}	Change of phase profile contribution to Ω_{A}
γ	ratio of shortening speed and advective speed
η	dimensionless quantity describing effects of changing frequency profile
Q	morphogen level of posteriorly expressed morphogen
R	morphogen level of anteriorly expressed morphogen
X	oscillatory signal associated to the phase ϕ
J	source function
$\mathbb{1}$	indicator function, equivalent to the Heaviside Theta function, $\mathbb{1}_{x>y} = \Theta(x-y)$

Chapter 4

Quantitative Biology of Vertebrate Segmentation

In this chapter, we quantify the key features of vertebrate segmentation from experiments with zebrafish embryos performed by our collaborators. We determine the morphological changes of the segmenting tissue over time and quantify the spatio-temporal wave patterns of gene expression. We compare this experimental data with theoretical predictions from the theory introduced in Chapter 3 and report a Doppler effect in embryonic pattern formation caused by the decreasing tissue length as predicted by our theory.

4.1 Tissue Shortening and Tissue Deformation

In this section, we quantify the time evolution of the presomitic mesoderm length and the velocity field in the segmented region in zebrafish embryos from experimental data. We use the results to parametrize the presomitic mesoderm length and the velocity field in the theory presented in Chapter 3.

4.1.1—
Analysis of brightfield time-lapse movies

The experimental data quantified here is a brightfield time-lapse movie of a segmenting wildtype zebrafish, published by Schröter *et al.* in Ref. [128] as Supplementary Movie 3. For each frame of the movie, we define a one-dimensional coordinate system whose origin is the tailbud tip and which points in anterior direction along the body axis (Fig. 4.1A). We then obtain the gray values along this axis for each frame, which allows us to locate the segment boundaries and to measure the length of the presomitic mesoderm at each point in time. This procedure yields the kymograph Fig. 4.2A, which shows the profile of gray values along the body axis as a function of time[1]. Dark gray lines indicate the motion of segment boundaries relative to the posterior tip. The time evolution of the position of the segment boundaries appear as 'world lines' indicating their motion away from the posterior tip.

4.1.2—
Time evolution of the presomitic mesoderm length

The time-dependent length of the presomitic mesoderm can be obtained by manually tracking the position where new segment boundaries appear (examples shown by white dots in Fig. 4.2A). This reveals that the time evolution of the length has a piecewise linear behavior (Fig. 4.3). We quantify this behavior by constructing a fit function $a(t)$ that smoothly interpolates between the two linear speeds v_1 and v_2 with which the tissue shortens. We here choose a hyperbolic tangent as a smooth

---

[1] For the time-lapse movie in Ref. [128], there is no scale available which would allow a direct identification of pixels and physical length units. However, from a comparison of the reported segment length upon formation with the length of segments in the movie, we estimate that one pixel in the movie corresponds to 2 μm.

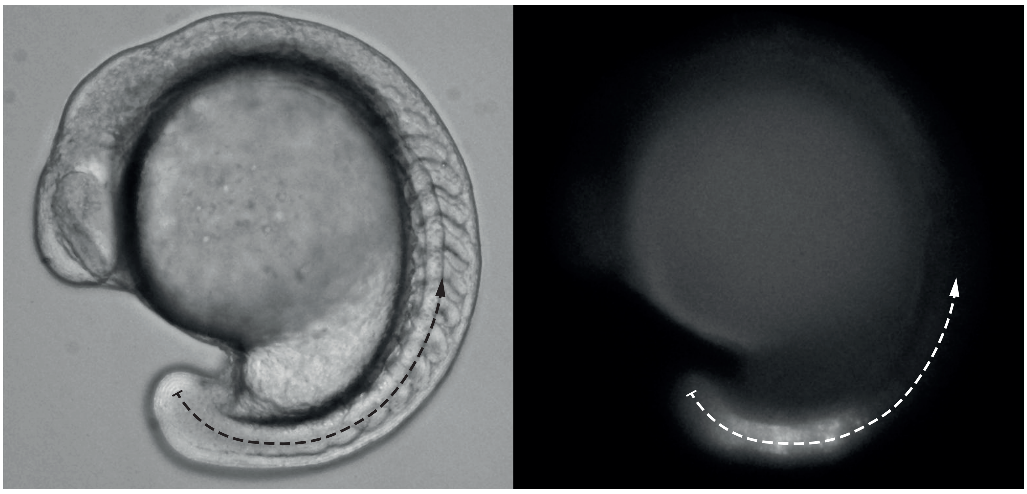

A. BRIGHTFIELD CHANNEL

B. YFP CHANNEL

Figure 4.1 Embryonic coordinate system in the reference frame comoving with the posterior tip of the presomitic mesoderm, cf. Fig. 3.1. **A.** Zebrafish embryo (LOOPING line) during segmentation in the brightfield channel. Brightfield images are used to define the coordinate system, using the visible features such as the notochord (see also Fig. 1.3) as a guide. **B.** The same embryo as in the left image but in the YFP channel. [Images courtesy of Daniele Soroldoni.]

step function, which interpolates between the two shortening speeds,

$$\frac{\mathrm{d}a}{\mathrm{d}t} = -v_1 - \frac{v_2 - v_1}{2}\left(1 - \tanh\frac{t - t^*}{T^*}\right) , \tag{4.1}$$

where t^* is the transition point between the two rates and T^* characterizes the time interval of transition. Hence, the fit function $a(t)$ is given by

$$a(t) = a_0 - \frac{v_2 + v_1}{2}t - \frac{v_2 - v_1}{2}T^* \log\cosh\frac{t - t^*}{T^*} . \tag{4.2}$$

The resulting fit is shown as solid black line in Fig. 4.3A and the corresponding fit parameters are provided in Table 4.1. We use these quantified values as parameters for our theory of vertebrate segmentation presented in Chapter 3, see Table 3.2.

4.1.3— Velocity profile in the segmented region

In Fig. 4.2A, dark gray lines indicate the motion of the segment boundaries away from the posterior tip. The slope of these 'world lines' corresponds to the speed of the segment boundaries relative to the posterior tip and thus contains information about the velocity field in the segmented region. To track the motion of the segment boundaries systematically, a peak-finding and tracking algorithm for the gray level was developed[2]. The resulting traces of the segment boundaries are shown in Fig. 4.2C.

---

[2] This algorithm discriminates the segment boundaries from the interior of the segments and the presomitic mesoderm in Fig. 4.2A as follows. For each horizontal time slice in Fig. 4.2A, the intensity signal is smoothed with a moving average of width 6 pixels. Subsequently, the local intensity minima, which correspond to the positions of the segment boundaries, are determined with a peak-finding algorithm. The result is shown in Fig. 4.2B. In the next step, nearby points are connected to obtain time series of the segment boundaries' positions. This is accomplished by starting at the latest point in time ($t = 1000\,\mathrm{min}$) and using the positions of the corresponding points as starting values for the boundary traces. We then go back in time and successively connect points that are within a window of 14 pixels around the last point of the respective trace. Spurious traces are removed by hand. The resulting traces are shown in Fig. 4.2C.

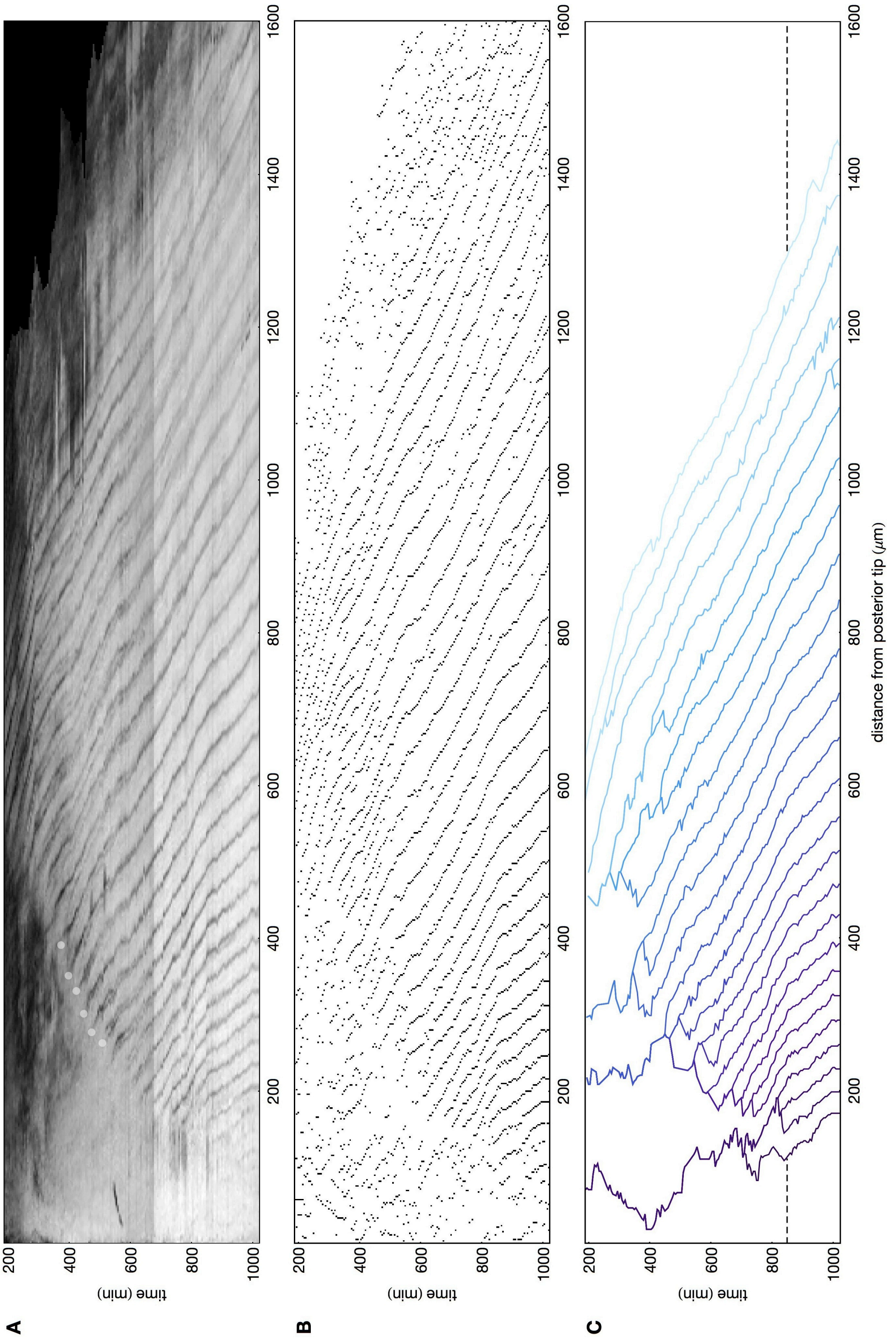

Figure 4.2 **A.** Intensity kymograph obtained from a time-lapse microscopy movie of zebrafish segmentation published by Schröter *et al.* [128]. The x-axis marks the distance along the coordinate system illustrated in Fig. 3.1. White dots are examples of points where segment boundaries are formed, marking the anterior end of the presomitic mesoderm. **B.** Algorithmically determined point set of local intensity minima indicating the position of segment boundaries. **C.** Sets of adjacent points were algorithmically grouped to obtain separate traces for each segment boundary (different colors indicate different boundaries). The dashed line marks the time point $t = t^{**}$ where the slope of the curves changes.

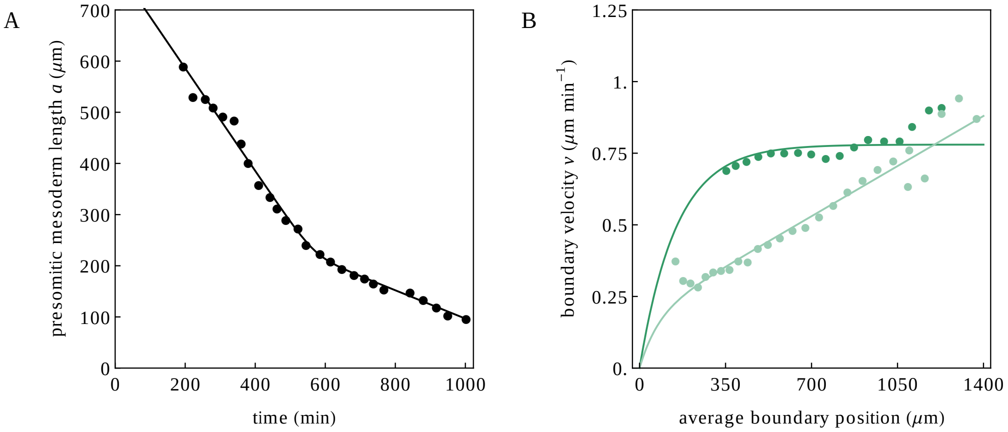

Figure 4.3 **A.** The time evolution of the presomitic mesoderm length a (black dots) and a fit to Eqs. (4.2) (solid line) with parameters in Table 4.1. (See Sec. 4.1.2 for details.) **B.** The velocity profile as a function of time in the two temporal regions $t < t^{**}$ (dark dots) and $t > t^{**}$ (bright dots). The curves show the phenomenological function (4.3) for the respective temporal region with parameters listed in Table 4.2. (See Sec. 4.1.3 for details.)

PARAM.	UNIT	VALUE	NV	
ϑ	°C	27.4		temperature at which movie was taken [128]
t^*	min	569	370	time point of transition between v_1 and v_2
T^*	min	57		length of transition time interval
a_0	μm	594	465	offset length of the presomitic mesoderm
v_1	$\mu\mathrm{m}\,\mathrm{min}^{-1}$	1.00		shortening speed for $t < t^*$
v_2	$\mu\mathrm{m}\,\mathrm{min}^{-1}$	0.28		shortening speed for $t > t^*$

Table 4.1 Parameters of a fit of the function $a(t)$, Eq. (4.2), to the quantified length of the presomitic mesoderm over time (Fig. 4.3). The column 'NV' indicates the normalized value obtained from requiring that $t = 0$ corresponds to the formation of the 6$^{\text{th}}$ segment ($t \simeq 200\,\text{min}$ in the movie). This convention is used in Chapter 3, Sec. 3.4. A blank entry means that the normalized value is the same as the one indicated in the 'Value' column.

PARAM.	UNIT	VALUE	
t^{**}	min	850	time point of transition between velocity profiles
			REGION $t < t^{**}$
$v_0^<$	$\mu\mathrm{m}\,\mathrm{min}^{-1}$	0.78	reference velocity
$k_0^<$	min^{-1}	0	asymptotic growth rate
$x_1^<$	μm	150	length of transition region
			REGION $t > t^{**}$
$v_0^>$	$\mu\mathrm{m}\,\mathrm{min}^{-1}$	0.18	reference velocity
$k_0^>$	min^{-1}	5×10^{-4}	asymptotic growth rate
$x_1^>$	μm	75	length of transition region

Table 4.2 Parameter sets for Eq. (4.3) to phenomenologically describe the velocity fields quantified from experimental data (Fig. 4.3).

At time $t = t^{**} \simeq 850\,\mathrm{min}$ (dashed line in Fig. 4.2C), a change in the slope of the world lines can be observed. Within the regions $t < t^{**}$ and $t > t^{**}$, the slopes of the world lines are approximately constant. For each segment boundary and for each of the two regions $t < t^{**}$ and $t > t^{**}$, we perform a linear fit of the boundary position over time to determine its velocity. To obtain a velocity profile, we compute the average position of each segment boundary in each of the two regions $t < t^{**}$ and $t > t^{**}$ and assign the velocity of the corresponding boundary to it. In this way, we obtain one velocity profile for each of the two temporal regions (dots in Fig. 4.3B).

We capture the features of these two velocity profiles by phenomenological functions. Since the velocity profile within the presomitic mesoderm is inaccessible with the available dataset, we make an assumption about its behavior. We here assume that the velocity in the direction of the body axis vanishes at the posterior tip, which marks the tissue boundary, and gradually increases towards the anterior,

$$v(x) = (1 - \mathrm{e}^{-x/x_1})v_0 + k_0 x \ . \tag{4.3}$$

Here, x_1 is the characteristic length over which the velocity increases to a finite value in anterior direction, v_0 is a reference velocity and k_0 is an asymptotic linear growth rate. This velocity field corresponds to a growth field

$$k(x) = \frac{\mathrm{d}v}{\mathrm{d}x} = k_0 + \frac{v_0}{x_1}\mathrm{e}^{-x/x_1} \ . \tag{4.4}$$

Hence, the velocity field (4.3) describes large growth in the posterior and decreasing growth towards the anterior. The growth rate k approaches the constant k_0 for large x. For the case $k_0 = 0$, the velocity v, Eq. (4.3), approaches the constant v_0 for large x. Instead of fitting Eq. (4.3) to the experimental data, which does not yield satisfactory results as data points in the presomitic mesoderm region are not available, we choose a phenomenological parameter set by hand. The corresponding parameter sets for $v(x)$ are given in Table 4.2, where the superscript '<' denotes the parameters for $t < t^{**}$ and '>' those for $t > t^{**}$. The corresponding curves are displayed in Fig. 4.3B along with experimental data (dots). We use the obtained velocity field at early times ($t < t^{**}$) for our theory of vertebrate segmentation presented in Chapter 3, see Table 3.2.

4.2 Wave Patterns of Gene Expression

In this section, we quantify experimental data on kinematic wave patterns of gene expression obtained from the transgenic zebrafish reporter line LOOPING, which has been generated by our experimental collaborators[3]. We obtain a phase representation of the spatio-temporal wave patterns in the presomitic mesoderm using a wavelet transform as explained below. We use this phase representation to determine the key features of the spatio-temporal wave patterns of gene expression from a population of different embryos and compare them with the theoretical predictions of the theory presented in Chapter 3. The research presented in this section is the result of a highly collaborative effort and part of the results have been published [133].

---

[3] The Her1–YFP reporter line LOOPING, which lays the ground for the experiments analyzed in this section, was generated by Daniele Soroldoni in the research group of Prof. Andrew C. Oates at the MRC National Institute for Medical Research, Mill Hill, London, UK, the University College London, UK, and the Max Planck Institute for Molecular Cell Biology and Genetics, Dresden, Germany. DS also generated the time-lapse movies and the intensity kymographs presented in this section and performed the frequency measurements shown in Fig. 4.9C.

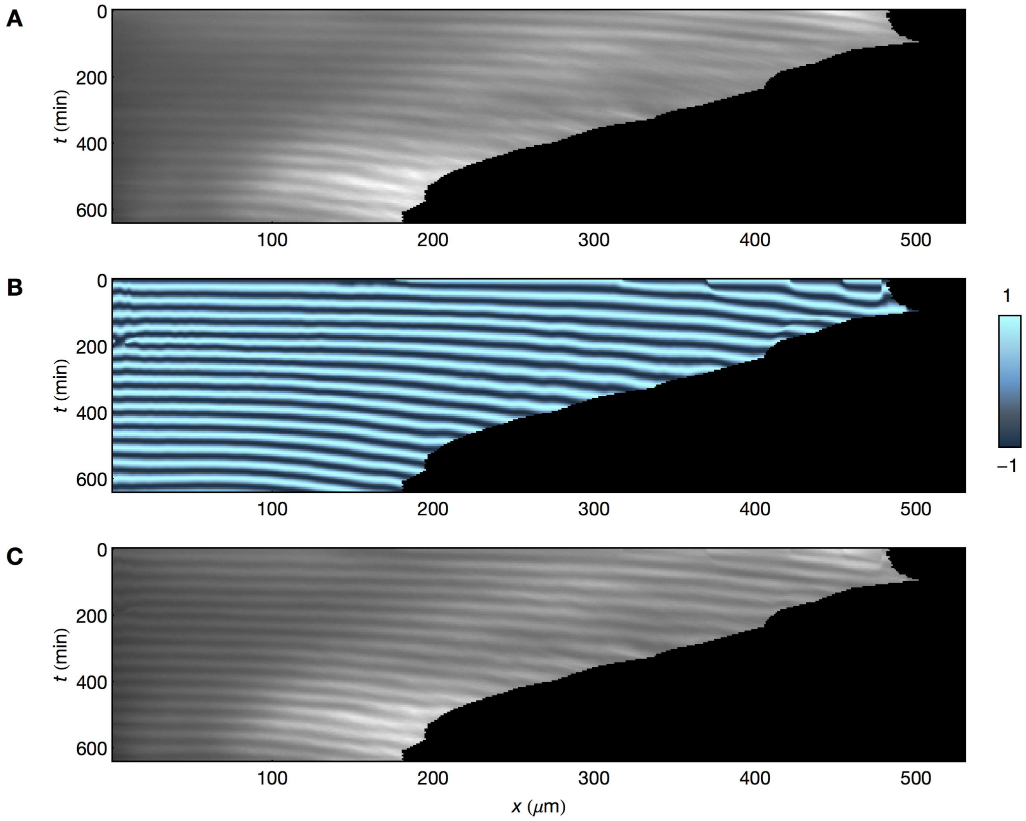

Figure 4.4 **A.** Intensity kymograph showing the YFP flourescence signal. The x-axis indicates the distance from the posterior tip in the coordinate system defined in Fig. 4.1. **B.** Phase map $\phi(x,t)$ corresponding to the intensity kymograph in panel A, obtained using the procedure explained in Sec. 4.2.2 and Appendix F. The plot shows $\sin\phi(x,t)$ in the same color code as used for the kymographs of theoretical results in Chapter 3. (e.g., Fig. 3.7). **C.** Overlay of the intensity kymograph A and the phase map B. Data also presented in Ref. [133].

4.2.1— Imaging gene expression at tissue level

The transgenic zebrafish reporter line LOOPING allows the visualization of oscillating genes in the presomitic mesoderm. In this line, the cyclic gene *her1* has been tagged with *yellow fluorescent protein* (YFP), which emits light at a characteristic wavelength upon exposure to laser light. It thus allows real-time imaging of genetic oscillations in the presomitic mesoderm at tissue level *in vivo* [133]. Our experimental collaborators generated time-lapse movies of segmenting transgenic zebrafish embryos, imaging them in parallel in a brightfield channel (Fig. 4.1A) and a YFP channel (Fig. 4.1B). To quantify the spatio-temporal patterns of gene expression at tissue level, the Her1–YFP signal was recorded along the presomitic mesoderm in the reference frame indicated in Fig. 4.1B (in analogy to the procedure explained in Sec. 4.1). For each embryo, this procedure yields an intensity kymograph containing the spatio-temporal dynamics of the kinematic wave patterns (Fig. 4.4A). The bright ridges in Fig. 4.4A indicate the motion of the kinematic waves in anterior direction.

4.2.2— Using a wavelet transform to generate phase maps

A systematic and robust way to construct a phase time series from an oscillatory signal, is the wavelet transform, which is similar to a windowed Fourier transform [30, 112, 143]. Consider a discrete time series $Q = (q_1, \ldots, q_n)$ sampled with time interval δ_{T}, so that q_k with $k = 1, \ldots, n$ is the signal at time point $t = k\delta_{\mathrm{T}}$.

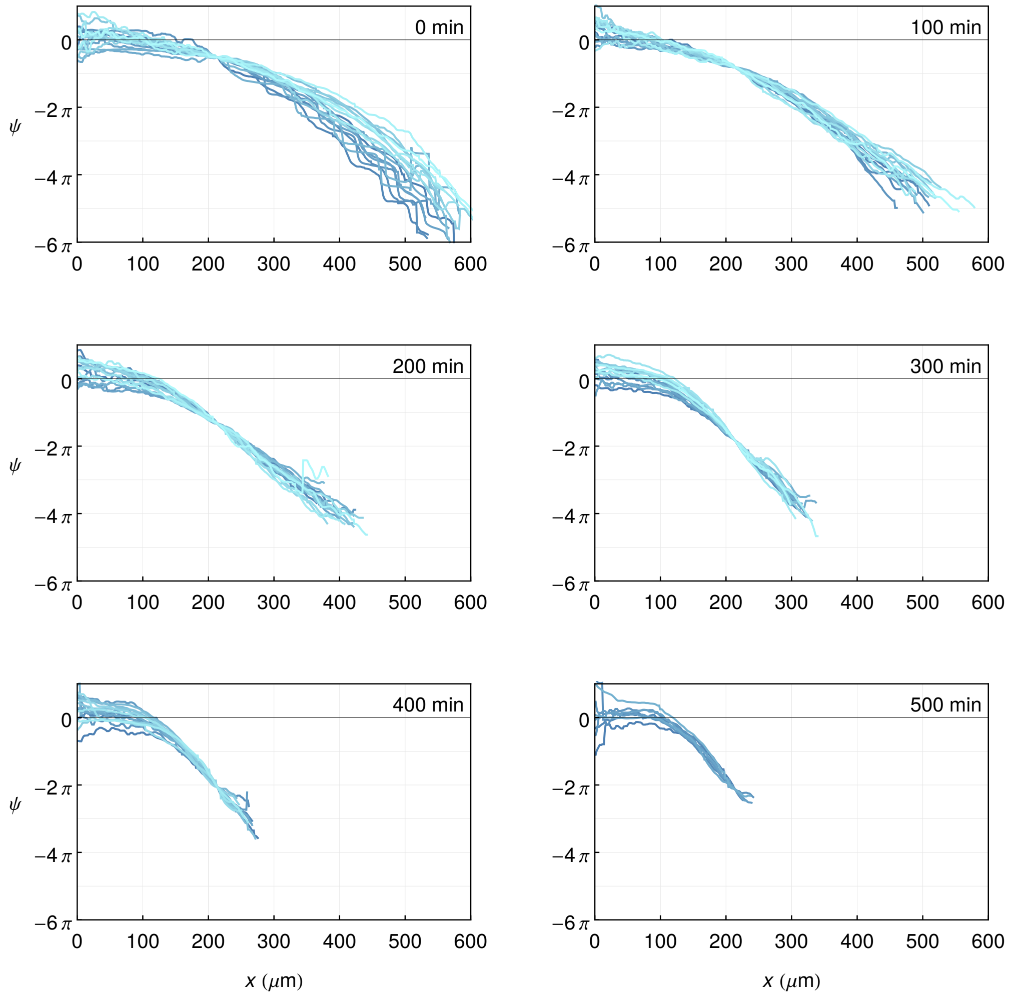

Figure 4.5 Phase profiles ψ_i, Eq. (4.9), from 18 different embryos (different shades of blue) at different developmental times, obtained as described in Appendix F, Sec. F.2. The x-axis indicates the distance from the posterior tip in anterior direction (Fig. 4.1). Data also presented in Ref. [133].

The continuous wavelet transform of the time series Q is defined by

$$W_\sigma(k) = \sigma^{-1/2} \sum_{j=1}^{n} q_j \Psi^* \left(\frac{j-k}{\sigma} \right) . \tag{4.5}$$

The parameter σ, called ‘wavelet scale’, is a dimensionless time scale whose inverse σ^{-1} has a function similar to the frequency in a Fourier transform. The function $\Psi(u)$ is the so-called ‘mother wavelet’, a complex oscillatory function that quickly decays for increasing $|u|$. Ψ^* denotes its complex conjugate. Here we use the Gabor wavelet function [159]

$$\Psi(u) = \pi^{-1/4} \mathrm{e}^{6iu - u^2/2} , \tag{4.6}$$

a complex plane wave damped by a Gaussian. The wavelet transform W_σ is a complex function and can be expressed in terms of its magnitude and phase, $W_\sigma(k) =$

$R_\sigma(k)\mathrm{e}^{\mathrm{i}\varphi_\sigma(k)}$. The phase φ_σ can be interpreted as the phase of oscillation at the time scale associated with σ [112],

$$\varphi_\sigma(k) = \arg W_\sigma(k)\ . \tag{4.7}$$

Hence, to obtain a viable phase signal, the wavelet scale σ has to be chosen close to the characteristic period of oscillations of the time series Q. However, the resulting phase signal $\varphi_\sigma(k)$ is robust under small variations of the time scale σ.

By applying the wavelet transform to the oscillatory signal of each column of a YFP intensity kymograph, we generate phase maps that represent the spatio-temporal dynamics of the wave patterns (Fig. 4.4B). The details of this procedure are presented in Appendix F and Ref. [133]. The effectivity of this approach can be assessed by overlaying the generated phase maps with the original intensity kymograph (Fig. 4.4C).

4.2.3— Average phase map

In Fig. 4.5, we show the phase profiles

$$\psi_i(x,t) = \phi_i(x,t) - \phi_i(x,0) \tag{4.8}$$

from $m = 18$ different embryos ($i = 1,\dots,m$) at different developmental times. For each point in time, phase profiles from different embryos collapse to a remarkable degree. This shows that the spatio-temporal patterns of kinematic waves are well conserved throughout different embryos. Motivated by this observation, we construct a representative phase map $\Phi(x,t)$ by averaging experimental data from 18 embryos. This average phase map Φ represents the key features of the spatio-temporal wave pattern during segmentation. Details of the averaging procedure are found in Appendix F. Likewise, we obtain the average time-dependent length $A(t)$ of the presomitic mesoderm.

Fig. 4.6 shows the features of the average phase map Φ in different representations. Fig. 4.6A displays a kymograph of the corresponding oscillatory signal $\sin\Phi(x,t)$, a representation introduced in Chapter 3 (see, e.g., Fig. 3.7). Fig. 4.6B shows the oscillatory signal $\sin\Psi(x,t)$ of the average phase profile

$$\Psi(x,t) = \Phi(x,t) - \Phi(0,t)\ . \tag{4.9}$$

This representation reveals the changes in the overall shape of the wave pattern. Fig. 4.6C shows the local wavenumber $\partial\Phi/\partial x$ of the pattern. It shows that large wavelengths (red) occur in the posterior while short wavelengths (blue) occur in the anterior. Moreover, the wavelength locally changes over time. Fig. 4.6D shows the local oscillation frequency $\partial\Phi/\partial t$ and Fig. 4.6E the local rate of change $\partial\Psi/\partial t$ of the average phase profile.

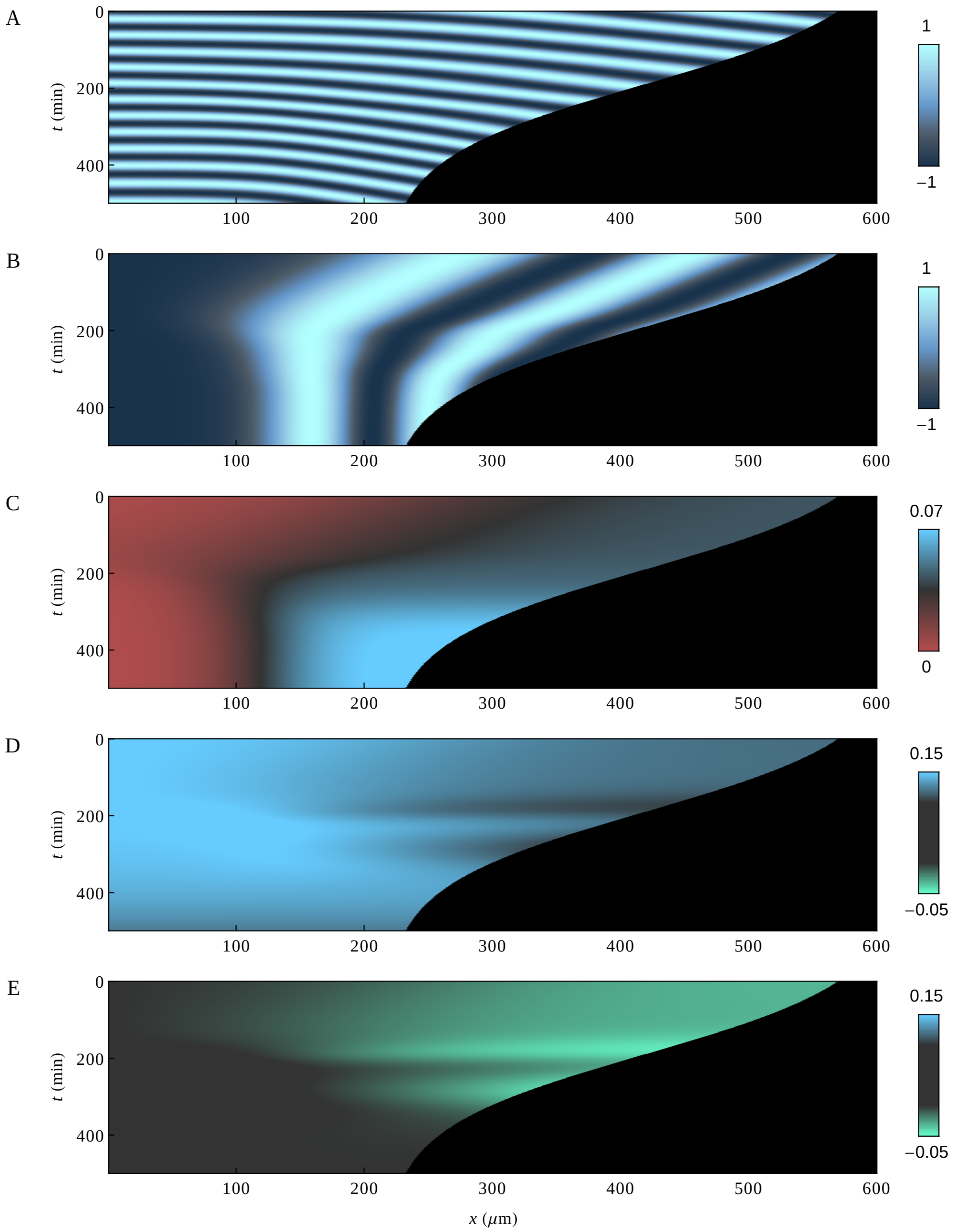

Figure 4.6 **A.** Oscillatory signal $\sin \Phi$ of the average phase map Φ. **B.** Oscillatory signal $\sin \Psi$ of the average phase profile $\Psi(x,t) = \Phi(x,t) - \Phi(0,t)$. **C.** Local wavenumber $\partial\Phi/\partial x$ in units of $\mu\mathrm{m}^{-1}$. **D.** Local frequency $\partial\Phi/\partial t$ in units of min^{-1}. **E.** Local rate of change of the phase profile, $\partial\Psi/\partial t$ in units of min^{-1}. Figures presented with minor modifications in Ref. [133].

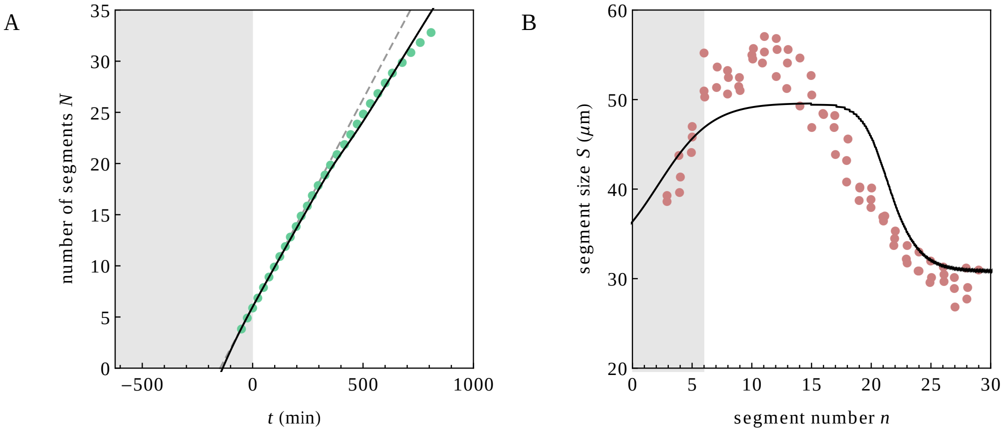

Figure 4.7 **A.** Number of formed segments N as a function of time in theory (black curve), Eq. (3.9), and experiment (green dots). The dashed gray line shows a linear fit to the initial 10 segments highlighting the deviation from this linear behavior at later times. **B.** Segment length S upon segment formation as a function of segment number in theory (black curve), Eq. (3.11), and experiment (red dots). In both plots, the shaded area is the initial transient region, which we ignore (see Sec. 4.3.1 for details). Experimental data in both plots from Ref. [128].

4.3 Comparison of Theoretical and Experimental Results

We use the experimentally obtained phase maps to show that the continuum theory of coupled oscillators in a tissue of changing length, presented in Chapter 3, Sec. 3.4, is capable of describing the key features of vertebrate segmentation. One strategy would be to use the experimentally obtained phase maps to fit the parameters of the theory, so that the theoretical results accurately reproduce the kinematic wave patterns observed in experiments. However, such an approach would not test the predictive power of our theory. Instead, we here choose to determine a parameter set by only demanding that the theory correctly reproduces the experimentally observed timing of segment formation and the length of the formed segments. To determine such a parameter set, we fit the parameters of our theory using only experimental data on *morphological* segment formation, not on the kinematic wave patterns. We then use this parameter set to obtain independent predictions for the kinematic wave patterns and compare them with experiments.

4.3.1—Morphological segmentation

We first show how to determine the reference parameter set in Table 3.2 for the continuum theory of coupled oscillators, presented in Chapter 3. This parameter set describes the morphological segmentation dynamics of a developing wildtype zebrafish embryo at a temperature of 27.4°C as published in Ref. [128]. The parameter values for the time evolution of the presomitic mesoderm length (a_0, v_1, v_2, t^*, T^*) and the velocity field (v_0, μ) have been determined in Sec. 4.1 from the data in Ref. [128]. The coupling strength ε_0 has been adopted from the literature, estimated from experiments in which intercellular coupling has been temporarily inhibited [93, 117]. The remaining parameters are obtained as follows: In our theory, the key features of morphological segmentation are represented by the number of formed segments $N(t)$ as a function of time, Eq. (3.9), and the segment length upon formation $S(n)$ as a function of segment number, Eq. (3.11). These observables have

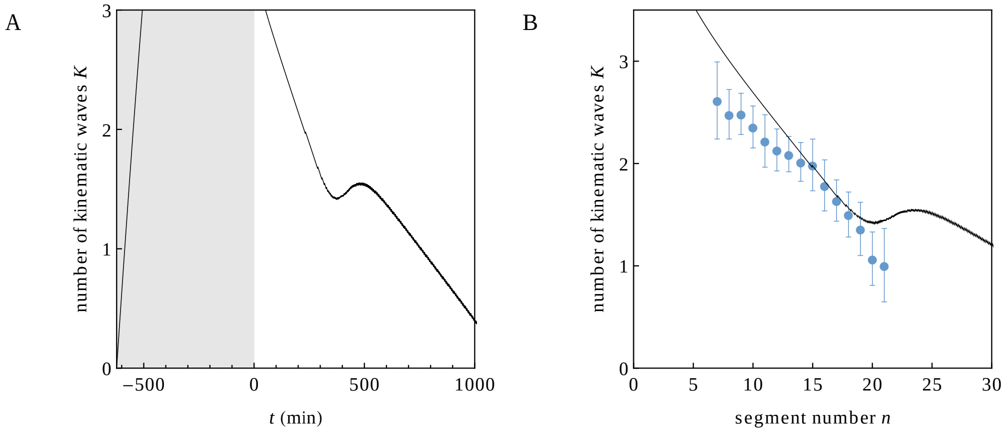

Figure 4.8 **A.** Number of kinematic waves K as a function of time, Eq. (3.6). Shaded area as in Fig. 4.7. **B.** Number of kinematic waves K as a function of segment number as predicted by theory (black), Eq. (3.12), as as quantified from experiments (blue dots), see Chapter 4, Sec. 4.2. Experimental data also presented in Ref. [133].

been measured in experiments in Ref. [128]. We use an optimization algorithm[4] that fits the theoretical results for $N(t)$ and $S(n)$ to the corresponding experimental data from Ref. [128] using the remaining model parameters (ω_0, κ_1, κ_0, t_0, t_1) as fit parameters. Fig. 4.7 shows $N(t)$ and $S(n)$ for the parameters in Table 3.2 along with experimental data.

With zero initial conditions, Eq. (3.5), there is an initial transient period, in which the kinematic wave pattern builds up (see Sec. 3.1.2 for details). However, the description of the initiation of pattern formation *in vivo* is outside the scope of our theory. We thus ignore the behavior of the system in this initial transient period, which is marked by shaded areas in Fig. 4.7. The number of formed segments $N(t)$ exhibits two regimes where it grows approximately linear but with different slopes The change of the slope takes place at the time point t^*, where the speed of length decrease of the presomitic mesoderm changes from v_1 to v_2. The theory also qualitatively captures the time evolution of the segment length $S(n)$ upon formation. After the initial transient, S reaches a maximum value at about $50\,\mu$m and then decreases to about $30\,\mu$m.

4.3.2— Kinematic wave patterns

As outlined in the previous section, the reference parameters in Table 3.2 have been obtained demanding that the theoretical result captures the timing and morphology of segmentation *in vivo*. No experimental information about the wave patterns of gene expression in the presomitic mesoderm have been used so far. Therefore, the theoretical results on the dynamics of kinematic waves are testable predictions that can be compared with experiments. An important observable is the number of kinematic waves K in the presomitic mesoderm, Eq. (3.6), shown as a function of time in Fig. 4.8A. After the initial transient, the number decreases from about 3 to 1.5, where it reaches a small plateau and then decreases more slowly. The plateau occurs where the shortening speed of the presomitic mesoderm changes from v_1 to v_2.

---

[4] The optimization algorithm works as follows. An initial parameter set for the theory is chosen by hand in a way that it qualitatively captures the experimentally observed behavior of $N(t)$ and $S(n)$. Starting from this initial parameter set, the algorithm creates new parameter sets by adding random numbers from Gaussian distributions with zero mean and chosen variance to the reference parameter set. If such a randomized parameter set achieves a better agreement with the experimental data, the parameter set is chosen as a new reference set. After a certain number of iterations, the algorithm only leads to minor improvements and is aborted. To check for robustness of the resulting fit parameters, the algorithm has been fed with different initial parameter sets and different variances of the Gaussian distributions.

In Fig. 4.8B, we compare the theoretical prediction for the number of kinematic waves (black curve) with experimental data (blue dots) from transgenic zebrafish embryos. From the experimental phase maps (Sec. 4.2.2), the number K of kinematic waves over time can be obtained as the phase difference between the anterior end and the posterior tip just as in the theory, Eq. (3.6). We compare the number of kinematic waves as a function of segment number instead of time for two important reasons: First, the timing of segmentation in the transgenic embryos is slightly different from that in wildtype embryos [133]. Second, we determined our reference parameter set using experimental data obtained from wildtype embryos segmenting at a temperature of 27.4°C [128], while experiments with transgenic embryos have been performed at 23.5°C [133]. Since the segmentation period is heavily temperature-dependent [128], a direct comparison of absolute times is not possible. Hence, we determine the number $K_i(n)$ of kinematic waves for each embryo i and for each segment number n and averaged over all $m = 18$ embryos for each value n of the segment number, $K(n) = m^{-1} \sum_{i=1}^{m} K_i(n)$, shown by blue dots in Fig. 4.8B. The error bars indicate the corresponding standard deviation. Fig. 4.8B shows that the theory independently predicts the correct number of kinematic waves as a function of segment number for the observed range of segments in experiments.

4.4 A Doppler Effect in Embryonic Pattern Formation

In Chapter 3, we theoretically predicted that the shortening of the presomitic mesoderm induces a Doppler effect and a dynamically changing wavelength at the anterior end of the tissue (Sec. 3.4). Since the wave pattern is converted into morphological segments at the anterior end, this implied that in addition to the time scale of genetic oscillations, the rate of segment formation depends on a second time scale set by the rate of tissue shortening and the wavelength of the kinematic waves. Using the experimental phase maps obtained in the previous section, we are able to test this prediction *in vivo*.

**4.4.1—
A Doppler effect and a dynamic wavelength effect occur *in vivo***

The decrease of the number of kinematic waves over developmental time (Fig. 4.8B) is a first hint for the presence of a Doppler effect: Intuitively, as the anterior end moves into the kinematic waves, waves are gradually 'cut off' from the anterior part of the presomitic mesoderm (see also Fig. 3.8). In our theoretical considerations in Chapter 3, Sec. 3.4, we found that the anterior frequency Ω_A, that is, the frequency of oscillations measured in a reference frame comoving with the anterior end of the presomitic mesoderm, could be expressed as a sum of three contributions, Eq. (3.41),

$$\Omega_\mathrm{A} = \Omega_\mathrm{P} + \Omega_\mathrm{D} + \Omega_\mathrm{W} \ . \tag{4.10}$$

Here, Ω_P is the posterior frequency, Eq. (3.40), Ω_D is the Doppler contribution, Eq. (3.42), and Ω_W is the dynamic wavelength contribution, Eq. (3.43). Note that Eq. (4.10) is an exact kinematic relation that holds independent of any theory. This equation implies that the anterior and the posterior frequency can only coincide if either (i) there is neither a Doppler nor a dynamic wavelength effect, $\Omega_\mathrm{D} = 0 = \Omega_\mathrm{W}$, or (ii) the contribution of Doppler and dynamic wavelength effect exactly compensate, $\Omega_\mathrm{D} = -\Omega_\mathrm{W}$. Since the time derivative of the number K of kinematic waves,

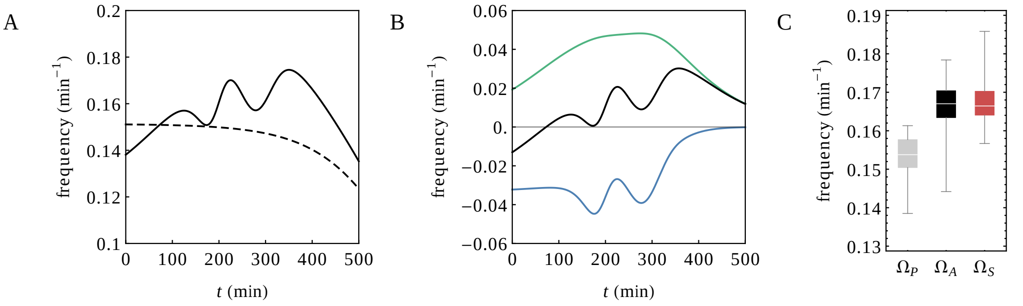

Figure 4.9 **A.** Experimentally determined posterior frequency Ω_{P} (dashed) and anterior frequency Ω_{A} (solid), Eqs. (4.12) and (4.10). **B.** Contributions to the offset between posterior and anterior frequency $\Omega_{\mathrm{P}} - \Omega_{\mathrm{A}} = \Omega_{\mathrm{D}} + \Omega_{\mathrm{W}}$ (black): the Doppler contribution Ω_{D} (green), Eq. (4.13), and the dynamic wavelength contribution Ω_{W} (blue), Eq. (4.14). **C.** Posterior frequency Ω_{P} (gray), anterior frequency Ω_{A} (black), and frequency of segment formation Ω_{S} (red) as measured from 40 embryos. Ω_{A} and Ω_{S} coincide and are significantly larger than Ω_{P} (t-test, Welch correction, *** $p < 0.0001$). Data in panel C obtained by our collaborators. Data in all plots also presented in Ref. [133].

Eq. (3.6), is proportional to the difference between posterior and anterior frequencies,

$$2\pi \frac{\mathrm{d}K}{\mathrm{d}t} = \Omega_{\mathrm{P}} - \Omega_{\mathrm{A}} = -(\Omega_{\mathrm{D}} + \Omega_{\mathrm{W}}) \ , \tag{4.11}$$

the observed decrease of the number of kinematic waves, $\mathrm{d}K/\mathrm{d}t < 0$, immediately rules out these two scenarios. Moreover, using the average phase map Φ, introduced in Sec. 4.2.3, we can explicitly determine the frequencies Ω_{P}, Ω_{D}, and Ω_{W}, given by Eqs. (3.40), (3.42), and (3.43), from experiments as

$$\Omega_{\mathrm{P}} \simeq \left.\frac{\partial \Phi}{\partial t}\right|_{x=0} , \tag{4.12}$$

$$\Omega_{\mathrm{D}} \simeq \left.\frac{\mathrm{d}A}{\mathrm{d}t}\frac{\partial \Psi}{\partial x}\right|_{x=A(t)} , \tag{4.13}$$

$$\Omega_{\mathrm{W}} \simeq \left.\frac{\partial \Psi}{\partial t}\right|_{x=A(t)} , \tag{4.14}$$

where $\Psi(x,t)$ is the average phase profile, Eq. (4.9), and $A(t)$ is the average time-dependent length of the presomitic mesoderm (Sec. 4.2.3). The anterior frequency Ω_{A} is given by the exact relation (4.10). Fig. 4.9 displays these contributions to the anterior frequency. Fig. 4.9A shows that the anterior frequency is in fact larger than the posterior frequency on average as already indicated by the decreasing number of kinematic waves. Fig. 4.9B reveals that the Doppler effect due to the decreasing tissue length indeed yields a positive contribution $\Omega_{\mathrm{D}} > 0$, while the changing wavelength at the anterior end yields a negative contribution $\Omega_{\mathrm{W}} < 0$. Hence, the Doppler effect and the dynamic wavelength effect oppose each other as predicted by our theory (Sec. 3.4.2). Over most of the time range, the magnitude of the Doppler contribution is larger, which yields a positive contribution to the anterior frequency on average.

Fig. 4.10 displays the Doppler effect and the dynamic wavelength effect and their combination schematically in a kymograph representation. In a classical simple

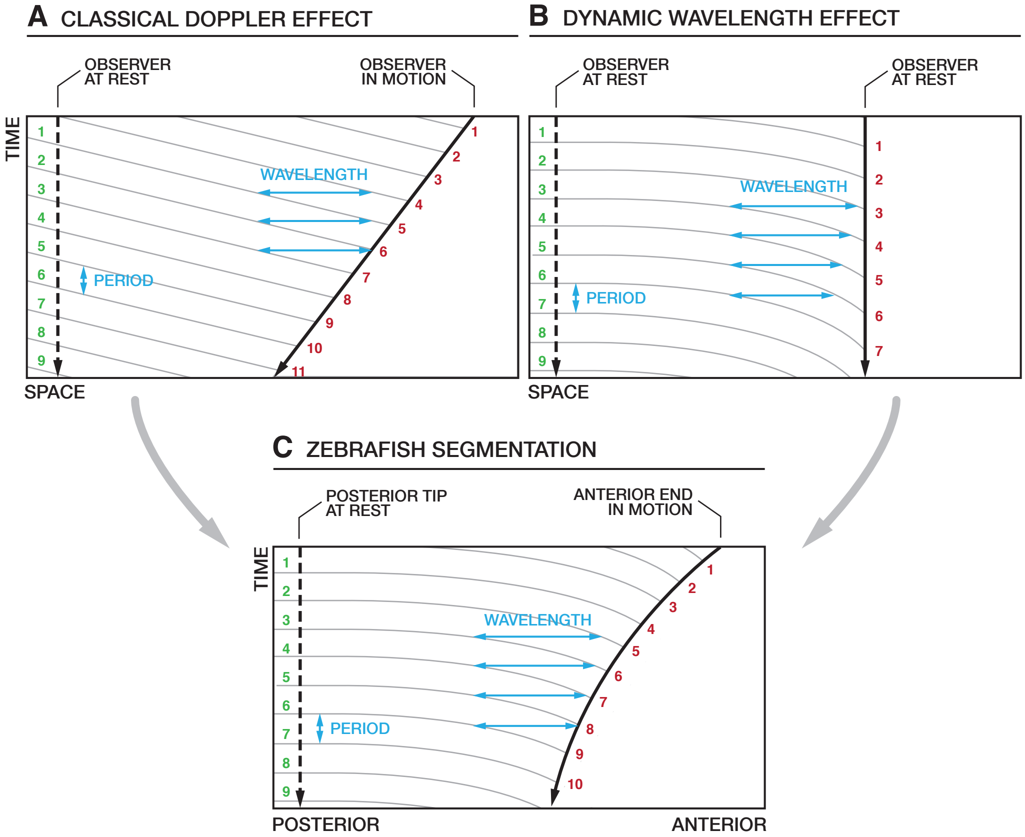
A CLASSICAL DOPPLER EFFECT
OBSERVER AT REST
OBSERVER IN MOTION
TIME
WAVELENGTH
PERIOD
SPACE
1
2
3
4
5
6
7
8
9
10
11
B DYNAMIC WAVELENGTH EFFECT
OBSERVER AT REST
OBSERVER AT REST
WAVELENGTH
PERIOD
SPACE
C ZEBRAFISH SEGMENTATION
POSTERIOR TIP AT REST
ANTERIOR END IN MOTION
TIME
WAVELENGTH
PERIOD
POSTERIOR
ANTERIOR

Figure 4.10 Schematic kymograph representations of a pure Doppler effect (A), a pure dynamic wavelength effect (B), and their interplay as observed during the segmentation of zebrafish embryos (C). Gray lines indicate the motion of wave peaks traversing the spatial domain. Thick black lines indicate two different observers (solid and dashed). Figure presented with minor modifications in Ref. [133].

Doppler effect (Fig. 4.10A), a source emits waves (motion of wave peaks indicated by gray lines) with a constant period and wavelength (blue lines). The slope of the gray lines indicates the propagation speed of the waves. For an observer at rest with respect to the source (dashed black line), the observed period coincides with the period of emission at the source. An observer moving towards the source (solid black line), experiences a smaller period (higher frequency) as more wave peaks are crossed in the same time interval. In a pure dynamic wavelength effect (Fig. 4.10B), both observers are at rest but the wavelength decreases locally in the vicinity of one observer, leading to a larger period (smaller frequency) compared to the other observer. In the zebrafish embryo, both effects combine and oppose each other, with the Doppler effect having the larger magnitude (Fig. 4.10C).

4.4.2— The anterior frequency coincides with the rate of segmentation

It remains to show that the anterior frequency Ω_A indeed coincides with the rate of morphological segment formation. The rate of segment formation can be obtained from the brightfield channel (Fig. 4.1A) of the time-lapse movies obtained for each embryo by measuring the times at which new segment boundaries are drawn. Fig. 4.9C shows the posterior frequency Ω_P, the anterior frequency Ω_A, and the frequency of segment formation Ω_S as measured from 40 embryos by our collaborators. As described above, the anterior frequency Ω_A is larger than the posterior frequency Ω_{P}. The relative offset between both frequencies is 9%. Moreover, the anterior frequency Ω_{A} indeed coincides with the frequency of segment formation Ω_{S}. We thus conclude that in addition to the time scale of genetic oscillations, a second time scale, which stems from a Doppler effect and a dynamic wavelength effect, regulate the rate of morphological segment formation.

4.5 Summary

In this chapter, we quantified experimental data on vertebrate segmentation obtained by our collaborators and compared them with theoretical predictions. First, we quantified the time-dependent length of the presomitic mesoderm and the velocity field in the segmented region from data published in Ref. [128] to determine an appropriate parameter set for the theory presented in Chapter 3. We then used the resulting theoretical predictions on the kinematic wave patterns to independently test the viability of our theory. To this end, we quantified the spatio-temporal patterns of kinematic waves obtained from transgenic zebrafish lines obtained by our collaborators. We used a wavelet transform to construct a phase representation of these wave patterns, which allowed us to systematically compare the patterns of different embryos, to extract the observables of interest, and to compare experimental with theoretical data. We found that the number of kinematic waves substantially decreases as a function of segment number and that this decrease is captured very well by our theory.

Moreover, the theory presented in Chapter 3 described the occurrence of a Doppler effect, which is caused by the anterior end of the tissue moving into the kinematic waves. This Doppler effect was accompanied by a dynamic change of the wavelength in the vicinity of the anterior end and contributed to the rate of segmentation. Using our experimental phase maps, we found that such a Doppler effect and a dynamic wavelength effect indeed occur *in vivo*. We quantified the magnitude of these effects and found that they induce a 9% offset between the posterior and anterior oscillation frequency. Moreover, using data obtained by our collaborators, we showed that the anterior frequency coincides with the rate of segment formation. We thus concluded that in addition to the time scale of genetic oscillations, a second time scale, which stems from a Doppler effect and a dynamic wavelength effect, regulate the rate of morphological segment formation. The research presented in this chapter is the result of a highly collaborative effort and part of the results have been published [133].

Chapter 5

Cell-based Model of Self-organized Segmentation

In this chapter, we present a cell-based computational model of vertebrate segmentation that combines tissue growth, morphogen gradient formation, coupled oscillations, and cell differentiation. We show that this model is capable of describing a growing tissue that segments in a self-organized way. Our model provides a starting point to study the interplay of cellular oscillation dynamics and tissue mechanics in a unified framework.

5.1 Cell-based Model with Dissipative Particle Dynamics

To complement the coarse-grained continuum theories presented in the previous chapters, we introduce a computational model in which the single cells of the presomitic mesoderm are distinct mechanical entities that interact with each other. We show that simple mechanisms of cell growth, division, and differentiation, together with morphogen production and coupled oscillations, are sufficient to generate a growing tissue that exhibits self-organized segmentation. Over the last years, several approaches to describe the properties of tissues using cell-based models have been developed [16, 20, 104, 114, 122, 124]. We here adapt and modify a cell-based tissue model developed by Basan *et al.* [16], which itself is based on *dissipative particle dynamics* [59]. Dissipative particle dynamics is a computational model for hydrodynamic simulations that represents fluid elements as particles. The particles are Newtonian mass points subject to pairwise repulsive, adhesive, dissipative and random forces. For their cell-based tissue model, Basan *et al.* represent a cell of a tissue by a pair of particles instead of a single particle. The interactions between particles belonging to such a pair determine the dynamics of cell growth and division. The interactions between particles belonging to different cells determine the cell-cell interactions and thus the collective behavior of the resulting tissue. We favor this cell model over simpler approaches since events like cell division, cell elongation, and mechanical feedback of surrounding cells can be implemented in a simple and conceptually clear manner.

We extend this model by equipping each cell with a phase variable that represents the state of its genetic oscillator and let the phases of the cells be subject to coupled dynamics with coupling delays. Furthermore, each cell is able to express a morphogen, which diffuses through the tissue. The morphogen concentration in a cell sets the frequency of the cell-autonomous oscillator and determines when cell differentiation takes place. Different cell types are implemented through their individual mechanical properties. The interplay of these mechanisms of tissue growth, morphogen production, oscillator dynamics, and cell differentiation leads to a separation of cell clusters that correspond to formed segments, as we will show later.

5.1.1— State space

The central entities of the model are the particles and the cells that they constitute. We now give formal definitions.

- *Particle.* A particle is a Newtonian mass point. Hence, its state is specified by the 6-tuple
$$P = (\mathbf{x}, \mathbf{v}) = (x^1, x^2, x^3, v^1, v^2, v^3)\ , \tag{5.1}$$
where $\mathbf{x} = (x^1, x^2, x^3)$ is its position and $\mathbf{v} = (v^1, v^2, v^3)$ is its velocity. All particles have the same mass m. Particle indices are denoted by latin letters $i, j, \ldots$, e.g., $P_i = (\mathbf{x}_i, \mathbf{v}_i)$.
- *Cell.* A cell is constituted by a pair of particles and characterized by a cell type that determines its mechanical properties as well as its ability to exhibit genetic oscillations. Moreover, the cell can express a morphogen. The state of a cell is specified by the 5-tuple
$$C = (X, Q, \phi, i, j)\ , \tag{5.2}$$
where X denotes the cell type, Q denotes the morphogen level within the cell, ϕ denotes the phase of its autonomous intracellular oscillator, and i and j refer to the indices of the two particles P_i and P_j belonging to this cell. The four cell types in our model are presomitic mesoderm (PSM), rostral somite (RST), caudal somite (CDL) and mesenchymal somite (MSC). The cell types RST and CDL constitute segment boundaries, while MSC constitutes the interior of the formed segments. Cell indices are denoted by greek letters $\mu, \nu, \ldots$, e.g., $C_\mu = (X_\mu, Q_\mu, \phi_\mu, i_\mu, j_\mu)$. Since each particle belongs to a unique cell, we define μ_i as the index of the cell that particle i belongs to.
- *System.* At each point in time, the system Σ is specified by the number of cells n (implying $2n$ particles) and the configurations of all particles $P_1, \ldots, P_{2n}$ and cells $C_1, \ldots, C_n$,
$$\Sigma = (n, x_\mathrm{W}, v_\mathrm{W}; P_1, \ldots, P_{2n}; C_1, \ldots, C_n)\ . \tag{5.3}$$
Moreover, it depends on the position x_W and speed v_W of a movable wall representing a tissue boundary that we introduce in Sec. 5.1.4.

For any pair of particles (P_i, P_j), we define the following coordinates (Fig. 5.1),

$$\begin{aligned}
\mathbf{x}_{ij} &= \mathbf{x}_i - \mathbf{x}_j\ ,\\
x_{ij} &= |\mathbf{x}_{ij}|\ ,\\
\mathbf{e}_{ij} &= \mathbf{x}_{ij}/x_{ij}\ ,\\
\mathbf{c}_{ij} &= (\mathbf{x}_i + \mathbf{x}_j)/2\ ,\\
\mathbf{v}_{ij} &= \mathbf{v}_i - \mathbf{v}_j\ .
\end{aligned} \tag{5.4}$$

For each cell C_μ, we define the center of mass $\mathbf{q}_\mu$ and the cell size s_μ by

$$\begin{aligned}
\mathbf{q}_\mu &= (\mathbf{x}_{i_\mu} + \mathbf{x}_{j_\mu})/2\ ,\\
s_\mu &= |\mathbf{x}_{i_\mu} - \mathbf{x}_{j_\mu}|\ ,
\end{aligned} \tag{5.5}$$

where i_μ and j_μ are indices of the two particles that belong to cell μ.

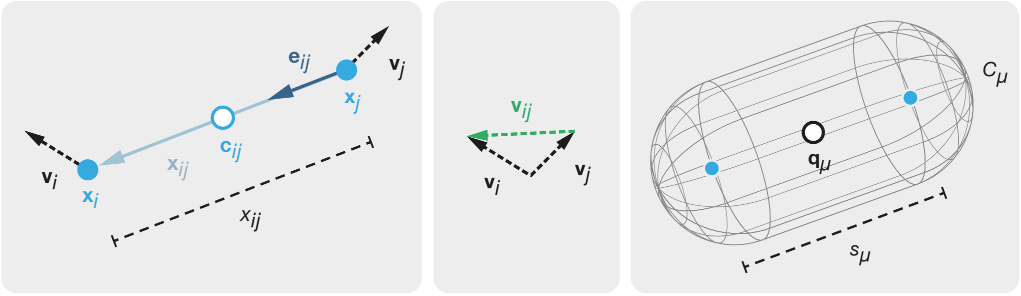

PARTICLE COORDINATES VELOCITIES CELL COORDINATES

Figure 5.1 Schematic depiction of particle and cell coordinates introduced in Eqs. (5.4) and (5.5). We graphically represent cells as tubes with spherical caps around the corresponding pair of particles. The radius of the tube is determined by the typical distance of particles in the tissue due to interparticle interactions, see also Figs. 5.4 and 5.5.

5.1.2—Equations of motion

The time evolution of the particles is governed by Newtonian mechanics: the coordinates of particle i evolve according to

$$\begin{aligned} \frac{\mathrm{d}\mathbf{x}_i}{\mathrm{d}t} &= \mathbf{v}_i \ , \\ \frac{\mathrm{d}\mathbf{v}_i}{\mathrm{d}t} &= \frac{\mathbf{F}_i}{m} \ , \end{aligned} \tag{5.6}$$

where m is the mass of a particle. The total force acting on a particle is the sum of three types of forces: a conservative force F^{C}, a dissipative force F^{D}, and a random force F^{R}, specified in the next section. All interparticle forces on particle i act in the direction $\mathbf{e}_{ij}$, Eq. (5.4), and are symmetric in i and j,

$$\mathbf{F}_i = \sum_{j \neq i} (F_{ij}^{\mathrm{C}} + F_{ij}^{\mathrm{D}} + F_{ij}^{\mathrm{R}})\, \mathbf{e}_{ij} \ . \tag{5.7}$$

5.1.3—Interparticle forces

All particles are subject to three types of interparticle forces: conservative, dissipative, and random forces, specified in the following.

- *Conservative forces.* The conservative forces between particles cause cells to grow to a certain preferred cell size and ensure volume exclusion and adhesion [16]. The conservative force between two particles i and j belonging to the same cell ($\mu_i = \mu_j$) is given by

  $$F_{ij}^{\mathrm{C}} = f_0 \left(\mathrm{e}^{-(x_{ij} - \rho_0)/\rho} - 1 \right) \ , \tag{5.8}$$

  where the length scale ρ determines the range of the force and ρ_0 is the preferred cell size as $F_{ij}^{\mathrm{C}} = 0$ for $x_{ij} = \rho_0$ (Fig. 5.2A).

  The conservative force between two particles i and j belonging to different cells ($\mu_i \neq \mu_j$) is given by

  $$F_{ij}^{\mathrm{C}} = \left[f_{ij}^{\mathrm{R}} \left(\frac{\rho^5}{x_{ij}^5} - 1 \right) - f_{ij}^{\mathrm{A}} \right] \mathbb{1}_{x_{ij} < \rho} \ , \tag{5.9}$$

  see Fig. 5.2B. The coefficients f_{ij}^{R} and f_{ij}^{A} determine the strength of the interparticle repulsive and attractive forces, respectively. These coefficients depend

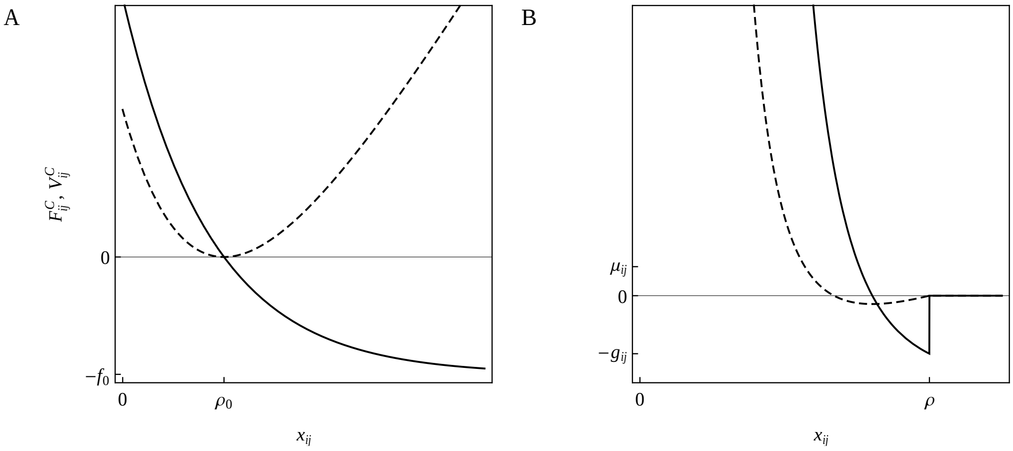

Figure 5.2 Schematic depiction of the forces $F^{\mathrm{C}}_{ij}(x_{ij})$ (solid) and corresponding potentials $V^{\mathrm{C}}_{ij}(x_{ij})$ (dashed) between particles i and j belonging to the same cell (A), Eq. (5.8), and particles belonging to different cells (B), Eq. (5.9). Forces and potentials are related by $F^{\mathrm{C}}_{ij}(x) = -\mathrm{d}V^{\mathrm{C}}_{ij}(x)/\mathrm{d}x$.

on the cell types involved in the interaction in order to describe different cell types with different mechanical properties. The force (5.9) is zero whenever particles are sufficiently far away, $x_{ij} > \rho$, or at the stable equilibrium point, $x_{ij} = \rho/(1+f^{\mathrm{A}}_{ij}/f^{\mathrm{R}}_{ij})^{1/5}$, where repulsive and adhesive forces balance (Fig. 5.2B). The coefficients f^{R}_{ij} and f^{A}_{ij} are parametrized in the following way. We specify reference strengths f^{R}_0 and f^{A}_0 and scale them by dimensionless numbers Z^{R}_{ij} and Z^{A}_{ij},

$$f^{\mathrm{R}}_{ij} = f^{\mathrm{R}}_0 Z^{\mathrm{R}}_{ij} \ , \tag{5.10}$$

$$f^{\mathrm{A}}_{ij} = f^{\mathrm{A}}_0 Z^{\mathrm{A}}_{ij} \ . \tag{5.11}$$

To reduce the number of parameters, we set $Z^{\mathrm{R}}_{ij} = Z^{\mathrm{A}}_{ij} = 1$ unless one of the following cases applies:

(1) particles i and j both belong to RST cells *or* both belong to CDL cells,

(2) one of particles i and j belongs to a CDL cell and one belongs to a RST cell,

(3) one of particles i and j belongs to a MSC cell and one belongs to either a CDL cell or a RST cell

In such a case, $Z^{\mathrm{R}}_{ij} = z^{\mathrm{R}}_c$ and $Z^{\mathrm{A}}_{ij} = z^{\mathrm{A}}_c$, where $c = 1, 2, 3$ denotes the corresponding case number. In summary, the conservative forces for particles belonging to different cells are specified by the parameters f^{R}_0, f^{A}_0, z^{R}_1, z^{R}_2, z^{R}_3, z^{A}_1, z^{A}_2, and z^{A}_3.

We typically choose these parameters such that cells of the RST and CDL type repel each other, while all other cell types tend to adhere. As will be shown later, this choice of parameters makes it possible that clusters of cells segregate from the tissue and can therefore be identified with formed segments.

- *Dissipative force.* The dissipative force describes cell–cell friction [114]. The dissipative force between two particles i and j is given by

  $$F_{ij}^{\mathrm{D}} = -\Lambda(x_{ij})^2(\mathbf{v}_{ij} \cdot \mathbf{e}_{ij}) \times \begin{cases} \tilde{\gamma} & \mu_i = \mu_j \\ \gamma & \mu_i \neq \mu_i \end{cases} , \tag{5.12}$$

  where γ and $\tilde{\gamma}$ are intercellular and intracellular dissipation constants, respectively, and

  $$\Lambda(x) = \left(1 - \frac{x}{\rho}\right) \mathbb{1}_{x \leq \rho} \ . \tag{5.13}$$

  is a function that linearly interpolates between $\Lambda|_{x=0} = 1$ and $\Lambda|_{x=\rho} = 0$ and satisfies $\Lambda|_{x>\rho} = 0$ [99]. Here, $\mathbb{1}_{a<b} = \Theta(b-a)$ is an indicator function equivalent to the Heaviside Theta function Θ.

- *Random force.* The random force mimics motility forces from the cytoskeleton [16]. The random force between two particles i and j is given by

  $$F_{ij}^{\mathrm{R}} = \sqrt{2\gamma\vartheta}\,\Lambda(x_{ij})\xi_{ij} \ , \tag{5.14}$$

  where ϑ is an effective temperature and ξ_{ij} is additive Gaussian white noise satisfying the relations $\langle \xi_{ij}(t) \rangle = 0$ and $\langle \xi_{ij}(t)\xi_{kl}(t') \rangle = (\delta_{ik}\delta_{jl} + \delta_{il}\delta_{jk})\delta(t-t')$. Moreover, ξ_{ij} is symmetric, $\xi_{ij} = \xi_{ji}$, to ensure momentum conservation [99]. The relation between the functional forms of the dissipative and random forces, Eqs. (5.12) and (5.14), is motivated by the fluctuation–dissipation theorem [42].

5.1.4— Boundary forces

To direct the growth of the tissue, we confine it to a cuboid bounding box with edge lengths b_1, b_2, and b_3. We here define the 1-direction as the direction of the body axis (see also Fig. 3.1A). Hence, we choose the length b_1 of the bounding box to be much larger than the width b_2 and the height b_3, which determine the extension of the growing tissue in the transversal directions. We define the positive 1-direction as the posterior direction and the negative 1-direction as the anterior direction. The walls of the bounding box have infinite mass and interact with particles through a smooth but steep wall potential which exerts a force

$$F_{\mathrm{W}}(x) = \frac{f_{\mathrm{W}}}{\mathrm{e}^{x/\rho_{\mathrm{W}}} - 1} \tag{5.15}$$

on the particles, where f_{W} is a force scale, ρ_{W} is a length scale that sets the steepness of the wall potential, and x is the distance from the wall in perpendicular direction. The simulation starts by placing a single cell near one end of the cuboid bounding box (Fig. 5.4). From this cell, a tissue grows by cell division (see next section). Growth proceeds isotropically until the tissue hits the walls of the bounding box in 2- and 3-direction. Subsequently, the tissue can only grow in positive 1-direction (Fig. 5.4). In this way, the initial condition breaks the directional symmetry.

To ensure that the tissue remains confined to the anterior part of the bounding box, we put a movable two-dimensional wall inside the box that has to be pushed in posterior direction by the outgrowing tissue (Fig. 5.4). This mimics the effects of the tissues that surround and confine the cells of the presomitic mesoderm. The state of the wall is characterized by its position x_{W} and velocity v_{W} in 1-direction. The wall has a mass m_{W} and its motion is damped by friction with friction coefficient

γ_{W}. The wall interacts with particles through the same force as the bounding box, Eq. (5.15). Hence, the equations of motion for the wall are given by

$$\frac{\mathrm{d}x_{\mathrm{W}}}{\mathrm{d}t} = v_{\mathrm{W}} \ , \tag{5.16}$$

$$\frac{\mathrm{d}v_{\mathrm{W}}}{\mathrm{d}t} = -\gamma_{\mathrm{W}} v_{\mathrm{W}} + \sum_i F_{\mathrm{W}}(|x_i^1 - x_{\mathrm{W}}|) \ , \tag{5.17}$$

where the sum runs over all particles, x_i^1 is the 1-component of the position vector of particle i, and $F_{\mathrm{W}}(x)$ is the force (5.15). The position x_{W} of the wall also marks the position of the posterior tip and serves as a reference point for a restricted region in which cells divide (Sec. 5.1.5) and produce the morphogen (Sec. 5.1.6).

5.1.5— Cell division

In the model, cell division is the main mechanism of tissue growth. It occurs in a restricted outgrowth region of length x_0 adjacent to the posterior tip. A cell divides when the cell size reaches a certain threshold value. Upon cell division, two new particles are inserted in a random direction at a specific distance from the particles of the mother cell [16]. Cells inherit their cell type from their mother cell as well as their phase, which is perturbed by a random contribution upon division. The morphogen level is divided half and half between the two cells. Formally, division of a cell $C_\mu = (X_\mu, Q_\mu, \phi_\mu, i_\mu, j_\mu)$ corresponds to a discrete process[1] that takes place if (i) the cell is in the outgrowth region, $\Delta_\mu < x_0$, where

$$\Delta_\mu = |q_\mu^1 - x_{\mathrm{W}}| \tag{5.18}$$

is the distance of cell μ from the movable wall, and (ii) the cell size exceeds the division threshold, $s_\mu \geq \rho$, where the s_μ was defined in Eq. (5.5).

5.1.6— Morphogen dynamics

Morphogen production and decay takes places inside the cells. Adjacent cells can exchange morphogen, which leads to diffusion of the morphogen throughout the tissue. Morphogen production only takes place in the vicinity of the posterior tip[2], in the same region where cells divide (Sec. 5.1.5). The morphogen level Q_μ of cell μ evolves according to

$$\frac{\mathrm{d}Q_\mu}{\mathrm{d}t} = \beta_\mu + E \sum_{\nu=1}^{n} U_{\mu\nu}(Q_\nu - Q_\mu) - hQ_\mu \ . \tag{5.19}$$

The first term describes morphogen production with a production rate β_μ, which is non-vanishing only in the posterior region where cells divide,

$$\beta_\mu = \beta_0 \mathbb{1}_{\Delta_\mu < x_0} \ . \tag{5.20}$$

---

[1] Upon cell division, the system goes from the state

$$\Sigma = (n, x_{\mathrm{W}}, v_{\mathrm{W}}; P_1, \ldots, P_{i_\mu}, \ldots, P_{j_\mu}, \ldots, P_{2n}; C_1, \ldots, C_\mu, \ldots, C_n) \ ,$$

where $P_{i_\mu} = (\mathbf{x}_{i_\mu}, \mathbf{v}_{i_\mu})$ and $P_{j_\mu} = (\mathbf{x}_{j_\mu}, \mathbf{v}_{j_\mu})$, to the state

$$\Sigma' = (n+1, x_{\mathrm{W}}, v_{\mathrm{W}}; P_1, \ldots, P'_{i_\mu}, \ldots, P'_{j_\mu}, \ldots, P_{2n}, P_{2n+1}, P_{2n+2}; C_1, \ldots, C'_\mu, \ldots, C_n, C_{n+1}) \ ,$$

where

$$C'_\mu = (X_\mu, Q_\mu/2, \phi_\mu, i_\mu, 2n+1) \ , \qquad C_{n+1} = (X_\mu, Q_\mu/2, \phi_\mu + \eta^* \xi, j_\mu, 2n+2) \ ,$$

and

$$\begin{aligned} P'_{i_\mu} &= (\mathbf{x}_{i_\mu}, \mathbf{0}) \ , & P_{2n+1} &= (\mathbf{x}_\mu + \rho^* \boldsymbol{\zeta}, \mathbf{0}) \ , \\ P'_{j_\mu} &= (\mathbf{x}_{j_\mu}, \mathbf{0}) \ , & P_{2n+2} &= (\mathbf{x}_{j_\mu} + \rho^* \boldsymbol{\zeta}', \mathbf{0}) \ . \end{aligned}$$

Here, ξ is a Gaussian distributed random number and $\boldsymbol{\zeta}$ and $\boldsymbol{\zeta}'$ are unit vectors with random direction.

[2] We have used a similar prescription for the theory presented in Chapter 3, Sec. 3.5.1, see Eq. (3.48).

Here, $\mathbb{1}$ is the indicator function introduced below Eq. (5.13), Δ_μ is the distance of cell μ from the wall, defined in Eq. (5.18), and x_0 is the length of the region in which cell division takes place (Sec. 5.1.5). The second term in Eq. (5.19) describes the exchange of morphogens between adjacent cells: E is the morphogen exchange rate, and $U_{\mu\nu}$ is a time-dependent proximity matrix that depends on the distances to particles of other cells,

$$U_{\mu\nu} = \frac{1}{4}\left[\Lambda(x_{i_\mu i_\nu}) + \Lambda(x_{i_\mu j_\nu}) + \Lambda(x_{j_\mu i_\nu}) + \Lambda(x_{j_\mu j_\nu})\right] , \tag{5.21}$$

where Λ is given by Eq. (5.13) and $x_{i_\mu j_\nu}$ is the distance between the particles i_μ and j_ν of cells μ and ν (see Sec. 5.1.1 for notational conventions). Note that $U_{\mu\nu}$ takes values from 0 to 1 and satisfies $U_{\mu\nu} = U_{\nu\mu}$, which ensures conservation of mass. The third term in Eq. (5.19) describes morphogen decay with decay rate h.

5.1.7— Phase dynamics

Cells of the PSM type can exhibit genetic oscillations. The intrinsic frequency ω_μ of the cellular oscillators depends on the morphogen level of the corresponding cell μ,

$$\omega_\mu = \omega_0 Q_\mu / Q_0 , \tag{5.22}$$

where Q_0 is a reference morphogen level that is chosen to be of the same order as the maximum morphogen level that levels out at the posterior tip[3]. To describe coupling upon cell contact[4], the coupling strength to other cellular oscillators depends on their distance through the same proximity matrix as used for morphogen exchange, Eq. (5.21). To account for delays in cell-cell signaling, we also include an effective coupling delay[5] [93]. The dynamic equation for the phase of PSM type cells is given by

$$\frac{\mathrm{d}\phi_\mu}{\mathrm{d}t} = \omega_\mu + \frac{\varepsilon}{u_\mu}\sum_{\nu=1}^{n} U_{\mu\nu}\sin(\phi_{\nu,\tau} - \phi_\mu) + \eta\xi_\mu , \tag{5.23}$$

where $\phi_{\nu,\tau}(t) = \phi_\nu(t-\tau)$, $U_{\mu\nu}$ is the proximity matrix defined in Eq. (5.21), $u_\mu = \sum_\nu U_{\mu\nu}$ is a normalization factor for the coupling strength, and η is the noise strength. The Gaussian white noise term ξ_μ satisfies $\langle \xi_\mu(t) \rangle = 0$ and $\langle \xi_\mu(t)\xi_\nu(t')\rangle = \delta_{\mu\nu}\delta(t-t')$ and represents the effects of stochasticity in gene expression on the oscillatory dynamics. For cell types other than PSM, the phase is irrelevant and does not change over time, $\mathrm{d}\phi_\mu/\mathrm{d}t = 0$.

5.1.8— Cell differentiation

To describe physical segmentation of the tissue, that is, segregation of cell clusters from the presomitic mesoderm, we include a mechanism of cell differentiation that leads to a formation of segment boundaries. In our model, cell differentiation takes place when the morphogen level Q_μ of a cell μ drops below a threshold level Q^*. Hence, the position where the average morphogen level drops below Q^* marks the anterior end of the presomitic mesoderm. Differentiation of a cell $C_\mu = (X_\mu, Q_\mu, \phi_\mu, i_\mu, j_\mu)$ with cell type $X_\mu = \text{PSM}$ is a discrete process that changes the cell type according to the value ϕ_μ of the phase at the time of differentiation,

$$X_\mu \to X'_\mu = \begin{cases} \text{CDL} & 0 \le \phi_\mu < \psi_1 \\ \text{RST} & \psi_1 \le \phi_\mu < \psi_2 \\ \text{MSC} & \psi_2 \le \phi_\mu < 2\pi \end{cases} . \tag{5.24}$$

---

[3] We have used a similar prescription for the theory presented in Chapter 3, Sec. 3.5.1, see Eq. (3.53).

[4] Note that the Notch signaling pathway, which is thought to couple the oscillations in the presomitic mesoderm, requires cell contact, see Sec. 1.2.4 and Fig. 1.6.

[5] For details on the effects of coupling delays, see Chapter 2, Sec. 2.4; Chapter 3, Sec. 3.2; and Chapter 6.

Here, ψ_1 and ψ_2 are phase thresholds that determine which phase intervals give rise to which cell type.

5.2 Self-organized Segmentation

We now demonstrate with a proof-of-principle result that the cell-based model introduced here is able to describe tissue formation and extension, morphogen gradient formation, pattern formation, and segment formation. To this end, we study a realization of the system with parameters given in Table 5.1. Details on the numerical procedure are given in Appendix H. Fig. 5.3 shows global system properties as a function of time, such as the position of the movable wall, the number of cells of different cell types, the length of the presomitic mesoderm, and the average cell size. Figs. 5.4 and 5.5 show snapshots of the system at different times in a three-dimensional representation. Fig. 5.6 shows one-dimensional averaged profiles along the axial direction[6] of the cell density ϱ, the normalized morphogen level Q/Q_0, the cell speed v^1 in 1-direction, the oscillation amplitude A, and a phase order parameter Z indicating synchrony. The order parameter Z takes values between 0 and 1, where 1 indicates perfect synchrony and 0 indicates total phase dispersion [77].

5.2.1— Tissue formation and extension

The simulation starts with the movable wall being located near the anterior end of the bounding box and a single cell located inside the space confined by the wall (Fig. 5.4). A tissue is formed by ongoing cell division in the outgrowth region near the wall. As the tissue grows and fills the confined space, it exerts a pressure on the movable wall and causes it to move in posterior direction. Since cell division is restricted to a region near the movable wall, whose filling with cells is nearly constant, tissue growth is nearly linear. This behavior is illustrated by tracking the total cell number and the position x_{W} of the wall over time and finding a linear behavior after the initial transient (Figs. 5.3A,B). In a reference frame comoving with the posterior tip, the anteroposterior velocity profile of cells (Fig. 5.6) qualitatively agrees with the shape that we have considered for the continuum theory presented in Chapter 3, cf. Eq. (3.28).

---

[6] These profiles are obtained by averaging in 2- and 3-direction. To obtain smooth profiles, contributions of different cells were weighted by a Gaussian $f(x) = (2\pi c^2)^{-1/2} \mathrm{e}^{-x^2/2c^2}$ with variance $c = \rho/2$, centered around a position x^1 on the 1-axis. The profiles of the different observables are given by

$$\varrho(x^1) = \sum_\mu f(q^1_\mu - x^1) \ , \qquad \text{cell density} \qquad (5.25)$$

$$Q(x^1) = \frac{1}{\varrho(x^1)} \sum_\mu f(q^1_\mu - x^1)\, Q_\mu \ , \qquad \text{morphogen level} \qquad (5.26)$$

$$v^1(x^1) = \frac{1}{\varrho(x^1)} \sum_\mu f(q^1_\mu - x^1)\, v^1_\mu \ , \qquad \text{velocity in 1-direction} \qquad (5.27)$$

$$A(x^1) = \frac{1}{\varrho(x^1)} \sum_\mu f(q^1_\mu - x^1) \sin\phi_\mu \ , \qquad \text{oscillation amplitude} \qquad (5.28)$$

$$Z(x^1) = \frac{1}{\varrho(x^1)} \left| \sum_\mu f(q^1_\mu - x^1)\, \mathrm{e}^{\mathrm{i}\phi_\mu} \right| . \qquad \text{phase order parameter} \qquad (5.29)$$

Here, q^1_μ is the 1-component of the center of mass of cell μ as defined in Eq. (5.5).

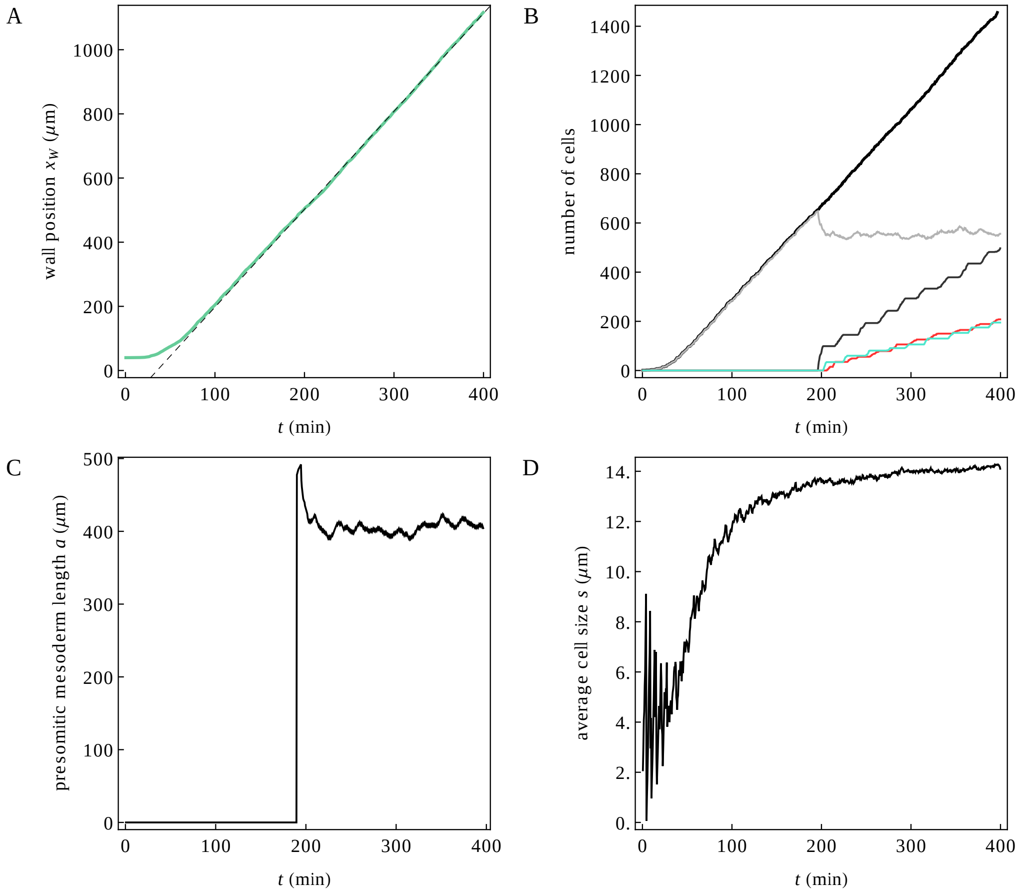

Figure 5.3 Global system properties as a function of time for a realization with parameter given in Table 5.1. **A.** Position x_{W} of the movable wall as a function of time (green) and linear fit (black dashed). **B.** Number of cells of different cell types in the system as a function of time: PSM (light gray), MSC (dark gray), CDL (cyan), RST (red), and total number of cells (black thick). **C.** Length a of the presomitic mesoderm, Eq. (5.30), as a function of time. **D.** Average cell size s as a function of time.

5.2.2— Formation of a morphogen gradient and the presomitic mesoderm

As the tissue grows, the morphogen is produced in the same region where cells divide (Figs. 5.5 and 5.6). Due to diffusion and decay in the tissue, a robust morphogen gradient emerges that decays in anterior direction. Since cells of the PSM type are only found in the region where $Q > Q^*$, we characterize this region as the presomitic mesoderm. At each time point, the length of the presomitic mesoderm is accordingly given by

$$a = \max_{x^1}\{x_{\mathrm{W}} - x^1 \; ; \; Q(x^1) \geq Q^*\} \; . \qquad (5.30)$$

After an initial transient, during which the tissue grows and builds up the morphogen gradient, a presomitic mesoderm of roughly constant length evolves (Fig. 5.3C).

5.2.3— Formation of kinematic waves

Since the frequency of oscillations in the cells is proportional to the morphogen concentration, the emerging morphogen gradient corresponds to a frequency gradient[7]. This frequency gradient leads to the formation of kinematic waves in the tissue

---

[7] This is the same mechanism that we have already invoked in the continuum theory of interacting morphogens and oscillators, presented in Chapter 3, Sec. 3.5.

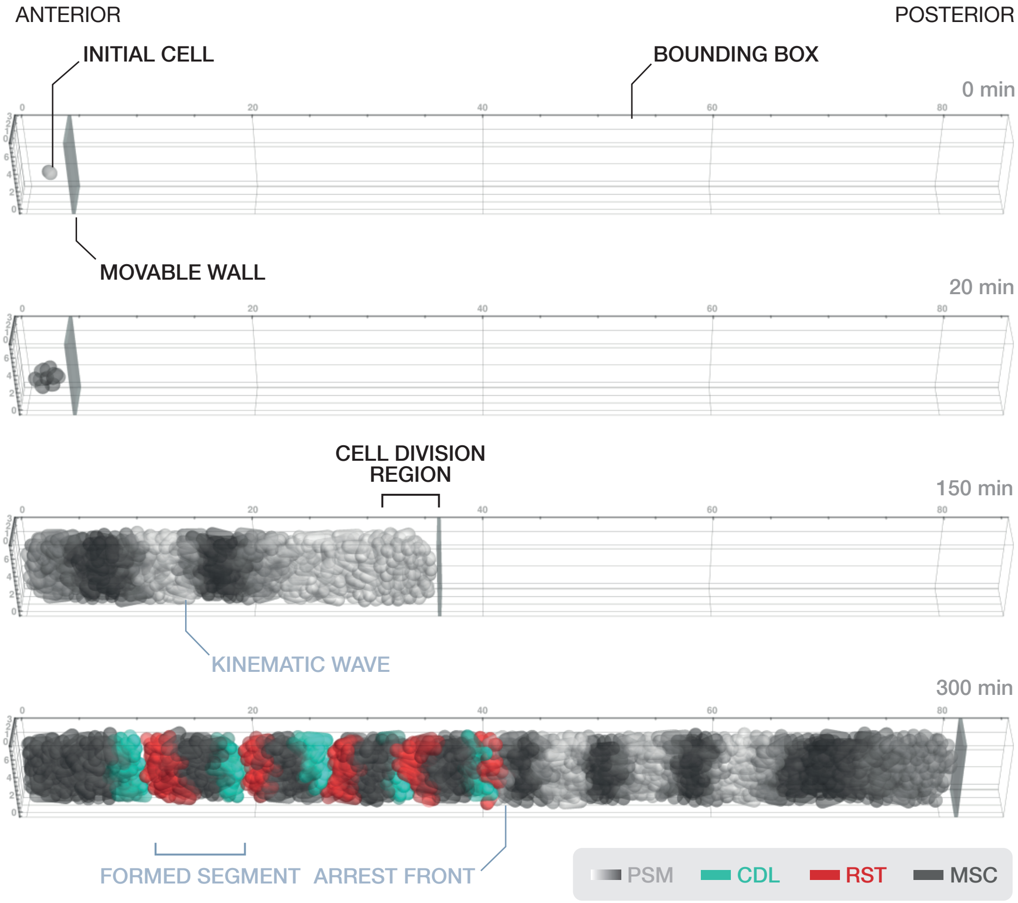

Figure 5.4 Snapshots of a simulation at different points in time. Cell types are color coded (see legend). For cells of the PSM type, the brightness indicates the sine of the cell's phase. Black labels indicate model specifications, blue labels indicate phenomena that emerge from the model dynamics. Parameters are given in Table 5.1.

by the same pattern forming mechanism introduced in Chapter 3, Sec. 3.1. In the presomitic mesoderm, the coupling of oscillations in neighboring cells tends to even out phase differences and thus promotes the formation of a coherent pattern that is robust against frequency noise and random cell movement[8]. This is reflected in the behavior of the phase order parameter Z, showing a large degree of phase coherence in the presomitic mesoderm (Fig. 5.6).

5.2.4— Segment formation

The morphogen level decays in anterior direction and, when the tissue has extended sufficiently, falls below the threshold for cell differentiation. Cells differentiate into different cell types according to their phase at this arrest front (Fig. 5.4). The formation of a kinematic wave pattern with a fairly smooth phase profile thus implies that the three cell types RST, MSC, and CDL follow each other in the order determined in Sec. 5.1.8, thereby forming a segment. Due to the lack of adhesion between the rostral (RST) and caudal (CDL) cell types, an intersegmental furrow (apparent in Fig. 5.4) forms when these two cell types immediately follow each other. A signa-

---

[8] In fact, is has been shown that random cell movement in the posterior presomitic mesoderm can promote phase coherence as it effectively increases the coupling range [148].

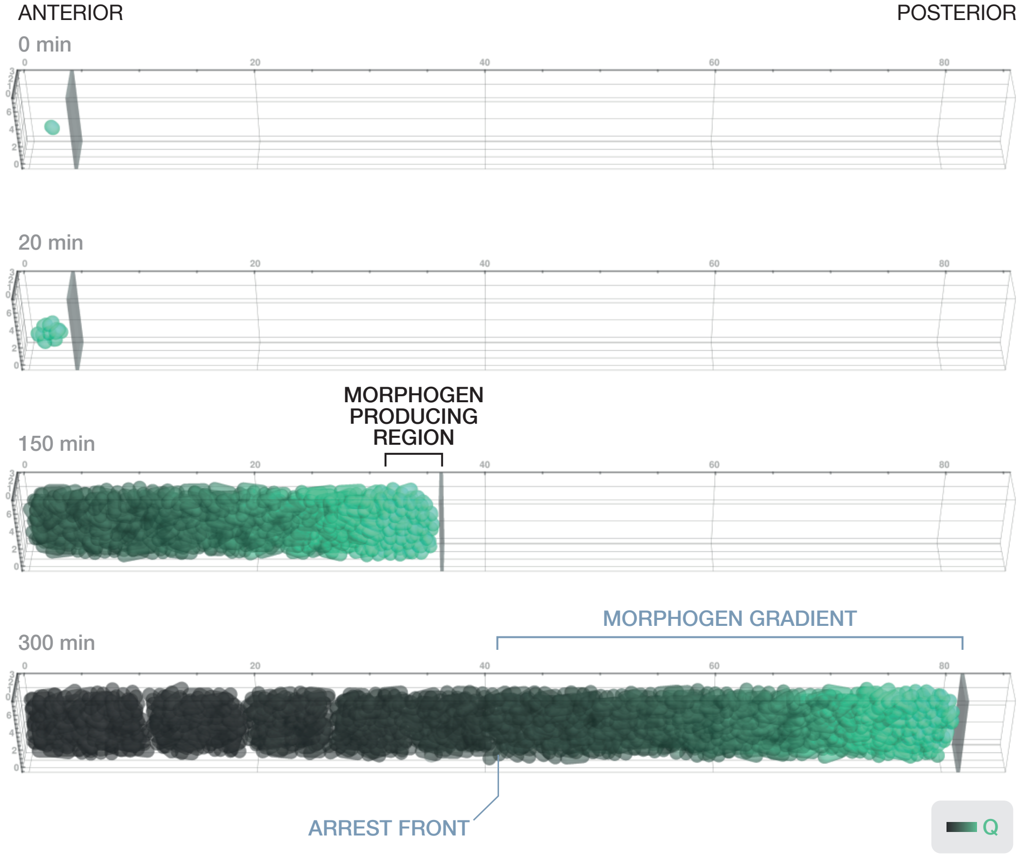

Figure 5.5 Snapshots of the same simulation as in Fig. 5.4, illustrating the formation of the morphogen gradient. Brightness indicates the relative morphogen concentration Q/Q_0.

ture of this furrow is the decreased cell density ϱ between the formed segments (see Fig. 5.6 at 300 min). The timing of segment formation can be studied by tracking the global number of cells of different cell types. Whenever a new segment is formed, the number of segment boundary cells (RST and CDL) increases during a short period of time after which it remains constant (Fig. 5.3B).

5.3 Summary

In this chapter, we have introduced a cell-based model of segmentation based on local rules of cell mechanics, cell differentiation, morphogen dynamics, and oscillator dynamics. To this end, we have modified a tissue model based on dissipative particle dynamics [16] and extended it with phase oscillator dynamics, the dynamics of morphogen production, exchange, and decay, and cell differentiation. Previous cell-based models of vertebrate segmentation have involved computationally intensive multi-scale 2D models with a multitude of parameters [57] and 3D models which represent the underlying tissue as a rigid cubic lattice [139]. In contrast, our model describes the cells of the presomitic mesoderm and the formed segments as mechanical entities in three dimensions, while keeping the number of parameters at a manageable level.

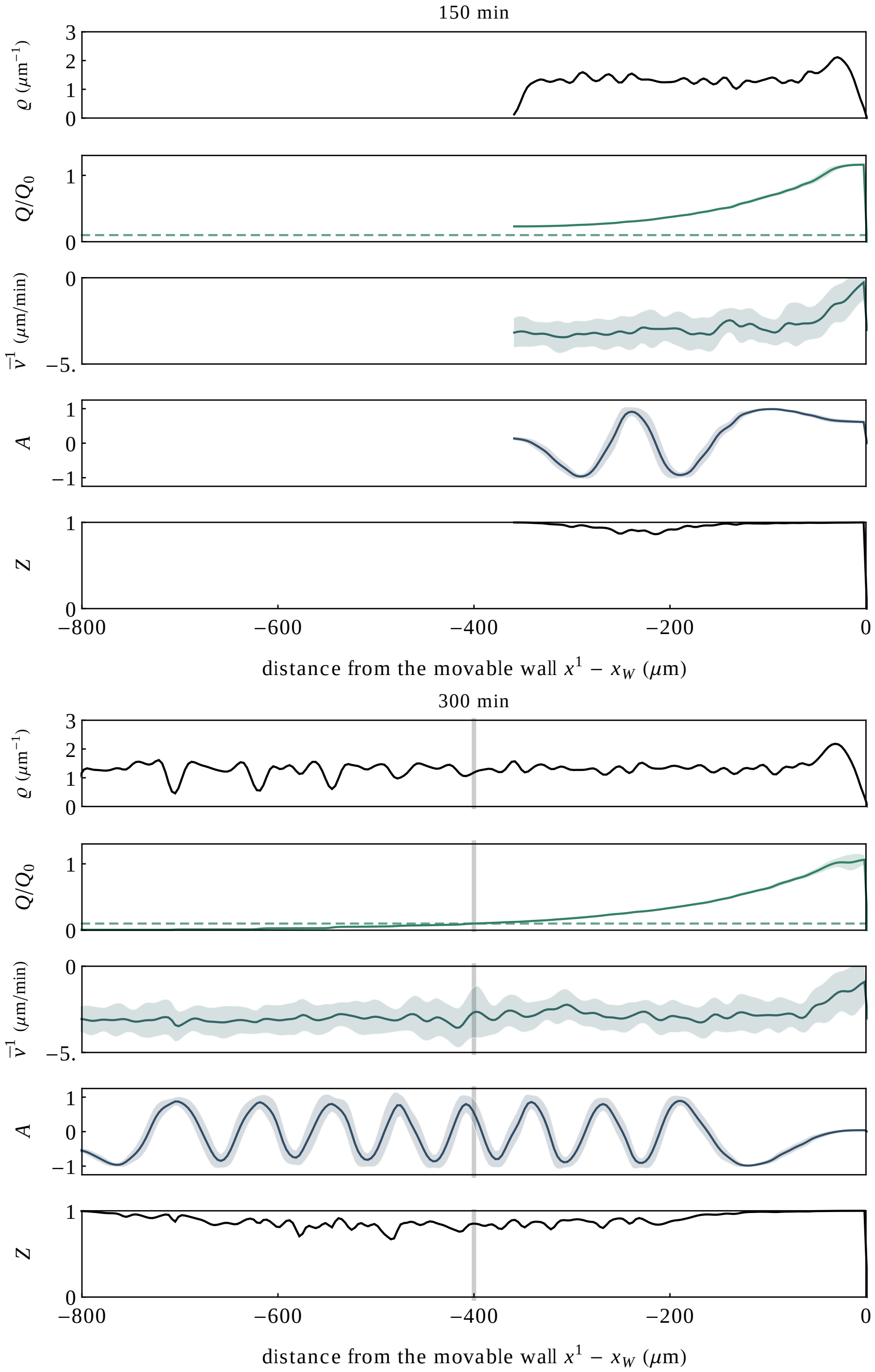

Figure 5.6 One-dimensional profiles of observables, Eqs. (5.25–5.29), in the reference frame comoving with the wall at 150 min and 300 min (corresponding snapshots also shown in Figs. 5.4 and 5.5). The x-axis indicates the distance from the movable wall in 1-direction. The plots show the cell density ϱ, the relative morphogen level Q/Q_0, the speed in 1-direction relative to the wall, $\bar{v}_1 = v_1 - \dot{x}_{\mathrm{W}}$, the oscillation amplitude A, and the order parameter Z. The shaded areas indicate the standard deviation. The horizontal dashed line indicates the threshold concentration Q^*/Q_0 for cell differentiation. The vertical gray line indicates the position a of the anterior end of the presomitic mesoderm, Eq. (5.30). Parameters are given in Table 5.1.

We have shown with an example that this cell-based model is able to describe tissue formation and extension, morphogen gradient formation, pattern formation, and segment formation in a self-organized way. While we here illustrated the phenomenology of the model with a specific example, systematic investigations of the model can be carried out by statistical analysis of different noise realizations of the model trajectories. Taking into account the interplay of biochemical and mechanical mechanisms [61], our model provides a starting point for the theoretical description of pattern formation and tissue dynamics during vertebrate segmentation in a unified framework. It complements the continuum theories of vertebrate segmentation introduced in the previous chapters, which describe pattern formation on a coarse-grained level. In going beyond such a coarse-grained description, the cell-based model presented here enables to address, e.g., the interplay of random cell movement and oscillator synchronization, the sharpness of segment boundaries depending on the noise in both the oscillator dynamics and the cell dynamics, and the interplay of time scales of oscillations, morphogen production, and tissue extension. Moreover, this cell-based model can easily be extended to include other types of tissue growth such as inflow of cells and convergence-extension. Hence, it permits to study the compatibility of these growth mechanisms and tissue reorganization by convergence-extension cell movements with the mechanism of pattern formation through a frequency gradient.

Parameters and Symbols used in Chapter 5

PARAMETER	UNIT	VALUE	
			CELL MECHANICS
f_0	PL^2	0.7	growth coefficient
ρ_0	L	1.4	typical cell size
ρ	L	1.2	range of pair potentials / threshold for division
$\tilde{\gamma}$	PLT	10.0	intracellular dissipation constant
γ	PLT	5.0	intercellular dissipation constant
ρ^*	L	1.2×10^{-5}	distance at which new particles are inserted
ϑ	PL^3	5.0×10^{-3}	effective temperature
f_0^{R}	PL^2	0.1	repulsive cell–cell potential coefficient
f_0^{A}	PL^2	0.2	attractive cell–cell potential coefficient
m	PLT^2	0.33	particle mass
$z_1^{\mathrm{R}}, z_2^{\mathrm{R}}, z_3^{\mathrm{R}}$	1	1.0, 5.0, 1.0	coefficients determining repulsive forces
$z_1^{\mathrm{A}}, z_2^{\mathrm{A}}, z_3^{\mathrm{A}}$	1	1.5, 0.0, 1.5	coefficients determining adhesive forces
x_0	L	4	length of outgrowth region
			MORPHOGEN DYNAMICS
β_0	NT^{-1}	0.2	morphogen production rate
E	T^{-1}	5	morphogen exchange rate
h	T^{-1}	0.03	morphogen decay rate
Q^*	N	0.15	threshold level for cell differentiation
Q_0	N	1.5	morphogen reference level
			OSCILLATOR DYNAMICS
ω_0	T^{-1}	0.22	maximum autonomous oscillator frequency
ε	T^{-1}	0.07	oscillator coupling strength
τ	T	21	coupling delay
η	T^{-1}	0	noise intensity
η^*	1	0	noise intensity upon cell division
ψ_1	1	$\pi/2$	phase threshold for cell differentiation
ψ_2	1	π	phase threshold for cell differentiation
			WALL AND BOUNDING BOX PROPERTIES
b_1, b_2, b_3	L	200, 2.5, 7	size of the bounding box
γ_{W}	PLT	1	friction coefficient
m_{W}	PLT^2	0.1	mass of the wall
ρ_{W}	L	0.3	repulsion range of the wall
f_{W}	PL^2	0.3	repulsion strength of the wall
			SIMULATION SPECIFICATIONS
Δt	T	0.006	integration time step

Table 5.1 List of parameters and typical values used in this chapter. The physical units are $T = 1\,\mathrm{min}$, $L = 10\,\mu\mathrm{m}$, and $P = 1\,\mathrm{kPa}$ [16].

LIST OF SYMBOLS

$\mu, \nu, \ldots$	cell index
$i, j, \ldots$	particle indices
μ_i	index of the cell that particle i belongs to
Σ	state of the system
C_μ	state of cell μ
P_i	state of particle i
$\mathbf{x}_i = (x_i^1, x_i^2, x_i^3)$	position vector of particle i
$\mathbf{v}_i = (v_i^1, v_i^2, v_i^3)$	velocity vector of particle i
$\mathbf{x}_{ij}$	distance vector between particles i and j
x_{ij}	distance between particles i and j
$\mathbf{e}_{ij}$	unit vector in direction of $\mathbf{x}_{ij}$
$\mathbf{c}_{ij}$	center of mass of particles i and j
$\mathbf{v}_{ij}$	velocity difference vector between particles i and j
$\mathbf{q}_\mu$	center of mass of cell μ
s_μ	size of cell μ
X_μ	cell type of cell μ
Q_μ	morphogen level of cell μ
Q_{ij}	average morphogen level of particles i and j
ϕ_μ	phase of cell μ
i_μ, j_μ	indices of particles belonging to cell μ
x_W	position of the movable wall
v_W	velocity of the movable wall
$\mathbf{F}_i$	net force on particle i
F_{ij}^C	conservative forces between particles i and j
F_{ij}^D	dissipative forces between particles i and j
F_{ij}^R	random forces between particles i and j
Λ	cutoff function specifing the range of forces
ξ_{ij}	Gaussian white noise
F_W	force that boundary walls exert on particles
Δ_μ	distance of cell μ to the movable wall
β_μ	morphogen production rate of cell μ
$U_{\mu\nu}$	proximity of cells μ and ν
u_μ	normalization factor for the coupling strength
ω_μ	intrinsic frequency of the oscillator of cell μ
f	Gaussian distribution
a	position of the arrest front
$\mathbb{1}$	indicator function, equivalent to the Heaviside Theta function, $\mathbb{1}_{x>y} = \Theta(x-y)$

Chapter 6

Regulation of Synchronization by Coupling Delays and Phase Shifts

In this chapter, we investigate the synchronization dynamics of a generic assembly of coupled oscillators in the presence of coupling delays and phase shifts. We show that while phase shifts and coupling delays have equivalent effects on the collective frequency of the synchronized state, they can have profoundly different effects on the synchronization dynamics.

6.1 Coupled Oscillators with Delays and Phase Shifts

6.1.1—
Synchronization dynamics depends on coupling properties

In the previous chapters, we investigated systems of coupled genetic oscillators, with and without noise, in small and large assemblies, in static and dynamic media, and with moving oscillators and oscillators at rest. Despite these differences, these systems share generic properties with each other as well as with other coupled oscillator systems. This is reflected by the fact that synchronization phenomena of very different nature can be described by the same class of phase oscillator models, introduced by Kuramoto [1, 77]. Earlier in this thesis, we have demonstrated that such phase oscillator models are capable of describing the collective frequency and the modes of synchrony of a nonlinear stochastic system of coupled genetic oscillators (Chapter 2). Moreover, we found that continuum limits of coupled phase oscillators are viable theories to describe pattern formation during vertebrate segmentation (Chapters 3 and 4). All these systems had in common that the properties of oscillator coupling such as time delays had profound impact on the oscillator dynamics (Secs. 2.4 and 3.2). Motivated by these observations, we here address the question of how synchronization dynamics of generic systems of coupled phase oscillators depend on the properties of the coupling.

6.1.2—
Complex signaling induces coupling delays and phase shifts

In general, if the processes involved in signaling take a time τ comparable to the oscillation cycle, they introduce a delay in the coupling that can play a significant role for the dynamics of the system [5, 38, 93, 129, 163]. They can lead to multistability of several synchronized states with different collective frequencies [38, 163], see also Chapter 2, Sec. 2.4. While coupling delays are often regarded as undesired features which inevitably arise from the slow dynamics of the system's constituents, constructive roles of delays on the synchronization dynamics have been reported [33, 120].

In addition to coupling delays, there are several ways how the receiving oscillator can internally coordinate its response to the received signal. It may tend to minimize or maximize the phase difference to the received signal, or to keep it at a constant

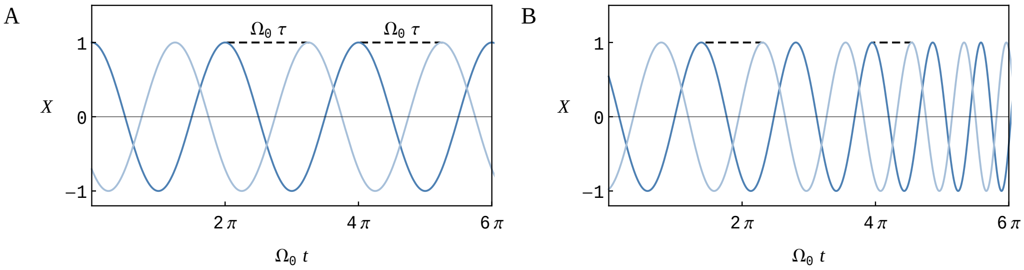

Figure 6.1 **A.** For an oscillatory signal with a constant frequency, $X(t) = \cos\phi(t)$ with $\phi(t) = \Omega_0 t$ (dark blue), the delayed signal $X(t-\tau)$ (light blue), is equivalent to a phase-shifted signal, $X(t-\tau) = \cos(\phi(t) - \alpha)$ with $\alpha = \Omega_0\tau$. The dashed black lines indicate the phase shift $\Omega_0\tau$ between the instantaneous and the delayed signal. **B.** For an oscillatory signal with varying frequency, the relation between $X(t)$ and $X(t-\tau)$ cannot be characterized by a single phase shift as the same phase shift occurs in different time intervals (dashed lines).

value α. In phase oscillator models, a simple way to account for these differences in coupling mechanisms is a phase shift α in a generic coupling function. It provides a rigid offset to the received phase signal that alters the coupling behavior. Depending on the phase shift α, coupling between oscillators may thus be attractive or repulsive.

Intuitively, it is clear that in a synchronized state, where all oscillators evolve with a collective frequency Ω_0, a transmission delay τ between the oscillators renders the delayed signal indistinguishable from a signal that has been phase-shifted by $\alpha = \Omega_0\tau$ (Fig. 6.1A). However, away from such a perfectly synchronized state, coupled oscillator systems usually exhibit transient periods during which the frequency is not constant. In such a case, the simple equivalence between delays and phase shifts breaks down (Fig. 6.1B). We are thus led to the question whether the dynamics of the system in the vicinity of the synchronized state is indeed similar if coupling delays are substituted by phase shifts.

In the remainder of this chapter, we will investigate the synchronization dynamics of coupled oscillator systems in the presence of phase shifts and coupling delays using a generic theory of coupled phase oscillators. Since we obtain exact results for the linearized dynamics of the system, this chapter is of a more technical nature than the previous ones.

6.1.3— Phase oscillator description

The phase dynamics for a network of coupled identical phase oscillators in the presence of a discrete coupling delay τ and a phase shift α is given by [121, 163]

$$\frac{\mathrm{d}}{\mathrm{d}t}\phi_\mu(t) = \omega + \frac{\varepsilon}{u_\mu}\sum_{\nu=1}^{n} c_{\mu\nu}\, g(\phi_\nu(t-\tau) - \phi_\mu(t) - \alpha)\ . \tag{6.1}$$

Here, ϕ_μ is the phase of oscillator μ, ω is the intrinsic frequency of the oscillators, ε is the coupling strength, and n is the total number of oscillators. Oscillator coupling is described by the 2π-periodic coupling function g. The coupling topology is defined by the adjacency matrix $c_{\mu\nu}$ with $c_{\mu\nu} \geq 0$, where $c_{\mu\nu} \neq 0$ indicates a link between oscillators μ and ν. The coupling strength is normalized by the total weight of links of oscillator μ, given by $u_\mu = \sum_\nu c_{\mu\nu}$. For the generic case $g(\varphi) = \sin\varphi$, a vanishing phase shift ($\alpha = 0$) corresponds to an attractive coupling that tends to minimize the phase difference between coupled oscillators in the absence of coupling delays, whereas $\alpha = \pi$ corresponds to a repulsive coupling that tends to maximize it. In such a case, the phase shift α can be considered as interpolating between attractive and repulsive coupling.

The system Eq. (6.1) can exhibit an in-phase synchronized state[1],

$$\phi_\mu(t) = \Omega t \ , \tag{6.2}$$

in which all oscillators evolve with the same collective frequency Ω. Using Eq. (6.2) in the dynamic equation (6.1), we find that the collective frequency Ω obeys[2] [129, 163]

$$\Omega = \omega + \varepsilon g(-\Omega\tau - \alpha) \tag{6.3}$$

and thus depends on τ and α. For non-vanishing delays, multiple synchronized states with different collective frequencies can coexist [163] (see Chapter 2, Sec. 2.4.3, Fig. 2.16B for the case $g(\varphi) = \sin\varphi$ and $\alpha = 0$).

6.1.4—Equivalence of delays and phase shifts in the synchronized state

Intuitively, in a synchronized state with a well-defined constant frequency Ω_0, a coupling delay τ induces an effective phase shift $\Omega_0\tau$ in the signal transmitted between oscillators that is indistinguishable from a rigid phase shift $\alpha = \Omega_0\tau$. This is reflected by the fact that the collective frequency, Eq. (6.3), only depends on the sum $\Omega\tau + \alpha$. Hence, the existence of an in-phase synchronized solution with collective frequency $\Omega = \Omega_0$ is preserved under the transformation

$$\begin{aligned} &\tau \to \tau' \ , \\ &\alpha \to \alpha + \Omega_0(\tau - \tau') \end{aligned} \tag{6.4}$$

for arbitrary $\tau' > 0$. For a fixed value of $\Delta \equiv \Omega_0\tau + \alpha$, we thus find a one-parameter family of systems in the (τ, α)-plane that can exhibit the same in-phase synchronized state with collective frequency

$$\Omega_0 = \omega + \varepsilon g(-\Delta) \ . \tag{6.5}$$

We parametrize these systems by letting the phase shift α be a function of the coupling delay according to

$$\alpha(\tau) = \Delta - \Omega_0\tau \ , \tag{6.6}$$

where Δ is chosen to fix the collective frequency according to Eq. (6.5). While the collective frequency does not change under the transformation (6.4), we will show that the synchronization dynamics, that is, the dynamics of the system in the vicinity of the synchronized state, does change. To this end, we linearize the dynamics in the vicinity of the synchronized state and determine the relaxation rate r_0 of small perturbations for the class of systems parametrized by Eq. (6.6). Since r_0 determines the rate at which the system converges towards the synchronized state, we call it the synchronization rate. A precise definition of r_0 will be given in Sec. 6.3. Before performing a general analysis of the synchronization rate, we introduce two motivating examples that will guide our analysis.

---

[1] This ansatz has already been used in Chapter 2, Eq. (2.56).

[2] Note that the earlier encountered equations for the collective frequency of delay-coupled phase oscillators, Eqs. (2.60) and (3.24), are special cases of Eq. (6.3) for $g(\varphi) = \sin\varphi$ and $\alpha = 0$.

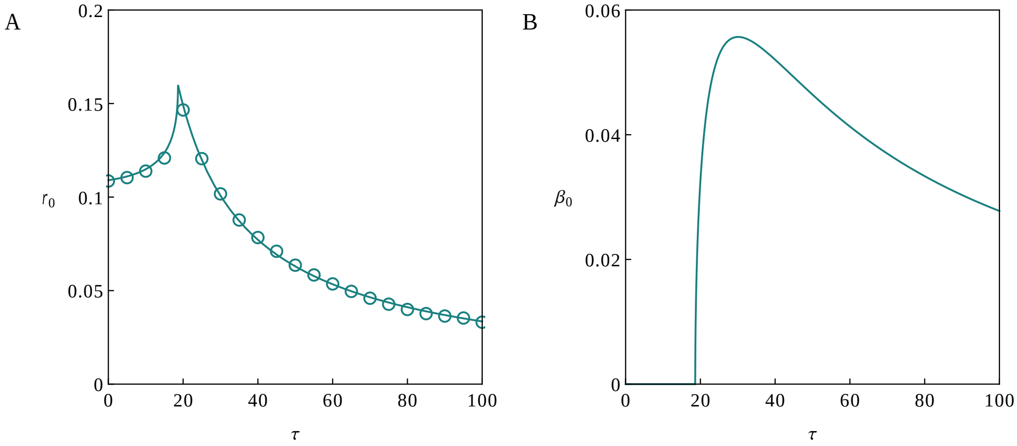

Figure 6.2 **A.** Synchronization rate r_0 as a function of the coupling delay τ for a globally coupled system, obtained from numerical simulations of Eqs. (6.1) and (6.6) (circles) and from Eq. (6.15) (line) for a globally coupled system with $g(\varphi) = \sin\varphi$ and $n = 40$. **B.** Imaginary part $\beta_0 = \operatorname{Im}\gamma_0$ from Eq. (6.15). Parameters are $\Delta = 5.5$, $\omega = 1$, and $\varepsilon = 0.15$. All systems exhibit the same collective frequency $\Omega_0 = 1.11$.

6.2 Motivating Examples

6.2.1— Synchronization of a globally coupled system

As a first example, we consider globally coupled oscillators, for which the adjacency matrix is given by $c_{\mu\nu} = 1 - \delta_{\mu\nu}$, and a sinusoidal coupling function, $g(\varphi) = \sin\varphi$. Fig. 6.2A displays the relaxation rate r_0 of small perturbations to the synchronized state as a function of the coupling delay τ. The circles show r_0 obtained from numerical solutions to Eq. (6.1)[3]. The solid line in Fig. 6.2A shows the analytical solution for r_0, derived below. Fig. 6.2A indicates that for global coupling, a maximum of the synchronization rate r_0 occurs at a non-vanishing value of the coupling delay τ. The analytical solution exhibits a characteristic cusp at this value of the delay.

6.2.2— Synchronization of a nearest-neighbor coupled system

As a second example, we consider nearest-neighbor coupled oscillators in one dimension with periodic boundary conditions (Fig. 6.3A,A'). The curves display analytical solutions for r_0, derived below, each curve corresponding to a Fourier mode of the oscillator lattice. Each Fourier mode, characterized by its wavevector $k = 2\pi p/n$ with $p \in \{-n/2, -n/2+1, \ldots, n/2-1\}$, relaxes independently with a relaxation rate $r_0(k)$. (We here consider the system size n to be even.) For long-wavelength modes, $|k| < \pi/2$, the relaxation rate r_0 decreases with increasing wavelength and coupling delay (Fig. 6.3A, dashed red lines). For short-wavelength modes, $|k| > \pi/2$, r_0 displays a cusplike maximum (Fig. 6.3A, solid blue lines), which we already found in the globally coupled system considered above (Fig. 6.2A). Both the position and the height of this maximum depend on the wavevector k.

---

[3] The relaxation rate can be obtained by starting the system in the synchronized state with a random perturbation added and determining the exponential relaxation time of the perturbation to perfect synchrony [156].

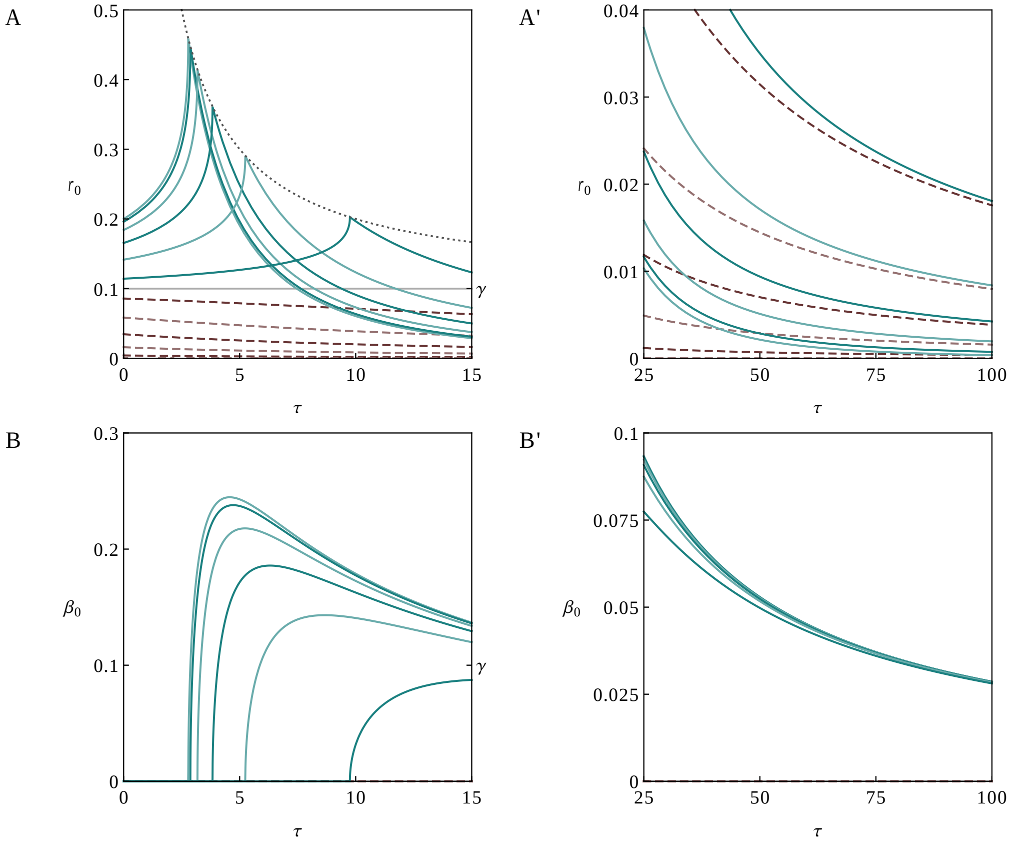

Figure 6.3 A, A'. Synchronization rates r_0 for a system with nearest-neighbor coupling and periodic boundary conditions in $d = 1$ dimension with a system size of $n = 22$ oscillators and $\Lambda = 0.1$. Different curves correspond to different wavevectors $k = 2\pi p/n$ and have different brightness for visual clarity. Dashed red lines correspond to $p = 1, \ldots, 5$ (long-wavelength modes), solid blue lines correspond to $p = 6, \ldots, 11$ (short-wavelength modes), ordered in direction of increasing p at $\tau = 0$. The dotted line shows the curve $\Lambda + 1/\tau$, Eq. (6.32), which is an envelope for the maxima. **B, B'.** Imaginary part $\beta_0 = \operatorname{Im}\gamma_0$ from Eq. (6.15) for the same modes as in panels A, A'. Long-wavelength modes (red dashed curves in A, A') have zero imaginary part.

6.3 General Analysis of Synchronization Rates

6.3.1— Linear stability analysis

Motivated by these examples, we investigate the synchronization rate of the general class of systems described by Eqs. (6.1) and (6.6) as a function of coupling delay and phase shift. Earl and Strogatz [38] showed that the in-phase synchronized state (6.2) is stable if and only if $\Lambda > 0$, where

$$\Lambda = \varepsilon \frac{\mathrm{d}g}{\mathrm{d}\varphi}\bigg|_{\varphi=-\Delta} . \tag{6.7}$$

The constant Λ depends on the coupling strength ε, the coupling function g, and the value of Δ, which sets the collective frequency according to Eq. (6.5). We only consider these stable cases and linearize the dynamics near the synchronized state. To this end, we use the ansatz[4]

$$\phi_\mu(t) = \Omega_0 t + \delta\xi_\mu(t) \tag{6.8}$$

---

[4] This ansatz has already been used in Chapter 2, Eq. (2.63).

in Eq. (6.1), where δ is an expansion parameter and ξ_μ is a perturbation of order unity. For simplicity, we restrict the coupling topologies to cases, for which the normalized adjacency matrix

$$b_{\mu\nu} = \frac{c_{\mu\nu}}{u_\mu} \tag{6.9}$$

satisfies $b_{\mu\nu} = b_{\nu\mu}$ and $b_{\mu\mu} = 0$. Global coupling and nearest-neighbor coupling with periodic boundary conditions, as introduced above, fall within this class of systems. The time evolution of the perturbation is given by

$$\frac{\mathrm{d}}{\mathrm{d}t}\xi_\mu(t) = \Lambda \sum_{\nu=1}^{n} b_{\mu\nu}(\xi_\nu(t-\tau) - \xi_\mu(t)) + \mathcal{O}(\delta) \ . \tag{6.10}$$

We drop all terms of order δ and higher and introduce the collective perturbation modes

$$\psi_\mu(t) = \sum_{\nu=1}^{n} d^{-1}_{\mu\nu}\xi_\nu(t) \ , \tag{6.11}$$

where $d_{\mu\nu}$ is the change of basis matrix that diagonalizes the adjacency matrix $b_{\mu\nu}$ according to $\sum_{\nu\eta} d^{-1}_{\mu\nu} b_{\nu\eta} d_{\eta\sigma} = v_\mu \delta_{\mu\sigma}$ and v_μ with $\mu = 1, \ldots, n$ are the n eigenvalues of $b_{\mu\nu}$. The eigenvalues v_μ are real and obey $|v_\mu| \leq 1$, as can be shown using Gershgorin's circle theorem [38, 46]. The collective modes ψ_μ evolve independently according to

$$\frac{\mathrm{d}}{\mathrm{d}t}\psi_\mu(t) = \Lambda v_\mu \psi_\mu(t-\tau) - \Lambda\psi_\mu(t) \ . \tag{6.12}$$

Since this expression is diagonal in μ, we drop the index μ for notational simplicity.

6.3.2—Characteristic equation

The characteristic equation for the relaxation rates γ of a collective mode ψ with eigenvalue v is obtained using the ansatz $\psi(t) = \mathrm{e}^{-\gamma t}$ in Eq. (6.12) [6, 84]. This yields

$$\Lambda - \gamma = v\Lambda \mathrm{e}^{\gamma\tau} \ . \tag{6.13}$$

The solutions to Eq. (6.13) in γ can be expressed through the Lambert W function [3], which is defined by the relation

$$W(z)\mathrm{e}^{W(z)} = z \tag{6.14}$$

for $z \in \mathbb{C}$. Since the equation $W\mathrm{e}^W = z$ has infinitely many solutions in W, the Lambert W function has discrete branches $W_\sigma(z)$ separated by branch cuts, where $\sigma \in \mathbb{Z}$ is the branch index [25]. The solution to Eq. (6.13) is thus given by $\gamma_\sigma = \Lambda - \tau^{-1}W_\sigma(v\Lambda\tau\mathrm{e}^{\Lambda\tau})$. Hence, each branch σ of W corresponds to one relaxation rate $r_\sigma = \mathrm{Re}\,\gamma_\sigma$. We here only consider the smallest relaxation rate for a given collective mode ψ, since it describes the long time behavior of ψ. This smallest rate is given by the principal branch $\sigma = 0$ of the Lambert W function (Fig. 6.4A), which has the property $\mathrm{Re}\,W_0 \geq \mathrm{Re}\,W_\sigma$ for all $\sigma \in \mathbb{Z}$ [132]. Hence, the solution with the smallest relaxation rate is given by

$$\gamma_0 = \Lambda - \frac{1}{\tau}W_0(z_\tau) \ , \tag{6.15}$$

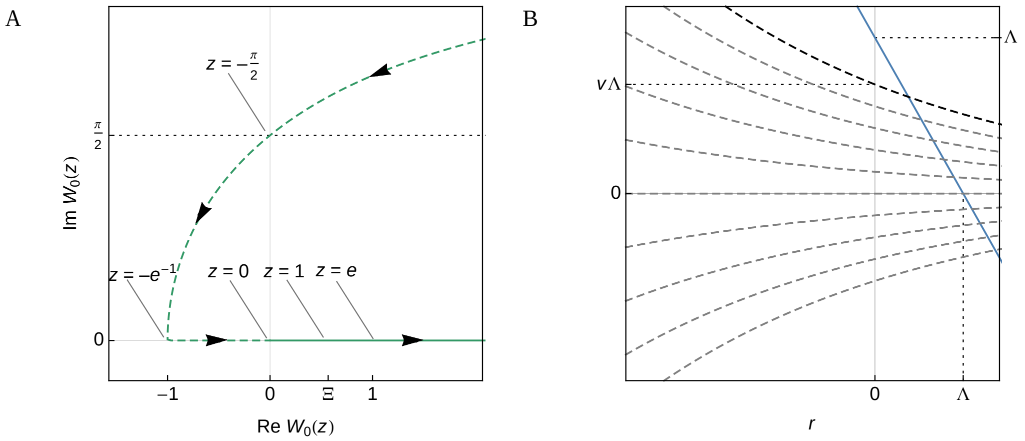

Figure 6.4 **A.** Principal branch $W_0(z)$ of the Lambert W function for $z \in \mathbb{R}$. The dashed green line shows regions with $z < 0$, the solid green shows regions with $z > 0$. The black arrows indicate the direction of increasing z. The value $\Xi = W_0(1) \approx 0.567$ is the so-called Omega constant. **B.** The blue solid line shows $\Lambda - r$ as a function of r for fixed Λ. The dashed lines show $v\Lambda e^{r\tau}\cos(\beta\tau)$ as a function of r for different values of $\cos(\beta\tau) \in [-1, 1]$. The leftmost intersection with $\Lambda - r$ is found for $\cos(\beta\tau) = 1$ (thick dashed line).

where

$$z_\tau = v\Lambda\tau e^{\Lambda\tau} \ . \tag{6.16}$$

In the following, we consider collective modes with $v > 0$ and $v < 0$ separately. In nearest-neighbor coupled systems, collective modes with $v < 0$ are Fourier modes with short wavelengths and $v > 0$ are Fourier modes with long wavelengths, as shown below (Sec. 6.4). Hence, we occasionally refer to modes with $v < 0$ and $v > 0$ as ‘short-wavelength modes’ and ‘long-wavelength modes’, respectively, even though the corresponding modes might have a different interpretation for other coupling topologies.

6.3.3—Synchronization rates of long-wavelength modes

For modes with $v > 0$, the synchronization rate r_0 decreases monotonically with increasing coupling delay τ and satisfies $r_0 \to 0$ for $\tau \to \infty$ (Fig. 6.3A’, dashed red lines). To show this, we separate Eq. (6.13) into real and imaginary parts. This yields

$$\Lambda - r = v\Lambda e^{r\tau}\cos(\beta\tau) \ , \tag{6.17a}$$

$$-\beta = v\Lambda e^{r\tau}\sin(\beta\tau) \ , \tag{6.17b}$$

where $\beta = \operatorname{Im}\gamma$. By plotting both sides of Eq. (6.17a) as a function of r, we note that the solutions to Eq. (6.17a), indicated by intersections of both curves, decrease monotonically with increasing $\cos(\beta\tau)$ (Fig. 6.4B). Since $\beta_0 = 0$ is a solution to Eq. (6.17b), and $\cos(\tau\beta_0) = 1$, the real part r_0 corresponding to $\beta_0 = 0$ is the smallest among all solutions to Eqs. (6.17). Differentiating the remaining real part equation

$$\Lambda - r_0 = v\Lambda e^{r_0\tau} \tag{6.18}$$

with respect to τ shows that r_0 satisfies the differential equation

$$\frac{dr_0}{d\tau} = -\frac{r_0}{\tau + (\Lambda - r_0)^{-1}} \ . \tag{6.19}$$

Since $\tau > 0$, $r_0 > 0$, and $\Lambda - r_0 > 0$ according to Eq. (6.18), we find the bound

$$\frac{\mathrm{d}r_0}{\mathrm{d}\tau} < 0 \; . \tag{6.20}$$

Furthermore, Eq. (6.18) implies that

$$\tau = \frac{1}{r_0} \log\left(v \left[1 - \frac{r_0}{\Lambda} \right] \right) \; , \tag{6.21}$$

which reveals that $r_0 \to 0$ corresponds to $\tau \to \infty$. Hence, the collective modes with $v > 0$ become stationary for large coupling delays.

Eq. (6.18) furthermore implies that for two modes with $v_1 \geq v_2 > 0$, the respective synchronization rates satisfy $r_0^{(1)} \geq r_0^{(2)}$ by an argument similar to the one given below Eqs. (6.17). In Fig. 6.3A, this is illustrated by the fact that the dashed lines never cross.

6.3.4—Synchronization rates of short-wavelength modes

For collective perturbation modes with $v > 0$, the synchronization rate r_0 displays a cusp at a specific coupling delay $\tau = \tau^*$. We will now show that τ^* is given by

$$\tau^* = \frac{1}{\Lambda} W_0 \left(\frac{\mathrm{e}^{-1}}{|v|} \right) \; . \tag{6.22}$$

The cusp of r_0 at $\tau = \tau^*$ is a consequence of the definition of the principal branch W_0 of the Lambert W function. We show that $\mathrm{d}r_0/\mathrm{d}\tau$ has opposite sign in the two regions $\tau \leq \tau^*$ and $\tau > \tau^*$, which implies that the cusp is located at the maximum of r_0, as suggested by the examples shown in Figs. 6.2A and 6.3A. To obtain $\mathrm{d}r_0/\mathrm{d}\tau$, we first compute $\mathrm{d}\gamma_0/\mathrm{d}\tau$ and then take the real part. The derivative of γ_0, Eq. (6.15), with respect to τ is given by

$$\frac{\mathrm{d}\gamma_0}{\mathrm{d}\tau} = \frac{1}{\tau^2} W_0(z_\tau) - \frac{1}{\tau} \frac{\mathrm{d}z_\tau}{\mathrm{d}\tau} \frac{\mathrm{d}W_0}{\mathrm{d}z}\bigg|_{z=z_\tau} \; . \tag{6.23}$$

The derivative $\mathrm{d}W_0/\mathrm{d}z$ of the Lambert W function can be obtained by differentiating the defining relation (6.14) with respect to z and solving for $\mathrm{d}W/\mathrm{d}z$,

$$\begin{aligned} \frac{\mathrm{d}W}{\mathrm{d}z} &= \frac{1}{\mathrm{e}^{W(z)}} \frac{1}{1 + W(z)} \\ &= \frac{1}{z} \frac{W(z)}{1 + W(z)} \; , \end{aligned} \tag{6.24}$$

where, in the second line, we have multiplied numerator and denominator by $W(z)$ and again used the defining relation (6.14). The derivative of z_τ, Eq. (6.16), is obtained straightforwardly as

$$\frac{\mathrm{d}z_\tau}{\mathrm{d}\tau} = z_\tau \frac{1 + \Lambda\tau}{\tau} \; . \tag{6.25}$$

Using the results (6.24) and (6.25) in Eq. (6.23), and using $W(z_\tau) \equiv U + \mathrm{i}V$, we obtain

$$\begin{aligned} \frac{\mathrm{d}\gamma_0}{\mathrm{d}\tau} &= \frac{W_0(z_\tau)}{\tau^2} \frac{W_0(z_\tau) - \Lambda\tau}{1 + W_0(z_\tau)} \\ &= \frac{1}{\tau^2} \frac{(U - \Lambda\tau)(U + U^2 + V^2) - V^2}{(1+U)^2 + V^2} + \mathrm{i} \frac{V}{\tau^2} \frac{2U - \Lambda\tau + U^2 + V^2}{(1+U)^2 + V^2} \; . \end{aligned} \tag{6.26}$$

Hence, the derivative of the real part r_0 is given by

$$\frac{\mathrm{d}r_0}{\mathrm{d}\tau} = \frac{1}{\tau^2}\frac{(U-\Lambda\tau)(U+U^2+V^2)-V^2}{(1+U)^2+V^2} \ . \tag{6.27}$$

For $\tau \leq \tau^*$, which implies $z_\tau < \mathrm{e}^{-1}$, we find $V=0$, which follows from the properties of the principal branch W_0 (see also Fig. 6.4A). Eq. (6.27) thus simplifies to

$$\frac{\mathrm{d}r_0}{\mathrm{d}\tau} = \frac{U-\Lambda\tau}{\tau^2}\frac{U}{1+U} \ , \tag{6.28}$$

and, since $U \in [-1,0]$, implies $\mathrm{d}r_0/\mathrm{d}\tau \geq 0$ for $\tau \leq \tau^*$.

We complete our proof by showing that $\mathrm{d}r_0/\mathrm{d}\tau < 0$ for $\tau > \tau^*$ using Eq. (6.27). The term $U - \Lambda\tau$ is negative. This can be seen by taking the real part of Eq. (6.15) and using the fact that $r_0 > 0$. Furthermore, $V \neq 0$ in this region, which implies that γ_0 acquires an imaginary part (Fig. 6.3B). The term $U+U^2+V^2$ is positive. To see this, we express this factor entirely in terms of V: We insert the definition $W(z_\tau) = U + \mathrm{i}V$ into the defining relation of the Lambert W function, Eq. (6.14), which we write in the form $W(z_\tau) = z_\tau \mathrm{e}^{-W(z_\tau)}$. This yields a complex equation whose real and imaginary parts are given by

$$U = z_\tau \mathrm{e}^{-U}\cos V \ , \tag{6.29}$$

$$V = -z_\tau \mathrm{e}^{-U}\sin V \ . \tag{6.30}$$

These equations yield the relation $U = -V\cot V$. Hence, the term $U+U^2+V^2$ can be rewritten as

$$U+U^2+V^2 = \frac{V}{(\sin V)^2}\left(V - \frac{\sin(2V)}{2}\right) \ . \tag{6.31}$$

Since $V \in [0,\pi]$, the above expression is positive. We have thus found that for $v<0$, $\mathrm{d}r_0/\mathrm{d}\tau \leq 0$ for $\tau > \tau^*$. The corresponding synchronization rate r_0 thus decreases as the coupling delay increases. According to Eqs. (6.15) and (6.22), the maximal synchronization rate r_0^* at $\tau = \tau^*$ is given by

$$r_0^* = \Lambda + \frac{1}{\tau^*} \ . \tag{6.32}$$

6.3.5—
Symmetry of short and long wavelengths for large delays

We obtain the behavior of r_0 in the limit of large τ by an expansion of r_0 in powers of τ^{-1},

$$r_0 = -\frac{\ln|v|}{\tau} + \mathcal{O}(\tau^{-2}) \ . \tag{6.33}$$

This shows that the asymptotic behavior of the synchronization rate only depends on the absolute value $|v|$ of the eigenvalue v characterizing the collective mode. Hence, modes with same $|v|$ but opposite signs approach the same asymptotic behavior. Fig. 6.3A' illustrates this behavior for the case of nearest-neighbor coupling.

6.4 Globally Coupled and Spatially Extended Systems

So far, all our results have been completely general and hold for all coupling topologies that fall within the class specified in the beginning of Sec. 6.3. We now apply our results from Sec. 6.3 to two prominent cases, namely, systems with global coupling and spatially extended systems with nearest-neighbor interactions and periodic boundary conditions.

6.4.1— Fastest synchronization for non-zero delays

In Sec. 6.2.1, we have considered a globally coupled system to numerically illustrate the non-monotonic behavior of the synchronization rate as a function of the coupling delay (Fig. 6.2A). Using the results from Sec. 6.3, we are now able to understand this behavior in detail. For a globally coupled system, the normalized adjacency matrix, Eq. (6.9), is given by

$$b_{\mu\nu} = \frac{1-\delta_{\mu\nu}}{n-1} \; . \tag{6.34}$$

The largest eigenvalue of $b_{\mu\nu}$ is $v_0 = 1$ and corresponds to the neutrally stable global phase shift. All other collective modes have the same eigenvalue $v_1 = -(n-1)^{-1}$ and therefore exhibit the same synchronization rate. Since $v_1 < 0$, their τ-dependence is non-monotonic (Sec. 6.3.4). According to Eq. (6.22), the system synchronizes fastest for the delay

$$\tau^* = \frac{1}{\Lambda} W_0(\mathrm{e}^{-1}[n-1]) \; , \tag{6.35}$$

which depends on the system size and the constant Λ.

Fig. 6.2B shows the imaginary part $\beta_0 = \operatorname{Im}\gamma_0$ corresponding to the solution γ_0 with smallest real part r_0. As described in Sec. 6.3.4, β_0 vanishes for $\tau < \tau^*$ but attains non-zero values for $\tau > \tau^*$. A non-zero imaginary part corresponds to an oscillatory decay of the collective perturbation mode ψ, Eq. (6.11).

Note that for the example shown in Fig. 6.2, fastest synchronization is found for the delay $\tau^* \simeq 18.6$. The corresponding phase shift is given by Eq. (6.6) as $\alpha^* = \alpha(\tau^*) \simeq -15.1$, which is equivalent to $(\alpha^* \bmod 2\pi) \simeq 1.2\pi$. For this phase shift and sinusoidal coupling, $g(\varphi) = \sin\varphi$, the shifted coupling function in Eq. (6.1) effectively describes repulsive coupling, since $\sin(\varphi - \alpha^*) \simeq \sin(\varphi - \pi) = -\sin\varphi$. The system without delays, $\tau = 0$, has a phase shift of $\alpha_0 = \alpha(0) \simeq 1.8\pi$, describing attractive coupling. This demonstrates that a system with non-attractive coupling and coupling delays can synchronize faster than a system with attractive coupling and no delays.

6.4.2— Fastest synchronization for intermediate wavelengths

We now apply our results to spatially extended systems with nearest-neighbor coupling and periodic boundary conditions. We have encountered the special case of such a system in one dimension in Sec. 6.2.2. For the generalized case of d dimensions, the collective modes are Fourier modes of the linear perturbations ξ to the synchronized state (Appendix G),

$$\psi_{k_1,\ldots,k_d}(t) = \sum_{\mu_1=0}^{n_1-1} \cdots \sum_{\mu_d=0}^{n_d-1} \mathrm{e}^{-\mathrm{i}\sum_{i=1}^{d} k_i\mu_i} \xi_{\mu_1,\ldots,\mu_d}(t) \; . \tag{6.36}$$

It is straightforward to check that the Fourier modes ψ satisfy Eq. (6.12) as the perturbations ξ satisfy Eq. (6.10). The corresponding eigenvalues are given by

$$v_{k_1,\ldots,k_d} = \frac{1}{d}\sum_{i=1}^{d} \cos k_i \; , \tag{6.37}$$

where $k_i = 2\pi p_i/n_i$ with $p_i \in \{-n_i/2, -n_i/2+1, \ldots, n_i/2-1\}$, and n_i is the size of the system in i-direction ($i = 1, \ldots, d$). The eigenvalues $v_{k_1,\ldots,k_d}$ thus refer to the respective Fourier modes with wavevector $(k_1, \ldots, k_d)$. Hence, our results from Sec. 6.3 explain the mode structure observed in Fig. 6.3A: the synchronization rates

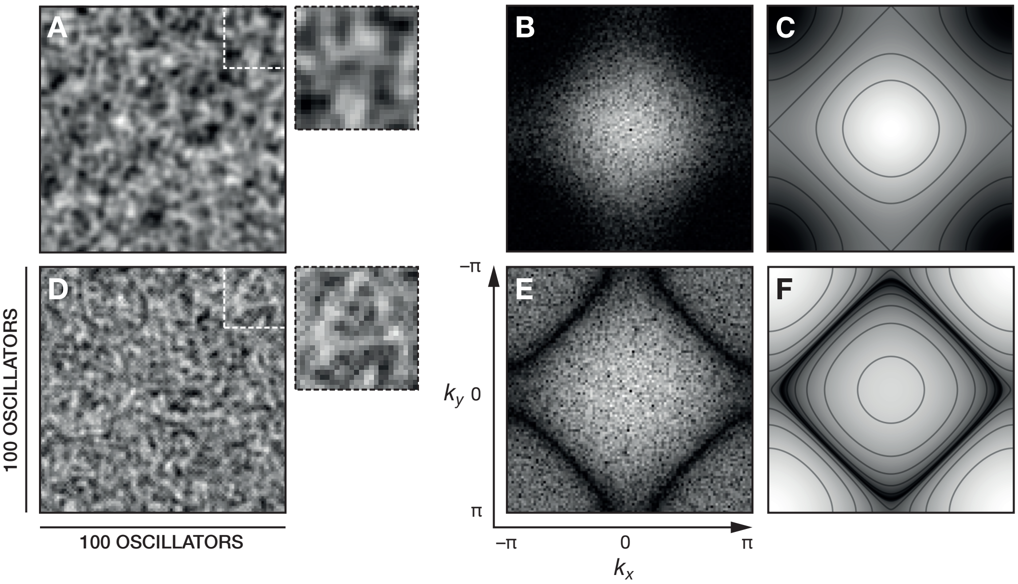

Figure 6.5 Oscillator synchronization in a two-dimensional nearest-neighbor coupled system of 100×100 oscillators with periodic boundary conditions for no coupling delay (A–C) and finite delay (D–F) with the same collective frequency. **A,D.** Snapshots of simulations of Eqs. (6.1) and (6.6) at time $t = 24$. Each lattice site corresponds to one oscillator μ and its brightness indicates the relative value of $\sin\phi_\mu$. Initial conditions at $t = 0$ are the synchronized state, Eq. (6.2), perturbed by phases randomly chosen from the interval $[-0.4\pi, 0.4\pi]$. The separated plots show 2× magnifications of the dashed regions. **B,E.** Logarithmic power spectra of images A,D. Axes scaling is the same in both panels. **C,F.** Synchronization rate r_0 as a function of the wavevector (k_x, k_y) as obtained from Eq. (6.15). Bright colors correspond to small, dark colors to large values. Axes are the same as in panels B,E. Parameters are $\Delta = 6$, $\omega = 1$, $\varepsilon = 0.2$, with $\tau = 0$ (A–C) and $\tau = 10$ (D–F) and α given by Eq. (6.6). The coupling function is $g(\varphi) = \sin\varphi$. Both systems exhibit the same collective frequency $\Omega = 1.06$.

of long-wavelength modes monotonically decrease with increasing delay, whereas the synchronization rates of short-wavelength modes show a non-monotonic behavior in τ.

In addition, we illustrate the effects on nearest-neighbor coupled systems for the case of two dimensions (Fig. 6.5). We consider two systems of 100×100 oscillators on a square lattice with periodic boundary conditions, one without coupling delay and one with finite coupling delay. The corresponding phase shifts $\alpha(\tau)$ are given by Eq. (6.6), all other parameters are identical. We prepare these systems in the same synchronized state, perturbed by randomly chosen phases in the interval $[-0.4\pi, 0.4\pi]$. We then let the system relax towards the synchronized state and investigate the spatial features of the relaxing pattern. Fig. 6.5A,D shows simulation snapshots at a point in time when not all of the perturbations have relaxed yet. For the case of no delays (Fig. 6.5A), the system first synchronizes on the shortest spatial scale. This behavior is clearly revealed by the logarithmic power spectrum Fig. 6.5B, where the intensity of long wavelengths (small wavevectors) is much larger than the one of short wavelengths (large wavevectors). As the oscillators are coupled to their nearest neighbors, such a synchronization behavior is expected. Interestingly, for the case of finite delays (Fig. 6.5B), the system exhibits partially synchronized clusters on intermediate length scales with persisting phase differences on nearest-neighbor scale. The logarithmic power spectrum Fig. 6.5E indeed reveals that perturbations have decayed fastest at intermediate wavelengths. Both behaviors are described by the results found in Sec. 6.3: For no delays, the synchronization rate of a Fourier mode increases with increasing wavevector (Fig. 6.5C, see also Fig. 6.3A at $\tau = 0$.) As the delay increases, the curves for short-wavelength collective modes reverse their ordering (Fig. 6.3A), resulting in fastest synchronization on intermediate wavelengths (Fig. 6.5F). A similar reversal of the synchronization rate of collective modes has been observed in systems without delays as a function of the coupling strength [54].

6.5 Summary

In this chapter, we have investigated the synchronization dynamics of coupled phase oscillators whose coupling includes phase shifts and time delays. We started with the observation that the collective frequency of the synchronized state is invariant under a specific substitution of coupling delays by phase shifts, Eq. (6.4). This led us to study the synchronization dynamics of different systems connected by the transformation (6.4). To this end, we obtained exact results for the linearized dynamics around the synchronized state. We found that the synchronization dynamics crucially depend on the specific combination of phase shift and coupling delay. In globally coupled systems, the synchronization rate attains a maximum for non-zero coupling delay. This leads to the remarkable behavior that for the same collective frequency, a system with a non-attractive coupling and coupling delays can exhibit a synchronized state that is more robust against noise than a system with attractive coupling and without delays. In spatially extended systems with nearest-neighbor interaction, the combined effect of phase shifts and coupling delays can induce fastest synchronization on spatial scales larger than the interaction range.

In natural and engineered systems of coupled oscillators, the collective frequency is often intimately tied to the system's function. This is the case, e.g., for the circadian clock that regulates the metabolism in higher organisms with a period of about 24 hours (Chapter 1, Sec. 1.1.1), for the coupled genetic oscillations in the presomitic mesoderm of developing vertebrate embryos (Chapters 3–5), whose frequencies play a role for the length of body segments, but also for engineered systems of coupled lasers or electronic oscillators [74, 144]. Here we have shown that phase shifts and coupling delays are a viable way to regulate the synchronization rate while keeping the collective frequency at a specific value. The results presented in this chapter have been published in Ref. [66].

Parameters and Symbols used in Chapter 6

LIST OF SYMBOLS

ϕ_μ	phase of oscillator μ
ξ_μ	perturbation of oscillator μ to the synchronized state
ψ_μ	collective mode μ for which the linearized dynamics decouple
γ	exponent describing the relaxation of the collective mode ψ
r	synchronization rate ($r = \operatorname{Re}\gamma$)
r_0	slowest synchronization rate
β	$\beta = \operatorname{Im}\gamma$
ω	intrinsic frequency
ε	coupling strength
$c_{\mu\nu}$	adjacency matrix
$b_{\mu\nu}$	normalized adjacency matrix
$d_{\mu\nu}$	change of basis matrix that diagonalizes $b_{\mu\nu}$
v_μ	eigenvalues of $b_{\mu\nu}$
u_μ	total weight of links of oscillator μ
n	total number of oscillators
g	coupling function
τ	coupling delay
τ^*	coupling delay yielding maximum r_0 for collective modes with $v < 0$
α	coupling phase shift
Ω	collective frequency
Δ	total 'virtual' phase shift determining the collective frequency
Λ	quantity that indicates stability of the synchronized state
W_σ	σ^{th} branch of the Lambert W function
z_τ	$v\Lambda\tau\mathrm{e}^{\Lambda\tau}$
U	$\operatorname{Re} W_0(z_\tau)$
V	$\operatorname{Im} W_0(z_\tau)$
d	number of dimensions
k_i	wavevector in i-direction
p_i	integer number indexing the possible values for k_i

Chapter 7

Summary and Outlook

In this thesis, we investigated genetic oscillations and their role during the segmentation of the vertebrate body axis. We developed theoretical models of coupled genetic oscillators as well as quantification methods for experimental data using methods from dynamical systems theory, the theory of stochastic processes, nonlinear time series analysis, and particle-based simulations. Importantly, we showed that our theory of coupled phase oscillators in a dynamic medium can account for the key features of vertebrate segmentation as observed in experiments with zebrafish embryos.

Stochastic coupling regulates precision and synchronization of genetic oscillators

In Chapter 2, we presented a generic Markov chain model of coupled genetic oscillators, in which both the internal dynamics of an oscillator as well as the coupling mechanism are intrinsically stochastic. We first analyzed the dynamical features of an uncoupled oscillator and derived effective estimates for amplitude and frequency in terms of its biochemical parameters.

We then turned to the full system of two coupled oscillators and investigated the effects of stochastic coupling on precision, synchronization, and frequency of the oscillators. We found that coupling can considerably increase the precision of oscillators with the amount of precision increase being closely tied to the degree of synchrony that the oscillators exhibit. The increase in precision and the mode of synchrony of both oscillators, in-phase or anti-phase, crucially depend on the coupling delays induced by complex signaling processes. Furthermore, we found that the increase in precision was achieved without significantly altering the turnover of gene expression products of the oscillators. These findings indicate that stochastic coupling is a viable way to improve the precision of genetic oscillators. Moreover, we found that coupled oscillators can exhibit stochastic switching between in-phase and anti-phase synchronized states, a phenomenon induced by stochasticity.

We complemented this study with a phase oscillator approximation that takes into account distributed coupling delays. By comparison to the stochastic model, we showed that the phase model can capture the dependence of the collective frequency on the coupling delay as well as the stability of the in-phase and the anti-phase synchronized states. Hence, phase oscillator approximations can be used to describe the collective dynamics of systems of coupled genetic oscillators while being comparatively simple and easy to implement.

Large assemblies of coupled genetic oscillators are found, e.g., in the mammalian circadian clock and the rhythmically segmenting presomitic mesoderm of developing vertebrate embryos. Our results indicate that in these and similar systems, stochastic coupling might not only have a functional role in synchronizing the oscillations but also in substantially increasing their precision to keep a well-defined rhythm that is robust against internal and external fluctuations. Even though our model is inspired by cell-autonomous genetic oscillators that couple through a signaling pathway, it is generic and could equally well represent two genetic oscillators with different genetic components within the same cell but subject to intracellular coupling. A redundant genetic network of this kind has, for instance, been proposed to be at work in the cells of the presomitic mesoderm of developing vertebrate embryos [127]. Testing the model predictions in experiments requires the ability to independently measure oscillating gene expression in autonomous and coupled genetic oscillators. A corresponding experimental setup could be achieved by combining recently developed transgenic live reporters for oscillating gene expression in zebrafish [31, 133] with the ability to dissociate single oscillating cells from the embryo [154]. Using the fact that oscillations couple through the Notch signaling pathway, which requires cell contact, the precision and sychronization properties of coupled and uncoupled cellular genetic oscillators could be measured and compared with our theoretical results.

Continuum theories of coupled phase oscillator descibe the key features of vertebrate segmentation

In Chapter 3, we presented a continuum theory of coupled phase oscillators in a dynamic medium. We applied this theory to describe the kinematic wave patterns of gene expression in the presomitic mesoderm of vertebrate embryos. We started out with simplifying assumptions, describing a tissue of constant length with homogeneous cell flow to illustrate the basic mechanism of pattern formation with oscillators through a frequency gradient and advection. We then sequentially extended our theory to take into account biologically relevant factors such as coupling delays due to complex signaling processes, local growth of the tissue, and a time-dependent tissue length. We studied their effects on pattern formation and found that in particular the decreasing tissue length has important effects on the timing of segmentation. The decreasing tissue length was found to induce a Doppler effect as one end of the tissue moves into the kinematic wave pattern. In addition to the time scale of genetic oscillations, this Doppler effect introduces a second time scale that contributes to the rate of segment formation. This Doppler effect is accompanied by a dynamic modulation of the wavelength of the pattern, which leads to a complex interplay of the time scales of oscillations and tissue length decrease. We complemented this study with a hypothetic reaction-diffusion mechanism involving interacting morphogens and oscillators that describes the shortening of the tissue and the termination of the segmentation process in a self-organized way.

The theory of coupled oscillators in a dynamic medium presented here is highly general and can be applied to other scenarios than the ones studied here. Within the context of vertebrate segmentation, our theory could, for instance, be used to describe segmentation of different vertebrate species and mutant animals exhibiting different kinematic wave patterns in the presomitic mesoderm. In a broader context, our theory can be applied whenever coupled oscillations with long-wavelength phase patterns in a dynamic medium are studied.

Changing tissue length regulates the timing of vertebrate segmentation through a Doppler effect

In Chapter 4 we studied the dynamics of vertebrate segmentation in zebrafish using experimental data obtained by our collaborators and/or published in the literature. We measured the time evolution of the length of the segmenting tissue and the velocity field in the segmented region from brightfield time-lapse movies of zebrafish segmentation. We used these results to determine parameters of the theory introduced in Chapter 3. We showed that our theory is capable of capturing the time dependence of the morphological segmentation period and the segment size upon formation as observed in wildtype embryos.

We then quantified experimental data on kinematic wave patterns of gene expression in zebrafish embryos, for which the theory yielded independent predictions. To this end, we constructed a phase representation of the wave patterns using a wavelet transform, which allowed a quantitative analysis of their spatio-temporal properties. We compared the time-dependent number of kinematic waves in the presomitic mesoderm with results of the theory presented in Chapter 3 and found very good agreement. Moreover, the analysis of the experimental wave patterns revealed a Doppler effect and a dynamic modulation of the wavelength as described by our theory. Hence, we have successfully tested the viability of our theory by comparison to experimental data from wildtype and transgenic embryos. Moreover, we have shown that in addition to the time scale of genetic oscillations, a Doppler effect induced by the changing tissue length regulates the timing of segment formation in a hitherto unanticipated way.

The quantification methods developed here are easily adaptable tools that can be employed to study and compare the spatio-temporal dynamics of kinematic wave patters under different conditions, e.g., in mutant animals, animals in which gene expression has been experimentally inhibited or enhanced, and animals of different vertebrate species. Together with the theory introduced in Chapter 3, quantified data on perturbed kinematic wave patterns can be used to perform precise tests of our understanding of vertebrate segmentation on tissue level.

A cell-based model describes segmentation as a self-organized process

In Chapter 5, we introduced a three-dimensional cell-based model of a segmenting tissue. This model builds on an existing tissue model based on dissipative particle dynamics [16, 114] and extends it by the dynamics of coupled oscillators, morphogen expression, and cell differentiation. It describes cells as distinct entities with mechanical properties, which can divide, differentiate, and grow a tissue. The cells carry autonomous genetic oscillators which couple with those of adjacent cells. Moreover, these cells produce, degrade, and exchange a morphogen that sets the local frequency of oscillations and controls cell fate decisions. We showed proof-of-principle results demonstrating that self-organized pattern formation and segmentation emerges from the interplay of these mechanisms of tissue growth, morphogen gradient formation, and oscillation dynamics.

We propose this model as a starting point to study the interplay of pattern formation and tissue mechanics during vertebrate segmentation in a unified framework involving a three-dimensional tissue with cells as distinct mechanical entities. Going beyond the coarse-grained theories of segmentation presented in Chapter 3, this cell-based model enables to address, e.g., the effects of random cell movement on pattern formation and on the morphology of segments as well as the compatibility of different growth mechanisms (cell division, inflow of cells, convergence-extension) with the established mechanisms of pattern formation with oscillators. Combined with the coarse-grained continuum theories, this model permits to address new questions about how the embryonic body axis grows and how growth interacts with biochemical patterning to generate the vertebrate body plan.

Coupling delays and phase shifts regulate synchronization of dynamic oscillators

Motivated by the biological oscillator systems studied in the previous chapter, we turned to generic systems of coupled oscillators in Chapter 6. We analyzed their synchronization behavior in the presence of coupling delays and phase shifts, properties of oscillator coupling that generically arise in complex signaling processes. While the collective frequency of the synchronized state is invariant under an appropriate substitution of coupling delays by phase shifts, we showed that the synchronization dynamics is not invariant under this substitution. For globally coupled systems with a constant collective frequency, our results imply than fastest synchronization occurs for non-vanishing coupling delays. In particular, we showed that non-attractive oscillator coupling together with coupling delays can yield a synchronized state that is more robust to phase noise than attractive coupling without coupling delays. In spatially extended systems, we found that fastest synchronization can occur on length scales larger than the coupling range, giving rise to novel synchronization scenarios.

In natural and engineered systems of coupled oscillators, the collective frequency is often intimately tied to the system's function. This is the case, e.g., for the circadian clock regulating the metabolism in higher organisms, for the coupled genetic oscillations in the presomitic mesoderm of developing vertebrate embryos, but also for engineered systems of coupled lasers or electronic oscillators [35, 74, 102, 144]. Our results show that phase shifts and coupling delays can regulate the dynamic behaviors and the resilience of coupled oscillator networks, while keeping the collective frequency at a specific value.

In summary, we used discrete and continuous theories of genetic oscillators to study their dynamic behavior, comparing our theoretical results to experimental data where available. We covered a wide range of different topics, contributing to the general understanding of genetic oscillators and synchronization and revealing a hitherto unknown mechanism regulating the timing of embryonic pattern formation. Parts of the results presented in this thesis have been published [5, 66, 133].

Appendices

Appendix A
Analytical Treatment of the Markov Chain Models

A.1 Time Evolution of Expectation Values

In this section, we show how to obtain Eqs. (2.21–2.23) governing the time evolution of the expectation values $\langle x_i \rangle = \sum_{\mathbf{x}} x_i P(\mathbf{x}, t)$ from the master equation (2.1). The time derivative of $\langle x_i \rangle$ is given by

$$\frac{\mathrm{d}}{\mathrm{d}t} \langle x_i \rangle = \sum_{\mathbf{x}} x_i \frac{\partial P}{\partial t}(\mathbf{x}, t) = \sum_{\mathbf{x}} x_i (\Lambda P)(\mathbf{x}, t) \ , \tag{A.1}$$

where $\sum_{\mathbf{x}} \equiv \sum_{x_0=0}^{\infty} \dots \sum_{x_n=0}^{\infty}$ and Λ is the operator describing the dynamics of an autonomous oscillator, Eq. (2.2). In the last equality, we have used the master equation (2.1) to replace the time derivative of P. For the sake of brevity, we introduce the notation $\sum_{\mathbf{x}}^{[i_1,\dots,i_m]}$, which indicates that summation over the occupation numbers $x_{i_1}, \dots, x_{i_m}$ is omitted. For $1 \le j \le n-1$, we find

$$\begin{aligned}
&\frac{\mathrm{d}}{\mathrm{d}t} \langle x_j \rangle \\
&= \lambda \sum_{i=0}^{n-1} \left(\sum_{\mathbf{x}} x_j (x_i + 1) P(x_0, \dots, x_i + 1, x_{i+1} - 1, \dots, x_n, t) - \sum_{\mathbf{x}} x_j x_i P(\mathbf{x}, t) \right) \\
&\quad + \kappa \left(\sum_{\mathbf{x}} x_j (x_n + 1) P(x_0, \dots, x_n + 1, t) - \sum_{\mathbf{x}} x_j x_n P(\mathbf{x}, t) \right) \\
&\quad + \alpha \left(\sum_{\mathbf{x}} x_j h(x_n) P(x_0 - 1, \dots, x_n, t) - \sum_{\mathbf{x}} x_j h(x_n) P(\mathbf{x}, t) \right) \\
&= \lambda \sum_{i \neq j-1, j} \left(\sum_{\mathbf{x}}^{[i,i+1]} \sum_{x_i=1}^{\infty} \sum_{x_{i+1}=-1}^{\infty} x_j x_i P(\mathbf{x}, t) - \sum_{\mathbf{x}} x_j x_i P(\mathbf{x}, t) \right) \\
&\quad + \lambda \left(\sum_{\mathbf{x}}^{[j-1,j]} \sum_{x_{j-1}=1}^{\infty} \sum_{x_j=-1}^{\infty} (x_j + 1) x_{j-1} P(\mathbf{x}, t) - \sum_{\mathbf{x}} x_j x_{j-1} P(\mathbf{x}, t) \right) \\
&\quad + \lambda \left(\sum_{\mathbf{x}}^{[j,j+1]} \sum_{x_j=1}^{\infty} \sum_{x_{j+1}=-1}^{\infty} (x_j - 1) x_j P(\mathbf{x}, t) - \sum_{\mathbf{x}} x_j^2 P(\mathbf{x}, t) \right) \\
&\quad + \kappa \left(\sum_{\mathbf{x}}^{[n]} \sum_{x_n=1}^{\infty} x_j x_n P(\mathbf{x}, t) - \sum_{\mathbf{x}} x_j x_n P(\mathbf{x}, t) \right)
\end{aligned}$$

$$\begin{aligned}
&\quad+\alpha\Bigg(\sum_{\mathbf{x}}^{[0]}\sum_{x_0=-1}^{\infty} x_j h(x_n)P(\mathbf{x},t) - \sum_{\mathbf{x}} x_j h(x_n) P(\mathbf{x},t)\Bigg)\\
&=\lambda \sum_{i\neq j-1,j}\sum_{\mathbf{x}}\Big(x_jx_i - x_jx_i\Big)P(\mathbf{x},t)\\
&\quad+\lambda\sum_{\mathbf{x}}\Big((x_j+1)x_{j-1} - x_jx_{j-1}\Big)P(\mathbf{x},t)\\
&\quad+\lambda\sum_{\mathbf{x}}\Big((x_j-1)x_j - x_j^2\Big)P(\mathbf{x},t)\\
&\quad+\kappa\sum_{\mathbf{x}}\Big(x_jx_n - x_jx_n\Big)P(\mathbf{x},t)\\
&\quad+\alpha\sum_{\mathbf{x}}\Big(x_jh(x_n) - x_jh(x_n)\Big)P(\mathbf{x},t)\\
&=\lambda\sum_{\mathbf{x}}\Big(x_{j-1}-x_j\Big)P(\mathbf{x},t)\\
&=\lambda\left(\langle x_{j-1}\rangle - \langle x_j\rangle\right)\ .
\end{aligned}$$

In the first identity, we have used Eq. (A.1) and have evaluated the action of the creation and annihilation operators $\mathbb{E}_i^{\pm}$ on P. In the second identity, we have treated the indices $j-1$ and j in the sum $\sum_{i=0}^{n-1}$ separately and performed index shifts in the appropriate sums to restore the form $P(\mathbf{x},t)$ in every term. In the third identity, we have restored the original lower summation bound to 0. This is possible because the respective term to sum over contains either a factor of x_i that does not contribute if the case $x_i = 0$ is included, or a factor of $P(\mathbf{x},t)$, which is zero for negative molecule numbers. In the fourth identity, we have removed all terms that cancel.

In a similar fashion, the time evolution for $\langle x_0\rangle$ and $\langle x_n\rangle$ is obtained. We here omit the now obvious steps,

$$\begin{aligned}
\frac{\mathrm{d}}{\mathrm{d}t}\langle x_0\rangle &= \lambda\Bigg(\sum_{\mathbf{x}}^{[0,1]}\sum_{x_0=1}^{\infty}\sum_{x_1=-1}^{\infty}(x_0-1)x_0P(\mathbf{x},t) - \sum_{\mathbf{x}} x_0^2 P(\mathbf{x},t)\Bigg)\\
&\quad+\alpha\Bigg(\sum_{\mathbf{x}}^{[0]}\sum_{x_0=-1}^{\infty}(x_0+1)h(x_n)P(\mathbf{x},t) - \sum_{\mathbf{x}} x_0h(x_n)P(\mathbf{x},t)\Bigg)\\
&= \langle h(x_n)\rangle - \lambda\langle x_0\rangle\ ,\\
\frac{\mathrm{d}}{\mathrm{d}t}\langle x_n\rangle &= \lambda\Bigg(\sum_{\mathbf{x}}^{[n-1,n]}\sum_{x_{n-1}=1}^{\infty}\sum_{x_n=-1}^{\infty}(x_n+1)x_{n-1}P(\mathbf{x},t) - \sum_{\mathbf{x}} x_nx_{n-1}P(\mathbf{x},t)\Bigg)\\
&\quad+\kappa\Bigg(\sum_{\mathbf{x}}^{[n]}\sum_{x_n=1}^{\infty}(x_n-1)x_nP(\mathbf{x},t) - \sum_{\mathbf{x}} x_n^2P(\mathbf{x},t)\Bigg)\\
&= \lambda\langle x_{n-1}\rangle - \kappa\langle x_n\rangle\ .
\end{aligned}$$

Analogous dynamic equations can be derived for correlation functions of the type

$$\langle x_i(t)x_j(0)\rangle = \sum_{\mathbf{x},\mathbf{x}'} x_i x_j' P(\mathbf{x},t|\mathbf{x}',0)P(\mathbf{x}',0)\ , \tag{A.2}$$

where $P(\mathbf{x},t|\mathbf{x}',t')$ is the conditional probability of finding the state $\mathbf{x}$ at time t given that the system was in state $\mathbf{x}$ at time $t' < t$. It satisfies the equal-time relation $P(\mathbf{x},t|\mathbf{x}',t) = \delta_{\mathbf{x}\mathbf{x}'}$. In this case, the time evolution is given by

$$\frac{\mathrm{d}}{\mathrm{d}t}\langle x_i(t)x_j(0)\rangle = \sum_{\mathbf{x},\mathbf{x}'} x_i x_j' (\Lambda P)(\mathbf{x},t|\mathbf{x}',0)P(\mathbf{x}',0)\ , \tag{A.3}$$

which can be evaluated in the same way as in the examples above.

A.2 Closed Governing Equations for Expectation Values

A.2.1—Closed integro-differential equation for $\langle x_n\rangle$

We show the derivation of Eq. (2.25) from Eqs. (2.21–2.23), which govern the time evolution of the expectation values $\langle x_i\rangle$. The solution of Eq. (2.21) for the initial product x_0 reads

$$\langle x_0(t)\rangle = c_0 \mathrm{e}^{-\lambda t} + \alpha \int_0^t \mathrm{e}^{-\lambda(t-t')}\langle h(x_n(t'))\rangle\,\mathrm{d}t'\ , \tag{A.4}$$

where c_0 depends on the initial condition. The equations for the intermediate products Eq. (2.22) have analogous solutions,

$$\langle x_i(t)\rangle = c_i \mathrm{e}^{-\lambda t} + \lambda \int_0^t \mathrm{e}^{-\lambda(t-t')}\langle x_{i-1}(t')\rangle\,\mathrm{d}t'\ , \tag{A.5}$$

for $1 \le i \le n-1$. For any i in this range, repeated insertion of Eq. (A.5) yields

$$\begin{aligned}
\langle x_i(t)\rangle &= c_i \mathrm{e}^{-\lambda t} + c_{i-1}\lambda \mathrm{e}^{-\lambda t}\int_0^t \mathrm{d}t' + \lambda^2 \int_0^t \mathrm{d}t' \int_0^{t'} \mathrm{d}t''\ \mathrm{e}^{-\lambda(t-t'')}\langle x_{i-2}(t'')\rangle \\
&= c_i \mathrm{e}^{-\lambda t} + c_{i-1}\lambda t \mathrm{e}^{-\lambda t} + \lambda^2 \int_{\mathbb{D}} \mathrm{d}(t',t'')\ \mathrm{e}^{-\lambda(t-t'')}\langle x_{i-2}(t'')\rangle \\
&= (c_i + c_{i-1}\lambda t)\mathrm{e}^{-\lambda t} + \lambda^2 \int_0^t \mathrm{d}t'' \int_{t''}^{t} \mathrm{d}t'\ \mathrm{e}^{-\lambda(t-t'')}\langle x_{i-2}(t'')\rangle \\
&= (c_i + c_{i-1}\lambda t)\mathrm{e}^{-\lambda t} + \lambda^2 \int_0^t \mathrm{d}t''\,(t-t'')\,\mathrm{e}^{-\lambda(t-t'')}\langle x_{i-2}(t'')\rangle\ ,
\end{aligned} \tag{A.6}$$

where the integration domain $\mathbb{D}$ is the triangle $\mathbb{D} = \{(t',t'') : 0 \le t'' \le t' \le t\}$. With this result, it is straightforward to show by induction that in general,

$$\langle x_i(t)\rangle = \mathrm{e}^{-\lambda t}\sum_{k=0}^{j}\frac{(\lambda t)^k}{k!}c_{i-k} + \int_0^t G_{\lambda,j+1}(t-t')\,\langle x_{i-j-1}(t')\rangle\,\mathrm{d}t'\ , \tag{A.7}$$

for $0 \le j < i \le n-1$, where $G_{\lambda,n}$ is the Gamma distribution (2.26). The solution to Eq. (2.23) for the final product x_n can thus be expressed in the form

$$\frac{\mathrm{d}}{\mathrm{d}t}\langle x_n(t)\rangle \simeq -\kappa\langle x_n(t)\rangle + \alpha\int_0^t G_{\lambda,n}(t-t')\,\langle h(x_n(t'))\rangle\,\mathrm{d}t'\ , \tag{A.8}$$

where all terms of order $t^k \mathrm{e}^{-\lambda t}$ for $0 \le i \le n$ have been dropped.

A.2.2— Closed integro-differential equation for Γ

The differential equation (2.42) governing the time evolution of the autocorrelation Γ can be obtained as follows [94]. The time evolution of the correlation functions $\langle x_i(t)x_n(0)\rangle$ is calculated by the method presented in Sec. A.1. The resulting hierarchy of differential equations, similar to Eqs. (2.21–2.23), can be closed with a procedure analogous to the one that leads to Eq. (A.8). This yields

$$\frac{\mathrm{d}\Gamma}{\mathrm{d}t} \simeq -\kappa\Gamma(t) + \alpha \int_0^t G_{\lambda,n}(t-t')\,\Sigma(t')\,\mathrm{d}t' \;, \tag{A.9}$$

where

$$\Sigma(t) = \langle h(x_n(t'+t))x_n(t')\rangle - \langle h(x_n)\rangle\langle x_n\rangle \;. \tag{A.10}$$

Expansion of $h(x)$ to third order at $x = \bar{x}$, where $\bar{x}$ is the mean product level Eq. (2.44), yields

$$\begin{aligned}\Sigma(t) = {}& h'(\bar{x})\Gamma_2(x_n(t'+t), x_n(t')) \\ &+ \frac{h''(\bar{x})}{2}\Gamma_3(x_n(t'+t), x_n(t'+t), x_n(t')) \\ &+ \frac{h'''(\bar{x})}{6}\Big(3\Gamma_2(x_n(t'), x_n(t'))\Gamma_2(x_n(t'+t), x_n(t')) \\ &\qquad + \Gamma_4(x_n(t'+t), x_n(t'+t), x_n(t'+t), x_n(t'))\Big) \\ &+ \mathcal{O}(\langle(x_n-\bar{x})^4\rangle) \;,\end{aligned} \tag{A.11}$$

where Γ_m is the connected correlation function of m-th order, defined by

$$\Gamma_m(x_{i_1}(t_1), \ldots, x_{i_m}(t_m)) = (-\mathrm{i})^m \frac{\delta^m \log \mathcal{Z}}{\delta y_{i_1}(t_1)\ldots\delta y_{i_m}(t_m)}\bigg|_{y_1=0,\ldots,y_n=0} \;. \tag{A.12}$$

Here, $\delta/\delta y_i(t)$ denotes the functional derivative with respect to the function $y_i(t)$ and $\mathcal{Z}$ is the generating functional of the correlation functions, defined by [44]

$$\mathcal{Z} = \left\langle \exp\left(\mathrm{i}\sum_{i=1}^{n}\int y_i(t)x_i(t)\,\mathrm{d}t\right)\right\rangle \;. \tag{A.13}$$

Note that $\Gamma_2(x_n(t'+t), x_n(t')) = \Gamma(t)$, Eq. (2.41). We thus obtain a closed equation for Γ by neglecting all connected correlation functions of order $m = 3$ and higher in Eq. (A.11) [161],

$$\Sigma(t) \simeq \left(h'(\bar{x}) + h'''(\bar{x})\frac{\Gamma(0)}{2}\right)\Gamma(t) \;. \tag{A.14}$$

Using this result and the definition of η, Eq. (2.43), in Eq. (A.9), we obtain Eq. (2.42) [94].

A.3 Characteristic Equation for the Autocorrelation

A.3.1— Characterisic equation

We show the derivation of the approximate characteristic equation (2.46) from Eq. (2.42). Consider the integral

$$\Pi(t) = \int_0^t G_{\lambda,n}(t-t')\,\Gamma(t')\,\mathrm{d}t' \;, \tag{A.15}$$

which appears in Eq. (2.42). Using the definition of the Gamma distribution $G_{\lambda,n}$, Eq. (2.26), this integral can be expressed as

$$\begin{aligned} \Pi(t) &= \frac{\lambda^n}{(n-1)!}\int_0^t (t-t')^{n-1}\mathrm{e}^{-\lambda(t-t')}\,\Gamma(t')\,\mathrm{d}t' \\ &= \frac{\lambda^n}{(n-1)!}\left(-\frac{\partial}{\partial\lambda}\right)^{n-1}\int_0^t \mathrm{e}^{-\lambda(t-t')}\,\Gamma(t')\,\mathrm{d}t' \ . \end{aligned} \tag{A.16}$$

To find a characteristic equation for Γ, we use the exponential ansatz $\Gamma(t) = \mathrm{e}^{-zt}$ with $z = k + \mathrm{i}\omega$ as introduced in Sec. 2.2.4. Inserting this ansatz into Eq. (A.16) yields

$$\Pi(t) = \frac{\lambda^n}{(n-1)!}\left(-\frac{\partial}{\partial\lambda}\right)^{n-1}\frac{\mathrm{e}^{-zt}-\mathrm{e}^{-\lambda t}}{\lambda - z} \ . \tag{A.17}$$

We now assume the following hierarchy of time scales, motivated in Sec. 2.2.4,

$$k < \omega \ll \lambda \ . \tag{A.18}$$

Hence, if $\Pi(t)$ is evaluated at times larger than ω^{-1}, we can safely approximate $\mathrm{e}^{-\lambda t} \simeq 0$ and obtain

$$\Pi(t)\Big|_{t>\omega^{-1}} \simeq \mathrm{e}^{-zt}\left(\frac{\lambda}{\lambda - z}\right)^n \ . \tag{A.19}$$

Using this result in Eq. (2.42), we obtain the approximate characteristic equation (2.46).

A.3.2—Closed frequency estimate

We derive a closed analytical approximation for the oscillator frequency $\omega = \operatorname{Im} z$ from Eq. (2.46). Defining $r\mathrm{e}^{\mathrm{i}\theta} = \lambda - z = \lambda - k - \mathrm{i}\omega$, the characteristic equation (2.46) can be rewritten as

$$z = \kappa - \eta\frac{\lambda^n}{r^n}\mathrm{e}^{-\mathrm{i}n\theta} \ . \tag{A.20}$$

Using the hierarchy of time scales (A.18), we approximate

$$\begin{aligned} r^2 &= |\lambda - z|^2 \\ &= (\lambda - k)^2 + \omega^2 \\ &\simeq \lambda^2 + \omega^2 \end{aligned} \tag{A.21}$$

and

$$\begin{aligned} \tan\theta &= \frac{\operatorname{Im}(\lambda - z)}{\operatorname{Re}(\lambda - z)} \\ &= -\frac{\omega}{\lambda - k} \\ &\simeq -\frac{\omega}{\lambda} \ . \end{aligned} \tag{A.22}$$

Taking the imaginary part of Eq. (A.20) and using these approximations, we find an implicit equation for ω,

$$\omega \simeq -\eta\left(\frac{1}{1+\omega^2/\lambda^2}\right)^{n/2}\sin\left(n\arctan\frac{\omega}{\lambda}\right) \ . \tag{A.23}$$

We use Eq. (A.23) to compute a correction to the simple estimate Eq. (2.40) using the ansatz $\omega = \pi/u + \varepsilon$ and expanding Eq. (A.23) to first order in ε at $\varepsilon = 0$. This yields a closed equation for ε which can be solved exactly. The result for ω is given by

$$\begin{aligned} \omega &\simeq \pi \left[\frac{n}{\lambda} - \frac{1}{\eta} \left(1 + \frac{\pi^2}{n^2} \right)^{n/2+1} \right]^{-1} , \\ &= \frac{\pi}{u} \left(1 + \frac{1}{\eta u} \right) + \mathcal{O}(n^{-3}) , \end{aligned} \tag{A.24}$$

where $u = n/\lambda$ is the mean feedback delay, Eq. (2.27).

A.3.3— Approximation of η

We show how to derive Eq. (2.48) from the definition of η, Eq. (2.43),

$$\eta = \alpha h'(\bar{x}) + \alpha h'''(\bar{x}) \frac{\Gamma(0)}{2} , \tag{A.25}$$

where the mean product level $\bar{x}$ and the variance $\Gamma(0)$ of the product level are given by Eqs. (2.44) and (2.45). Using the explicit Hill-type form of h, Eq. (2.24), with Hill exponent $p = 2$, we find that its derivatives satisfy

$$h'(x) = -\frac{2}{q^2} x h(x)^2 , \tag{A.26a}$$

$$h'''(x) = \frac{1}{q} f(x) h''(x) , \tag{A.26b}$$

where

$$f(x) = -\frac{6x}{q} \left(\frac{1}{1 + (x/q)^2} + \frac{1}{1 - 3(x/q)^2} \right) . \tag{A.27}$$

Using Eqs. (A.26a,b) to replace the derivatives in Eq. (A.25), we obtain

$$\eta q = f_0 + \varepsilon f(\bar{x}) . \tag{A.28}$$

where

$$f_0 = -2\alpha \frac{\bar{x}}{q} h(\bar{x})^2 , \tag{A.29}$$

$$\varepsilon = \alpha h''(\bar{x}) \frac{\Gamma(0)}{2} . \tag{A.30}$$

Eq. (2.25), which describes the time evolution of $\langle x_n(t) \rangle$, can be used to obtain an expression for ε that only depends on $\bar{x}$, so that its dependence on the variance $\Gamma(0)$ can be eliminated: in Eq. (2.25), we expand the function $h(x)$ inside the expectation value to second order at $x = \bar{x}$, and consider the limit of large times, $t \to \infty$. In this limit, $\langle x_n(t)\rangle$ attains its steady state value $\bar{x}$, which implies $\mathrm{d}\langle x_n\rangle/\mathrm{d}t \to 0$ and thus

$$\begin{aligned}
0 &\simeq \lim_{t\to\infty}\left(-\kappa\langle x_n(t)\rangle + \alpha\int_0^t G_{\lambda,n}(t-t')\,\langle h(x_n(t'))\rangle\,\mathrm{d}t'\right)\\
&\simeq -\kappa\bar{x} + \alpha\lim_{t\to\infty}\int_0^t G_{\lambda,n}(t-t')\,\bigg(h(\bar{x}) + h'(\bar{x})(\langle x_n(t')\rangle - \bar{x})\\
&\qquad\qquad\qquad\qquad + \frac{h''(\bar{x})}{2}(\langle x_n(t')^2\rangle - \bar{x}^2)\bigg)\,\mathrm{d}t'\\
&= -\kappa\bar{x} + \alpha\left(h(\bar{x}) + h'(\bar{x})(\bar{x}-\bar{x}) + h''(\bar{x})\frac{\Gamma(0)}{2}\right)\lim_{t\to\infty}\int_0^t G_{\lambda,n}(t-t')\,\mathrm{d}t'\\
&= -\kappa\bar{x} + \alpha\left(h(\bar{x}) + h''(\bar{x})\frac{\Gamma(0)}{2}\right)\ ,\\
&= -\kappa\bar{x} + \alpha h(\bar{x}) + \varepsilon\ ,
\end{aligned} \tag{A.31}$$

where in the last identity, we have used the definition of ε, Eq. (A.30). We can solve this equation for ε and obtain

$$\varepsilon \simeq \kappa\bar{x} - \alpha h(\bar{x})\ . \tag{A.32}$$

We have thus eliminated $\Gamma(0)$ from the equation for η. The only remaining unknown is the mean product level $\bar{x}$. We estimate $\bar{x}$ through the method introduced in Sec. 2.2.3 as $\bar{x} \simeq x^*$ with x^* defined in Eq. (2.37). Since x^* satisfies $\kappa x^* - \alpha h(x^*) = 0$ (see Sec. 2.2.3) implying $\varepsilon \simeq 0$, it seems natural to approximate the term $\varepsilon f(\bar{x})$ in Eq. (A.28) to zero. Indeed, we expect that ε is much smaller than each of the contributions in Eq. (A.32),

$$\varepsilon \ll \kappa\bar{x}\ , \tag{A.33a}$$

$$\varepsilon \ll \alpha h(\bar{x})\ , \tag{A.33b}$$

but, since $\bar{x} \simeq x^*$ only holds approximately, $\varepsilon \neq 0$. Hence, we have to analyze the magnitude of $f(\bar{x})$ and confirm that it does not spoil the approximation $\varepsilon f(\bar{x}) \simeq 0$. To this end, we compare the term $\varepsilon f(\bar{x})$ to the contribution f_0 in Eq. (A.28). We assume that $\bar{x} \sim q$ (where $\sim$ denotes 'of the same order as') and later show that this is the case for typical scenarios. For $x > q$, it is straightforward to obtain the bounds

$$h(x) < 0.5 \qquad \text{for } x > q\ , \tag{A.34a}$$

$$|f(x)| < 1.32 \qquad \text{for } x > q\ . \tag{A.34b}$$

Using these bounds and assuming $\bar{x} \sim q$, we find from Eq. (A.29) that $f_0 \sim \alpha$. Ineqs. (A.33b) and (A.34b) imply $\varepsilon f(\bar{x}) \ll \alpha h(\bar{x}) < \alpha$. Taken together, we obtain $\varepsilon f(\bar{x}) \ll f_0$. These considerations show that under the condition $\bar{x} \sim q$, neglecting the term $\varepsilon f(\bar{x})$ in Eq. (A.28) is warranted. We now have to evaluate under which circumstances $\bar{x} \sim q$ and to this end, we use the approximation $x \simeq x^*$ introduced above. Using the definition of x^*, Eq. (2.37), we find that $x^* > q$ if the condition

$$g_0 > 1 \tag{A.35}$$

holds, where $g_0 = \alpha/2\kappa q$ has been defined in Eq. (2.38). For typical parameter values for which the system exhibits oscillations, this threshold is satisfied, see Fig. 2.6. Our approximation $\varepsilon f(\bar{x}) \simeq 0$ thus relies on the condition (A.35) to be fulfilled. From Eq. (A.28), we thus obtain

$$\eta \simeq \alpha h'(x^*) \ , \tag{A.36}$$

where we have used the identity (A.26) to restore the original form of the contribution f_0, given in Eq. (A.25). With the definitions of h, Eq. (2.24), and x^*, Eq. (2.37), this equation yields an explicit analytical estimate for η. However, the resulting expression is lengthy and can be further simplified. The estimate x^* for the mean product level, Eq. (2.37), depends on the two dimensionless quantities g_0 and g_1, Eqs. (2.38) and (2.39). Since our approximation only holds under the condition (A.35), we can assume that $g_0^2 \gg 1/27$ and Eq. (2.39) can thus be approximated by

$$g_1 \simeq (2g_0)^{1/3} \ . \tag{A.37}$$

This yields

$$\eta \simeq 2\kappa \frac{g_1^2(1-3g_1^2)}{1/3+g_1^2(2+3g_1^2)} \ . \tag{A.38}$$

The condition (A.35) implies $g_1 > 2^{1/3}$, which implies $g_1^2(2+3g_1^2) > 10.7$ for the second term in the denominator. We can thus safely neglect the term $1/3$ in the denominator and obtain

$$\eta \simeq 2\kappa \frac{1-3g_1^2}{2+3g_1^2} = -2\kappa \left(1 - \frac{1}{2/3+g_1^2}\right) \ . \tag{A.39}$$

Using Eq. (A.37) and the definition of g_0, Eq. (2.38), we thus obtain Eq. (2.48).

Appendix B

Phase Oscillators with Distributed Delays

B.1 Phase Dynamics with Distributed Delays

We seek a description of coupled oscillators in terms of their phase dynamics that takes into account a distribution of delay times in the coupling. We demand that the dynamics of this equation is invariant under the transformation

$$\phi_\mu \to (\phi_\mu \bmod 2\pi) \ , \tag{B.1}$$

where ϕ_μ is the dynamical phase. The invariance of the dynamics under the transformation (B.1) characterizes the parametrization of a limit cycle in terms of a phase variable [107]. To include distributed delay times into a phase oscillator description, we first consider phase dynamics without coupling delays, given by [77]

$$\frac{\mathrm{d}\phi_\mu}{\mathrm{d}t} = \omega_\mu + \frac{\varepsilon_\mu}{u_\mu} \sum_\nu c_{\mu\nu} \sin(\phi_\nu - \phi_\mu) \ , \tag{B.2}$$

where ϕ_μ is the phase of oscillator μ, ω_μ is its intrinsic frequency, ε_μ is the coupling strength, $c_{\mu\nu}$ is an adjacency matrix that encodes the coupling topology, and $u_\mu = \sum_\nu c_{\mu\nu}$ is the number of oscillators that oscillator μ couples to. The strategy pursued here is to write the phase equation without delays in terms of the complex oscillatory signal

$$X_\mu = \mathrm{e}^{\mathrm{i}\phi_\mu} \tag{B.3}$$

and then include distributed delays in the signals X_ν of the sending oscillators. This procedure preserves the invariance of the dynamics under the transformation (B.1) and intuitively accounts for the fact that it is information about the oscillatory signal rather than the phase that is transmitted between oscillators via coupling. The time evolution of X_μ can be obtained using Eq. (B.2),

$$\frac{\mathrm{d}X_\mu}{\mathrm{d}t} = \mathrm{i}\omega_\mu X_\mu + \mathrm{i}\varepsilon_\mu X_\mu \operatorname{Im} Z_\mu X_\mu^* \ , \tag{B.4}$$

where $Z_\mu = u_\mu^{-1} \sum_\nu c_{\mu\nu} X_\nu$ represents the combined signals of the sending oscillators[1]. We introduce a distribution $G(t)$ of delay times in the signal Z_μ through the replacement

---

[1] Note that the Z_μ are order parameters associated to the adjacency matrix $c_{\mu\nu}$. For the case of global coupling, $c_{\mu\nu} = 1$, we recover the Kuramoto order parameter $Z_\mu = Z = n^{-1} \sum_{\nu=1}^{n} \mathrm{e}^{\mathrm{i}\phi_\nu}$, where n is the total number of oscillators [77].

$$Z_\mu(t) \to \int_0^\infty G(t')\, Z_\mu(t-t')\,\mathrm{d}t' \ , \tag{B.5}$$

which yields

$$\frac{\mathrm{d}X_\mu}{\mathrm{d}t} = \mathrm{i}\omega_\mu X_\mu(t) + \mathrm{i}\varepsilon_\mu X_\mu(t) \,\mathrm{Im} \int_0^\infty G(t')\, Z_\mu(t-t') X_\mu^*(t)\,\mathrm{d}t' \ . \tag{B.6}$$

Transforming this equation back to a phase equation yields

$$\begin{aligned} \frac{\mathrm{d}\phi_\mu}{\mathrm{d}t} &= \frac{1}{\mathrm{i}X_\mu}\frac{\mathrm{d}X_\mu}{\mathrm{d}t} \\ &= \omega_\mu + \varepsilon_\mu \sum_\nu c_{\mu\nu} \int_0^\infty G(t') \sin(\phi_\nu(t-t') - \phi_\mu(t))\,\mathrm{d}t' \ . \end{aligned} \tag{B.7}$$

For the case of two identical coupled oscillators, in which $\omega_\mu = \omega$, $\varepsilon_\mu = \varepsilon$, and

$$(c_{\mu\nu}) = \begin{pmatrix} 0 & 1 \\ 1 & 0 \end{pmatrix} \ , \tag{B.8}$$

we obtain Eq. (2.55).

Alternative approaches to account for the effects of distributed coupling delays on oscillator dynamics have been forwarded by others [7, 156]. In these approaches, the integral over delay times appears inside the coupling function instead of outside as in Eq. (B.7). This yields qualitatively different results. However, to describe the negative-feedback oscillator presented in Chapter 2 of this Thesis, the above description is the appropriate one as demonstrated in Sec. 2.4.

B.2 Analytical Results for Synchronized States

B.2.1— Collective frequency

In this section, we derive Eq. (2.58) for the collective frequency of the in-phase synchronized state of two coupled phase oscillators with distributed coupling delays. We will recast occurring expressions into a form where we can use the identity

$$\int_0^\infty t^{n-1}\mathrm{e}^{-zt}\,\mathrm{d}t = \frac{(n-1)!}{z^n} \tag{B.9}$$

for $z \in \mathbb{C}$, given that $\mathrm{Re}\, z > 0$ and $n \in \mathbb{N}$. Using the in-phase synchronized state ansatz $\phi_\mu(t) = \Omega t$ and the definition of the Gamma distribution $G_{\tilde\lambda,\tilde n}$, Eq. (2.49), in Eq. (2.55) yields

$$\begin{aligned} \Omega &= \omega - \varepsilon \frac{\tilde\lambda^{\tilde n}}{(\tilde n-1)!} \int_0^\infty t^{\tilde n-1}\mathrm{e}^{-\tilde\lambda t} \sin(\Omega t)\,\mathrm{d}t \\ &= \omega - \varepsilon \frac{\tilde\lambda^{\tilde n}}{(\tilde n-1)!}\,\mathrm{Im} \int_0^\infty t^{\tilde n-1}\mathrm{e}^{-(\tilde\lambda - \mathrm{i}\Omega)t}\,\mathrm{d}t \\ &= \omega - \varepsilon\tilde\lambda^{\tilde n}\,\mathrm{Im}\,\frac{1}{(\tilde\lambda-\mathrm{i}\Omega)^{\tilde n}} \end{aligned} \tag{B.10}$$

In the last equality, Eq. (B.9) was used. We define $r\mathrm{e}^{\mathrm{i}\theta} = \tilde{\lambda} - \mathrm{i}\Omega$ and obtain

$$\begin{aligned}
\Omega &= \omega - \varepsilon\tilde{\lambda}^{\tilde{n}} \operatorname{Im} \frac{\mathrm{e}^{-\mathrm{i}\tilde{n}\theta}}{r^{\tilde{n}}} \\
&= \omega + \varepsilon \frac{\tilde{\lambda}^{n}}{r^{\tilde{n}}} \sin(\tilde{n}\theta) \\
&= \omega - \varepsilon \left(\frac{1}{1 + \Omega^2/\tilde{\lambda}^2} \right)^{\tilde{n}/2} \sin\left(\tilde{n} \arctan \frac{\Omega}{\tilde{\lambda}} \right) ,
\end{aligned} \tag{B.11}$$

which is Eq. (2.58). Note that the simple identity $\theta = \arctan \Omega/\tilde{\lambda}$ holds since $\tilde{\lambda} > 0$.

B.2.2—Characteristic equation

In this section, we derive the characteristic equation (2.67), which determines the stability of the in-phase synchronized state of of two coupled phase oscillators with distributed coupling delays. Eq. (2.66) can be rewritten as

$$\frac{\gamma_\nu}{\varepsilon} = \nu E(\gamma_\nu) - E(0) , \tag{B.12}$$

where

$$E(\gamma) = \int_0^\infty G_{\tilde{\lambda},\tilde{n}}(t) \cos(\Omega t)\, \mathrm{e}^{-\gamma t}\, \mathrm{d}t . \tag{B.13}$$

For notational simplicity, we define

$$\begin{aligned}
\gamma &= \gamma' + \mathrm{i}\gamma'' , \\
a &= \tilde{\lambda} + \gamma' , \\
b_\pm &= \Omega \pm \gamma'' , \\
z_\pm &= a - \mathrm{i}b_\pm ,
\end{aligned} \tag{B.14}$$

and remind the reader of the trigonometric identities

$$(\cos x)(\cos y) = \frac{\cos(x+y) + \cos(x-y)}{2} , \tag{B.15a}$$

$$(\sin x)(\cos y) = \frac{\sin(x+y) + \sin(x-y)}{2} . \tag{B.15b}$$

Using the definition of the Gamma distribution, Eq. (2.26), we obtain for Eq. (B.13)

$$\begin{aligned}
E(\gamma) &= \frac{\tilde{\lambda}^{\tilde{n}}}{(\tilde{n}-1)!} \int_0^\infty t^{\tilde{n}-1} \mathrm{e}^{-(\tilde{\lambda}+\gamma)t} \cos(\Omega t)\, \mathrm{d}t \\
&= \frac{\tilde{\lambda}^{\tilde{n}}}{(\tilde{n}-1)!} \Bigg(\int_0^\infty t^{\tilde{n}-1} \mathrm{e}^{-(\tilde{\lambda}+\gamma')t} \cos(\gamma'' t) \cos(\Omega t)\, \mathrm{d}t \\
&\qquad\qquad - \mathrm{i} \int_0^\infty t^{\tilde{n}-1} \mathrm{e}^{-(\tilde{\lambda}+\gamma')t} \sin(\gamma'' t) \cos(\Omega t)\, \mathrm{d}t \Bigg) \\
&= \frac{\tilde{\lambda}^{\tilde{n}}}{(\tilde{n}-1)!} \Bigg(\int_0^\infty t^{\tilde{n}-1} \mathrm{e}^{-at} \frac{\cos(b_+ t) + \cos(b_- t)}{2}\, \mathrm{d}t \\
&\qquad\qquad - \mathrm{i} \int_0^\infty t^{\tilde{n}-1} \mathrm{e}^{-at} \frac{\sin(b_+ t) - \sin(b_- t)}{2}\, \mathrm{d}t \Bigg) \\
&= \frac{1}{2} \frac{\tilde{\lambda}^{\tilde{n}}}{(\tilde{n}-1)!} \Bigg(\operatorname{Re} \int_0^\infty t^{\tilde{n}-1} \left(\mathrm{e}^{-z_+ t} + \mathrm{e}^{-z_- t} \right) \mathrm{d}t
\end{aligned}$$

$$
\begin{aligned}
&\qquad - \mathrm{i}\,\mathrm{Im} \int_0^\infty t^{\tilde{n}-1} \left(\mathrm{e}^{-z_+ t} - \mathrm{e}^{-z_- t} \right) \, \mathrm{d}t \Bigg) \\
&= \frac{1}{2} \frac{\tilde{\lambda}^{\tilde{n}}}{(\tilde{n}-1)!} \left(\mathrm{Re}\, \frac{(\tilde{n}-1)!}{z_+^{\tilde{n}}} + \mathrm{Re}\, \frac{(\tilde{n}-1)!}{z_-^{\tilde{n}}} - \mathrm{i}\,\mathrm{Im}\, \frac{(\tilde{n}-1)!}{z_+^{\tilde{n}}} + \mathrm{i}\,\mathrm{Im}\, \frac{(\tilde{n}-1)!}{z_-^{\tilde{n}}} \right) \\
&= \frac{\tilde{\lambda}^{\tilde{n}}}{2} \left(\mathrm{Re}\, z_+^{-\tilde{n}} - \mathrm{i}\,\mathrm{Im}\, z_+^{-\tilde{n}} + \mathrm{Re}\, z_-^{-\tilde{n}} + \mathrm{i}\,\mathrm{Im}\, z_-^{-\tilde{n}} \right) \\
&= \frac{\tilde{\lambda}^{\tilde{n}}}{2} \left[(z_+^{-\tilde{n}})^* + z_-^{-\tilde{n}} \right] \\
&= \frac{\tilde{\lambda}^{\tilde{n}}}{2} \left[(z_+^*)^{-\tilde{n}} + z_-^{-\tilde{n}} \right] \\
&= \frac{\tilde{\lambda}^{\tilde{n}}}{2} \left(\frac{1}{(\tilde{\lambda} + \gamma + \mathrm{i}\Omega)^{\tilde{n}}} + \frac{1}{(\tilde{\lambda} + \gamma - \mathrm{i}\Omega)^{\tilde{n}}} \right) .
\end{aligned}
$$

The characteristic equation (2.67) follows from this.

Appendix C

Spatial Continuum Limits of Coupled Phase Oscillators

In this appendix, we provide the derivation of the spatial continuum limits of coupled phase oscillators with and without coupling delays used in Chapter 3. These continuum limits are viable for long-wavelength solutions in which the phase differences between neighboring oscillators are small in a sense specified below. The resulting continuum theories are more amenable to analytical manipulations than the discrete theories they are derived from.

C.1 Continuum Limit of Coupled Oscillators

C.1.1—Derivation of the continuum limit

We start with a system of phase oscillators with nearest-neighbor coupling in $d = 1$ dimension,

$$\frac{\mathrm{d}\varphi_\mu}{\mathrm{d}t} = \omega_\mu + \frac{\tilde{\varepsilon}_\mu}{u_\mu} \sum_{\nu=\pm 1} g(\varphi_{\mu+\nu}(t) - \varphi_\mu(t)) \ . \tag{C.1}$$

Here, φ_μ is the phase of oscillator μ, ω_μ is its intrinsic frequency, $\tilde{\varepsilon}_\mu$ is its coupling strength, u_μ is the number of neighbors of oscillator μ, and g is a 2π-periodic coupling function. We replace the discrete lattice of oscillators φ_μ by a continuous phase field $\varphi(x,t)$ and assume an infinite chain of oscillators, for which the number of neighbors is given by $u_\mu = 2$. Furthermore, we assume that there are continuous interpolations of the intrinsic frequency and the coupling strength, $\omega(x,t)$ and $\tilde{\varepsilon}(x,t)$, which satisfy $\omega(\mu s, t) = \omega_\mu(t)$ and $\tilde{\varepsilon}(\mu s, t) = \tilde{\varepsilon}_\mu(t)$, where s is the lattice spacing. The generalized dynamics of φ is given by

$$\frac{\partial \varphi}{\partial t}(x,t) = \omega(x,t) + \frac{\tilde{\varepsilon}(x,t)}{2} \sum_{\nu=\pm 1} g(\varphi(x+\nu s, t) - \varphi(x,t)) \ . \tag{C.2}$$

The long-wavelength approximation that we introduce relies on two assumptions: (i) the phase differences on the length scale s are small in the sense that the coupling function g can be approximated by the first terms of its power series expansion[1], and (ii) the variation of φ on the length scale of s does not significantly differ from a quadratic behavior[2].

---

[1] For the common choice $g(\varphi) = \sin\varphi$, a second order expansion of g about an arbitrary expansion point φ_0 yields a reasonable approximation for $|\varphi - \varphi_0| \lesssim \pi/4$.

[2] Note that these two assumptions do not imply each other. For instance, assumption (ii) is fulfilled for $\varphi(x) = px$ with arbitrary p, which however violates assumption (i) for sufficiently large p. Likewise, assumption (i) is fulfilled for $\varphi(x) = q \sin px$ with sufficiently small q and arbitrary p, which however violates assumption (ii) for sufficiently large p.

Using assumption (i), we rewrite the argument of the coupling function as $\varphi(x+\nu s,t)-\varphi(x,t)=\gamma\Delta_\nu(x,t)$, where Δ_ν is a function of order unity and γ is small in the above sense. We expand the coupling function to second order in γ,

$$g(\gamma\Delta_\nu)=g(0)+g'(0)(\gamma\Delta_\nu)+\frac{1}{2}g''(0)(\gamma\Delta_\nu)^2+\mathcal{O}(\gamma^3)\ . \tag{C.3}$$

Using assumption (ii), we expand the function $\gamma\Delta_\nu$ to second order in s,

$$\gamma\Delta_\nu=\nu s\frac{\partial\varphi}{\partial x}+\frac{s^2}{2}\frac{\partial^2\varphi}{\partial x^2}+\mathcal{O}(s^3)\ , \tag{C.4}$$

where we have used $\nu^2=1$. Using this expansion in Eq. (C.3), we obtain

$$g(\gamma\Delta_\nu)=g(0)+\nu s g'(0)\frac{\partial\varphi}{\partial x}+\frac{s^2}{2}g''(0)\left(\frac{\partial\varphi}{\partial x}\right)^2+\frac{s^2}{2}g'(0)\frac{\partial^2\varphi}{\partial x^2}+\mathcal{O}(s^3)\ . \tag{C.5}$$

Dropping all orders higher than quadratic in s, and using this expansion in Eq. (C.2) thus yields

$$\frac{\partial\varphi}{\partial t}=\omega+\tilde{\varepsilon}g(0)+\frac{\tilde{\varepsilon}s^2}{2}g''(0)\left(\frac{\partial\varphi}{\partial x}\right)^2+\frac{\tilde{\varepsilon}s^2}{2}g'(0)\frac{\partial^2\varphi}{\partial x^2}\ . \tag{C.6}$$

Note that terms of linear order in s cancel out. This implies that keeping only zeroth order terms yields an equation that is exact to first order in s. Similar derivations for coupled phase oscillator systems without delays have been presented previously, see, e.g., Ref. [96].

C.1.2— Phase dynamics in a comoving frame

We now derive the dynamic equation for the phase field in a co-moving reference frame with speed v_0,

$$\phi(x,t)=\varphi(x-v_0t,t)\ . \tag{C.7}$$

The time evolution of ϕ is therefore given by

$$\frac{\partial\phi}{\partial t}=-v_0\frac{\partial\varphi}{\partial x}(x-v_0t,t)+\frac{\partial\varphi}{\partial t}(x-v_0t,t)\ . \tag{C.8}$$

The resulting terms can be expressed in terms of ϕ using $\varphi(x,t)=\phi(x+v_0t,t)$. We thus obtain

$$\frac{\partial\phi}{\partial t}+v_0\frac{\partial\phi}{\partial x}=\omega+\tilde{\varepsilon}g(0)+\frac{\tilde{\varepsilon}s^2}{2}g''(0)\left(\frac{\partial\phi}{\partial x}\right)^2+\frac{\tilde{\varepsilon}s^2}{2}g'(0)\frac{\partial^2\phi}{\partial x^2} \tag{C.9}$$

For the case of sinusoidal coupling, $g(\varphi)=\sin\varphi$, we obtain $g(0)=g''(0)=0$ and $g'(0)=1$. Hence, we find Eq. (3.1) using the renormalized coupling strength

$$\varepsilon=s^2\tilde{\varepsilon}\ , \tag{C.10}$$

which has the dimension of a diffusion constant.

C.2 Continuum Limit of Delay-Coupled Oscillators

C.2.1— Derivation of the continuum limit

We now extend the derivation presented in the previous section to a system of coupled oscillators with discrete coupling delays. We have presented this derivation in Ref. [5]. We start with a system of phase oscillators with nearest-neighbor coupling and coupling delays in $d = 1$ dimension,

$$\frac{\mathrm{d}\varphi_\mu}{\mathrm{d}t} = \omega_\mu + \frac{\tilde{\varepsilon}_\mu}{2} \sum_{\nu=\pm 1} g(\varphi_{\mu+\nu}(t-\tau) - \varphi_\mu(t)) \ , \tag{C.11}$$

where $\tau > 0$ is the coupling delay and all other parameters are the same as in Eq. (C.1). We repeat the steps in Sec. C.1 and write down the corresponding equation for a continuous phase field $\varphi(x, t)$,

$$\frac{\partial \varphi}{\partial t}(x,t) = \omega(x,t) + \frac{\tilde{\varepsilon}(x,t)}{2} \sum_{\nu=\pm 1} g(\varphi(x+\nu s, t-\tau) - \varphi(x,t)) \ . \tag{C.12}$$

We introduce the notation

$$\varphi_\tau(x,t) = \varphi(x, t-\tau) \ , \tag{C.13}$$

$$\varphi_{\nu,\tau}(x,t) = \varphi(x+\nu s, t-\tau) \ , \tag{C.14}$$

and rewrite Eq. (C.12) as

$$\frac{\partial \varphi}{\partial t} = \omega + \frac{\tilde{\varepsilon}}{2} \sum_{\nu=\pm 1} g(\varphi_{\nu,\tau} - \varphi) \ . \tag{C.15}$$

We decompose the argument of the coupling function $\varphi_{\nu,\tau} - \varphi = (\varphi_{\nu,\tau} - \varphi_\tau) + (\varphi_\tau - \varphi)$ into a part that is local in time but non-local in space, $\varphi_{\nu,\tau} - \varphi_\tau$, and a part that is local in space but non-local in time, $\varphi_\tau - \varphi$. Using the same argument as in Sec. C.1, we define $\gamma\Delta_{\nu,\tau} = \varphi_{\nu,\tau} - \varphi_\tau$, and expand the coupling function to second order in γ,

$$\begin{aligned} g(\varphi_{\nu,\tau} - \varphi) &= g(\varphi_\tau - \varphi + \gamma\Delta_{\nu,\tau}) \\ &= g(\varphi_\tau - \varphi) + g'(\varphi_\tau - \varphi)(\gamma\Delta_{\nu,\tau}) + \frac{1}{2} g''(\varphi_\tau - \varphi)(\gamma\Delta_{\nu,\tau})^2 + \mathcal{O}(\gamma^3) \end{aligned} \tag{C.16}$$

In the spirit of Sec. C.1, we expand the function $\gamma\Delta_{\nu,\tau}$ to second order in s,

$$\gamma\Delta_{\nu,\tau} = \nu s \frac{\partial \varphi_\tau}{\partial x} + \frac{s^2}{2} \frac{\partial^2 \varphi_\tau}{\partial x^2} + \mathcal{O}(s^3) \ . \tag{C.17}$$

Using this expansion in Eq. (C.16), we obtain

$$\begin{aligned} g(\varphi_{\nu,\tau} - \varphi) = g(\varphi_\tau - \varphi) + \nu s g'(\varphi_\tau - \varphi) \frac{\partial \varphi_\tau}{\partial x} + \frac{s^2}{2} g''(\varphi_\tau - \varphi) \left(\frac{\partial \varphi_\tau}{\partial x} \right)^2 \\ + \frac{s^2}{2} g'(\varphi_\tau - \varphi) \frac{\partial^2 \varphi_\tau}{\partial x^2} + \mathcal{O}(s^3) \ . \end{aligned} \tag{C.18}$$

Dropping all orders higher than quadratic in s, and using this expansion in Eq. (C.15) thus yields

$$\frac{\partial \varphi}{\partial t} = \omega + \tilde{\varepsilon} g(\varphi_\tau - \varphi) + \frac{\tilde{\varepsilon} s^2}{2} g''(\varphi_\tau - \varphi) \left(\frac{\partial \varphi_\tau}{\partial x} \right)^2 + \frac{\tilde{\varepsilon} s^2}{2} g'(\varphi_\tau - \varphi) \frac{\partial^2 \varphi_\tau}{\partial x^2} \ . \tag{C.19}$$

Note that terms of linear order in s cancel out. The extension of this derivation to nearest-neighbor coupled oscillators on cubic lattices in arbitrary dimension d is straightforward. Introducing a phase field $\varphi(\mathbf{x}, t)$ with $\mathbf{x} \in \mathbb{R}^d$, we obtain

$$\frac{\partial \varphi}{\partial t} = \omega + \tilde{\varepsilon} g(\varphi_\tau - \varphi) + \frac{\tilde{\varepsilon} s^2}{2d} g''(\varphi_\tau - \varphi)(\nabla \varphi_\tau)^2 + \frac{\tilde{\varepsilon} s^2}{2d} g'(\varphi_\tau - \varphi) \nabla^2 \varphi_\tau \ , \tag{C.20}$$

where $\nabla = (\partial/\partial x_1, \ldots, \partial/\partial x_d)^{\mathrm{T}}$.

C.2.2— Phase dynamics in a comoving frame

We now derive the dynamic equation for the phase field in a co-moving reference frame with speed v_0,

$$\phi(x,t) = \varphi(x - v_0 t, t) \ . \tag{C.21}$$

The time evolution of ϕ is therefore given by

$$\frac{\partial \phi}{\partial t} = -v_0 \frac{\partial \varphi}{\partial x}(x - v_0 t, t) + \frac{\partial \varphi}{\partial t}(x - v_0 t, t) \ . \tag{C.22}$$

We use Eq. (C.19) to replace the partial time derivative of φ. The resulting terms can be expressed in terms of ϕ using $\varphi(x,t) = \phi(x + v_0 t, t)$,

$$\varphi(x - v_0 t, t) = \phi(x,t) \ , \tag{C.23}$$

$$\begin{aligned} \varphi_\tau(x - v_0 t, t) &= \varphi(x - v_0 t, t - \tau) \\ &= \phi(x - v_0 t + v_0(t-\tau), t - \tau) \\ &= \phi(x - v_0 \tau, t - \tau) \\ &\equiv \bar{\phi}_\tau(x,t) \ . \end{aligned} \tag{C.24}$$

We thus obtain

$$\begin{aligned} \frac{\partial \phi}{\partial t} + v_0 \frac{\partial \phi}{\partial x} = \omega + \tilde{\varepsilon} g(\bar{\phi}_\tau - \phi) + \frac{\tilde{\varepsilon} s^2}{2} g''(\bar{\phi}_\tau - \phi) \left(\frac{\partial \bar{\phi}_\tau}{\partial x} \right)^2 \\ + \frac{\tilde{\varepsilon} s^2}{2} g'(\bar{\phi}_\tau - \phi) \frac{\partial^2 \bar{\phi}_\tau}{\partial x^2} \ . \end{aligned} \tag{C.25}$$

We find Eq. (3.21) for the case of sinusoidal coupling, $g(\varphi) = \sin\varphi$, using the renormalized coupling constant ε, Eq. (C.10), and the renormalizing factor

$$Z = \frac{1}{s^2} \ . \tag{C.26}$$

C.3 Steady State Solution

C.3.1— Phase profile

For time-independent frequency and coupling profiles, $\omega(x,t) = \omega(x)$ and $\tilde{\varepsilon}(x,t) = \tilde{\varepsilon}(x)$, the system described by Eq. (C.19) can exhibit a steady state solution of the type Eq. (3.13), $\phi(x,t) = \Omega t + \psi(x)$. Using this ansatz and the definition $\bar{\psi}_\tau(x) = \psi(x - v_0 \tau)$, we find

$$\begin{aligned} \Omega + v_0 \frac{\mathrm{d}\psi}{\mathrm{d}x} = \omega + \tilde{\varepsilon} g(\bar{\psi}_\tau - \psi - \Omega\tau) - \frac{\tilde{\varepsilon} s^2}{2} g''(\bar{\psi}_\tau - \psi - \Omega\tau) \left(\frac{\mathrm{d}\bar{\psi}_\tau}{\mathrm{d}x} \right)^2 \\ + \frac{\tilde{\varepsilon} s^2}{2} g'(\bar{\psi}_\tau - \psi - \Omega\tau) \frac{\mathrm{d}^2 \bar{\psi}_\tau}{\mathrm{d}x^2} \ , \end{aligned} \tag{C.27}$$

which can be solved given appropriate boundary conditions. For the case of sinusoidal coupling, $g(\varphi) = \sin\varphi$, using the renormalized coupling constant ε, Eq. (C.10), and the renormalizing factor Z, Eq. (C.26), we find Eq. (3.21).

Appendix D

Analytical Approximation of Doppler Effect and Dynamic Wavelength Effect

In this appendix, we derive the approximate relation Eq. (3.45) between the anterior and the posterior frequency for a presomitic mesoderm whose length decreases linearly with time. This approximation is valid if (i) the effects of coupling on pattern formation are weak (see Sec. 3.1) and (ii) the approximation of the velocity profile by a constant, $v(x) \simeq v_0$, does not yield a significantly different kinematic wave pattern (see Sec. 3.3). We thus approximate the dynamic equation (3.32) by

$$\frac{\partial \phi}{\partial t} + v_0 \frac{\partial \phi}{\partial x} = \omega(x/a(t)) \ , \tag{D.1}$$

where $a(t)$ is the time-dependent length of the presomitic mesoderm. The general solution to this equation is given by

$$\phi(x,t) = \psi(t - x/v_0) + \frac{1}{v_0} \int_0^x \omega\left(\frac{x'}{a(t-(x-x')/v_0)} \right) \mathrm{d}x' \ , \tag{D.2}$$

where the function $\psi(u)$ depends on the initial and boundary conditions. The partial derivatives of this solution are given by

$$\frac{\partial \phi}{\partial t}(x,t) = \quad \dot{\psi}(t - x/v_0) - \nu(x,t) \ , \tag{D.3}$$

$$v_0 \frac{\partial \phi}{\partial x}(x,t) = -\dot{\psi}(t - x/v_0) + \nu(x,t) + \omega(x/a(t)) \ , \tag{D.4}$$

where $\dot{\psi} = \mathrm{d}\psi/\mathrm{d}u$, and

$$\nu(x,t) = \frac{1}{v_0} \int_0^x x' \frac{\dot{a}(t-(x-x')/v_0)}{a(t-(x-x')/v_0)^2} \ \omega'\left(\frac{x'}{a(t-(x-x')/v_0)} \right) \mathrm{d}x' \ , \tag{D.5}$$

with $\dot{a} = \mathrm{d}a/\mathrm{d}t$. Note that for $\dot{a} = 0$, we find $\nu = 0$.

The explicit form of $\psi(u)$ can be found using initial and boundary conditions. We evaluate Eq. (D.4) at $x = 0$ using open boundary conditions, $\partial\phi/\partial x|_{x=0} = 0$, Eq. (3.4), to obtain

$$\dot{\psi}(t) = \omega_0 \ . \tag{D.6}$$

Using the initial condition $\phi|_{t=0} = 0$ and evaluating Eq. (D.2) at $t = 0$, we likewise find

$$\psi(-x/v_0) = -\frac{1}{v_0} \int_0^x \omega\left(\frac{x'}{a(-(x-x')/v_0)} \right) \mathrm{d}x' \ . \tag{D.7}$$

Since we solve for $\phi(x,t)$ in the domain $t>0$, $x>0$, Eq. (D.6) determines $\psi(u)$ for $u>0$ whereas Eq. (D.7) determines $\psi(u)$ for $u<0$. According to Eq. (D.2), $u>0$ describes the solution at positions $x<v_0 t$. We are only interested in the behavior of the anterior frequency at large times, for which $a(t)<v_0 t$, and thus neglect the solution of $\psi(u)$ for $u<0$. From Eq. (D.6), we thus obtain

$$\psi(u)\Big|_{u>0} = \omega_0 u \ , \tag{D.8}$$

where we have set the arbitrary integration constant to zero. Using Eq. (D.8) in Eqs. (D.3) and (D.4), we find for the anterior frequency Ω_{A}, Eq. (3.39),

$$\begin{aligned}\Omega_{\mathrm{A}}(t) &= \frac{\partial\phi}{\partial t}(a(t),t) + \dot{a}\frac{\partial\phi}{\partial x}(a(t),t)\\ &= \omega_0 - \nu_{\mathrm{A}}(t) + \frac{\dot{a}}{v_0}\left[\omega_1 - \omega_0 + \nu_{\mathrm{A}}(t)\right]\\ &= \left(1-\frac{\dot{a}}{v_0}\right)\left[\omega_0 - \nu_{\mathrm{A}}(t)\right] + \frac{\dot{a}\omega_1}{v_0}\end{aligned} \tag{D.9}$$

where $\nu_{\mathrm{A}}(t) = \nu(a(t),t)$ and $\omega_1 = \omega(1)$. So far, we have not assumed a specific time-dependence of $a(t)$ and the result is completely general. We now consider linear tissue shortening with shortening speed v_*,

$$a(t) = a_0 - v_* t \ . \tag{D.10}$$

Using Eq. (D.10) in Eq. (D.5), we find for ν_{A},

$$\nu_{\mathrm{A}}(t) = -\int_0^{a(t)} \frac{\gamma x}{((1+\gamma)a(t)-\gamma x)^2}\,\omega'\!\left(\frac{x}{(1+\gamma)a(t)-\gamma x}\right)\mathrm{d}x \tag{D.11}$$

where

$$\gamma = \frac{v_*}{v_0} \ . \tag{D.12}$$

For $a(t)>0$, we can transform the integration variable to

$$\xi = \frac{x}{(1+\gamma)a(t)-\gamma x} \ . \tag{D.13}$$

This reveals that ν_{A} is independent of time,

$$\nu_{\mathrm{A}} = -\int_0^1 \frac{\gamma\xi}{1+\gamma\xi}\,\omega'(\xi)\,\mathrm{d}\xi \ . \tag{D.14}$$

Integration by parts yields

$$\begin{aligned}\nu_{\mathrm{A}} &= -\frac{\gamma\xi}{1+\gamma\xi}\omega(\xi)\Big|_0^1 + \int_0^1 \frac{\gamma}{(1+\gamma\xi)^2}\,\omega(\xi)\,\mathrm{d}\xi\\ &= -\frac{\gamma}{1+\gamma}\omega_1 + \eta\omega_0 \ ,\end{aligned} \tag{D.15}$$

where

$$\eta = \int_0^1 \frac{\gamma}{(1+\gamma\xi)^2}\frac{\omega(\xi)}{\omega_0}\,\mathrm{d}\xi \ . \tag{D.16}$$

Using the result (D.15) and $\dot{a} = -v_*$ in Eq. (D.9), we thus obtain

$$\Omega_{\mathrm{A}} = (1+\gamma)(1-\eta)\omega_0 \ . \tag{D.17}$$

The posterior frequency $\Omega_{\mathrm{P}} = \partial\phi/\partial t|_{x=0}$ can be obtained using Eq. (D.3) and (D.8), which yields $\Omega_{\mathrm{P}} = \omega_0$. Thus, we can interpret Eq. (D.17) as a relation between anterior and posterior frequency,

$$\Omega_{\mathrm{A}} = (1+\gamma)(1-\eta)\Omega_{\mathrm{P}} \ . \tag{D.18}$$

Appendix E

Steady States of Morphogen Gradients

E.1 Approximation of the Steady State of Q

In this section, we compute an analytic approximation of the steady state of the morphogen Q, Eq. (3.48), in the absence of interactions with the morphogen R. This approximation sheds light on the effects of parameters on the overall shape of the morphogen gradient. To decouple the dynamics of Q from R, we set $h_1 = 0$ throughout this section. Furthermore, we use the nondimensionalization scheme introduced in Sec. 3.5, in which $\alpha = E = h_0 = 1$. The governing equation for the steady state $Q(x)$ is therefore given by Eq. (3.48) with $\partial Q/\partial t = 0$,

$$\frac{\mathrm{d}}{\mathrm{d}x}(vQ) = \frac{\mathrm{d}^2 Q}{\mathrm{d}x^2} - Q + J(x) \ , \tag{E.1}$$

where the source J is of the form $J(x) = \mathbb{1}_{0<x<x_0}$ as introduced in Sec. 3.5. Since the velocity field depends on Q through Eq. (3.52),

$$\frac{\mathrm{d}v}{\mathrm{d}x} = \kappa Q \ , \tag{E.2}$$

the steady state equation is a non-linear integro-differential equation,

$$\kappa Q^2 + \kappa \frac{\mathrm{d}Q}{\mathrm{d}x} \int_0^x Q(x')\,\mathrm{d}x' = \frac{\mathrm{d}^2 Q}{\mathrm{d}x^2} - Q + \mathbb{1}_{0<x<x_0} \ . \tag{E.3}$$

Due to the simple nature of the integral, this equation could be written as a nonlinear third-order ordinary differential equation. However, in the subsequent treatment, we do not have to resort to this rewriting.

Region $0 < x < x_0$

We first derive an approximation in the region $0 < x < x_0$, in which the source of Q is active. The solution in this region is denoted by $Q_< = Q|_{x<x_0}$. We make a steady-state ansatz that relies on the assumption that $Q_<$ only slightly deviates from a constant value q_0,

$$Q_<(x) = q_0 + \delta q(x) \ , \tag{E.4}$$

where δ is a formal expansion parameter and q is the deviation. According to Eq. (E.2), the corresponding velocity field is given by

$$v(x) = \kappa q_0 x + \delta\kappa \int_0^x q(x')\,\mathrm{d}x' \ . \tag{E.5}$$

Using this ansatz, we expand the governing equation (E.3) to first order in δ,

$$0 = 1 - q_0 - \kappa q_0^2 + \left(\frac{\mathrm{d}^2 q}{\mathrm{d}x^2} - \kappa q_0 x \frac{\mathrm{d}q}{\mathrm{d}x} - (2\kappa q_0 + 1) q \right) \delta + \mathcal{O}(\delta^2) \ . \tag{E.6}$$

To zeroth order in δ, we obtain an equation for q_0, whose only positive solution is given by

$$q_0 = \frac{\sqrt{4\kappa + 1} - 1}{2\kappa} \ . \tag{E.7}$$

Note that for $\kappa \to 0$, the solution behaves as $q_0 \to 1$. To first order in δ, we obtain a differential equation for q,

$$\kappa q_0 x \frac{\mathrm{d}q}{\mathrm{d}x} = \frac{\mathrm{d}^2 q}{\mathrm{d}x^2} - (2\kappa q_0 + 1) q \ . \tag{E.8}$$

Since we consider the region $0 < x < x_0$, the coefficient $\kappa q_0 x$ on the l.h.s. is bounded from above by $\kappa q_0 x_0$. For the typical parameter values that we choose (Table 3.3), we find that $0 < \kappa q_0 x \lesssim 0.6$, while the coefficient of $\mathrm{d}^2 q/\mathrm{d}x^2$ is unity and the coefficient of q is $2\kappa q_0 + 1 \simeq 1.6$. We therefore propose an approximation scheme, in which we set the l.h.s. to zero. With boundary conditions $\mathrm{d}Q/\mathrm{d}x|_{x=0} = 0$ (implying $\mathrm{d}q/\mathrm{d}x|_{x=0} = 0$) and $Q(x_0) = q_0 - q_1$ (implying $q(x_0) = -q_1$), we find the solution

$$q(x) = -q_1 \frac{\cosh \mu x}{\cosh \mu x_0} \ , \tag{E.9}$$

where

$$\mu = (4\kappa + 1)^{1/4} \ . \tag{E.10}$$

The constant q_1 has to be determined from smoothness conditions (see below).

Region $x > x_0$

We now derive an approximation in the region $x > x_0$, in which there is no source of Q. We denote the solution in this region by $Q_> = Q|_{x>x_0}$. Since we expect Q to form a gradient that is rapidly decaying outside the source region, we use Eq. (E.2) to approximate the velocity field v in this region by a constant, $v \simeq v_0$. Numerical solutions to the exact steady state equation (E.1) confirm that for small values of κ this assumption is warranted. The value of v_0 has to be determined self-consistently from the relation

$$v_0 = \kappa \int_0^\infty Q(x) \, \mathrm{d}x \tag{E.11}$$

after deriving the functional form of $Q(x)$. In the region $x > x_0$, we thus obtain the governing equation

$$v_0 \frac{\mathrm{d}Q}{\mathrm{d}x} = \frac{\mathrm{d}^2 Q}{\mathrm{d}x^2} - Q \ . \tag{E.12}$$

Using the boundary condition $\lim_{x\to\infty} Q(x) = 0$, we find the solution

$$Q_>(x) = q_2 \mathrm{e}^{-\nu(x - x_0)} \ , \tag{E.13}$$

where

$$\nu = \frac{\sqrt{4 + v_0^2} - v_0}{2} \ . \tag{E.14}$$

Junction $x = x_0$

We connect the functional forms found for the two regions at the junction $x = x_0$ via smoothness conditions. Since the steady state equation (E.1) is of second order, we require $Q_<(x_0) = Q_>(x_0)$ and $Q'_<(x_0) = Q'_>(x_0)$. From these two conditions, we obtain the constants q_1 and q_2,

$$q_1 = \frac{q_0}{1 + \mu\nu^{-1}\tanh\mu x_0} \ , \tag{E.15}$$

$$q_2 = q_0 - q_1 \ . \tag{E.16}$$

For typical parameter values used here (Table 3.3), we find $\mu x_0 \gg 1$ and we may thus approximate $\tanh\mu x_0 \simeq 1$ to obtain

$$q_1 \simeq \frac{q_0}{1 + \mu\nu^{-1}} \ . \tag{E.17}$$

Together with Eqs. (E.4) and (E.9), this leads to

$$Q_<(x) = q_0 - \frac{q_0}{1 + \mu\nu^{-1}}\frac{\cosh\mu x}{\cosh\mu x_0} \ . \tag{E.18}$$

Furthermore, using Eq. (E.13), we obtain

$$Q_>(x) = \frac{q_0}{1 + \mu^{-1}\nu}\mathrm{e}^{-\nu(x - x_0)} \ . \tag{E.19}$$

We can now fix v_0 via Eq. (E.11),

$$\begin{aligned}\frac{v_0}{\kappa} &= \int_0^{x_0} Q_<(x)\,\mathrm{d}x + \int_{x_0}^{\infty} Q_>(x)\,\mathrm{d}x \\ &= q_0\left(x_0 + \frac{1 - (\mu^{-1}\nu)^2\tanh\mu x_0}{\nu(1 + \mu^{-1}\nu)}\right) \\ &\simeq q_0(x_0 - \mu^{-1} + \nu^{-1}) \ .\end{aligned} \tag{E.20}$$

The last equality again employs the approximation $\tanh\mu x_0 \simeq 1$ (see above). The r.h.s. of Eq. (E.20) depends on v_0 through ν, Eq. (E.14). Since solving for v_0 is cumbersome, we solve for ν instead. From Eq. (E.14), we obtain $v_0 = \nu^{-1} - \nu$, which we insert into the l.h.s. of Eq. (E.20) to obtain

$$\nu = \frac{\kappa q_0}{2}\left(\mu^{-1} - x_0 + \left[(\mu^{-1} - x_0)^2 - \frac{4}{\kappa q_0}\left(1 - \frac{1}{\kappa q_0}\right)\right]^{1/2}\right) \ . \tag{E.21}$$

In summary, we have found the approximate steady state solution

$$Q(x) = q_0 \times \begin{cases} 1 - \dfrac{1}{1 + \mu\nu^{-1}}\dfrac{\cosh\mu x}{\cosh\mu x_0} & x < x_0 \\ \dfrac{1}{1 + \mu^{-1}\nu}\mathrm{e}^{-\nu(x - x_0)} & x \geq x_0 \end{cases} \ , \tag{E.22}$$

where q_0, μ, and ν are given in terms of the parameters through Eqs. (E.7), (E.10), and (E.21). Comparison of the analytical approximation Eq. (E.22) with numerical solutions of Eq. (E.1) show that the approximation is in very good agreement with the exact solution in the limit of small κ (Fig. E.1). This is expected as κ determines the

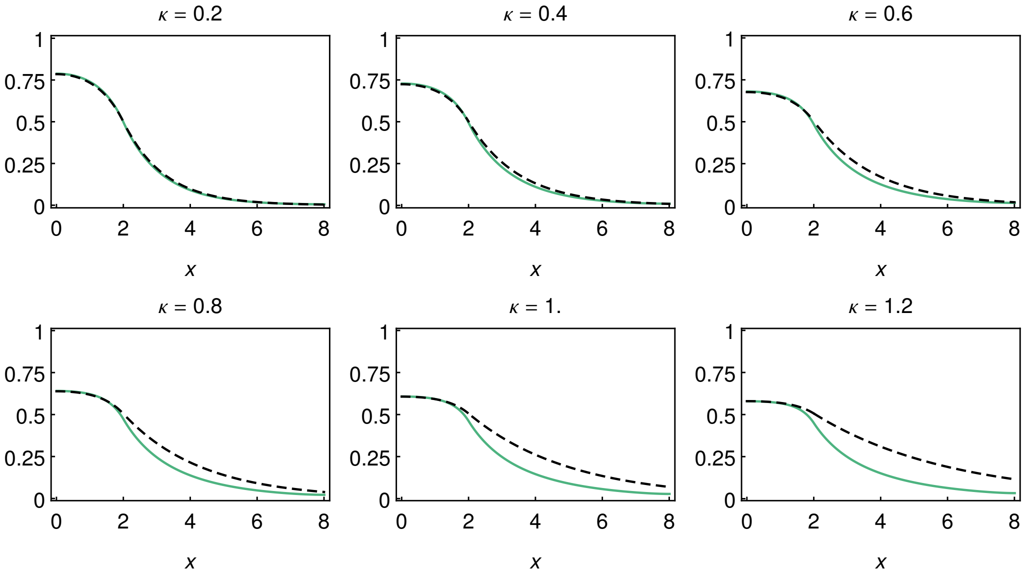

Figure E.1 Comparison of the analytical approximation for the steady state of Q (dashed black), Eq. (E.22), and the exact numerical solution of Eq. (E.1) (solid green) for different values of κ. All other parameters are provided in Table 3.3.

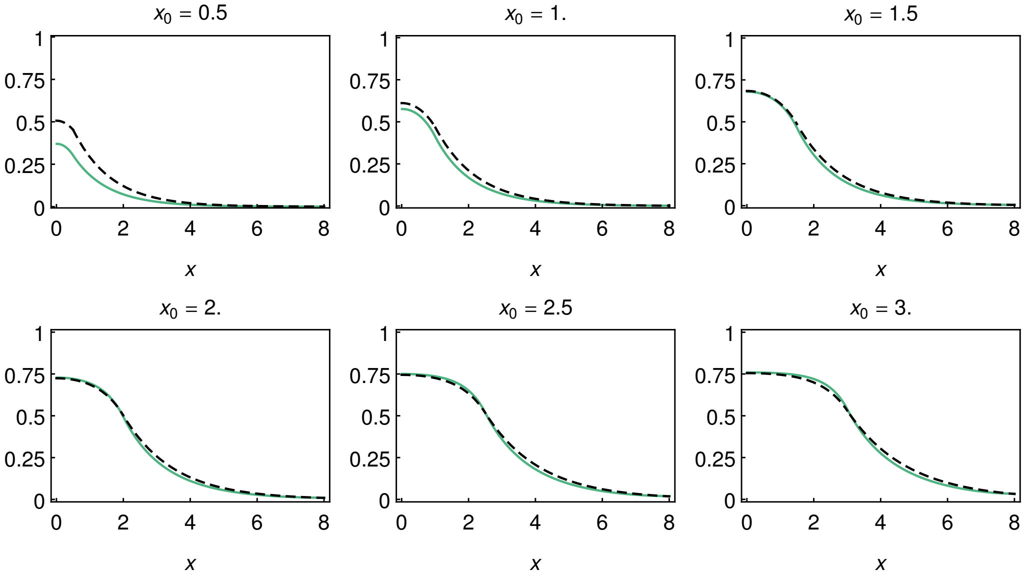

Figure E.2 Comparison of the analytical approximation for the steady state of Q (dashed black), Eq. (E.22), and the exact numerical solution of Eq. (E.1) (solid green) for different values of x_0. All other parameters are provided in Table 3.3.

strength of self-interaction. Furthermore, the approximation shows better agreement with the exact solution for increasing values of x_0 (Fig. E.2).

The terminal speed v_0 is given by Eq. (E.20) as

$$v_0 = \kappa q_0 (x_0 - \mu^{-1} + \nu^{-1}) \ . \tag{E.23}$$

Since v_0 is related to $Q(x)$ via Eq. (E.11), the expression (E.23) is consistent with the naive assumption that $Q(x)$ can be approximated by a rectangle with side lengths x_0 and q_0, but includes the correction terms μ^{-1} and ν^{-1} that account for diffusion and advection. From Eq. (E.22), we also obtain an approximation for the length a_0 of the presomitic mesoderm in the steady state by solving $Q(a_0) = Q^*$ for a,

$$a_0 \simeq \begin{cases} x_0 - \nu^{-1} \log\left([1+\mu^{-1}\nu] \dfrac{Q^*}{q_0} \right) & Q^* \le \dfrac{q_0}{1+\mu^{-1}\nu} \\ \mu^{-1} \operatorname{arcosh}\left([1+\mu\nu^{-1}] \left(1 - \dfrac{Q^*}{q_0}\right) \cosh \mu x_0 \right) & Q^* > \dfrac{q_0}{1+\mu^{-1}\nu} \end{cases} \ . \tag{E.24}$$

E.2 Approximation of the Steady State of R

In this section, we compute an analytic approximation of the steady state of the morphogen R, Eq. (3.49), in the absence of interactions with the morphogen Q. To decouple the dynamics of R from Q, we here set $k_1 = 0$. Typically, non-vanishing levels of R are found in the region where $Q < Q^*$. In this region, we assume that the velocity is constant, $v = v_0$ (for arguments warranting this assumption, see Sec. E.1). For simplicity, we consider a case in which the phase field ϕ exhibits a single wavenumber, $\phi(x) = px$. The governing equation for the steady state distribution $R(x)$ is therefore given by Eq. (3.49) with $\partial R/\partial t = 0$,

$$v_0 \frac{\mathrm{d}R}{\mathrm{d}x} = D \frac{\mathrm{d}^2 R}{\mathrm{d}x^2} - k_0 R + \beta_0 + \beta_1 X(px) \ , \tag{E.25}$$

where $X(\phi)$ is the oscillatory signal associated to the phase ϕ, Eq. (3.51). We make the ansatz

$$R(x) = R_0 + R_1 \cos px + R_2 \sin px \tag{E.26}$$

and obtain

$$\begin{aligned} 0 = \beta_0 + \frac{\beta_1}{2} - k_0 R_0 + (v_0 R_1 p - D R_2 p^2 - k_0 R_2) \sin px \\ + \left(\frac{\beta_1}{2} - v_0 R_2 p - D R_1 p^2 - k_0 R_1 \right) \cos px \end{aligned} \tag{E.27}$$

Comparison of coefficients of $\sin px$, $\cos px$, and the constant term yields three equations for the three unknowns R_0, R_1, and R_2. The solution to this system of equations is given by

$$R_0 = \frac{\beta_0 + \beta_1/2}{k_0} \ , \tag{E.28}$$

$$R_1 = \frac{\beta_1}{2} \frac{Dp^2 + k_0}{(Dp^2 + k_0)^2 + (pv_0)^2} \ , \tag{E.29}$$

$$R_2 = \frac{\beta_1}{2} \frac{pv_0}{(Dp^2 + k_0)^2 + (pv_0)^2} \ . \tag{E.30}$$

We express the ansatz (E.26) in the form

$$R(x) = R_0 + r\cos(px + \phi_0) \ . \tag{E.31}$$

Using standard trigonometric identities, we obtain

$$\tan\phi_0 = \frac{R_2}{R_1} = \frac{pv_0}{Dp^2 + k_0} \ , \tag{E.32}$$

$$r = \sqrt{R_1^2 + R_2^2} = \frac{\beta_1}{2}\frac{1}{\sqrt{(Dp^2 + k_0)^2 + (pv_0)^2}} \ . \tag{E.33}$$

We thus find that in such a scenario, the steady state of R can be described by a base level R_0, Eq. (E.28), which is modulated by spatial oscillations with the same wavenumber p as the phase field and amplitude r, Eq. (E.33). The amplitude r grows linearly with the production rate β_1 and decreases with diffusion D, wavenumber p, decay rate k_0, and velocity v_0.

Appendix F

Experimental Phase Maps of Kinematic Wave Patterns

In this appendix, we describe how to obtain the phase maps presented in Chapter 4, Sec. 4.2, from experimental intensity kymographs. The method presented here has been published with minor modifications in Ref. [133].

F.1 Generating Phase Maps using a Wavelet Transform

In Chapter 4, Sec. 4.2.1, we have described how to obtain intensity kymographs of the spatio-temporal wave patterns along the presomitic mesoderm from time-lapse movies of $m = 18$ embryos (example shown in Fig. F.1A). The time interval between rows in the kymograph is $\delta_{\mathrm{T}} = 5\,\mathrm{min}$ and the spacing between columns is $\delta_{\mathrm{X}} = 1.26\,\mu\mathrm{m}$. To convert these intensity kymographs into phase maps, we apply the following steps to each kymograph (summary shown in Fig. F.1).

Step 1. We apply a Gaussian filter of radius 3 in spatial direction to the intensity kymograph to enhance the coherence of the resulting phase map in the posterior.

Step 2. For each column c of the intensity kymograph, we carry out the following procedure: we consider the time series of the intensity signal along this column (Fig. F.1A) and apply a wavelet transform (Chapter 4, Sec. 4.2.2) to obtain the corresponding phase time series $\varphi_\sigma(k)$ (Fig. F.1B). By applying this procedure to every column c, we obtain a phase map $\varphi_\sigma(c, k)$ for the entire intensity kymograph (Fig. F.1C). The characteristic period of oscillation depends on the column c. Typically, the period along the columns slightly increases from posterior to anterior. Hence, we choose a wavelet scale $\sigma(c)$ for each column c that is appropriate for the respective characteristic period. By convention, wavelet scales are parameterized in an equal-tempered scheme,

$$\sigma_{\alpha\beta} = 2^{\alpha-1+\beta/\bar{\beta}}\bar{T}^{-1} \ , \tag{F.1}$$

where α is called the octave number, β the voice number, $\bar{\beta}$ is the number of voices per octave, and $\bar{T}$ is the so-called Fourier period of the Gabor wavelet function, Eq. (4.6), which is given by [143]

$$\bar{T} = \frac{4\pi}{6 + \sqrt{2 + 6^2}} \ . \tag{F.2}$$

We here choose $\alpha = 4$ and $\bar{\beta} = 50$ for all columns. We choose the voice β to depend

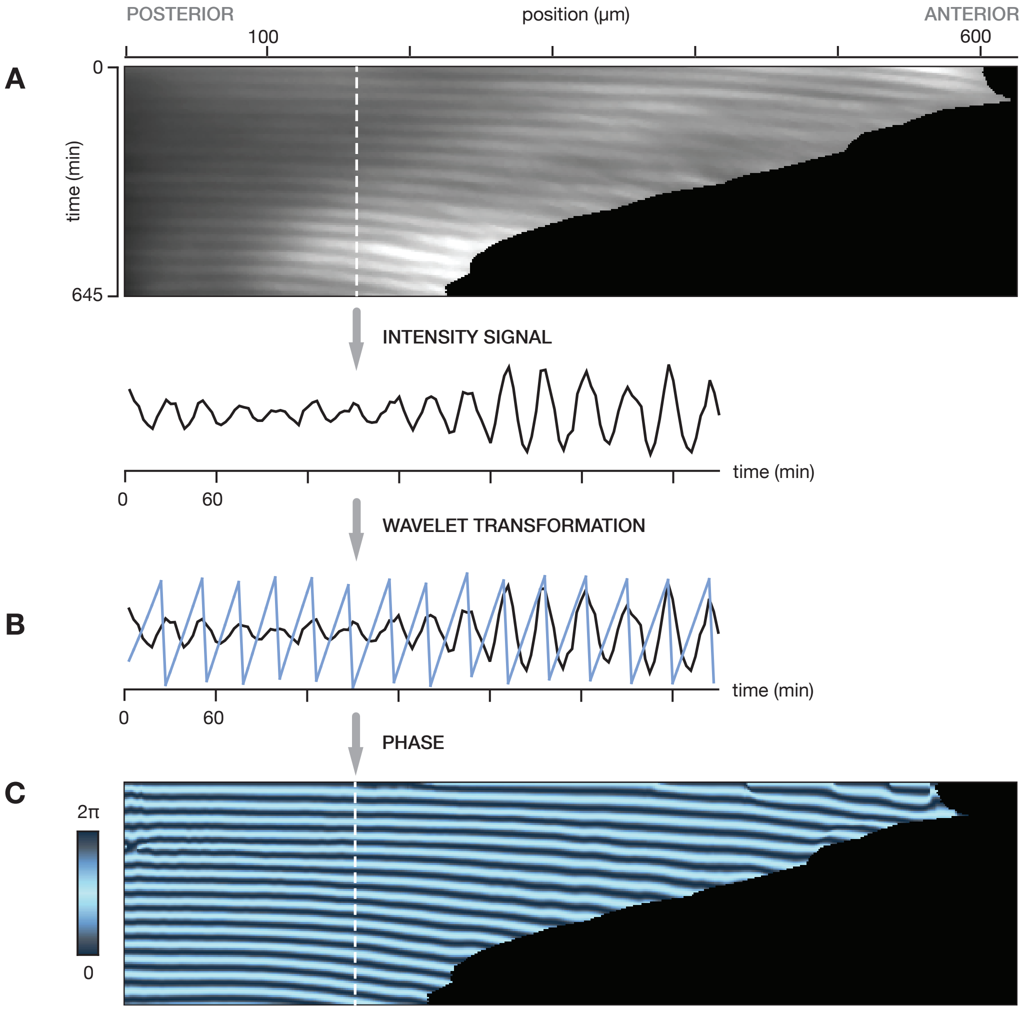

Figure F.1 Flow chart of the procedure to obtain phase maps (C) from intensity kymographs (A) using a wavelet transformation. See Sec. F.1 for details. Figure adapted from Ref. [133].

on the column c, counted from the posterior, in the following way,

$$\beta(c) = \begin{cases} 5 & c \leq 100 \\ [\frac{c-5}{20}] & 100 < c \leq 400 \\ 20 & 400 < c \end{cases}, \tag{F.3}$$

where $[\cdot]$ denotes the nearest integer value. This yields $\sigma(c) = 2^{3+\beta(c)/50}\bar{T}^{-1}$. Hence, we obtain a phase map $\varphi(x,t)$ that assigns a phase to every point in time $t = k\delta_{\mathrm{T}}$ and space $x = c\delta_{\mathrm{X}}$, using the wavelet scale $\sigma(c)$. We choose $x = 0$ to correspond to the position of the posterior tip and $t = 0$ to the formation time of the 7th segment.

Step 3. For a fixed time t, the phase $\varphi(x)$ displays jumps from 2π to 0. We obtain a continuous phase signal $\phi(x)$ by removing these jumps, $\phi(x) = \mathcal{C}_x\varphi(x)$, where $\mathcal{C}_x$ denotes the removal of jumps in x-direction. Practically, we use an algorithm that first smoothes the signal using a moving median of width 5 in x-direction and then detects the phase jumps and eliminates them. Carrying out this procedure for every time point t, we obtain a phase map $\phi(x,t) = \mathcal{C}_x\varphi(x,t)$, which displays no jumps in

x-direction. In a similar way, we obtain a continuous signal of the posterior phase, $\phi_{\mathrm{P}}(t) = \mathcal{C}_t \varphi(0,t)$, where $\mathcal{C}_t$ denotes the removal of jumps in t-direction.

We apply this procedure to the intensity kymographs of $m = 18$ embryos and thus obtain 18 phase maps, denoted by $\phi_i(x,t)$ with $i = 1,\ldots,m$, and the corresponding posterior phases $\phi_{\mathrm{P},i}(t)$. Furthermore, we determine the time-dependent length $a_i(t)$ of the presomitic mesoderm from the kymographs for each embryo.

F.2 Construction of the Average Phase Map

In this section, we show how to obtain the average phase map $\Phi(x,t)$ from $m = 18$ embryos, presented in Chapter 4, Fig. 4.6. From the phase maps $\phi_i(x,t)$ obtained in the previous section, we determine the phase profiles

$$\theta_i(x,t) = \phi_i(x,t) - \phi_i(x_0,t) \tag{F.4}$$

with $x_0 = 210\,\mu\mathrm{m}$ for each embryo $i = 1,\ldots,m$. We use the position $x_0 = 210\,\mu\mathrm{m}$ as subtraction point since the phase maps show the least degree of noise in this region (see, e.g., Fig. 4.5). We then determine the median of θ_i at each x and t,

$$\bar{\theta}(x,t) = \mathrm{median}_i\, \theta_i(x,t) \ . \tag{F.5}$$

The median profile $\bar{\theta}$ is considerably less noisy than each single phase profile but still not smooth enough to take numerical derivatives. As a smoothing technique, we perform fits of differentiable functions to the median phase profile $\bar{\theta}$ that capture its spatio-temporal key features. For a fixed time t, we fit the median phase profile $\bar{\theta}(x)$ with the function $\Theta(x)$ given in Table F.1 using the fit parameters θ_0, β, χ, and ξ. Carrying out this procedure for every time point, we obtain a time series for each of the fit parameters (green dots in Fig. F.2). We then calculate the phase profile

$$\Psi(x) = \Theta(x) - \Theta(0) \ , \tag{F.6}$$

which renders Ψ independent of the parameter θ_0. We capture the time dependence of the remaining parameters β, χ, and ξ by fits of the functions $f_\beta(t)$, $f_\chi(t)$, and $f_\xi(t)$ given in Table F.1. Using these fits in $\Psi(x)$, we obtain a differentiable function $\Psi(x,t)$. Likewise, we compute the median of the posterior phase $\bar{\phi}_{\mathrm{P}}(t) = \mathrm{median}_i\, \phi_{\mathrm{P},i}(t)$ and perform a fit of the function $\Phi_{\mathrm{P}}(t)$ given in Table F.1. The average phase map is thus given by

$$\Phi(x,t) = \Phi_{\mathrm{P}}(t) + \Psi(x,t) \ . \tag{F.7}$$

Furthermore, we compute the average length of the presomitic mesoderm from all embryos at each time point t, $\bar{a}(t) = \mathrm{mean}_i\, a_i(t)$ and perform a fit of the function $A(t)$ given in Table F.1. All fit results are shown in Fig. F.2 (dashed black curves) and the resulting fit parameters are provided in Table F.2. Note that all used fit functions are phenomenological and not derived from a dynamic theory.

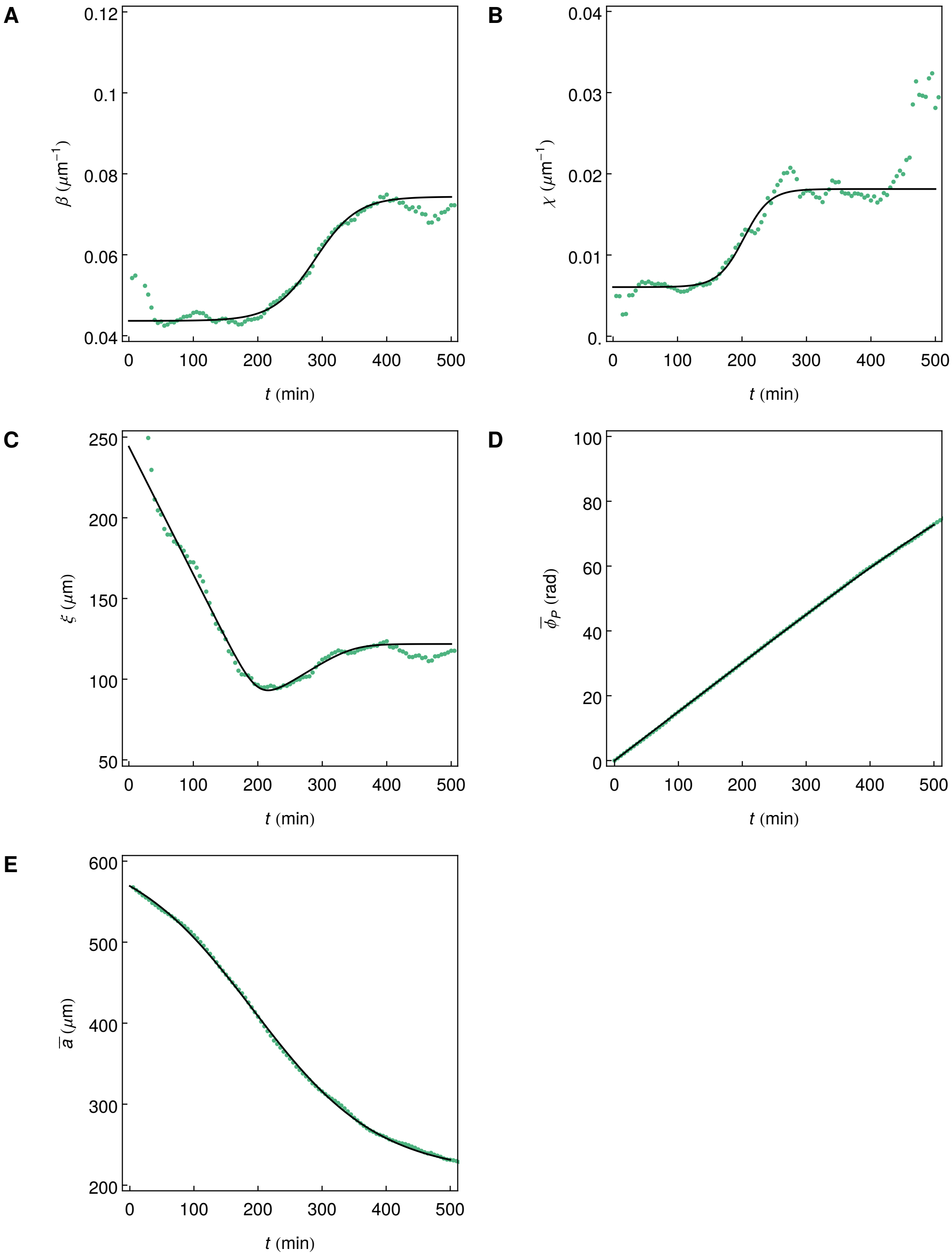

Figure F.2 **A–C.** Time dependence of the fit parameters β, χ, and ξ that parametrize the phase profile $\Theta(x)$ for each time point (green dots). The black dashed lines show fits of the time evolution of these parameters by the functions f_β (A), f_χ (B), and f_ξ (C) (black curves). **D.** Averaged posterior phase $\bar{\phi}_{\mathrm{P}}$ for each time point (green dots) and fit of the function Φ_{P} (black curve). **E.** Averaged length $\bar{a}$ of the presomitic mesoderm (green dots) and fit to the function $A(t)$ (black curve). All fit functions are provided in Table F.1. Data also published in Ref. [133].

FIT FUNCTION	**FIT PARAMETERS**
$\Theta(x) = \theta_0 - \dfrac{\beta}{2}\left(x + \dfrac{1}{\chi}\log\cosh\chi(x-\xi)\right)$	$\theta_0, \beta, \chi, \xi$
$f_\beta(t) = \beta_0 + \beta_1 \tanh\beta_2(t-\beta_3)$	$\beta_0, \ldots, \beta_3$
$f_\chi(t) = \chi_0 + \chi_1 \tanh\chi_2(t-\chi_3)$	$\chi_0, \ldots, \chi_3$
$f_\xi(t) = \xi_0 + \dfrac{\xi_1}{2}\left(t + \dfrac{1-\xi_2/\xi_1}{\xi_3}\log\cosh\xi_3(t-\xi_4)\right) - \dfrac{\xi_2}{2\xi_5}\log\cosh\xi_5(t-\xi_6)$	$\xi_0, \ldots, \xi_6$
$\Phi_\mathrm{P}(t) = \dfrac{p_0}{2}t + \dfrac{p_0}{2p_1}\left(\log\cosh p_1 p_2 - \log\cosh p_1(t-p_2)\right)$	$p_0, \ldots, p_2$
$A(t) = a_0 + a_1 \tanh a_2(t-a_3)$	$a_0, \ldots, a_3$

Table F.1. Fit functions used in Sec. F.2.

PARAMETER	**UNIT**	**VALUE**
β_0	$\mu\mathrm{m}^{-1}$	5.90024×10^{-2}
β_1	$\mu\mathrm{m}^{-1}$	1.53338×10^{-2}
β_2	min^{-1}	1.53837×10^{-2}
β_3	min	2.8925×10^{2}
χ_0	$\mu\mathrm{m}^{-1}$	1.20872×10^{-2}
χ_1	$\mu\mathrm{m}^{-1}$	6.03996×10^{-3}
χ_2	min^{-1}	2.48799×10^{-2}
χ_3	min	2.0299×10^{2}
ξ_0	$\mu\mathrm{m}$	1.89063×10^{2}
ξ_1	$\mu\mathrm{m}\,\mathrm{min}^{-1}$	-7.91625×10^{-1}
ξ_2	$\mu\mathrm{m}\,\mathrm{min}^{-1}$	2.54169×10^{-1}
ξ_3	min^{-1}	3.69293×10^{-2}
ξ_4	min	2.00622×10^{2}
ξ_5	min^{-1}	2.38447×10^{-2}
ξ_6	min	3.44444×10^{2}
p_0	min^{-1}	1.51274×10^{-1}
p_1	min^{-1}	5.28693×10^{-3}
p_2	min	6.40844×10^{2}
a_0	$\mu\mathrm{m}$	4.17045×10^{2}
a_1	$\mu\mathrm{m}$	2.02541×10^{2}
a_2	min^{-1}	-5.08818×10^{-3}
a_3	min	1.919×10^{2}

Table F.2. Numerical values of the fit parameters of the functions given in Table F.1.

Appendix G

Decoupling Perturbation Modes by Fourier Transformation

In this appendix, we show that a spatial Fourier transformation decouples the collective perturbation modes for the phase oscillator system Eq. (6.1) if nearest-neighbor coupling on a square lattice in d dimensions with periodic boundary conditions is considered. Concretely, we derive Eqs. (6.36) and (6.37) from Eqs. (6.10) and (6.12). According to Eq. (6.10), the time evolution of the perturbations $\xi_{\mu_1,\dots,\mu_d}$ for such a system is given by

$$\frac{\mathrm{d}}{\mathrm{d}t}\xi_{\mu_1,\dots,\mu_d} = \Lambda \sum_{i=1}^{d} \sum_{\nu=0}^{n_i-1} B_{\mu_i\nu}\left(\xi^{(\tau)}_{\mu_1,\dots,\mu_{i-1},\nu,\mu_{i+1},\dots,\mu_d} - \xi_{\mu_1,\dots,\mu_d}\right) , \tag{G.1}$$

where n_i is the number of oscillators in i-direction, $\xi^{(\tau)}_{\mu_1,\dots,\mu_d}(t) = \xi_{\mu_1,\dots,\mu_d}(t-\tau)$ is the perturbation with delayed argument, and

$$B_{\mu\nu} = \frac{1}{2d}(\delta_{\mu,\nu-1} + \delta_{\mu,\nu+1}) . \tag{G.2}$$

Instead of encoding the nearest-neighbor coupling topology in d dimensions in a single adjacency matrix $b_{\mu\nu}$, which is cumbersome, we here use the one-dimensional nearest-neighbor adjacency matrix $B_{\mu\nu}$ and perform the summation for each dimension $i = 1,\dots,d$ separately in Eq. (G.1). The spatial Fourier transform of the perturbations and its inverse are given by

$$\psi_{k_1,\dots,k_d}(t) = \sum_{\mu_1=0}^{n_1-1} \cdots \sum_{\mu_d=0}^{n_d-1} \mathrm{e}^{-\mathrm{i}\sum\limits_{i=1}^{d} k_i\mu_i} \xi_{\mu_1,\dots,\mu_d}(t) , \tag{G.3}$$

$$\xi_{\mu_1,\dots,\mu_d}(t) = \frac{1}{\prod_{i=1}^{d} n_i} \sum_{\mathbf{k}} \mathrm{e}^{\mathrm{i}\sum\limits_{i=1}^{d} k_i\mu_i} \psi_{k_1,\dots,k_d}(t) , \tag{G.4}$$

where $\sum_{\mathbf{k}}$ denotes the summation over all $k_i = 2\pi p_i/n_i$ with $p_i \in \{-n_i/2, -n_i/2+1,\dots,n_i/2-1\}$ and n_i being the size of the system in i-direction ($i = 1,\dots,d$), which we consider to be even. Inserting Eq. (G.4) into Eq. (G.1) yields

$$\begin{aligned}&\frac{1}{\prod_i n_i}\sum_{\mathbf{k}} \mathrm{e}^{\mathrm{i}\sum\limits_{i=1}^{d} k_i\mu_i} \frac{\mathrm{d}}{\mathrm{d}t}\psi_{k_1,\dots,k_d} \\ &= \frac{\Lambda}{\prod_i n_i} \sum_{i=1}^{d}\sum_{\nu=0}^{n_i-1} B_{\mu_i\nu} \sum_{\mathbf{k}} \left(\mathrm{e}^{\mathrm{i}k_i\nu + \mathrm{i}\sum\limits_{j\neq i} k_j\mu_j} \psi^{(\tau)}_{k_1,\dots,k_d} - \mathrm{e}^{\mathrm{i}\sum\limits_{i=1}^{d} k_i\mu_i}\psi_{k_1,\dots,k_d}\right).\end{aligned} \tag{G.5}$$

Carrying out the summation over ν on the r.h.s. yields

$$\begin{aligned}
\sum_{\mathbf{k}} \mathrm{e}^{\mathrm{i}\sum\limits_{i=1}^{d} k_i\mu_i} \frac{\mathrm{d}}{\mathrm{d}t}\psi_{k_1,\dots,k_d}
&= \frac{\Lambda}{2d}\sum_{i=1}^{d}\sum_{\mathbf{k}} \Big([\mathrm{e}^{\mathrm{i}k_i(\mu_i+1)} + \mathrm{e}^{\mathrm{i}k_i(\mu_i-1)}]\mathrm{e}^{\mathrm{i}\sum\limits_{j\neq i} k_j\mu_j} \psi^{(\tau)}_{k_1,\dots,k_d} \\
&\qquad\qquad - \mathrm{e}^{\mathrm{i}\sum\limits_{j=1}^{d} k_j\mu_j}\psi_{k_1,\dots,k_d}\Big) \qquad\qquad (G.6)\\
&= \frac{\Lambda}{2d}\sum_{i=1}^{d}\sum_{\mathbf{k}} \mathrm{e}^{\mathrm{i}\sum\limits_{j=1}^{d} k_j\mu_j}\Big([\mathrm{e}^{\mathrm{i}k_i} + \mathrm{e}^{-\mathrm{i}k_i}]\psi^{(\tau)}_{k_1,\dots,k_d} - 2\psi_{k_1,\dots,k_d}\Big)\\
&= \sum_{\mathbf{k}} \mathrm{e}^{\mathrm{i}\sum\limits_{i=1}^{d} k_i\mu_i} \frac{\Lambda}{d}\sum_{i=1}^{d}\Big((\cos k_i)\psi^{(\tau)}_{k_1,\dots,k_d} - \psi_{k_1,\dots,k_d}\Big) \ .
\end{aligned}$$

Comparison of coefficients for all $i = 1,\dots,d$ yields

$$\frac{\mathrm{d}}{\mathrm{d}t}\psi_{k_1,\dots,k_d} = \left(\frac{1}{d}\sum_{i=1}^{d}\cos k_i\right)\Lambda\psi^{(\tau)}_{k_1,\dots,k_d} - \Lambda\psi_{k_1,\dots,k_d} \ . \qquad (G.7)$$

This shows that the dynamics of the Fourier modes decouple. Moreover, comparing Eq. (G.7) with Eq. (6.12), we find that the eigenvalues $v_{k_1,\dots,k_d}$ are given by

$$v_{k_1,\dots,k_d} = \frac{1}{d}\sum_{i=1}^{d}\cos k_i \ . \qquad (G.8)$$

This completes the derivation of Eqs. (6.36) and (6.37).

Appendix H
Numerical Simulations and Data Processing

Chapter 2. In Chapter 2, direct numerical solutions of the master equations (2.1) and (2.5) are impracticable due to the high dimensionality of the state space. Instead, a stochastic simulation algorithm of the Gillespie-type was written that yields exact realizations of trajectories of the model [48]. Expectation values were obtained by computing averages of the respective observable over multiple realizations. The data shown in Figs. 2.9, 2.10, 2.13, and 2.15 were obtained by averaging over 50 realizations for each data point.

Chapter 3. The dynamic equations investigated in Chapter 3 are formally equivalent to advection-diffusion equations. To numerically integrate these partial differential equations, simple finite-difference algorithms of the FTCS type (forward-time central-space) were written [108].

Chapter 4. Image analysis of experimental time lapse movies and images were carried out using FIJI image analysis software [125]. Data processing and plotting was done using Wolfram Mathematica [159].

Chapter 5. To integrate the equation of motion of the cell-based model, a velocity-Verlet based integration scheme as described in Refs. [16, 99] was implemented and extended by the dynamics of coupled phase oscillators, morphogen reactions, and cell differentiation as described in Chapter 5.

Chapter 6. Numerical results for the phase oscillator model presented in Chapter 6 were obtained using an Euler algorithm.

All algorithms have been written in Fortran 90 and compiled with the Intel Fortran Compiler IFORT, partly using the Intel Math Kernel Library IMKL. The OpenMP API has been used to parallelize the code whenever appropriate. Simulations were run on workstations and/or the computer cluster of the Max Planck Institute for the Physics of Complex Systems, Dresden, Germany.

List of Figures

1.1 Schematic depiction of a genetic oscillator 2
1.2 Segmentation of the embryonic body axis in zebrafish 3
1.3 Schematic depictions of the zebrafish presomitic mesoderm 4
1.4 Clock-and-wavefront model of vertebrate segmentation 5
1.5 Cyclic mRNA expression patterns in the zebrafish presomitic mesoderm 6
1.6 Schematic depiction of the Delta–Notch signal transduction pathway 8
1.7 Three-tier framework of vertebrate segmentation 9
1.8 Adult zebrafish 10

2.1 Markov chain model of a genetic oscillator and Hill functions 14
2.2 Markov chain model of two coupled genetic oscillators 15
2.3 Sample trajectories of exact realizations 17
2.4 Fixed points and limit cycles of the deterministic limit 21
2.5 Numerical solutions to the deterministic limit 22
2.6 Frequencies of occupation numbers from simulations and analytical estimates . . 24
2.7 Frequencies and decorrelation rates from simulations and analytical estimates . . 27
2.8 Gamma distribution 28
2.9 Quality and cross correlation as a function of the signaling delay 29
2.10 Quality factor Q and cross correlation C 30
2.11 Quality of coupled and uncoupled oscillators 32
2.12 Stochastic switching between in-phase and anti-phase correlations 34
2.13 Frequency ω and mutual information I 35
2.14 Synchrony relations between different parts of the system 36
2.15 Cross correlations C_{out} and C_{in} 37
2.16 Collective frequency for the phase models with distributed and discrete delays . . 39
2.17 Solutions to the characteristic equation for the in-phase synchronized state . . . 42
2.18 Solutions to the characteristic equation for the anti-phase synchronized state . . 43
2.19 Logarithmic power spectra of the oscillations in the Markov chain model 44
2.20 Collective frequency of the Markov chain model and the phase model 45

3.1 Schematic depiction of the embryonic coordinate system and frequency profile . . 52
3.2 Snapshots of numerical solutions to the continuum theory 53
3.3 Kymograph of the system shown in Fig. 3.2 54
3.4 Key observables of pattern formation and segmentation 55
3.5 Effects of coupling delays on pattern formation 59
3.6 Effects of growth on pattern formation 60
3.7 Kymograph of the system with decreasing tissue length 63
3.8 Schematic depiction of the Doppler effect 64
3.9 Contributions to the anterior frequency 65
3.10 Location of morphogen gradients and interaction structure of the model 67
3.11 Snapshots of numerical solutions to the interacting morphogen model 69
3.12 Kymograph of the system of interacting morphogens and oscillators 70

4.1 Embryonic coordinate system 78
4.2 Intensity kymograph from time-lapse microscopy movie 79
4.3 Time evolution of the presomitic mesoderm length and velocity profiles 80
4.4 Intensity kymographs and phase maps of the fluorescent signal 82

4.5 Time evolution of phase profiles . . . 83
4.6 Kymographs of the average phase map . . . 85
4.7 Number of formed segments and segment length . . . 86
4.8 Number of kinematic waves as a function of time and segment number . . . 87
4.9 Contributions to the anterior frequency determined from experiments . . . 89
4.10 Schematic representations of Doppler and dynamic wavelength effects . . . 90

5.1 Particle and cell coordinates . . . 95
5.2 Forces and corresponding potentials . . . 96
5.3 Global system properties as a function of time . . . 101
5.4 Simulation snapshots: oscillatory dynamics and cell differentiation . . . 102
5.5 Simulation snapshots: morphogen dynamics . . . 103
5.6 One-dimensional profiles in the reference frame comoving with the wall . . . 104

6.1 Relation of coupling delays and phase shifts for constant and varying frequencies 110
6.2 Synchronization rate for a globally coupled system . . . 112
6.3 Synchronization rate for a nearest-neighbor coupled system . . . 113
6.4 Lambert W function (principal branch) / graphical proof . . . 115
6.5 Oscillator synchronization in two-dimensional nearest-neighbor coupled systems . 119

E.1 Steady state of Q for different values of κ . . . 152
E.2 Steady state of Q for different values of x_0 . . . 152

F.1 Flow chart: obtaining phase maps from intensity kymographs . . . 156
F.2 Time dependence of the fit parameters . . . 158

References

[1] J. A. Acebrón, L. L. Bonilla, and C. J. P. Vicente, *The Kuramoto model: A simple paradigm for synchronization phenomena*, Rev. Mod. Phys. **77** (2005), no. 1, 137.

[2] B. Alberts, A. Johnson, J. Lewis, M. Raff, K. Roberts, and P. Walter, *Molecular Biology of the Cell*, Fifth ed., Taylor & Francis Group, 2007.

[3] A. Amann, E. Schöll, and W. Just, *Some basic remarks on eigenmode expansions of time-delay dynamics*, Physica A **373** (2007), 191–202.

[4] X. Ao, P. Hänggi, and G. Schmid, *In-phase and anti-phase synchronization in noisy Hodgkin-Huxley neurons*, Math. Biosci. **245** (2013), no. 1, 49–55.

[5] S. Ares, L. G. Morelli, D. J. Jörg, A. C. Oates, and F. Jülicher, *Collective Modes of Coupled Phase Oscillators with Delayed Coupling*, Phys. Rev. Lett. **108** (2012), 204101.

[6] F. M. Atay, *Complex Time-Delay Systems: Theory and Applications*, Springer complexity, Springer, 2010.

[7] ———, *The consensus problem in networks with transmission delays*, Phil. Trans. R. Soc. A **371** (2013), no. 1999.

[8] A. Aulehla and O. Pourquié, *Signaling gradients during paraxial mesoderm development*, Cold Spring Harbor Perspectives in Biology **2** (2010), no. 2, a000869.

[9] A. Aulehla, C. Wehrle, B. Brand-Saberi, R. Kemler, A. Gossler, B. Kanzler, and B. G. Herrmann, *Wnt3a plays a major role in the segmentation clock controlling somitogenesis*, Dev. Cell **4** (2003), no. 3, 395–406.

[10] A. Aulehla, W. Wiegraebe, V. Baubet, M. B. Wahl, C. Deng, M. Taketo, M. Lewandoski, and O. Pourquié, *A beta-catenin gradient links the clock and wavefront systems in mouse embryo segmentation*, Nat. Cell Biol. **10** (2008), no. 2, 186–193.

[11] L. Bajard, L. G. Morelli, S. Ares, J. Pecreaux, F. Jülicher, and A. C. Oates, *Wnt-regulated dynamics of positional information in zebrafish somitogenesis*, Development **141** (2014), no. 6, 1381–1391.

[12] L. Bajard and A. C. Oates, *Breathe in and Straighten your Back: Hypoxia, Notch, and Scoliosis*, Cell **149** (2012), no. 2, 255–256.

[13] R. E. Baker and P. K. Maini, *Travelling gradients in interacting morphogen systems*, Math. Biosci. **209** (2007), no. 1, 30–50.

[14] R. E. Baker, S. Schnell, and P. K. Maini, *A clock and wavefront mechanism for somite formation*, Dev. Biol. **293** (2006), no. 1, 116–126.

[15] ———, *A mathematical investigation of a Clock and Wavefront model for somitogenesis*, J. Math. Biol. **52** (2006), no. 4, 458–482.

[16] M. Basan, J. Prost, J.-F. Joanny, and J. Elgeti, *Dissipative particle dynamics simulations for biological tissues: rheology and competition*, Phys. Biol. **8** (2011), no. 2, 026014.

[17] R. Bellman and K. L. Cooke, *Differential-difference equations*, Academic Press, New York / London, 1963.

[18] S. Bernard, J. Bélair, and M. C. Mackey, *Sufficient conditions for stability of linear differential equations with distributed delay*, Discrete Cont. Dyn–B **1** (2001), no. 2, 233–256.

[19] Y. Bessho, H. Hirata, Y. Masamizu, and R. Kageyama, *Periodic repression by the bHLH factor Hes7 is an essential mechanism for the somite segmentation clock*, Gene Dev. **17** (2003), no. 12, 1451–1456.

[20] T. Bittig, O. Wartlick, A. Kicheva, M. González-Gaitán, and F. Jülicher, *Dynamics of anisotropic tissue growth*, New J. Phys. **10** (2008), no. 6, 063001.

[21] D. Bratsun, D. Volfson, L. S. Tsimring, and J. Hasty, *Delay-induced stochastic oscillations in gene regulation*, Proc. Natl. Acad. Sci. USA **102** (2005), no. 41, 14593—14598.

[22] X. Cai, *Exact stochastic simulation of coupled chemical reactions with delays*, J. Chem. Phys. **126** (2007), no. 12, 124108.

[23] R. H. Chisholm, B. D. Hughes, K. A. Landman, G. Mayer, and P. M. Whitington, *When are cellular oscillators sufficient for sequential segmentation?*, J. Theor. Biol. **279** (2011), no. 1, 150–160.

[24] J. Cooke and E. C. Zeeman, *A clock and wavefront model for control of the number of repeated structures during animal morphogenesis*, J. Theor. Biol. **58** (1976), 455–476.

[25] R. Corless, G. Gonnet, D. Hare, D. Jeffrey, and D. Knuth, *On the Lambert W function*, Adv. Comput. Math. **5** (1996), 329–359.

[26] T. M. Cover and J. A. Thomas, *Elements of Information Theory*, John Wiley & Sons, Inc., 2006.

[27] F. Cramer, *Forschen und tun, was möglich ist? – Humangenomprojekt und Ethik*, Gentechnologie am Menschen? Wie können Forscher, Arzt und Patient die Verantwortung tragen? (G. Orth, ed.), LIT Verlag Münster, 2002.

[28] C. Dahmann, A. C. Oates, and M. Brand, *Boundary formation and maintenance in tissue development*, Nat. Rev. Genet. **12** (2011), no. 1, 43–55.

[29] T. Danino, O. Mondragón-Palomino, L. Tsimring, and J. Hasty, *A synchronized quorum of genetic clocks*, Nature **463** (2010), no. 7279, 326–330.

[30] I. Daubechies, *The wavelet transform, time-frequency localization and signal analysis*, IEEE T. Inform. Theory **36** (1990), no. 5, 961–1005.

[31] E. A. Delaune, P. François, N. P. Shih, and S. L. Amacher, *Single-Cell-Resolution Imaging of the Impact of Notch Signaling and Mitosis on Segmentation Clock Dynamics*, Dev. Cell **23** (2012), no. 5, 995–1005.

[32] T. d'Eysmond, A. De Simone, and F. Naef, *Analysis of precision in chemical oscillators: implications for circadian clocks*, Phys. Biol. **10** (2013), no. 5, 056005.

[33] M. Dhamala, V. K. Jirsa, and M. Ding, *Enhancement of Neural Synchrony by Time Delay*, Phys. Rev. Lett. **92** (2004), 074104.

[34] J. Dubrulle and O. Pourquié, *fgf8 mRNA decay establishes a gradient that couples axial elongation to patterning in the vertebrate embryo*, Nature **427** (2004), no. 6973, 419–422.

[35] J. C. Dunlap, *Molecular Bases for Circadian Clocks*, Cell **96** (1999), 271–290.

[36] J. C. Dunlap, J. J. Loros, and P. J. DeCoursey, *Chronobiology: Biological timekeeping*, Sinauer Associates, 2004.

[37] P. Dziekan, L. Signon, B. Nowakowski, and A. Lemarchand, *Reaction-diffusion approach to prevertebrae formation: effect of a local source of morphogen*, J. Chem. Phys. **139** (2013), no. 11, 114107.

[38] M. Earl and S. Strogatz, *Synchronization in oscillator networks with delayed coupling: A stability criterion*, Phys. Rev. E **67** (2003), no. 3, 1–4.

[39] M. B. Elowitz and S. Leibler, *A synthetic oscillatory network of transcriptional regulators*, Nature **403** (2000), 335–338.

[40] G. A. Enciso, *A dichotomy for a class of cyclic delay systems*, Math. Biosci. **208** (2007), no. 1, 63–75.

[41] B. Ermentrout, *Type I Membranes, Phase Resetting Curves, and Synchrony.*, Neural Comput. **8** (1996), no. 5, 979–1001.

[42] P. Español and P. Warren, *Statistical mechanics of dissipative particle dynamics*, EPL–Europhys. Lett. **191** (1995), 191–196.

[43] J. Garcia-Ojalvo, M. B. Elowitz, and S. H. Strogatz, *Modeling a synthetic multicellular clock: repressilators coupled by quorum sensing*, Proc. Natl. Acad. Sci. USA **101** (2004), no. 30, 10955–10960.

[44] C. Gardiner, *Stochastic methods: A handbook for the natural and social sciences*, Springer Series in Synergetics, Springer, 2009.

[45] L. Geisler, *Dynamik der Wirbeltiersegmentierung*, Bachelor thesis, Technische Universität Dresden, 2012.

[46] S. Gerschgorin, *Über die Abgrenzung der Eigenwerte einer Matrix*, Izv. Akad. Nauk. USSR Otd. Fiz.-Mat. Nauk (1931), no. 6, 749–754.

[47] N. Geva-Zatorsky, N. Rosenfeld, S. Itzkovitz, R. Milo, A. Sigal, E. Dekel, T. Yarnitzky, Y. Liron, P. Polak, G. Lahav, and U. Alon, *Oscillations and variability in the p53 system*, Mol. Syst. Biol. **2** (2006), no. 1, 1–13.

[48] D. T. Gillespie, *Exact Stochastic Simulation of Coupled Chemical Reactions*, J. Phys. Chem. **81** (1977), no. 25, 2340–2361.

[49] F. Giudicelli, E. M. Ozbudak, G. J. Wright, and J. Lewis, *Setting the tempo in development: an investigation of the zebrafish somite clock mechanism*, PLoS Biol. **5** (2007), no. 6, e150.

[50] L. Glass and M. C. Mackey, *From Clocks to Chaos: The Rhythms of Life*, Princeton paperbacks, Princeton University Press, 1988.

[51] C. Gomez, E. M. Özbudak, J. Wunderlich, D. Baumann, J. Lewis, and O. Pourquié, *Control of segment number in vertebrate embryos*, Nature **454** (2008), no. 7202, 335–339.

[52] Z. Gong and V. Korzh, *Fish Development and Genetics: The Zebrafish and Medaka Models*, Molecular aspects of fish and marine biology, World Scientific, 2004.

[53] M. Hastings, J. S. O'Neill, and E. S. Maywood, *Circadian clocks: regulators of endocrine and metabolic rhythms*, J. Endocrinol. **195** (2007), no. 2, 187–198.

[54] J. F. Heagy, L. M. Pecora, and T. L. Carroll, *Short Wavelength Bifurcations and Size Instabilities in Coupled Oscillator Systems*, Phys. Rev. Lett. **74** (1995), no. 21, 4185–4188.

[55] C. A. Henry, M. K. Urban, K. K. Dill, J. P. Merlie, M. F. Page, C. B. Kimmel, and S. L. Amacher, *Two linked hairy/Enhancer of split-related zebrafish genes, her1 and her7, function together to refine alternating somite boundaries*, Development **129** (2002), no. 15, 3693–3704.

[56] L. Herrgen, S. Ares, L. G. Morelli, C. Schröter, F. Jülicher, and A. C. Oates, *Intercellular Coupling Regulates the Period of the Segmentation Clock*, Curr. Biol. **20** (2010), no. 14, 1244–1253.

[57] S. D. Hester, J. M. Belmonte, J. S. Gens, S. G. Clendenon, and J. A. Glazier, *A Multi-cell, Multi-scale Model of Vertebrate Segmentation and Somite Formation*, PLoS Comput. Biol. **7** (2011), no. 10, e1002155.

[58] S. A. Holley, R. Geisler, and C. Nüsslein-Volhard, *Control of her1 expression during zebrafish somitogenesis by a Delta-dependent oscillator and an independent wave-front activity*, Gene Dev. **14** (2000), no. 13, 1678–1690.

[59] P. J. Hoogerbrugge and J. M. V. A. Koelman, *Simulating Microscopic Hydrodynamic Phenomena with Dissipative Particle Dynamics*, Europhys. Lett. **19** (1992), no. 3, 155.

[60] K. Horikawa, K. Ishimatsu, E. Yoshimoto, S. Kondo, and H. Takeda, *Noise-resistant and synchronized oscillation of the segmentation clock*, Nature **441** (2006), no. 7094, 719–723.

[61] J. Howard, S. W. Grill, and J. S. Bois, *Turing's next steps: the mechanochemical basis of morphogenesis.*, Nat. Rev. Mol. Cell Bio. **12** (2011), no. 6, 392–398.

[62] M. X. G. Ilagan and R. Kopan, *SnapShot: Notch Signaling Pathway*, Cell **128** (2007), no. 6, 1246.

[63] E. Izhikevich, *Phase models with explicit time delays*, Phys. Rev. E **58** (1998), no. 1, 905–908.

[64] J. Jaeger and B. C. Goodwin, *A cellular oscillator model for periodic pattern formation*, J. Theor. Biol. **213** (2001), no. 2, 171–181.

[65] Y. J. Jiang, B. L. Aerne, L. Smithers, C. Haddon, D. Ish-Horowicz, and J. Lewis, *Notch signalling and the synchronization of the somite segmentation clock*, Nature **408** (2000), no. 6811, 475–479.

[66] D. J. Jörg, L. G. Morelli, S. Ares, and F. Jülicher, *Synchronization in the Presence of Phase Shifts and Coupling Delays*, Phys. Rev. Lett. **112** (2014), 174101.

[67] C. Jouve, T. Iimura, and O. Pourquié, *Onset of the segmentation clock in the chick embryo: evidence for oscillations in the somite precursors in the primitive streak*, Development **129** (2002), no. 5, 1107–1117.

[68] C. Jouve, I. Palmeirim, D. Henrique, J. Beckers, A. Gossler, D. Ish-Horowicz, and O. Pourquié, *Notch signalling is required for cyclic expression of the hairy-like gene HES1 in the presomitic mesoderm*, Development **127** (2000), no. 7, 1421–1429.

[69] M. Kærn, T. C. Elston, W. J. Blake, and J. J. Collins, *Stochasticity in gene expression: from theories to phenotypes*, Nat. Rev. Genet. **6** (2005), no. 6, 451–464.

[70] M. Kærn, M. Menzinger, and A. Hunding, *Segmentation and somitogenesis derived from phase dynamics in growing oscillatory media*, J. Theor. Biol. **207** (2000), no. 4, 473–493.

[71] D. M. Kammen, E. Niebur, and H. G. Schuster, *Collective Frequencies and Metastability in Networks of Limit-Cycle Oscillators with Time Delay*, Phys. Rev. Lett. **67** (1991), no. 20, 2753–2757.

[72] H. Kantz and T. Schreiber, *Nonlinear time series analysis*, Cambridge nonlinear science series, Cambridge University Press, 2004.

[73] K. Kotani, I. Yamaguchi, Y. Ogawa, Y. Jimbo, H. Nakao, and G. B. Ermentrout, *Adjoint Method Provides Phase Response Functions for Delay-Induced Oscillations*, Phys. Rev. Lett. **109** (2012), no. 4, 044101.

[74] G. Kozyreff, A. G. Vladimirov, and P. Mandel, *Global Coupling with Time Delay in an Array of Semiconductor Lasers*, Phys. Rev. Lett. **85** (2000), 3809–3812.

[75] A. J. Krol, D. Roellig, M.-L. Dequéant, O. Tassy, E. Glynn, G. Hattem, A. Mushegian, A. C. Oates, and O. Pourquié, *Evolutionary plasticity of segmentation clock networks*, Development **138** (2011), no. 13, 2783–2792.

[76] P. M. Kulesa and S. E. Fraser, *Cell dynamics during somite boundary formation revealed by time-lapse analysis*, Science **298** (2002), no. 5595, 991–995.

[77] Y. Kuramoto, *Chemical Oscillations, Waves, and Turbulence*, Springer-Verlag, Berlin, 1984.

[78] V. M. Lauschke, C. D. Tsiairis, P. François, and A. Aulehla, *Scaling of embryonic patterning based on phase-gradient encoding*, Nature **493** (2013), no. 7430, 101–105.

[79] T. L. Leise, C. W. Wang, P. J. Gitis, and D. K. Welsh, *Persistent cell-autonomous circadian oscillations in fibroblasts revealed by six-week single-cell imaging of PER2::LUC bioluminescence*, PLoS ONE **7** (2012), no. 3, e33334.

[80] A. Lemarchand and B. Nowakowski, *Do the internal fluctuations blur or enhance axial segmentation?*, EPL–Europhys. Lett. **94** (2011), no. 4, 48004.

[81] J. Lewis, *Autoinhibition with Transcriptional Delay: A Simple Mechanism for the Zebrafish Somitogenesis Oscillator*, Curr. Biol. **13** (2003), 1398–1408.

[82] Y. Li, U. Fenger, C. Niehrs, and N. Pollet, *Cyclic expression of esr9 gene in Xenopus presomitic mesoderm*, Differentiation **71** (2003), no. 1, 83–89.

[83] Y. Liu, N. F. Tsinoremas, C. H. Johnson, N. V. Lebedeva, S. S. Golden, M. Ishiura, and T. Kondo, *Circadian orchestration of gene expression in cyanobacteria*, Gene Dev. **9** (1995), no. 12, 1469–1478.

[84] N. MacDonald, *Biological delay systems: linear stability theory*, Cambridge University Press, 1989.

[85] M. C. Mackey and L. Glass, *Oscillation and chaos in physiological control systems*, Science **197** (1977), no. 4300, 287–289.

[86] A. Mara, J. Schroeder, C. Chalouni, and S. A. Holley, *Priming, initiation and synchronization of the segmentation clock by deltaD and deltaC*, Nat. Cell Biol. **9** (2007), no. 5, 523–530.

[87] T. T. Marquez-Lago, A. Leier, and K. Burrage, *Probability distributed time delays: integrating spatial effects into temporal models*, BMC Syst. Biol. **4** (2010), 19.

[88] Y. Masamizu, T. Ohtsuka, Y. Takashima, H. Nagahara, Y. Takenaka, K. Yoshikawa, H. Okamura, and R. Kageyama, *Real-time imaging of the somite segmentation clock: revelation of unstable oscillators in the individual presomitic mesoderm cells*, Proc. Natl. Acad. Sci. USA **103** (2006), no. 5, 1313–1318.

[89] J. Miękisz, J. Poleszczuk, M. Bodnar, and U. Foryś, *Stochastic Models of Gene Expression with Delayed Degradation*, Bull. Math. Biol. **73** (2011), no. 9, 2231–2247.

[90] I. Mihalcescu, W. Hsing, and S. Leibler, *Resilient circadian oscillator revealed in individual cyanobacteria*, Nature **430** (2004), 81–85.

[91] H. Momiji and N. Monk, *Oscillatory Notch-pathway activity in a delay model of neuronal differentiation*, Phys. Rev. E **80** (2009), no. 2, 021930.

[92] N. A. M. Monk, *Oscillatory Expression of Hes1, p53, and NF-κB Driven by Transcriptional Time Delays*, Curr. Biol. **13** (2003), 1409–1413.

[93] L. G. Morelli, S. Ares, L. Herrgen, C. Schröter, F. Jülicher, and A. C. Oates, *Delayed coupling theory of vertebrate segmentation*, HFSP J. **3** (2009), no. 1, 55.

[94] L. G. Morelli and F. Jülicher, *Precision of Genetic Oscillators and Clocks*, Phys. Rev. Lett. **98** (2007), 228101.

[95] M. A. Moreno-Risueno, J. M. Van Norman, A. Moreno, J. Zhang, S. E. Ahnert, and P. N. Benfey, *Oscillating gene expression determines competence for periodic Arabidopsis root branching*, Science **329** (2010), no. 5997, 1306–1311.

[96] P. J. Murray, P. K. Maini, and R. E. Baker, *The clock and wavefront model revisited*, J. Theor. Biol. **283** (2011), no. 1, 227–238.

[97] E. Nagoshi, C. Saini, C. Bauer, T. Laroche, F. Naef, and U. Schibler, *Circadian Gene Expression in Individual Fibroblasts: Cell-Autonomous and Self-Sustained Oscillators Pass Time to Daughter Cells*, Cell **119** (2004), no. 5, 693–705.

[98] Y. Nakamura, F. Tominaga, and T. Munakata, *Clustering behavior of time-delayed nearest-neighbor coupled oscillators*, Phys. Rev. E **49** (1994), no. 6, 4849–4856.

[99] P. Nikunen, M. Karttunen, and I. Vattulainen, *How would you integrate the equations of motion in dissipative particle dynamics simulations?*, Comput. Phys. Commun. **153** (2003), no. 3, 407–423.

[100] B. Novák and J. J. Tyson, *Design principles of biochemical oscillators*, Nat. Rev. Mol. Cell Bio. **9** (2008), no. 12, 981–991.

[101] A. C. Oates and R. K. Ho, *Hairy/E(spl)-related (Her) genes are central components of the segmentation oscillator and display redundancy with the Delta/Notch signaling pathway in the formation of anterior segmental boundaries in the zebrafish*, Development **129** (2002), no. 12, 2929–2946.

[102] A. C. Oates, L. G. Morelli, and S. Ares, *Patterning embryos with oscillations: structure, function and dynamics of the vertebrate segmentation clock*, Development **139** (2012), 625–639.

[103] I. Palmeirim, D. Henrique, D. Ish-Horowicz, and O. Pourquié, *Avian hairy gene expression identifies a molecular clock linked to vertebrate segmentation and somitogenesis*, Cell **91** (1997), no. 5, 639–648.

[104] P. Pathmanathan, J. Cooper, A. Fletcher, G. Mirams, P. Murray, J. Osborne, J. Pitt-Francis, A. Walter, and S. J. Chapman, *A computational study of discrete mechanical tissue models*, Phys. Biol. **6** (2009), no. 3, 036001.

[105] E. T. Pengelley (ed.), *Circannual Clocks: Annual Biological Rhythms*, Academic Press, 1964.

[106] A. Pikovsky and J. Kurths, *Coherence Resonance in a Noise-Driven Excitable System*, Phys. Rev. Lett. **78** (1997), no. 5, 775–778.

[107] A. Pikovsky, M. Rosenblum, and J. Kurths, *Synchronization: A Universal Concept in Nonlinear Sciences*, Cambridge Nonlinear Science Series, Cambridge University Press, 2003.

[108] R. H. Pletcher, J. C. Tannehill, and D. Anderson, *Computational fluid mechanics and heat transfer*, 3rd ed., Series in Computational and Physical Processes in Mechanics and Thermal Sciences, Taylor & Francis, 2012.

[109] D. A. Potoyan and P. G. Wolynes, *On the dephasing of genetic oscillators*, Proc. Natl. Acad. Sci. USA **111** (2014), no. 6, 2391—2396.

[110] O. Pourquié, *The Segmentation Clock: Converting Embryonic Time into Spatial Pattern*, Science **301** (2003), no. July, 10–12.

[111] ———, *Vertebrate segmentation: from cyclic gene networks to scoliosis*, Cell **145** (2011), no. 5, 650–663.

[112] R. Quian Quiroga, A. Kraskov, T. Kreuz, and P. Grassberger, *Performance of different synchronization measures in real data: A case study on electroencephalographic signals*, Phys. Rev. E **65** (2002), no. 4, 041903.

[113] A. Raj and A. van Oudenaarden, *Nature, nurture, or chance: stochastic gene expression and its consequences*, Cell **135** (2008), no. 2, 216–226.

[114] J. Ranft, M. Basan, J. Elgeti, J.-F. Joanny, J. Prost, and F. Jülicher, *Fluidization of tissues by cell division and apoptosis*, Proc. Natl. Acad. Sci. USA **107** (2010), no. 49, 20863—20868.

[115] J. M. Raser and E. K. O'Shea, *Noise in gene expression: origins, consequences, and control*, Science **309** (2005), no. 5743, 2010–2013.

[116] D. L. Richmond and A. C. Oates, *The segmentation clock: inherited trait or universal design principle?*, Curr. Opin. Genet. Dev. **22** (2012), no. 6, 600–606.

[117] I. H. Riedel-Kruse, C. Müller, and A. C. Oates, *Synchrony Dynamics During Initiation, Failure, and Rescue of the Segmentation Clock*, Science **317** (2007), no. 5846, 1911–1915.

[118] D. Roellig, L. G. Morelli, S. Ares, F. Jülicher, and A. C. Oates, *Enhanced SnapShot: The Segmentation Clock*, Cell **145** (2011), no. 5, 800–800.e1.

[119] K. W. Rogers and A. F. Schier, *Morphogen Gradients: From Generation to Interpretation*, Annu. Rev. Cell Dev. Biol. **27** (2011), 377–407.

[120] M. G. Rosenblum and A. S. Pikovsky, *Controlling Synchronization in an Ensemble of Globally Coupled Oscillators*, Phys. Rev. Lett. **92** (2004), no. 11, 114102.

[121] H. Sakaguchi and Y. Kuramoto, *A Soluble Active Rotator Model Showing Phase Transitions via Mutual Entrainment*, Prog. Theor. Phys. **76** (1986), no. 3, 576–581.

[122] S. A. Sandersius and T. J. Newman, *Modeling cell rheology with the Subcellular Element Model*, Phys. Biol. **5** (2008), no. 1, 015002.

[123] A. F. Sarrazin, A. D. Peel, and M. Averof, *A segmentation clock with two-segment periodicity in insects*, Science **336** (2012), no. 6079, 338–341.

[124] G. Schaller and M. Meyer-Hermann, *Multicellular tumor spheroid in an off-lattice Voronoi-Delaunay cell model*, Phys. Rev. E **71** (2005), no. 5, 051910.

[125] J. Schindelin, I. Arganda-Carreras, E. Frise, V. Kaynig, M. Longair, T. Pietzsch, S. Preibisch, C. Rueden, S. Saalfeld, B. Schmid, J.-Y. Tinevez, D. J. White, V. Hartenstein, K. Eliceiri, P. Tomancak, and A. Cardona, *Fiji: an open-source platform for biological-image analysis*, Nat. Methods **9** (2012), no. 7, 676–682.

[126] C. Schröter, *Segmentation Clock Dynamics in Zebrafish her Gene Mutants*, Ph.D. thesis, TU Dresden, 2009.

[127] C. Schröter, S. Ares, L. G. Morelli, A. Isakova, K. Hens, D. Soroldoni, M. Gajewski, F. Jülicher, S. J. Maerkl, B. Deplancke, and A. C. Oates, *Topology and Dynamics of the Zebrafish Segmentation Clock Core Circuit*, PLoS Biol. **10** (2012), no. 7, e1001364.

[128] C. Schröter, L. Herrgen, A. Cardona, G. J. Brouhard, B. Feldman, and A. C. Oates, *Dynamics of zebrafish somitogenesis*, Dev. Dynam. **237** (2008), no. 3, 545–553.

[129] H. G. Schuster and P. Wagner, *Mutual entrainment of two limit cycle oscillators with time delayed coupling*, Prog. Theor. Phys. **81** (1989), no. 5, 939–945.

[130] B. Schwanhäusser, D. Busse, N. Li, G. Dittmar, J. Schuchhardt, J. Wolf, W. Chen, and M. Selbach, *Global quantification of mammalian gene expression control*, Nature **473** (2011), no. 7347, 337–342.

[131] L. P. Shearman, *Interacting Molecular Loops in the Mammalian Circadian Clock*, Science **288** (2000), no. 5468, 1013–1019.

[132] H. Shinozaki and T. Mori, *Robust stability analysis of linear time-delay systems by Lambert function: Some extreme point results*, Automatica **42** (2006), no. 10, 1791–1799.

[133] D. Soroldoni, D. J. Jörg, L. G. Morelli, D. L. Richmond, J. Schindelin, F. Jülicher, and A. C. Oates, *A Doppler effect in embryonic pattern formation*, Science, in press.

[134] D. Soroldoni and A. C. Oates, *Live transgenic reporters of the vertebrate embryo's Segmentation Clock*, Curr. Opin. Genet. Dev. **21** (2011), no. 5, 600–605.

[135] C. Soza-Ried, E. Öztürk, D. Ish-Horowicz, and J. Lewis, *Pulses of Notch activation synchronise oscillating somite cells and entrain the zebrafish segmentation clock*, Development **141** (2014), no. 8, 1780–1788.

[136] D. B. Sparrow, G. Chapman, A. J. Smith, M. Z. Mattar, J. A. Major, V. C. O'Reilly, Y. Saga, E. H. Zackai, J. P. Dormans, B. A. Alman, L. McGregor, R. Kageyama, K. Kusumi, and S. L. Dunwoodie, *A mechanism for gene-environment interaction in the etiology of congenital scoliosis*, Cell **149** (2012), no. 2, 295–306.

[137] S. H. Strogatz, *Nonlinear Dynamics and Chaos: With Applications to Physics, Biology, Chemistry and Engineering*, Westview Press, 2001.

[138] S. H. Strogatz and I. Stewart, *Coupled oscillators and biological synchronization*, Sci. Am. **269** (1993), no. 6, 102–109.

[139] H. B. Tiedemann, E. Schneltzer, S. Zeiser, I. Rubio-Aliaga, W. Wurst, J. Beckers, G. K. H. Przemeck, and M. Hrabé de Angelis, *Cell-based simulation of dynamic expression patterns in the presomitic mesoderm*, J. Theor. Biol. **248** (2007), no. 1, 120–129.

[140] G. Tkačik, C. G. Callan, and W. Bialek, *Information capacity of genetic regulatory elements*, Phys. Rev. E **78** (2008), no. 1, 1–17.

[141] G. Tkačik, G. G. Callan, and W. Bialek, *Information flow and optimization in transcriptional regulation*, Proc. Natl. Acad. Sci. USA **105** (2008), no. 34, 12265–12270.

[142] G. Tkačik and A. M. Walczak, *Information transmission in genetic regulatory networks: a review*, J. Phys. Condens. Mat. **23** (2011), no. 15, 153102.

[143] C. Torrence and G. P. Compo, *A practical guide to wavelet analysis*, B. Am. Meteorol. Soc. **79** (1998), no. 1, 61–78.

[144] Y. M. Tousi, V. Pourahmad, and E. Afshari, *Delay Coupled Oscillators for Frequency Tuning of Solid-State Terahertz Sources*, Phys. Rev. Lett. **108** (2012), no. 2, 234101.

[145] L. S. Tsimring, *Noise in biology*, Rep. Prog. Phys. **77** (2014), no. 2, 026601.

[146] K. Uriu, S. Ares, A. C. Oates, and L. G. Morelli, *Optimal cellular mobility for synchronization arising from the gradual recovery of intercellular interactions*, Phys. Biol. **9** (2012), no. 3, 036006.

[147] ———, *Dynamics of mobile coupled phase oscillators*, Phys. Rev. E **87** (2013), no. 3, 032911.

[148] K. Uriu, L. G. Morelli, and A. C. Oates, *Interplay between intercellular signaling and cell movement in development*, Semin. Cell Dev. Biol. (2014), 1–7.

[149] K. Uriu, Y. Morishita, and Y. Iwasa, *Random cell movement promotes synchronization of the segmentation clock*, Proc. Natl. Acad. Sci. USA **107** (2010), no. 11, 4979–4984.

[150] F. J. van Eeden, M. Granato, U. Schach, M. Brand, M. Furutani-Seiki, P. Haffter, M. Hammerschmidt, C. P. Heisenberg, Y. J. Jiang, D. A. Kane, R. N. Kelsh, M. C. Mullins, J. Odenthal, R. M. Warga, M. L. Allende, E. S. Weinberg, and C. Nüsslein-Volhard, *Mutations affecting somite formation and patterning in the zebrafish,* Danio rerio, Development **123** (1996), no. 1, 153–164.

[151] J. M. G. Vilar, H. Y. Kueh, N. Barkai, and S. Leibler, *Mechanisms of noise-resistance in genetic oscillators*, Proc. Natl. Acad. Sci. USA **99** (2002), no. 9, 5988–5992.

[152] A. Wagner, *Energy Constraints on the Evolution of Gene Expression*, Mol. Biol. Evol. **22** (2005), no. 6, 1365–1374.

[153] J. Waterhouse, T. Reilly, G. Atkinson, and B. Edwards, *Jet lag: trends and coping strategies*, Lancet **369** (2007), no. 9567, 1117–1129.

[154] A. B. Webb, D. Soroldoni, A. Oswald, J. Schindelin, and A. C. Oates, *Generation of dispersed presomitic mesoderm cell cultures for imaging of the zebrafish segmentation clock in single cells*, J. Vis. Exp., in press.

[155] J. Wei and D. Fan, *Hopf Bifurcation Analysis in a Mackey–Glass System*, Int. J. Bifurcat. Chaos **17** (2007), no. 06, 2149–2157.

[156] L. Wetzel, *Effect of distributed delays in systems of coupled phase oscillators*, Ph.D. thesis, TU Dresden, 2012.

[157] A. Wilden, *System and Structure: Essays in Communication and Exchange*, Social Science Paperbacks Series, Tavistock, 1977.

[158] A. T. Winfree, *The Geometry of Biological Time*, 2nd ed., Springer-Verlag New York, Inc., 2001.

[159] Wolfram Research, Inc., *Mathematica, Version 9.0*, Champaign, Illinois, 2012.

[160] G. J. Wright, F. Giudicelli, C. Soza-Ried, A. Hanisch, L. Ariza-McNaughton, and J. Lewis, *DeltaC and DeltaD interact as Notch ligands in the zebrafish segmentation clock*, Development **138** (2011), no. 14, 2947–2956.

[161] W. F. Wu and Y. K. Lin, *Cumulant-neglect closure for non-linear oscillators under random parametric and external excitations*, Int. J. Nonlin. Mech. **19** (1984), no. 4, 349–362.

[162] S. Yamaguchi, H. Isejima, T. Matsuo, R. Okura, K. Yagita, M. Kobayashi, and H. Okamura, *Synchronization of cellular clocks in the suprachiasmatic nucleus*, Science **302** (2003), no. 5649, 1408–1412.

[163] M. K. S. Yeung and S. H. Strogatz, *Time Delay in the Kuramoto Model of Coupled Oscillators*, Phys. Rev. Lett. **82** (1999), no. 3, 648–651.

[164] D. Zwicker, D. K. Lubensky, and P. R. ten Wolde, *Robust circadian clocks from coupled protein-modification and transcription–translation cycles*, Proc. Natl. Acad. Sci. USA **107** (2010), no. 52, 22540–22545.

Versicherung

Hiermit versichere ich, dass ich die vorliegende Arbeit ohne unzulässige Hilfe Dritter und ohne Benutzung anderer als der angegebenen Hilfsmittel angefertigt habe; die aus fremden Quellen direkt oder indirekt übernommenen Gedanken sind als solche kenntlich gemacht. Die Arbeit wurde bisher weder im Inland noch im Ausland in gleicher oder ähnlicher Form einer anderen Prüfungsbehörde vorgelegt.

Die Arbeit wurde am Max-Planck-Institut für Physik komplexer Systeme angefertigt und von Prof. Frank Jülicher und Dr. Luis G. Morelli betreut.

Ich erkenne die Promotionsordnung der Fakultät Mathematik und Naturwissenschaften der Technischen Universität Dresden an.

DAVID JOSEF JÖRG